HOKKAIDO UNIVERSITY

Title	IMPACT OF FINITE VEGETATION PATCHES ON FLOW AND BED MORPHOLOGY IN OPEN CHANNELS
Author(s)	金, 亨碩
Degree Grantor	北海道大学
Degree Name	博士(工学)
Dissertation Number	甲第11170号
Issue Date	2013-12-25
DOI	https://doi.org/10.14943/doctoral.k11170
Doc URL	https://hdl.handle.net/2115/54650
Type	doctoral thesis
File Information	Kim_HyungSuk.pdf

Hokkaido University Collection of Scholarly and Academic Papers : HUSCAP

IMPACT OF FINITE VEGETATION PATCHES ON FLOW AND BED MORPHOLOGY IN OPEN CHANNELS

By

Hyung Suk Kim

A THESIS SUBMITTED IN PARTIAL FULFILLMENT OF THE

REQUIREMENTS FOR THE DEGREE OF DOCTOR OF ENGINNERING

Examination : Prof. Yasuyuki Shimizu

Prof. Norihiro Izumi

Assoc. Prof. Ichiro Kimura

Assoc. Prof. Tomohito Yamada

DOCTOR'S THESIS

DIVISION OF FIELD ENGINEERING FOR ENVIRONMENT

GRADUATE SCHOOL OF ENGINEERING, HOKKAIDO UNIVERSITY

December, 2013

ABSTRACT

For the planting management and stream restoration, isolated patches of vegetation are practical for improving stream habitat and ecology. Comprehensive understandings of flows and bed morphological changes with finite patches of vegetation are of high interest to practitioners and engineers to design stream restorations. This study is to investigate morphological responses to finite patches of vegetation in open channels and understand the sediment transport and scour processes around vegetation by means of laboratory experiments and numerical computations.

Firstly, the effect of a finite patch of vegetation on flow and bed morphology in an open channel was investigated. Laboratory experiments were carried out with a mobile bed included a finite patch placed along a side wall of the channel and various configurations (patch density, submergence ratio and obstruction ratio) were considered. Two flow conditions below and above threshold of sediment motion, were tested. Erosion and deposition near the patch of vegetation were analyzed.

Secondly, morphological responses to a finite patch in an open channel with erodible bank were described by employing laboratory experiments and numerical simulations. The patch was modeled as circular cylinders with a staggered array, and it was located in the middle of the channel. The morphological behavior of a channel with erodible bank was assessed. Numerical simulations were performed and the sensitivity to parameters related to sediment transport within the patch was investigated. The simulated results for erosion and deposition near the patch were compared with experimental data and a good agreement was found.

Thirdly, development of local scour pool produced by finite patches of vegetation was investigated by means of laboratory experiments and numerical simulations. Two finite patches were located along both side walls of the channel. Diverse ratio of the patch width was considered to examine impacts of spacing between patches with various patch densities. Local erosion at the leading edge and between patches was analyzed. Numerical simulations with adopting bed correction model were performed and compared with experimental data. Numerical model employing bed correction model demonstrated that the development of local scour pool near the patches can be

improved.

Lastly, in order to investigate local scour around cylinders, numerical simulations were performed by large-eddy simulation (LES). The sediment was simulated as particles in a Lagrangian framework and linked to the bed morphodynamic, which were directly incorporated with instantaneous flow on the bed. The numerical model was validated by comparison with experimental data available in literatures. After validation, the impact of cylinder spacing on local scour and deposition patterns was assessed. In addition, the global and local scour around square cylinder groups was examined and the influence of cylinder array on scour was assessed. Simulated maximum scour depth was compared with experimental data and showed a reasonable agreement.

Dedication

To my beloved family, Hanjeong Kim, Jeongsuk Kang, and Wanseok Kim

Acknowledgement

I wish to thank my advisor, Associated Professor Ichiro Kimura, for not only giving me the opportunity to study at the Hydraulic Research Laboratory, Hokkaido University, but also for his guidance and support throughout the course of my research. I would also like to thank Professors Yasuyuki Shimizu for accepting me as his student, and valuable suggestions and feedback

I wish to deeply thank Professor Sung Bum Yoon at Hanyang University, Ansan, South Korea, who encouraged me to go abroad to do further studies.

I am grateful to all my family, in particular, to my father and mother, for their love and support to me. Their unconditional support helped me complete my Ph.D. program. I thank my younger brother, Wan Seok Kim, for taking care of our parents while I was in Japan and also for his support and encouragement.

I would like to thank my current and previous lab mates, especially, Toshiki Iwasaki and Mohamed Nabi. I also wish to express my gratitude to HYCERG members in Hanyang University for their unconditional love.

I would like to give my deepest appreciation to my friend in Korea, Jeong Hyeon Park, Min Beom Ko, Bong Hun Ko, Maeng Yong Ko, Haeng Nam Ko and Seong Jun Mun, and endless support which enabled me to complete my Ph.D. work successfully.

Table of Contents

ABSTRACT ii

Dedication iv

Acknowledgement v

Table of Contents vi

List of Figures x

List of Tables xvi

CHAPTER 1 INTRODUCTION 1

1.1 BACKGROUND AND MOTIVATIONS 1

1.2 RESEARCH OBJECTIVES 3

1.3 ORGANIZATION OF THSIS 3

CHAPTER 2 CHARATERISTICS OF BED MORHOLOGICAL CHANGES AROUND A FINITE PATCH OF VEGETATION 6

2.1 INTRODUCTION 6

2.2 EXPERIMENTAL SET UP 9

2.3 RESULTS AND DISCUSSION ON LABORATORY EXPERIMENTS 14

2.3.1 Flow field 14

2.3.2 Bed morphology with flow below the threshold of sediment motion 19

2.3.2.1 Bed elevation 19

2.3.2.2 Longitudinal bed profiles 21

2.3.2.3 Scour in response to the patch 23

2.3.3 Bed morphology with flow above the threshold of sediment motion 25

2.3.3.1 Bed elevation 25

2.3.3.2 Longitudinal bed profiles 27

2.3.3.3 Scour in response to the patch 31

2.3.3.4 Deposition in response to the patch 32

2.4 SUMMARY 35

CHAPTER 3 EFFECT OF A PATCH OF VEGETATION IN OPEN CHANNEL FLOWS WITH ERODIBLE BANK 36

3.1 INTRODUCTION 36

3.2 EXPERIMENTAL SET UP 39

3.3 NUMERICAL MODEL 41

3.3.1 Governing equations of flow 41

3.3.2 Sediment transport models 45

3.3.3 Numerical scheme and model set up 47

3.4 RESULTS AND DISSCUSSION 48

3.4.1 Validation 48

3.4.2 Sensitivity to parameters 50

3.4.3 Variation of bed topography 52

3.4.4 Spatial variation of bed morphology 56

3.4.5 Channel widening and deposition near the patch 62

3.4.6 Change in flow and bank erosion 65

3.5 SUMMARY 68

CHAPTER 4 SCOUR AND DEPOSITION PATTERNS DUE TO MUTUAL INTERACTIONS OF FINITE PATCHES OF VEGETATION 69

4.1 INTRODUCTION 69

4.2 EXPERIMENTAL SET UP 73

4.3 COMPUTATIONAL MODEL 75

4.3.1 Governing equations 75

4.3.2 Turbulence closure 77

4.3.3 Sediment transport model 78

4.3.4 Bed correction model 80
4.3.5 Computational scheme and model set up 81
4.4 RESULTS AND DISCUSSION 81
4.4.1 Validation of the flow model 81
4.4.2 Flow field 83
4.4.3 Morphological change 86
4.4.3.1 Changes in bed topography 86
4.4.3.2 Lateral bed variation near the finite patches 89
4.4.3.3 Scour and deposition 97
4.5 SUMMARY 99
CHAPTER 5 NUMERICAL INVESTIGATION OF LOCAL SCOUR AROUND CYLINDERS IN A TURBULENT FLOW 101
5.1 INTRODUCTION 101
5.2 HYDRODYNAMIC MODEL 104
5.2.1 Governing equations of flow 104
5.2.2 Numerical methods 105
5.3 SEDIMENT TRANSPORT MODEL 106
5.4 MORPHODYNAMIC MODEL 108
5.5 VALIDATION 108
5.5.1 Flow field 108
5.5.2 Bed morphodynamics 110
5.6 COMPUTATIONAL EXPERIMENTS 113
5.7 RESULTS 115
5.7.1 Local scour around a single cylinder 115
5.7.2 Side-by-side arrangement of cylinders 117
5.7.3 Tandem arrangement of cylinders 124

5.7.4 Comparison of maximum scour depth 133

5.8 SUMMARY 134

CHAPTER 6 THREE-DIMENSIONAL NUMERICAL COMPUTATIONS OF LOCAL AND GLOBAL SCOUR AROUND CYLINDER GROUPS 136

6.1 INTRODUCTION 136

6.2 NUMERICAL COMPUTATIONS 140

6.3 RESULTS AND DISCUSSION 142

6.3.1 Grid arrangement 142

6.3.1.1 Morphological process 142

6.3.1.2 Lateral and longitudinal bed profiles 147

6.3.1.3 Bed topography 151

6.3.1.4 Time evolution of the bed 154

6.3.2 Staggered arrangement 159

6.3.3 Maximum local and global scour 163

6.4 SUMMARY 165

CHAPTER 7 CONCLUSIONS 167

7.1. CONCLUSIONS 167

REFERENCES 174

List of Figures

Fig. 1.1 Itachi river before (top: 1981) and after (bottom: 1993) river restoration. These photos were taken by yoshimura (http://www.a-rr.net/) 2

Fig. 2.1 Schematic diagrams of the laboratory experiment. 10

Fig. 2.2 Sensitivity of electromagnetic current meter where the solid symbols denote data of the longitudinal velocity, u, and the empty symbols indicate data of the transverse velocity, v. (Square symbol is the first measurement; circular symbol is the second measurement; nabla symbol is the third measurement.) 13

Fig. 2.3 Layout of the divided channel. 14

Fig. 2.4 Velocity vector and profiles. 16

Fig. 2.5 Variation of measured velocity according to flow blockage where dashed dot lines indicate the 95 % confidence limits. 17

Fig. 2.6 Conceptual picture for flow field near the patch of vegetation (Rominger and Nepf, 2011). 18

Fig. 2.7 Bed elevation; (a) $\lambda W_v = 0.98$($W_v = 0.3$ m, $\phi = 0.013$), (b) $\lambda W_v = 1.62$($W_v = 0.3$ m, $\phi = 0.021$), (c) $\lambda W_v = 3.57$($W_v = 0.3$ m, $\phi = 0.047$) (d) $\lambda W_v = 2.58$($W_v = 0.3$ m, $\phi = 0.034$). Flow is left to right and solid lines denote the patch. 20

Fig. 2.8 Laterally averaged longitudinal bed profiles; (a) Region (Ⅰ) with $\lambda W_v = 0.65$, 1.10 and 2.38 ($W_v = 0.2$ m), (b) Region (Ⅱ) with $\lambda W_v = 0.65$, 1.10 and 2.38 ($W_v = 0.2$ m), (c) Region (Ⅰ) with $\lambda W_v = 1.62$, 3.57 and 1.17 ($W_v = 0.3$ m), (d) Region (Ⅱ) with $\lambda W_v = 1.62$, 3.57 and 1.17 ($W_v = 0.3$ m). 22

Fig. 2.9 Scour depth according to the flow blockage under the flow below the threshold of sediment motion. 24

Fig. 2.10 Bed elevation; (a) $\lambda W_v = 0.65$($W_v = 0.2$ m, $\phi = 0.013$), (b) $\lambda W_v = 1.1$($W_v = 0.2$ m, $\phi = 0.021$), (c) $\lambda W_v = 2.38$($W_v = 0.2$ m, $\phi = 0.047$) (d) $\lambda W_v = 1.72$($W_v = 0.2$ m, $\phi = 0.034$). Flow is left to right and solid lines denote the patch. 26

Fig. 2.11 Laterally averaged longitudinal bed profiles; (a) $\lambda W_v = 0.65$($W_v = 0.2$ m, $L_v = 0.5$ m, $\phi = 0.013$), (b) $\lambda W_v = 1.1$($W_v = 0.2$ m, $L_v = 0.5$ m, $\phi = 0.021$),

(c) λW_v = 2.38(W_v = 0.2 m, L_v = 0.5 m, ϕ = 0.047), (d) λW_v = 1.1(W_v = 0.2 m, L_v = 1.0 m, ϕ = 0.021), (e) λW_v = 1.62(W_v = 0.3 m, L_v = 0.5 m, ϕ = 0.021), (f) λW_v = 1.2(W_v = 0.3 m, L_v = 0.5 m, ϕ = 0.015).....29

Fig. 2.12 Distance of deposition mound within and behind the patch, Ld, according to velocity, u_1, normalized by upstream velocity. 31

Fig. 2.13 Scour depth Scour depth according to the flow blockage under the flow above the threshold of sediment motion, where the solid symbols denote data of the emergent patches and the empty symbols denote data of the submerged patches. 32

Fig. 2.14 Ratio of depositional volume to input sediment according to the flow rate through the patch where the solid symbols denote data of the emergent patches and the empty symbols denote data of the submerged patches. 33

Fig. 2.15 Ratio of depositional volume to input sediment according to the flow rate through the patch where the solid symbols denote data of the emergent patches and the empty symbols denote data of the submerged patches. (when W_v = 0.2 m and L_v = 0.3 m, the data symbol is square; when W_v = 0.2 m and L_v = 0.5 m, the data symbol is circle; when W_v = 0.2 m and L_v = 1.0m, the data symbol is nabla; when W_v = 0.3 m and L_v = 0.5 m, the data symbol is diamond; when W_v = 0.4 m and L_v = 0.5 m, the data symbol is right-triangle.) 34

Fig. 3.1 Schematic diagram of the experimental flume. 40

Fig. 3.2 Definitions of U_v and U_{vm} in vegetation region (Stone and Shen, 2002). 43

Fig. 3.3 Definition of bank erosion process. Dash line is a slope before bank collapse and dot line is a slope after bank collapse. 47

Fig. 3.4 Comparison of experimental and computed profiles of the depth-averaged velocity and Reynolds stress. 49

Fig. 3.5 Comparison of cross-sectional bed elevation without the patch. 50

Fig. 3.6 Longitudinal bed profiles at y = 0.22m for the LD patch of Case 4. 52

Fig. 3.7 Comparison of variation of bed elevation between experiment and computation for case 3: (a) Non-vegetated channel; (b) Low density (LD); (c) Medium density (MD); (d) High density (HD). Flow is from left to right.

Solid line in the domain is a patch of vegetation. 54
Fig. 3.8 Local spatial patterns around the patch for case 2: (a) Low density (LD); (b) Medium density (MD); (c) High density (HD). Flow is from left to right. . 56
Fig. 3.9 Comparison of bed elevation between experiment and computation for case 2: (a) Low density; (b) Medium density; (c) High density. 57
Fig. 3.10 Longitudinal bed profiles at y = 0.22m for case 4: (a) low density (LD); (b) Medium density (MD); (c) High density (HD). 60
Fig. 3.11 Comparison of sediment deposition within and near the patch. 62
Fig. 3.12 Comparison of the widening rate with time: (a) Case 1; (b) Case 2; (c) Case 3; (d) Case 4. 63
Fig. 3.13 Maximum widening rate according to (a) the ratio of the patch width and (b) the ratio of the patch length. 64
Fig. 3.14 Sediment deposition volume within and around the patch according to (a) the ratio of the patch width and (b) the ratio of the patch length. 65
Fig. 3.15 Lateral profile of unit discharges and bed profiles with different times at y = 4.3m for case 2 of the MD patch. 66
Fig. 3.16 Lateral profile of unit discharges and bed profiles with different times at y = 4.3 m for case 2 of the MD patch. 67
Fig. 4.1 Schematic view of the flow and bed morphology near the finite patches. .. 72
Fig. 4.2 Experimental channel; a) Top view, b) Initial channel with patches in a cross section, c) Picture of the channel near the patches. 73
Fig. 4.3 Concept of the bed correction model. 80
Fig. 4.4 Schematic diagram of the model validation (Zong and Nepf, 2010). 82
Fig. 4.5 Comparison of observed and simulated results; a) depth-averaged velocity (x = 6.7 m), b) Reynolds stress (x = 6.7 m), c) turbulence intensity (y = 0.2 m). 82
Fig. 4.6 Contour of flow velocity with streamlines. Flow is left to right and the dash lines denote patches of vegetation. 84
Fig. 4.7 Flow velocity according to the flow blockage, $2\lambda W_v$. 86
Fig. 4.8 Flow rate through the patches with respect to patch density. 86
Fig. 4.9 Change in bed topography. 88

Fig. 4.10 Comparison of lateral bed profiles with emergent and submerged patches between experimental and computational data at x = 2.55 m; a) $2\lambda W_v$ = 1.0 (W_v = 0.02 m, λ = 25 m^{-1}, emergent), b) $2\lambda W_v$ = 2.0 (W_v = 0.04 m, λ = 25 m^{-1}, emergent), c) $2\lambda W_v$ = 3.0 (W_v = 0.06 m, λ = 25 m^{-1}, emergent), d) $2\lambda W_v$ = 4.0 (W_v = 0.08 m, λ = 25 m^{-1}, emergent), e) $2\lambda W_v$ = 1.875 (W_v = 0.06 m, λ = 15.63 m^{-1}, submerged), f) $2\lambda W_v$ = 2.5 (W_v = 0.08 m, λ = 15.63 m^{-1}, submerged). Solid symbols (experimental data), dash dot lines (computational data with angle of repose, 25°), solid lines (computational data with angle of repose, 35°), short dash lines (computational data with angle of repose, 45°) and dash lines (without angle of repose). 90

Fig. 4.11 Longitudinal profiles of experiment and computation along the center of the channel with emergent and submerged patches; a) $2\lambda W_v$ = 2.0 (W_v = 0.04 cm, λ = 25 m^{-1}, emergent), b) $2\lambda W_v$ = 3.0 (W_v = 0.06 cm, λ = 25 m^{-1}, emergent), c) $2\lambda W_v$ = 1.875 (W_v = 0.06 cm, λ = 15.63 m^{-1}, submerged), d) $2\lambda W_v$ = 4.0 (W_v = 0.08 cm, λ = 25 m^{-1}, emergent). 93

Fig. 4.12 Location of the maximum scour region with respect to the flow blockage, $2\lambda W_v$. 94

Fig. 4.13 Flow rate through the patches with respect to patch density. 95

Fig. 4.14 Maximum scour depth according to the flow blockage; a) experimental data of emergent and submerged patches, b) computational data of emergent and submerged patches, c) computation with different angle of repose, d) computation with different submergence ratio. 97

Fig. 4.15 Scoured volume around the patches according to the scour depth; a) experiment b) computation. 98

Fig. 5.1 Time-averaged streamwise velocity profiles at five locations. 109

Fig. 5.2 Streamwise turbulence intensity profiles at five locations. 110

Fig. 5.3 Comparison of bed topography and time evolution of maximum scour depth; (a) Bed topography (cm) at the equilibrium state; computation (top) and experiment (bottom), (b) Time evolution of maximum scour depth. 112

Fig. 5.4 Computational domain for the side-by-side arrangement of cylinders. 114

Fig. 5.5 Computational grid near the cylinders in a horizontal plane. 115

Fig. 5.6 Bed topography and time evolution of scour depth and deposition for a single cylinder; (a) Bed topography at the equilibrium state, (b) Time evolution of scour depth and deposition. 116
Fig. 5.7 Three-dimensional process of scour development around the side-by-side arrangement of cylinders of s / D = 1.25; (a) 1 min, (b) 5min, (c) 30 min, (d) 60 min, (e) 108 min, (f) streamlines around two cylinders at the equilibrium state. 118
Fig. 5.8 Three-dimensional process of scour development around the side-by-side arrangement of cylinders of s / D = 5.0; (a) 1 min, (b) 5min, (c) 30 min, (d) 60 min, (e) 108 min, (f) streamlines around two cylinders at the equilibrium state. 119
Fig. 5.9 Contour of bed elevations at the equilibrium state for the side-by-side arrangement; (a) s / D = 1.25, (b) s / D =1.875, (c) s / D = 2.5, (d) s / D = 3.75, (e) s / D = 5.0. 122
Fig. 5.10 Time evolutions of scour depth and deposition; (a) s / D = 1.25, (b) s / D =1.875, (c) s / D = 2.5, (d) s / D = 3.75, (e) s / D = 5.0 124
Fig. 5.11 Three-dimensional process of scour development around the tandem arrangement of cylinders of s / D = 1.25; (a) 1 min, (b) 5min, (c) 30 min, (d) 60 min, (e) 108 min, (f) streamlines around two cylinders at the equilibrium state. 125
Fig. 5.12 Three-dimensional process of scour development around the tandem arrangement of cylinders of s / D = 5.0; (a) 1 min, (b) 5min, (c) 30 min, (d) 60 min, (e) 108 min, (f) streamlines around two cylinders at the equilibrium state. 127
Fig. 5.13 Contour of bed elevations at the equilibrium state for the side-by-side arrangement; (a) s / D = 1.25, (b) s / D = 2.5, (c) s / D = 3.75, (d) s / D = 5.0 130
Fig. 5.14 Time evolutions of scour depth and deposition; (a) s / D = 1.25, (b) s / D = 2.5, (c) s / D = 3.75, (d) s / D = 5.0 132
Fig. 5.15 Maximum scour depth as a function of the distance of cylinders, G; (a) side-by-side arrangement, (b) tandem arrangement 133

Fig. 6.1 Computational domain with the cylinder group. 141
Fig. 6.2 Computational grid near the cylinder group in a horizontal plane. 141
Fig. 6.3 Three-dimensional process of scour development around the cylinder group of $s / D = 1.25$; (a) 1 min, (b) 5 min, (c) 20 min, (d) equilibrium state. 142
Fig. 6.4 Three-dimensional process of scour development around the cylinder group of $s / D = 2.5$; (a) 1 min, (b) 5 min, (c) 20 min, (d) equilibrium state. 144
Fig. 6.5 Three-dimensional process of scour development around the cylinder group of $s / D = 5.0$; (a) 1 min, (b) 5 min, (c) 20 min, (d) equilibrium state. 146
Fig. 6.6 Lateral and longitudinal bed profiles around the cylinder group. 150
Fig. 6.7 Contour of bed elevations at the equilibrium state around the cylinder group; (a) single cylinder, (b) $s / D = 1.25$, (c) $s / D = 1.875$, (d) $s / D = 2.5$, (b) $s / D = 1.25$, (e) $s / D = 3.75$. (f) $s / D = 5.0$. 152
Fig. 6.8 Time evolution of scour and deposition; (a) single cylinder, (b) $s / D = 1.25$, (c) $s / D = 1.875$, (d) $s / D = 2.5$, (b) $s / D = 1.25$, (e) $s / D = 3.75$. (f) $s / D = 5.0$. 157
Fig. 6.9 Three-dimensional process of scour development around the cylinder group with the staggered arrangement of $s / D = 5.0$; (a) 1 min, (b) 5 min, (c) 20 min, (d) equilibrium state. 160
Fig. 6.10 Time evolution of scour and deposition around the cylinder group with the staggered arrangement of $s / D = 5.0$. 162
Fig. 6.11 Time evolution of scour and deposition around the cylinder group with the staggered arrangement of $s / D = 5.0$. 164

List of Tables

Table 2.1 Experimental conditions of flow..... 11
Table 2.2 Experimental parameters of the patch 12
Table 3.1 Experimental parameters for a patch of vegetation. 41
Table 3.2 Experimental conditions. 41
Table 4.1 Experimental parameters of the patch 74

CHAPTER 1 INTRODUCTION

1.1 BACKGROUND AND MOTIVATIONS

Both riparian and aquatic vegetation in natural rivers and streams obstruct the flow due to additional drag, and it alters the turbulent flow compared to that of un-vegetated regions. Vegetation controls the mean and turbulent flow, and then affects sediment transport. The additional drag exerted by plants reduces the mean flow within the vegetated regions, and it strongly influences the velocity distributions and turbulent structures (Nepf, 1999). In particular, submerged plants or partly-vegetated channels can create shear layers between vegetated and un-vegetated regions, and induce strong vortices (Choi and Kang, 2006; Stoesser et al., 2009). Vegetation can reduce flow conveyance due to increased flow resistance, and it affects the flood route. It improves water quality by removing suspended sediment and nutrients, and provides aquatic habitats by creating diversity of flow for fishes and animals in natural rivers. Furthermore, riparian and aquatic vegetation can considerably affect the suspended load and the bedload. Those encourage accumulation of sediment within the vegetated regions by reducing bed shear stress. Vegetation on the bank and floodplain can reduce sediment load from bank erosion, increasing the bank strength and the plant root as well as reducing the flow velocity (Jang and Shimizu, 2007; Millar, 2000).

In the past, vegetation in the natural stream was considered as a component which had a negative impact of flood control and management due to an increase in flow resistance. Thus, aquatic and riparian vegetation have been cut and removed to increase flow conveyance, so that the channels have been straightened with concrete embankments as shown in Fig. 1.1. While the flooding risk has been reduced, the unintended effects have appeared in the stream such as destroyed ecosystem, reduced ecological habitat and deteriorated water quality (Rominger et al., 2010). Recently, the governments of many countries invest a portion of national budget in river and stream restorations. Especially, because aquatic plant colonies can provide ecosystem service by creating diverse habitats and removing pollutants, replanting of vegetation is preferred as shown in Fig. 1.1.



Fig. 1.1 Itachi river before (top: 1981) and after (bottom: 1993) river restoration. These photos were taken by yoshimura (http://www.a-rr.net/)

For the planting management and river restoration, the isolated patches of vegetation are not only more useful but also practical than fully vegetated zone at one side of the channel along the stream. While a lot of studies on flow through partly vegetated regions have been conducted, there are still lacks and limited data of the sediment transport and the morphological changes with finite patches of vegetation to quantify the spatial patterns near the patches, even though the study on bed morphology with finite patches of vegetation is fundamental interest.

The most immediate impact of finite patches of vegetation is that those alter flow directions, flow structure and turbulence quantities due to additional drag produced by

plants. The altered flow significantly influences sediment distributions near the patches, which in turn, affects morphological patterns. Thus, it is essential to understand mutual interactions among flow, sediment and vegetation. In addition, to have successful river or stream restorations, we need to know how the placement, density and size of patches of vegetation influence the flow and morphological changes near them.

1.2 RESEARCH OBJECTIVES

This work is to investigate bed morphological phenomena near the finite patches of vegetation in a mobile sand bed. Laboratory experiments and numerical simulations were employed as methods.

The objective of the research is to provide a better understanding of morphological response to finite patches of vegetation and local effects of erosion and deposition near the patch. To accomplish the overall aim, the following procedure was proposed:

1) Investigating erosion and deposition around a finite patch of vegetation on the ratio of submergence, density and the extent of patches using laboratory experiments.
2) Developing and validating a 2D numerical model that is able to simulate flow, sediment transport and morphological changes with vegetation.
3) Assessing morphological response to a finite patch of vegetation in open channels with erodible bank by means of laboratory experiments and numerical simulations.
4) Examining flow and bed morphology with respect to interactions between two finite patches using laboratory experiments and numerical simulations.
5) Analyzing local scour and deposition near circular cylinders in simple geometries by using large eddy simulation (LES) coupled with sediment transport and morphodynamic models.
6) Analyzing local and global scour around cylinder groups using LES.

1.3 ORGANIZATION OF THSIS

Chapter 2 presents flow field and changes in the bed topography near a finite patch of vegetation. Laboratory experiments are conducted in a straight open channel with mobile sand bed and a simple patch is introduced in open channels. Various configurations (i.e. obstruction ratio, length scale of the patch, patch density and submergence ratio) of the patch are tested. The flow and changes in bed topography within and around a finite patch

are presented and discussed, and thus, the trend of degree on erosion and deposition near the patch is presented.

Chapter 3 presents results of morphological response to a finite patch of vegetation in an open channel with erodible bank. To investigate morphological behavior of the channel, a finite patch of vegetation is placed at the middle of the channel. The bank erosion and morphological changes in response to the patch are described. Numerical model is developed and numerical calculations are performed for all cases experimentally studied. The results are compared to experimental data in terms of changes in bed topography and the channel widening due to bank erosion. The sensitivity to model parameters associated with sediment transport within the patch is examined.

Chapter 4 presents flow and spatial changes in bed topography on mutual interactions between finite patches. The numerical model is validated by comparing with literature data from laboratory experiments of flow through a finite patch of vegetation and the hydraulic characteristics in response to two patches are analyzed. Laboratory experiments are carried out to investigate morphological changes due to patches and local scour pool produced by the patches are discussed. Numerical simulations are conducted for all experimental cases and the results are compared to experimental results. The model capabilities and stability of the patches are investigated.

Chapter 5 presents results of numerical simulation of local scour around circular cylinders. Large eddy simulation coupled with sediment transport in Lagrangian framework and morphodynamic models is conducted. To investigate the effect of cylinder spacing, longitudinally and transversely, on scour evolution, phenomena and maximum scour depth, the side-by side and tandem arrangements are considered. The diverse cylinder spacing is tested and the scour and deposition patterns, and bed evolution of local scour are described. The computed maximum scour depth is compared with experimental data.

Chapter 6 presents results of numerical computation of local and global scour around cylinder groups. A computational study is performed to examine transport and scour process around cylinder groups. The square cylinder groups (2×2) are considered with various cylinder spacing. The features of scour and transport phenomena around cylinder groups are discussed. Computed maximum scour depth is compared with experimental

data available in a literature. In addition, impact of cylinder array on local and global scour is investigated by comparing with those around staggered cylinders.

Chapter 7 gives the conclusions.

CHAPTER 2 CHARATERISTICS OF BED MORHOLOGICAL CHANGES AROUND A FINITE PATCH OF VEGETATION

2.1 INTRODUCTION

Both riparian and aquatic vegetation in natural channels control the mean and turbulent flows, and then affect sediment transport. The additional drag exerted by plants reduces the mean flow within the vegetated regions, and it strongly influences the velocity distributions and turbulent structures (Nepf and Vivoni, 1999). In particular, submerged plants or partly-vegetated channels can create shear layers between vegetated and un-vegetated regions, and induce strong vortices (Choi and Kang, 2006; Stoesser et al., 2009). Vegetation can reduce flow conveyance due to increased flow resistance, and it affects the flood route. It improves water quality by removing suspended sediment and nutrients, and provides aquatic habitats by creating diversity of flow for fishes and animals in natural rivers (Chambers and Prepas, 1994; Kemp et al., 2000; Schulz et al., 2003). Furthermore, riparian and aquatic vegetation can considerably affect the suspended load and the bed load (Lopez and Garcia, 1997; Tal and Paola, 2010; Zong and Nepf, 2011). Vegetation encourages accumulation of sediment within the vegetated regions by reducing bed shear stress. Vegetation on the bank and floodplain can reduce sediment load from bank erosion, increasing the bank strength with the plant root as well as reducing the flow velocity (Millar, 2000; Jang and Shimizu, 2007).

Recently, vegetation is encouraged in river environment and landscape instead of concrete surfaces for revetments, and replanting in a stream is promoted to create close-to-nature streams (Choi and Kang, 2006; Bennett et al., 2008). For the planting management and river restoration, the isolated patches of vegetation are not only more useful but also practical than fully vegetated zone at one side of the channel along the stream. While a lot of studies on flow through partly vegetated regions have been conducted, there are still lacks and limited data of the sediment transport and the

morphological change with finite patches of vegetation to quantify the spatial patterns near the patches, even though the study on bed morphology with finite patches of vegetation is fundamental interest.

For the first time, Bennett et al. (2002) conducted laboratory experiments using semi-circular model patches for the purpose of creating a degraded straight channel to meandering channel. The emergent model patches were alternatively placed in the straight channel to alter the flow patterns and they measured surface flow velocities by means of particle image velocimetry (PIV). The study described that the flow velocities are significantly accelerated opposite the model patches, and the magnitude of them is controlled by the model patch density. Leu et al. (2008) investigated effects of cutting riparian vegetation on hydrodynamic behaviors by means of a depth-averaged numerical model to propose a cutting method for reducing the risk of flooding during the growing season. Five cutting scenarios, i.e., the original, cutting along the main channel side, cutting the bank side, alternative cutting and reducing vegetation density, were tested and they suggested that the cutting along the main channel was the most effective scenario for flood controls. Zong and Nepf (2012) described the turbulent wake behind a finite model patch, which consisted of emergent circular array of cylinders and placed at the mid-channel. A *von Kármán* vortex was formed behind the circular patch due to the interaction of shear layers, and the vortex street was weakened as the solid volume fraction of the model patch became lower.

Few studies have been made on the influence of the flow and the morphological change because the altered flow direction and pattern by finite patches can considerably affect sediment transport and bed morphology. Bennett et al. (2008) performed the experiment and numerical simulations to investigate channel responses due to finite patches, which consist of emergent and circular cylinders, in the straight compound channel based on the experiments conducted by Bennett et al. (2002). They showed that the channel change was significantly affected by vegetation density due to the magnitude of bank erosion and local scour pools opposite and near the patches, respectively, and numerical model could be used for long-term bed morphology with finite vegetation. However, they could not measure the bed elevation within the patch due to the limitation of experimental conditions. Bouma et al. (2007) investigated spatial sedimentation patterns within patches in an intertidal flat.

They were comprised of bamboo cans and two patch densities (low and high density patches) were tested. Over two-years monitoring in the field, higher erosion occurred in the high density patch and it was observed near the leading and lateral edges of the patch. After bed scouring near the leading edge of the patch, sediment was deposited. On the other hand, for the low density patch, there were no pronounced spatial patterns of erosion and deposition. It was observed, in turn, that very small-scale erosion took place in the vicinity of bamboo cans in the patch. Even though the flume experiment was also conducted, it was different from the field observation condition since there was the limitation of the flume width which was filled with bamboo cans over the whole width. For the purpose of stream restoration, Rominger et al. (2010) carried out a field scale experiment in a sand bed stream with meander bends and vegetation was added to point bars at the convex part of the meandering channel. They described that erosion was observed near the lateral edge of vegetation and thus it caused the removal of some added vegetation. Based on flow structure described by Zong and Nepf (2012), Follett and Nepf (2012) carried out laboratory experiments to investigate erosion pattern related to a circular patch of emergent vegetation placed at mid-channel under flow conditions above the threshold of sediment motion. They considered two patch densities and two patch diameters that had little effect of wall on the flow near the patch. The scour was observed within and around the patch, and the degree of scouring increased with increasing patch density. In addition, this trend was significantly associated with turbulence kinetic energy in the patch.

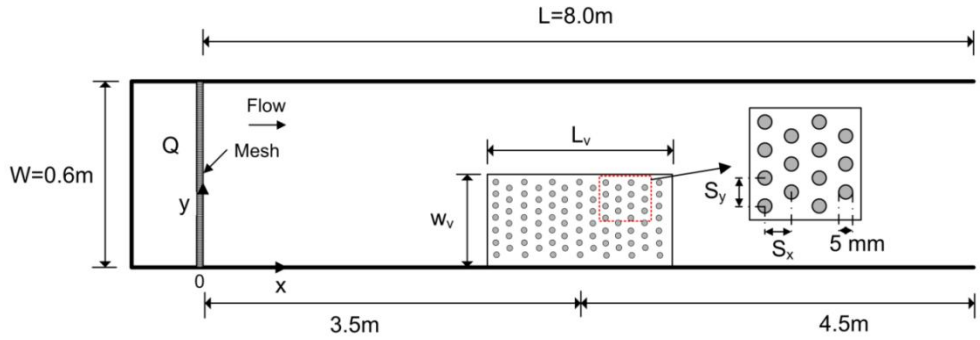
In general, as mentioned in the literature reviews, the patch density is a key parameter for clarifying the sediment erosion and deposition near the patch, whereas there are other un-investigated parameters related to bed morphology with finite patches of vegetation in the streams. Most previous studies investigated the channel response to rigid and emergent vegetation with varying patch density and shape, but no study had considered the submergence ratio, the ratio of the patch width to the channel width, and the extent of the patch length. Also, while the most of the previous researches observed and recognized an increase in deposition within the vegetated region, the recent studies had also shown the opposite trend (Bouma et al., 2007; Rominger et al., 2010; Follet and Nepf, 2012). However, few studies investigate the amount of sediment erosion and deposition, and the

parameters which affect the bed morphological changes within and near the finite patches of vegetation, since there are few detailed measurements of morphological patterns near the patch of vegetation, including within-patches.

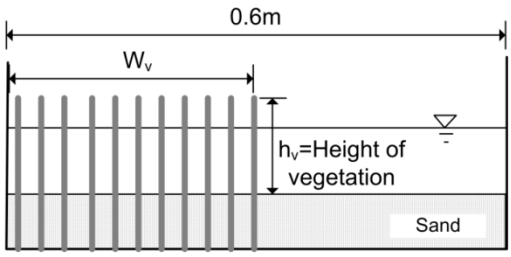
The objective of this paper is to investigate the flow field and changes in the bed topography near a finite patch in open channel flows with various configurations of the patch (i.e. varying obstruction ratio, length scale of the patch, model patch densities and submergence ratio). To address these topics, we consider a simple finite rectangular patch that consists of circular cylinders with staggered array and places at the mid-channel. Laboratory experiments are conducted with various configurations of the model patch which is modeled by circular cylinders. Two flow conditions, which are below and above the threshold of sediment entrainment, are considered. To characterize the flow field, transverse and longitudinal flow velocities are taken at several positions near and downstream of the patch. The changes in bed topography in and around a finite patch are presented, and the sediment erosion and deposition patterns are discussed. In addition, the trend of degree on erosion and deposition near the patch is described.

2.2 EXPERIMENTAL SET UP

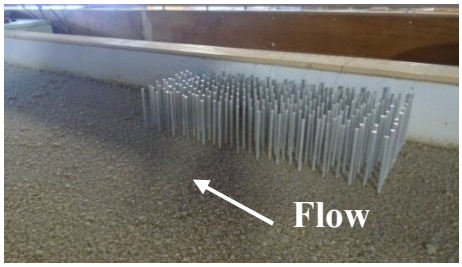
Laboratory experiments were carried out in a flume of 8 m long, L, 0.6 m wide, W, and 0.3 m deep with wooden side walls as shown in Fig. 2.1. The flume was filled with a 10 cm layer of uniform sediment with median diameter of 0.9 mm. Water discharge was controlled to be 0.00375 m^3/s by a manual valve at upstream tank. Initially, a small discharge was drawn to saturate the sand bed in the flume. A plastic mesh screen was installed to minimize water-surface oscillation at the entrance of the upstream channel. Two hydraulic cases were considered with below and above the threshold of sediment motion. In Case 1, bed shear stress upstream of the patch was lower than critical bed shear stress, $\tau_{*c} = 0.034$, obtained using Iwagaki's formula (Iwagaki, 1956), and thus the bed did not change upstream of the patch during experiments. In this case, channel slope was set to 1/500. For Case 1, the erosion was predominated within and near the patch, which was similar to local scour phenomenon observed around piers in the field. Through experiments on local scour around pile groups, Ataie-Ashtiani and Beheshti (2006) found that approximately 90 % of equilibrium scour depth was obtained after 5.5 hours. For Case 1, thus, the duration of experiments was set to 5 hours. On contrast, in Case 2, the bed shear



(a) Plane view



(b) Cross sectional view with the patch



(c) Picture of the flume near the patch

Fig. 2.1 Schematic diagrams of the laboratory experiment.

stress was above the threshold of sediment motion with channel slope of 1/200. The sediment was supplied regularly at the upstream end during the experiments. The amount of sediment was estimated using the empirical bedload formula (e.g. Meyer-Peter Muller, 1948) under without-patch. Unlike Case 1, the erosion as well as deposition within and near the patch was observed in Case 2. Several experimental studies on local scour under flows above the threshold of sediment motion showed that much less time was required to attain equilibrium scour depth than those below critical bed shear stress (Raudkivi, 1990). In this condition, experiments were maintained for 2 hours. From inspection of test cases, furthermore, 2 hours was sufficient to obtain distinct deposition pattern and to investigate how much sediment is accumulated within and near the patch according to diverse configurations. The experimental conditions of flow are summarized in Table 2.1. Each case was carried out with following experimental parameters of the patch.

Table 2.1 Experimental conditions of flow

	Q (m^3/s)	slope	Froude number	τ_*
Case 1	0.00375	1 / 500	0.65	0.03
Case 2	0.00375	1 / 200	0.82	0.06

For the previous experimental works on river restoration, patches of vegetation were located along the side wall in an open channel (Bennett et al., 2002, 2008). This placement can provide not only improvement in ecological functions but also local protection of stream banks because it can cause alteration of flow direction and diverse flows. Thus, the patch of vegetation placed along a side wall is very practical for river engineers. In addition, we can often find vegetation on the alternate sand bars along the side banks in natural rivers due to fact that dam constructions upstream of rivers create new environment, which inhibits sediment transport and stabilizes bars with vegetation downstream of dams. In present experiments, therefore, the leading edge of the patch was located at the mid-channel, 3.25 m from the upstream of the channel entrance along the side wall as shown in Fig. 2.1a. Rectangular patches were constructed with circular aluminum cylinders of 5 mm diameter, which are emergent or submerged with a staggered array. The circular cylinders have a good approximation for rigid vegetation (e.g. reeds). The patch density was described by the following two parameters: the patch density, λ (m^{-1}) that is a frontal area per unit volume of the patch (= $N_v d\min(h,h_v)$ / $W_v L_v h$ where N_v is the number of cylinders, d is diameter of a cylinder, L_v is length of the patch, W_v is width of the patch, h is water depth and h_v is height of a cylinder.) and the solid volume fraction, ϕ (= $N_v \pi d^2 \min(h,h_v) / 4 W_v L_v h$). In this study, three patch densities (ϕ = 0.013, 0.021 and 0.047 for the emergent patch) were tested. The ratio of the obstruction width, W_v, to channel width, W and the influence of the patch lengths, L_v, were considered. For the emergent patches, W_v / W was 1/3, 1/2 and 2/3 for W_v = 20, 30 and 40 cm, respectively, and L_v was 0.3, 0.5 and 1.0 m. The non-dimensional flow blockage, λW_v, which is the product of the patch density and the patch width, was considered, so that the corresponding range was λW_v = 0.65-4.76. Also, the effect of the submergence ratio (h / h_v = 1.38) was considered

with patch densities. For the submerged patch, W_v / W was 1/3 and 1/2 for W_v = 20 and 30 cm, respectively, and L_v was 0.5 and 1.0 m. The patch density was varied between ϕ= 0.009 and 0.034, and the corresponding flow blockage was λW_v=0.47-2.58. The patch density used in this experimental study was selected based on previous literatures (Bennett et al., 2008; Follett and Nepf, 2012) and actual data observed by Gambi et al. (1990). The experimental parameters of the patch are summarized in Table 2.2.

Table 2.2 Experimental parameters of the patch

Exp #	W_v (m)	L_v (m)	λ (m^{-1})	ϕ	h / h_v	λW_v
1	0.2	0.3	3.25	0.013	1.0	0.65
2	0.2	0.3	5.4	0.021	1.0	1.1
3	0.2	0.3	11.9	0.047	1.0	2.38
4	0.2	0.5	3.25	0.013	1.0	0.65
5	0.2	0.5	5.4	0.021	1.0	1.08
6	0.2	0.5	11.9	0.047	1.0	2.38
7	0.2	1.0	3.25	0.013	1.0	0.65
8	0.2	1.0	5.4	0.021	1.0	1.08
9	0.2	1.0	11.9	0.047	1.0	2.38
10	0.3	0.5	3.25	0.013	1.0	0.98
11	0.3	0.5	5.4	0.021	1.0	1.62
12	0.3	0.5	11.9	0.047	1.0	3.57
13	0.4	0.5	3.25	0.013	1.0	1.3
14	0.4	0.5	5.4	0.021	1.0	2.16
15	0.4	0.5	11.9	0.047	1.0	4.76
16	0.2	0.5	2.35	0.009	1.38	0.47
17	0.2	0.5	3.91	0.015	1.38	0.78
18	0.2	0.5	8.62	0.034	1.38	1.72
19	0.3	0.5	2.35	0.009	1.38	0.70
20	0.3	0.5	3.91	0.015	1.38	1.17
21	0.3	0.5	8.62	0.034	1.38	2.59
22	0.2	1.0	2.35	0.009	1.38	0.47
23	0.2	1.0	3.91	0.015	1.38	0.78
24	0.2	1.0	8.62	0.034	1.38	1.72

To investigate flow fields, velocities were measured using a two dimensional

electromagnetic current meter which are accurate to ± 2 %. The probe was mounted above the flume and it was able to move along and across the flume. Before measuring velocity, sensitivity analysis of electromagnetic current meter was carried out in a straight open channel and the velocity was measured at a fully-developed region. Each sampling was repeated three times (Fig. 2.2). It was found that sampling duration of 1 and 10 sec produced considerable uncertainty of velocities (u, v), but measured velocities become almost constant if the sampling time is larger than 20 sec, so we can see that recording time for averaged velocities should be larger than 20 sec. To secure accuracy, the averaged velocities were recorded for 40 sec, at each point. Under emergent condition of the patch on the fixed bed, longitudinal velocity profiles were measured along the lateral edge of the patch from x = 3.0 m, upstream of the patch to x = 6.0 m, downstream of the patch. Transverse profile surveys were made at several points near and behind the patch. On the other hand, under the movable bed, it was difficult to measure the velocities due to fact that the probe is able to influence the bed deformation in shallow flows. Thus, we only measured velocities at few points behind the emergent and submerged patch.

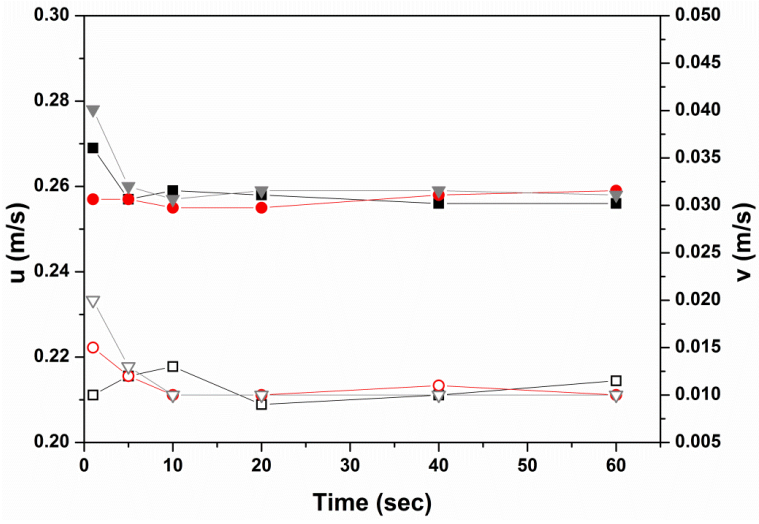


Fig. 2.2 Sensitivity of electromagnetic current meter where the solid symbols denote data of the longitudinal velocity, u, and the empty symbols indicate data of the transverse velocity, v. (Square symbol is the first measurement; circular symbol is the second measurement; nabla symbol is the third measurement.)

The bed surface was surveyed using the laser bed profiler (Keyence IL-065), which is

mounted on the flume. After each experiment, the flow was stopped and then the water was drained slowly, ensuring no change in deformed bed topography. The bed elevation was measured every 10 cm and 0.4 cm in longitudinal and transverse directions, respectively, except the region of the patch and close to the patch where the measurement was done every 2 cm (3 m to 4.5 m from upstream). The change in bed topography was found from differences between before and after bed elevations.

2.3 RESULTS AND DISCUSSION ON LABORATORY EXPERIMENTS

2.3.1 Flow field

To clarify the regions near the patch, we divide the channel into five regions (Region (a); upstream of the patch, Region (b); opposite the patch, Region (c); opposite and downstream from the patch, Region (d); the patch, Region (e); behind the patch) as shown in Fig. 2.3.

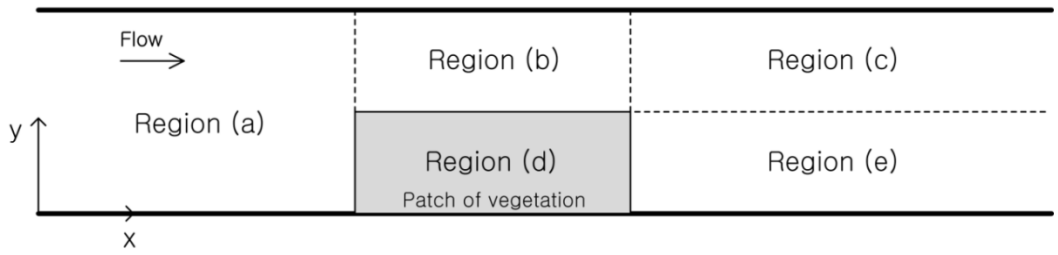
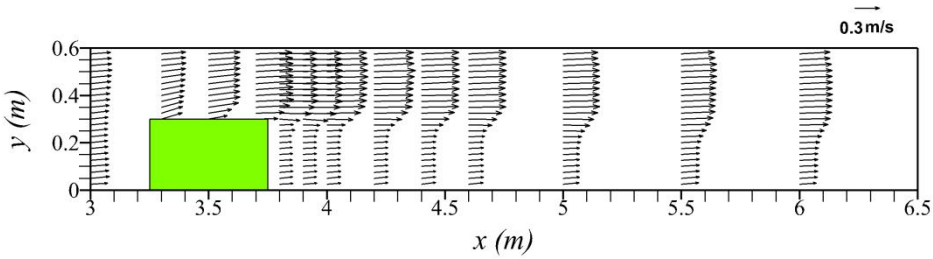


Fig. 2.3 Layout of the divided channel.

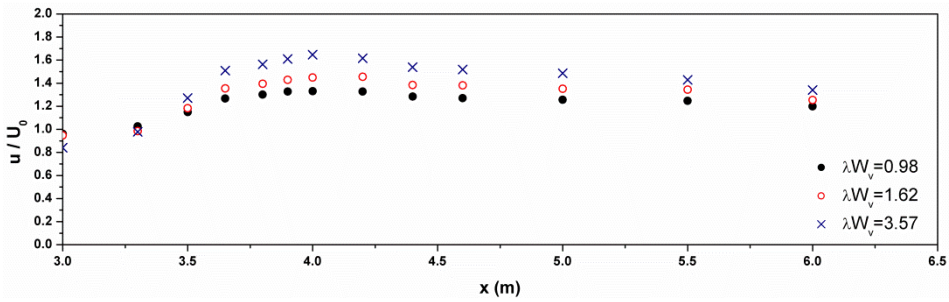
Fig. 2.4a shows the flow velocity vectors around and downstream of the patch for λW_v = 3.57 (W_v = 0.3m, ϕ = 0.047) under the emergent condition. The approaching flow from the Region (a) is nearly uniform, but velocity profiles are significantly changed with passing through the Region (d). Although, the flow velocity is accelerated in the Region (b) and (c), the velocity is decelerated after entering the Region (d), but it is laterally uniform in Region (e). Two different velocities are formed downstream of the Region (d) due to additional drag of the patch and those are able to create a shear layer. Zong and Nepf (2012) showed that the growth of a shear layer is developed between two different velocities and the peak of turbulent intensity is observed near the shear layer region. Longitudinal velocity profiles of u with three different flow blockages, λW_v = 0.98, 1.62 and 3.57 (W_v =

0.3 m, ϕ = 0.013; W_v = 0.3 m, ϕ = 0.021; W_v = 0.3 m, ϕ = 0.047) are presented along the center of the Region (b) and (c) (y = 0.45 m), and the Region (e) (y = 0.15 m) in Figs. 2.4b and c, respectively. Longitudinal velocity increases at x = 3.3 m in the Region (b) and those have peak values at x = 4.0 m regardless of the flow blockage (Fig. 2.4b). The flow velocity of u in the Regions (b) and (c) increases with increasing the flow blockage. On the other hand, in the Region (e), longitudinal velocity is considerably decelerated, compared to the Region (c) in Fig. 2.4c, for which the longitudinal velocity decreases as the patch density increases. In fact, the flow is not able to penetrate a solid obstruction with same width, so that the flow velocity becomes greater near the obstruction and it has negative value behind the solid obstruction due to a recirculation zone such as spur dikes (Koken and Constantinescu, 2008). Thus, unlike the flow with a solid obstruction, for the porous patch, the flow is able to move through or near the patch and it depends on the patch density. In other words, as the patch density becomes higher, the flow rate through the Region (d) decreases since the greater flow rate is diverted away from the Region (d). The acceleration of u in the Regions (b) and (c), and the deceleration of u in the Region (e) are accompanied by an increase in diversion of flow from the Region (d) in Figs. 2.4b and c. Transverse velocity of v along the longitudinal intersection at the edge of the patch at y = 0.3 m are shown in Fig. 2.4d. The transverse velocity shows an increasing behavior from the Region (a). It has a maximum value near the leading edge of the Region (d), and then decreases to the end of the Region (d). In the Region (e), the transverse velocity is nearly zero and it forms a uniform flow. For the flow blockage larger than 3.63, the negative transverse velocity is observed directly behind the Region (d). The transverse velocity of v near the leading edge, which is associated with diversion of flow, increases with increasing the flow blockage due to higher drag. Thus, the higher flow blockage leads to higher diversion of flow, so that it causes greater flow acceleration in the Regions (b) and (c) and it induces more deceleration of flow in the Regions (d) and (e). Even though we do not measure the velocity in the Regions (a) and (d), it is expected that the flow velocity begins to decrease from the Region (a) and it decreases continuously until the end of diversion of flow through the Region (d) (Rominger and Nepf, 2011; Zong and Nepf, 2011).

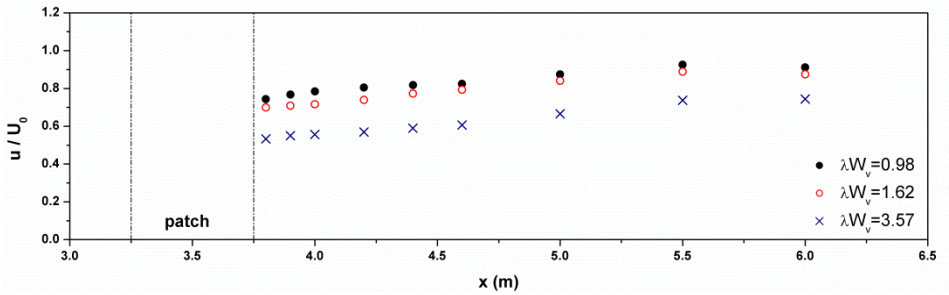
From experiments of flow structure in an open channel with a circular patch of emergent vegetation, Chen et al. (2012) developed predictive model for velocity downstream of the



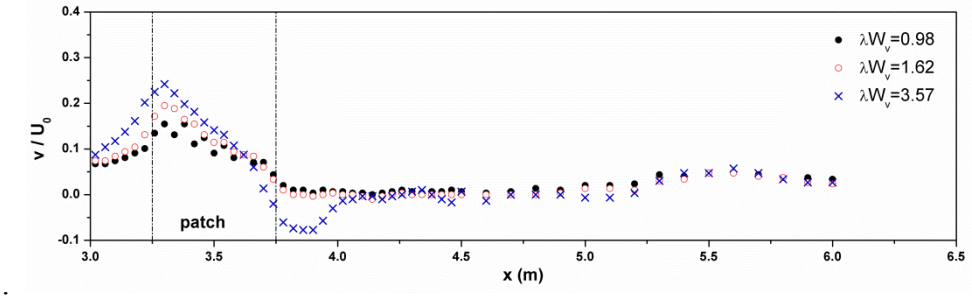
(a) Velocity vector for the patch with $\lambda W_v = 3.57$



(b) Longitudinal velocity profiles of u at $y = 0.45$ m



(c) Longitudinal velocity profiles of u at $y = 0.15$ m



(d) Transverse velocity of v along the longitudinal intersection of the edge at the patch at $y = 0.3$ m

Fig. 2.4 Velocity vector and profiles.

patch, u_1, which is comparable to velocity in Region (e). The velocity downstream of the patch is estimated as follow

$$\frac{u_1}{u_0} = 1 - (0.52 \pm 0.04)\frac{2W_v}{L_1} \tag{2.1}$$

In equation (2.1), u_0 is the velocity at upstream region and L_1 is the adjustment length and it is calculated by

$$L_1 = \left[\left(\frac{2(1-\phi)}{C_D\lambda}\right)^2 + W_v^2\right]^{1/2} \tag{2.2}$$

where, C_D is assumed to be 1.0 (Rominger and Nepf, 2011).

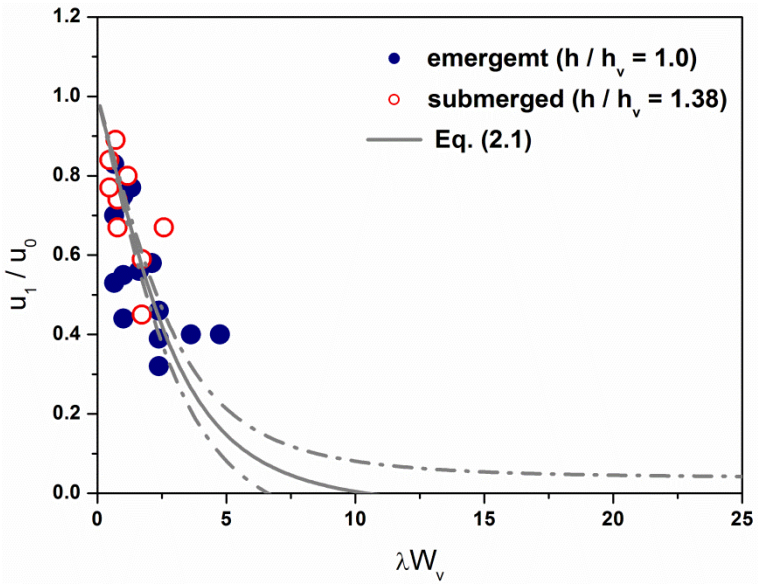
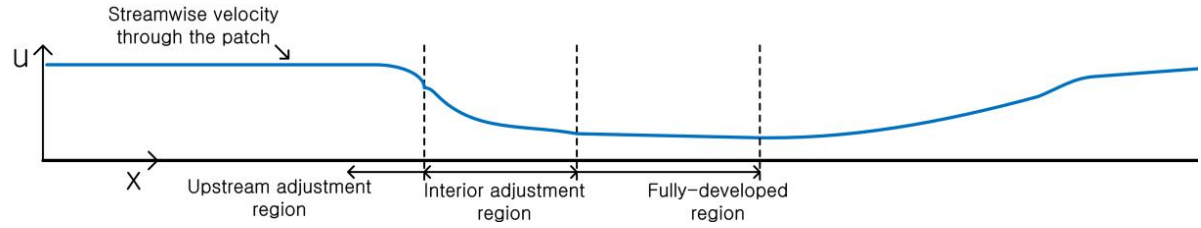


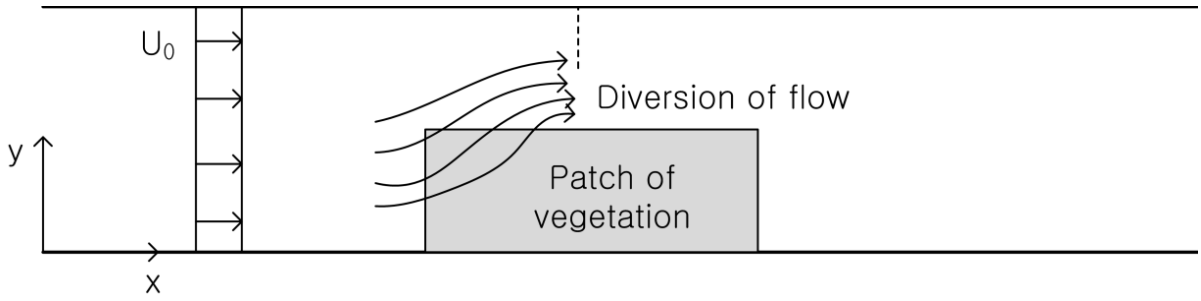
Fig. 2.5 Variation of measured velocity according to flow blockage where dashed dot lines indicate the 95 % confidence limits.

Fig. 2.5 shows variation of measured velocity, normalized by the upstream velocity, u_0, according to flow blockage, λW_v, together with equation (2.1). The measured velocity located 10 cm downstream from the end edge of the patch is used as a comparison with predictive model (i.e. Eq. 2.1). The equation (2.1) shows that for $\lambda W_v < 5$, the velocity decreases rapidly with an increase in flow blockage and then it slows down. The measured velocities are also reduced as the flow blockage increases because the flow blockage in present experiments is corresponding to λW_v = 0.47–4.76. The comparison between

measured velocity and predictive model shows a reasonable agreement with uncertainty, which implies that the impact of the side wall along the patch is negligible. In addition, the velocity downstream of the submerged patch is same trend versus the flow blockage and it is consistent with the result of predictive model, even though the model was developed based on the emergent patch. Thus, the velocity drops off with the flow blockage regardless of the submergence ratio, at least within the range of present experimental conditions (h / $h_v \leq 1.38$).



(a) Streamwise velocity along the centre of the patch.



(b) Plain view of flow field in the flume.

Fig. 2.6 Conceptual picture for flow field near the patch of vegetation (Rominger and Nepf, 2011).

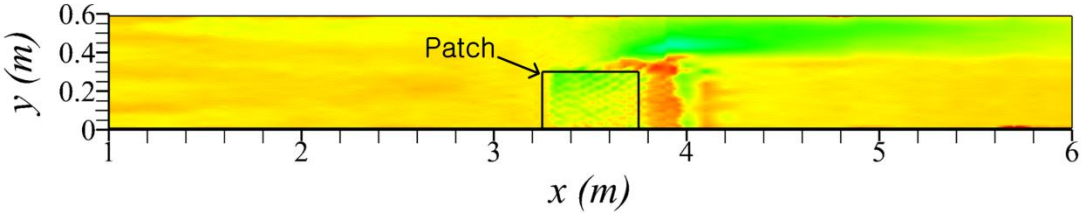
Rominger and Nepf (2011) defined upstream adjustment region as shown in Fig. 2.6, where the flow velocity through the patch begins to decelerate from upstream of the patch with distance of the patch width, W_v, due to the increase in pressure. Moreover, they defined the interior adjustment region as shown in Fig. 2.6, where flow diversion begins upstream of the patch and continues with some distance into the patch, which is end of flow divergence. They found that for the flow blockage, $\lambda W_v < 2$, the length of the interior

adjustment region is 2 / $C_D\lambda$, whereas for the high flow blockage ($\lambda W_v \geq 2$), it is equal to the patch width, W_v. Here, C_D is assumed to be 1.0. Thus, for λW_v = 1.62 and 3.57, the fully-developed region is formed within the Region (d) beyond x = 3.62 m and 3.55 m, respectively, whereas for λW_v = 0.98, the interior adjustment region is beyond the Region (d). It means the diversion of flow occurs until the end of the Region (d). The upstream adjustment region and the interior region have influences on bed morphological changes by affecting erosion and deposition within and near the Region (d). The effect of upstream and interior adjustment region on the bed morphology will be described in section 2.3.3.

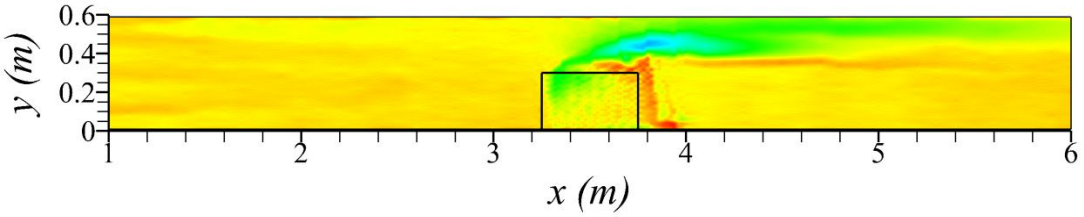
2.3.2 Bed morphology with flow below the threshold of sediment motion

2.3.2.1 Bed elevation

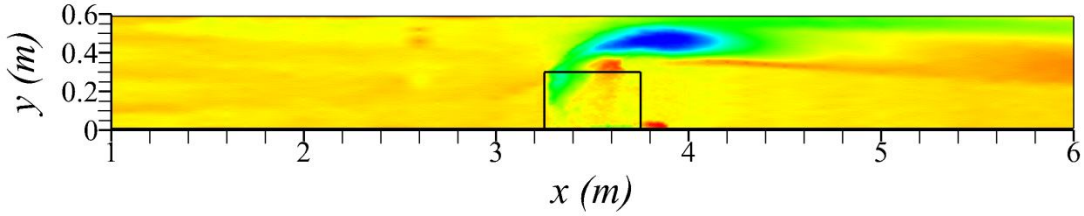
We first consider the condition in which the shear stress is below the critical shear stress (Case 1). The bed morphological changes with three different patch densities for the emergent condition and a high patch density for the submerged condition are depicted in Fig. 2.7. It can be seen that local erosion occurs in the Regions (b) and (c) due to acceleration of flow and elevated turbulence levels, causing additional drag. The bed morphological changes are similar to each other due to similar flow patterns in response to the patches. However, the magnitude of erosion observed in the Regions (b) and (c) and also near the leading edge of the Region (d) is significantly changed with an increase in the flow blockage. From comparisons between Figs. 2.7a, b and c, the local scour depth increases as the flow blockage becomes higher (higher patch density) due to fact that a higher flow blockage accompanies a higher diversion of flow. The enhanced flow velocities cause more erosion in the Regions (b) and (c). For the high flow blockage in Fig. 2.7c, the local scour becomes more pronounced. For lower blockages (λW_v = 0.98, ϕ = 0.013; λW_v = 1.62, ϕ = 0.021), small-scale scour appears at the vicinity of the cylinders inside the Region (d) and then sediment is transported downstream. Thus, deposition occurs just beyond the Region (d) but it is observed in the initial stage. It also moves slightly downstream, generating small-scale turbulence by each cylinder just behind the Region (d), which is quickly dissipated as observed by Zong and Nepf (2012). For the high blockage (λW_v = 3.57, ϕ = 0.047), however, sediment deposition does not occur in the Region (e) because most of the flow rate is diverted away from the Region (d) and thus, the flow is significantly decelerated within the Region (d), even though small deposition is



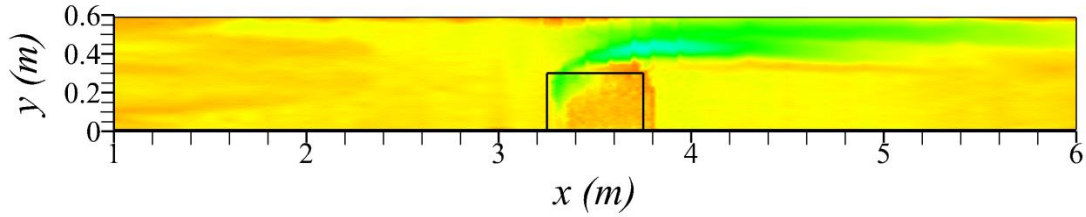
(a) $\lambda W_v = 0.98$ (emergent)



(b) $\lambda W_v = 1.62$ (emergent)



(c) $\lambda W_v = 3.57$ (emergent)



(d) $\lambda W_v = 2.58$ (submerged)

Fig. 2.7 Bed elevation; (a) $\lambda W_v = 0.98$($W_v = 0.3$ m, $\phi = 0.013$), (b) $\lambda W_v = 1.62$($W_v = 0.3$ m, $\phi = 0.021$), (c) $\lambda W_v = 3.57$($W_v = 0.3$ m, $\phi = 0.047$) (d) $\lambda W_v = 2.58$($W_v = 0.3$ m, $\phi = 0.034$). Flow is left to right and solid lines denote the patch.

observed near the lateral edge of the Region (d). In Fig. 2.7d, the bed elevation is shown for the high blockage ($\lambda W_v = 2.58$, $\phi = 0.034$) under the submerged condition. From comparing with the emergent one, the spatial patterns of bed morphology are similar, but the magnitude of erosion in the Regions (b) and (c) is lower for the submerged case

because the flow rate passing through the Region (d) is higher than the flow rate in the emergent case. In other words, in the submerged case, there is less flow acceleration in the Regions (b) and (c), even though the number of cylinders of the submerged patch is identical to that of the emergent patch. This implies that, as the submergence ratio increases, the diversion of flow decreases because the patch density or the flow blockage decreases where in turn, some flow passes over the patch (Bouma et al, 2013). Thus, the bed shear stress would decrease in the Regions (b) and (c) due to the reduction in the flow velocity.

2.3.2.2 Longitudinal bed profiles

Fig. 2.8 shows laterally-averaged longitudinal bed profiles in two regions where the Region (Ⅰ) is laterally averaged from the side wall at $y = 0$ to the lateral edge of the patch ($y = 0.2$, 0.3 and 0.4 m) and the Region (Ⅱ) is laterally averaged over the remaining area. In this figure, dashed lines denote the patches.

It can be seen in Fig. 2.8 that although the bed is not changed in upstream part of the patch, erosions are observed in the Region (Ⅱ), which increase with an increase in the flow blockage, and local scours occur near the leading edge (Region (Ⅰ)). Local scour begins at the leading edge of the patch and grows with distance inside the patch about 0.08 m from the leading edge. Then, the scour depth decreases until the end of the patch except for the high blockage ($\lambda W_v = 2.38$, $\phi = 0.047$) in which the scour depth is sharply reduced. Local scours observed in the experiments take place inside the patch, unlike a solid obstruction that the scour occurs at the front of solid one and the scour area is extended upstream of it. This is attributed to several mechanisms, mainly causing the diversion of flow, the horseshoe vortices and the turbulence. Firstly, the diversion of flow occurs near the leading edge, in which the patch of the higher blockage has higher diversion of flow, which is responsible for carrying more sediment away from the area near the leading edge of the patch. Secondly, this phenomenon is similar to scour patterns observed around pile groups in the laboratory experiments or the field (Rominger and Nepf, 2010). Several experimental series were conducted to investigate the scouring system around pile groups (Ataie-Ashtiani and Beheshti, 2006). They showed as the cylinder spacing is large enough, the scouring patterns are similar to an isolated cylinder. However, as long as the flow

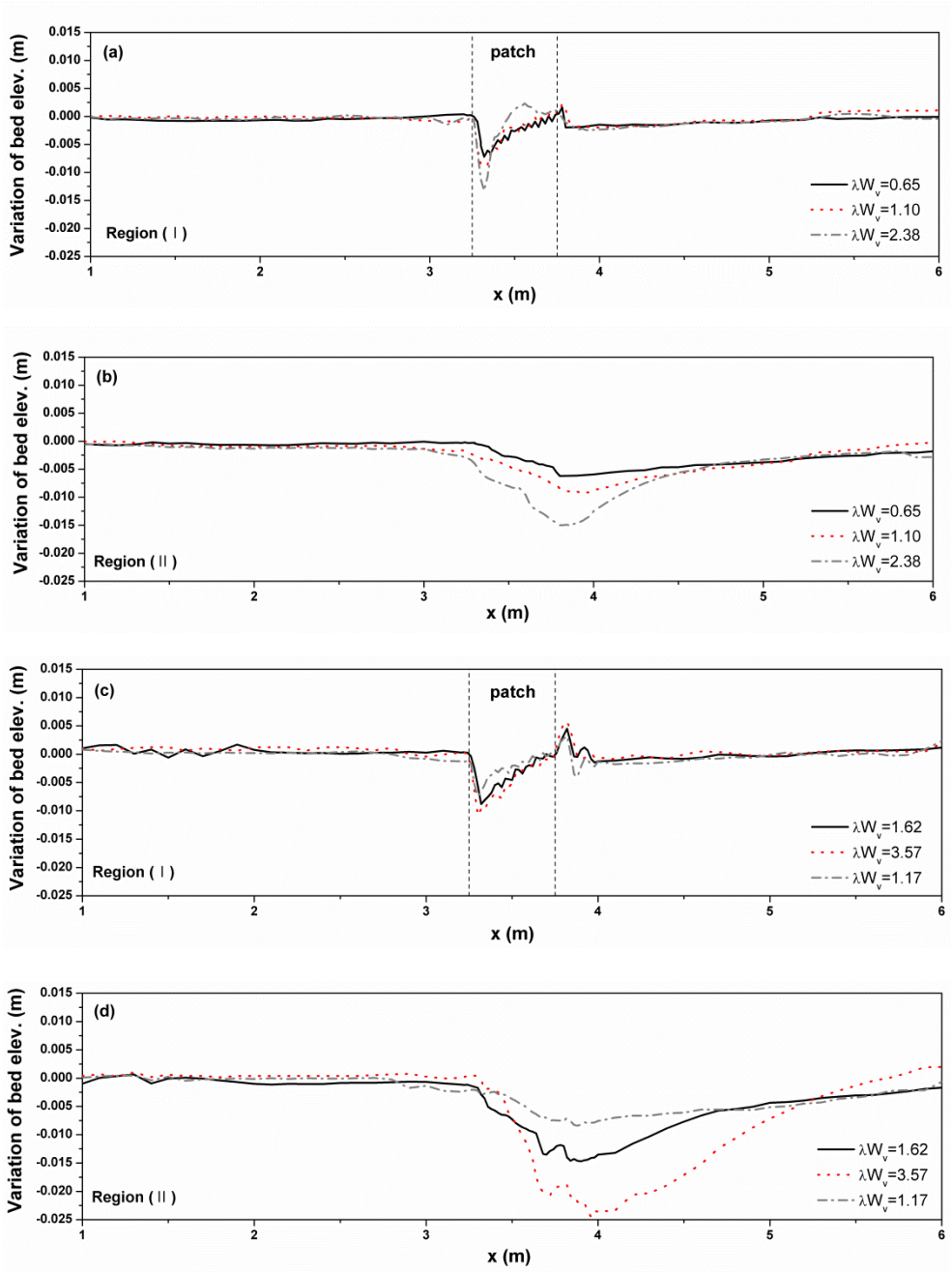


Fig. 2.8 Laterally averaged longitudinal bed profiles; (a) Region (Ⅰ) with λW_v = 0.65, 1.10 and 2.38 (W_v = 0.2 m), (b) Region (Ⅱ) with λW_v = 0.65, 1.10 and 2.38 (W_v = 0.2 m), (c) Region (Ⅰ) with λW_v = 1.62, 3.57 and 1.17 (W_v = 0.3 m), (d) Region (Ⅱ) with λW_v = 1.62, 3.57 and 1.17 (W_v = 0.3 m).

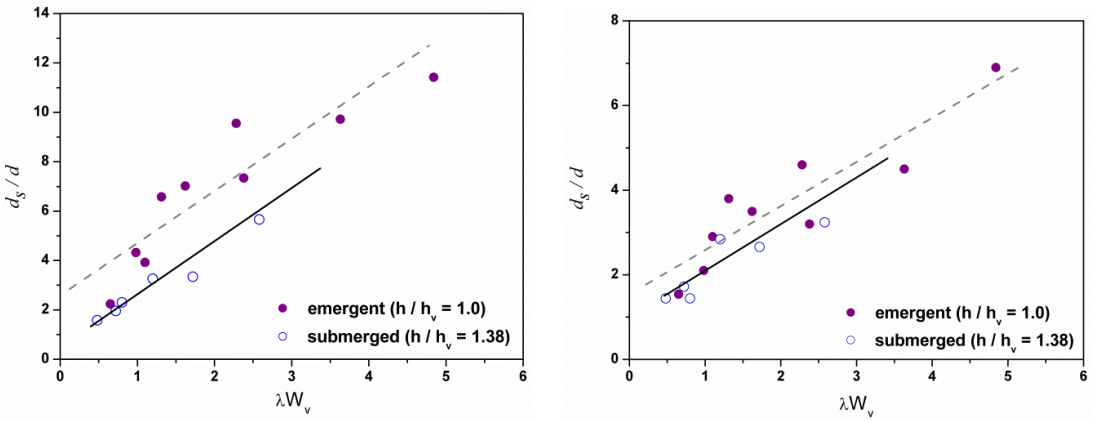
structure from the cylinders interferes from the other cylinders longitudinally or laterally,

turbulence intensity is increased with decreasing cylinder spacing. Also, for small cylinder spacing, the size of the horseshoe vortices close to the cylinders increases and an enhanced local flow is induced between two neighboring cylinders (Ataie-Ashtiani and Beheshti 2006). The scouring depth is strongly affected by such flow structures. Bouma et al. (2007) observed similar bed morphological changes in the field. They found the high within-patch eroded region near the leading edge of dense patch, which was placed on sand bed in the intertidal flat. Similarly, the scouring began near the front of the patch and it continued inside the patch. Then, deposition occurred just behind the scoured area. For the patch with submerged cylinders, $\lambda W_v = 1.17$, $\phi = 0.015$, in Fig. 2.8c, the local erosion observed near the leading edge of the patch (dash dot line) becomes lower than that scoured under emergent condition ($\lambda W_v = 1.62$, solid line). This may be because the size of horseshoe vortices decreases and the vortex shedding becomes weaker as the submergence ratio increases. The diversion of flow also decreases with decreasing the flow blockage. Indeed, the flow through submerged cylinders is very complex. If the patch length is long enough, spanwise rollers and vortices are generated at the top of the cylinders, producing an inflection of the streamwise velocity. The coherent structures play an important role for mass and momentum exchange between two regions and those affect the sediment transport. However, the local scouring does not seem to be influenced by such complex vortex structures because the patch is too short to develop and consequently, the scour depth of submerged one is lower than that of emergent one.

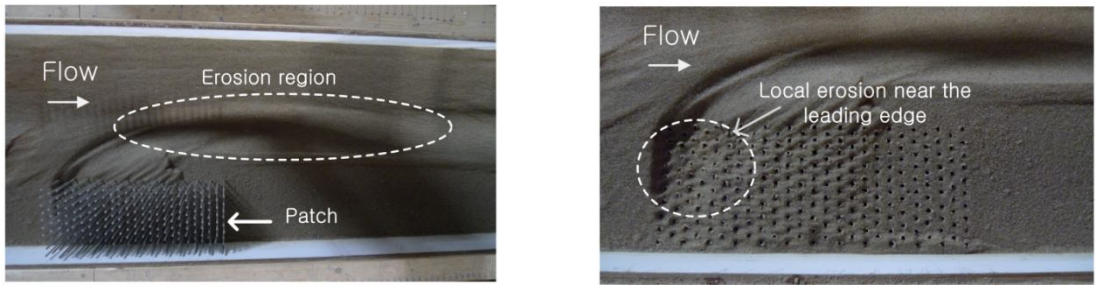
2.3.2.3 Scour in response to the patch

Figs. 2.9a and b show the maximum scour depth, d_s, normalized by a cylinder diameter, d, according to the flow blockage for both emergent and submerged conditions. In these figures, dashed and solid linear lines are fit to maximum scour depth of the emergent and submerged data, respectively, to emphasize difference between them.

The maximum scour depth in Fig. 2.9a is corresponding to the Region (b) as shown in Fig. 2.9c. It can be seen that the scour depth increases as the flow blockage increases. For the lower blockage ($\lambda W_v < 1.0$), the scour depth is similar between emergent and submerged cases, whereas it is shown that, for the flow blockage with $\lambda W_v \geq 1.0$, the scour depth observed in the emergent condition is deeper than that of the submerged condition. The maximum scour depth observed in the Region (b) not only increases with an increase



(a) Maximum scour depth (b) Scour at the leading edge



(c) Maximum scour region (d) Scour region near the leading edge

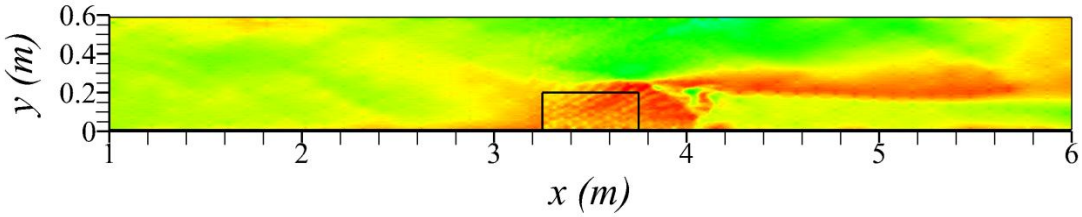
Fig. 2.9 Scour depth according to the flow blockage under the flow below the threshold of sediment motion.

in the flow blockage but also it is significantly influenced by the submergence ratio. Fig. 2.9b shows the maximum local scour depth observed near the leading edge of the Region (d) as shown in Fig. 2.9d with respect to the flow blockage for both emergent and submerged conditions. It can be seen that the trend of the local scour depth increases with an increase in the flow blockage in both conditions, whereas the magnitude of local scour is diminished as the submergence ratio increases. As a result, the local scouring occurred near the leading edge increases with increasing the flow blockage, λW_v. The fact supports that the relatively stronger flow (i.e. diversion of flow, horseshoe vortices and turbulence) is induced with an increase in the flow blockage.

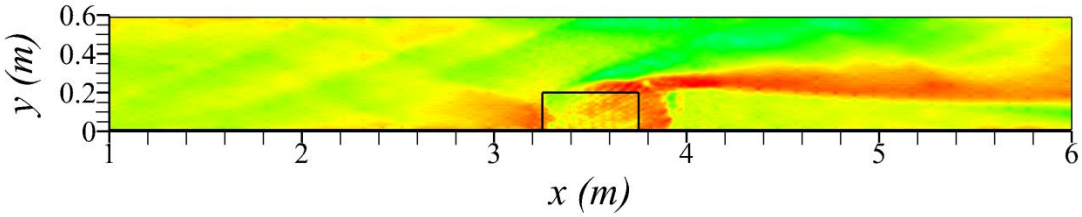
2.3.3 Bed morphology with flow above the threshold of sediment motion

2.3.3.1 Bed elevation

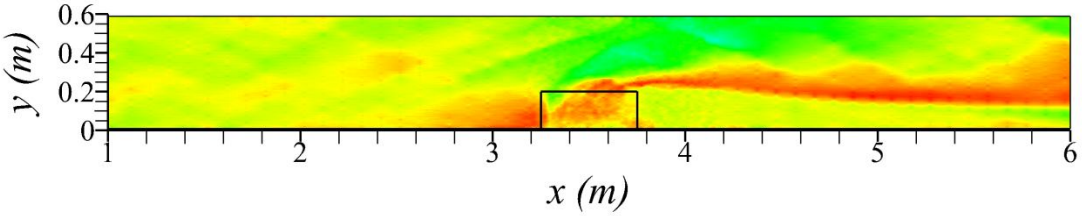
Fig. 2.10 depicts the bed morphological changes for three patch densities under the emergent condition and a high patch density under the submerged condition. Unlike experiments of the previous section (Case 1), the flow condition is above the threshold of sediment motions ($\tau_* > \tau_{*c}$), so sediment is transported from the Region (a). The bed deformations appear in the Region (a) and they migrate toward the downstream direction. Then, the bedforms pass through the Region (b) or (d), and the sediment passing through the Region (b) is deposited near the relatively low bed shear stress region along the lateral edge of the Region (d), which is consistent with the wake region, caused by the inflection of the streamwise velocity. Similarly, the erosion takes place in the Regions (b) and (c) due to diversion of flow and it increases with the increase in the flow blockage. It can be seen in Fig. 2.10 that sediment deposition is observed upstream of the Region (d) with distance about 0.25 m regardless of the flow blockage or the submergence ratio. Far upstream of the patch, the flow is uniform that is not affected by the patch. As the flow approaches the Region (d), the flow velocity becomes low due to an increase in pressure and then, deposition occurs near upstream of the Region (d) due to reduction in bed shear stress. The deposition regions correspond to the upstream adjustment region (see Fig. 2.6). We first discuss the results of the emergent condition in Figs. 2.10a, b and c ($\lambda W_v = 0.65$, $\phi = 0.013$, $\lambda W_v = 1.1$, $\phi = 0.021$, $\lambda W_v = 2.38$, $\phi = 0.047$). Unlike the local scouring near the leading edge of the Region (d) observed in the flow below the critical value of sediment motion (Section 3.2), sediment is deposited in the Regions (d) and (e). Sediment is entered passing through the leading edge of the Region (d), and then sediment is either transported further downstream or diverted away from the Region (d) due to diversion of flow. For the low flow blockage ($\lambda W_v = 0.65$, $\phi = 0.013$), deposition takes place in the Regions (d) and (e) without the local erosion, although small-scale erosion is observed in the vicinity of cylinders in the Region (d), which is negligible. It is found that, for the higher blockage, sediment is deposited within and near the Region (d), and the local erosion is observed near the leading edge of the Region (d). While the approaching velocity increases, the local scouring is considerably weakened due to the increase in sediment input from the Region (a) in comparison with that shown in section 3.2. Figs. 2.10c and d show that bed change



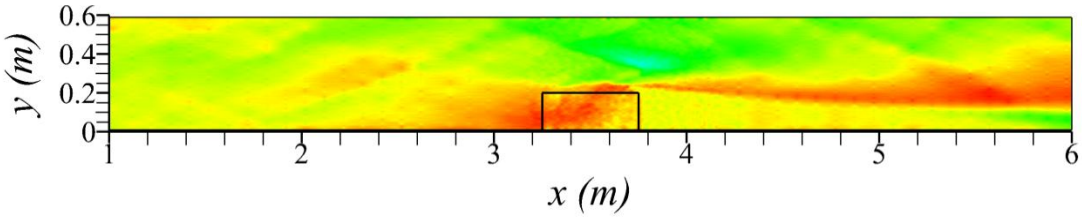
(a) $\lambda W_v = 0.65$ (emergent)



(b) $\lambda W_v = 1.1$ (emergent)



(c) $\lambda W_v = 2.38$ (emergent)



(d) $\lambda W_v = 1.72$ (submerged)

Fig. 2.10 Bed elevation; (a) $\lambda W_v = 0.65$($W_v = 0.2$ m, $\phi = 0.013$), (b) $\lambda W_v = 1.1$($W_v = 0.2$ m, $\phi = 0.021$), (c) $\lambda W_v = 2.38$($W_v = 0.2$ m, $\phi = 0.047$) (d) $\lambda W_v = 1.72$($W_v = 0.2$ m, $\phi = 0.034$). Flow is left to right and solid lines denote the patch.

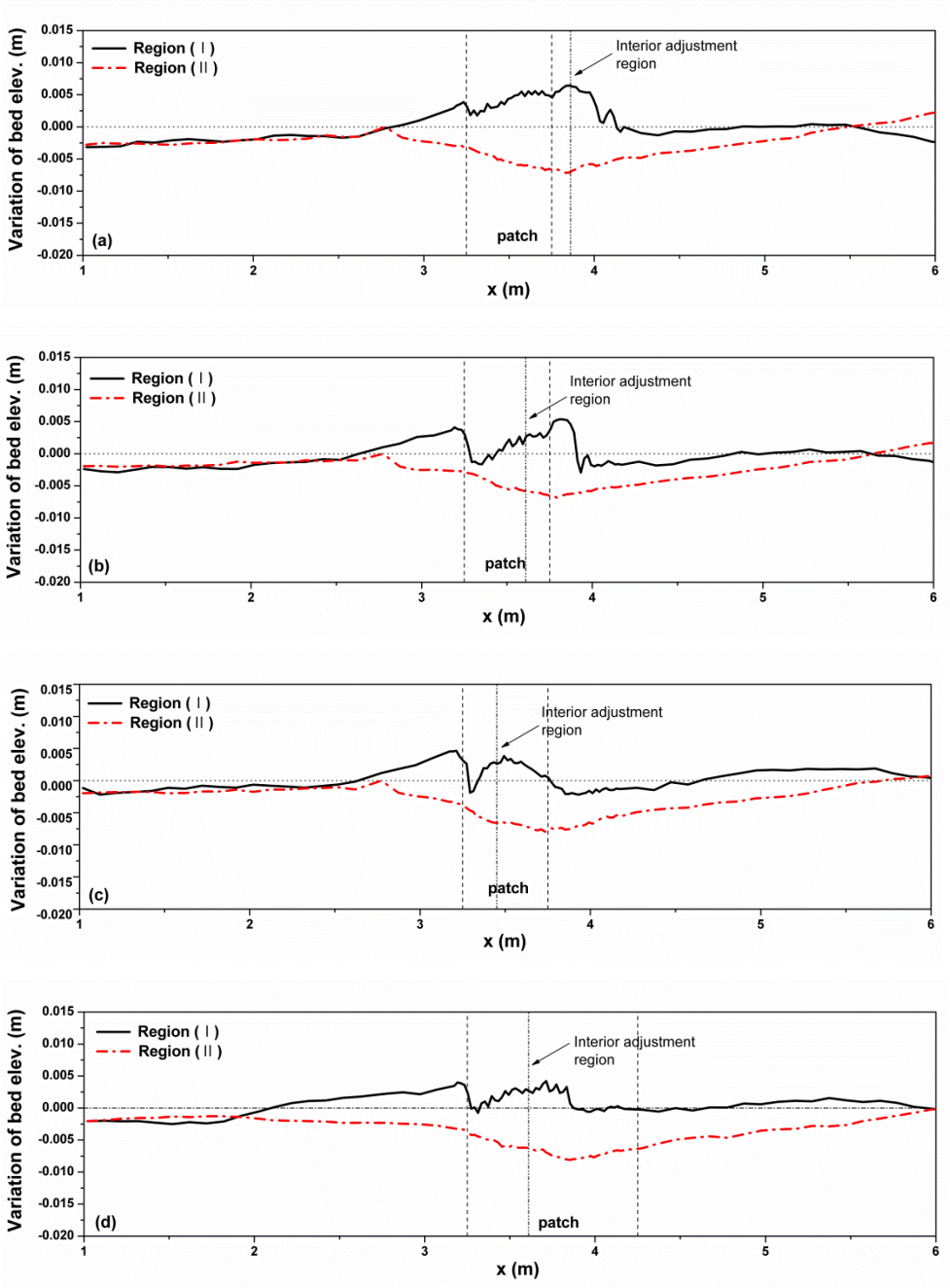
patterns under the submerged condition are similar to that observed in the emergent condition. However, the local scour becomes lower near the leading edge of the Region (d), and sediment deposition within the submerged patch increases since diversion of flow is

diminished with a decrease in the flow blockage. For the emergent patch, eddies are generated in the turbulent wakes of individual cylinders, whereas the submerged patch not only forms eddies behind the cylinders but also generates shear layer above the top of the cylinders. It is shown, however, that the shear layer generated near the top of cylinders does not affect sediment transport in our experiments. Nepf and Vivoni (1999) described that the wake turbulence decreases with an increase in the submergence ratio, so that it reflects that the local erosion is weakened near the leading edge and in the Region (d). In other words, deposition becomes higher in and near the Region (d) as the submergence ratio becomes larger. It is found in Fig. 2.10 that the distinct region is formed in the Region (e), where sediment transport does not take place as a result of the reduction in bed shear stress due to additional patch drag. It indicates that the *von Kármán* vortices are not formed by the patch until the end of the measured position (x = 6.0 m). Nicolle and Eames (2011) performed numerical simulations with the circular patch and they presented that it occurs when the solid volume fraction is larger than 0.15. In our experiments, we considered not only the solid volume fraction < 0.05, but also the half of the patch along the side wall. Those seem to be a reason why unsteady vortex shedding is not observed in the present experiment.

2.3.3.2 Longitudinal bed profiles

Fig. 2.11 shows laterally-averaged longitudinal bed profiles for two regions through the patch, Region (Ⅰ), and the open channel, Region (Ⅱ), relatively. The dashed lines denote boundaries of the patch and the dash dot lines are the interior adjustment regions, which are determined by scaling as explained in section 3.1. Sediment deposition begins upstream of the patch with distance about that slightly larger than the upstream adjustment region (= W_v). From the leading edge of the patch (x = 3.25 m), scour begins sharply over a finite distance toward downstream, and it becomes more pronounced with the increases in the flow blockage, after which deposition occurs within or behind the patch. It can be seen in Fig. 2.11 that for $\lambda W_v > 1.0$, the scoured area is observed within the range of the interior adjustment regions and scouring depth increases with the increase in the flow blockage. In particular, for $\lambda W_v = 1.62$, the erosion is found over the entire length of the patch and then sediment is deposited directly behind the patch. In Fig. 2.11d, even though the length of the patch is two times larger than that shown in Fig. 2.11b, it does not influence the bed

morphological changes inside the patch, which are consistent with each other. This result implies that the length scale has negligible effects if the patch length is longer than the



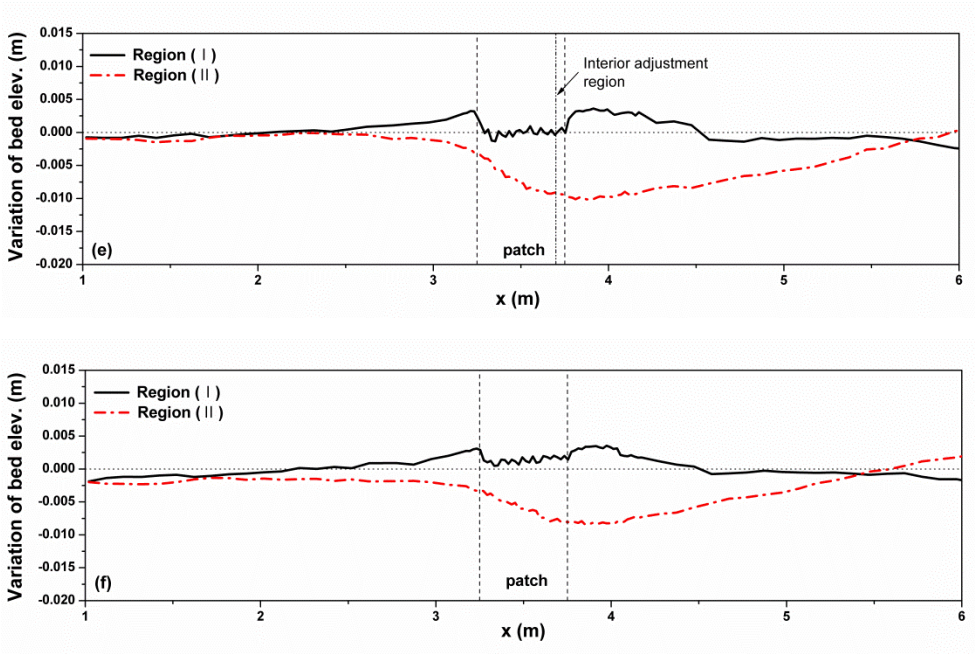


Fig. 2.11 Laterally averaged longitudinal bed profiles; (a) $\lambda W_v = 0.65$($W_v = 0.2$ m, $L_v = 0.5$ m, $\phi = 0.013$), (b) $\lambda W_v = 1.1$($W_v = 0.2$ m, $L_v = 0.5$ m, $\phi = 0.021$), (c) $\lambda W_v = 2.38$($W_v = 0.2$ m, $L_v = 0.5$ m, $\phi = 0.047$), (d) $\lambda W_v = 1.1$($W_v = 0.2$ m, $L_v = 1.0$ m, $\phi = 0.021$), (e) $\lambda W_v = 1.62$($W_v = 0.3$ m, $L_v = 0.5$ m, $\phi = 0.021$), (f) $\lambda W_v = 1.2$($W_v = 0.3$ m, $L_v = 0.5$ m, $\phi = 0.015$).

interior adjustment region. For $\lambda W_v < 1.0$ (the lowest blockage), the local scour becomes less pronounced near the leading edge of the patch, although the interior adjustment region is beyond the patch. This is attributed to the fact that the effect of diverging flow considerably reduces as the flow blockage decreases. For these patches of $\lambda W_v > 1.0$, the interior adjustment region is in a good agreement with scoured areas within the patch, which indicates that the erosion within the patch takes place throughout the interior adjustment region, after which sediment is deposited just behind that region. The interior adjustment region indicates that the flow deceleration, which begins from upstream of the patch in response to flow resistance by the patch drag, continues to the end of diversion of flow, after which the flow is fully developed with the low velocity if the patch length is long enough. On the other hand, Zong and Nepf (2011) showed that the turbulence increases rapidly from the leading edge of the patch, which is associated with

cylinder-wakes, and the turbulence levels increase as the patch density increases, even though the flow velocity is reduced continuously along the streamwise direction. The elevated levels of turbulence are reflected in the increase in the scouring depth near the leading edge of the patch, and sediment scoured within the patch is accumulated just behind the region or is diverted away from the region. Thus, the scoured bed within the patch supports elevated turbulence levels in comparison with non-vegetated channel at the same flow condition. Follett and Nepf (2012) also observed that the local scouring in the region is correlated with turbulence kinetic energy. From above discussion, we found that the upstream and interior adjustment regions are able to describe important characteristics of bed morphological changes within and near the patch. In Fig. 2.11f, the laterally-averaged longitudinal bed profile is depicted for the submerged condition (W_v = 1.2, ϕ = 0.021). Overall, the bed morphological changes of the submerged data are similar to that of the emergent case (Fig. 2.11e). The bed is eroded from the leading edge of patch and it continues to the end of the patch. However, the scoured bed within the patch is less pronounced in comparison with the emergent case in Fig. 2.11e due to diminished turbulence levels with an increase in the submergence ratio. For the submerged condition, we could not indicate the interior adjustment region because this scaling is only available for emergent patches.

Fig. 2.12 presents the distance of deposition mound within and behind the patch, L_d, according to velocity, u_1, measured at 10 cm downstream from the end edge of the patch where L_d is deposited distance from the leading edge of the patch to downstream edge of the deposition mound. A linear regression is fit to emphasize tendency. It can be seen that the distance of deposition mound increases with increasing velocity, u_1, regardless of whether the patch is submerged or not. The increase in the flow speed through the patch enhances sediment transport further downstream. It is shown in Fig. 2.11 that the distance of deposition throughout the patch tends to increases with the flow blockage. Because the velocity, u_1, increases with a decrease in the flow blockage in present experiments, as shown in Fig. 2.5, it can be said that the distance of deposition mound within and behind the patch increases with decreasing flow blockage.

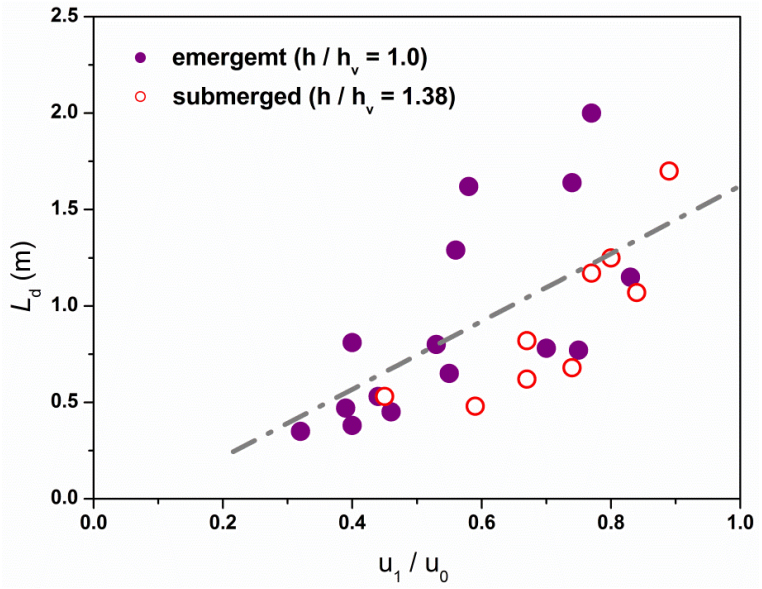


Fig. 2.12 Distance of deposition mound within and behind the patch, Ld, according to velocity, u_1, normalized by upstream velocity.

2.3.3.3 Scour in response to the patch

Fig. 2.13 shows the maximum scour depth versus the flow blockage for both emergent and submerged conditions. It can be seen that the maximum scour observed in the Region (b) increases with an increase in the flow blockage regardless of emergent or submerged condition. This is a similar trend to the result in which the flow condition is below the threshold of sediment motion in the section 3.2, which indicates that the scour depth increases almost linearly with the flow blockage, but it seems to be not uniform (See Fig. 2.9). This is attributed to the fact that the scour depth is changed due to the transition stage of sediment transport. Indeed, for the flow above the critical value of sediment motion, the scour depth fluctuates with time due to the migrations of bedforms such as bars or dunes (Ballio et al., 2010). In our experiments, there is perturbation near the entrance due to sand feeding, which generates the instability of flow induced by the bed. It leads to emergence of bedforms and migrates from the Region (a). This seems to be the reason why the trend in Fig. 2.13 is not uniform as the bedforms pass through the Regions (b) and (c).

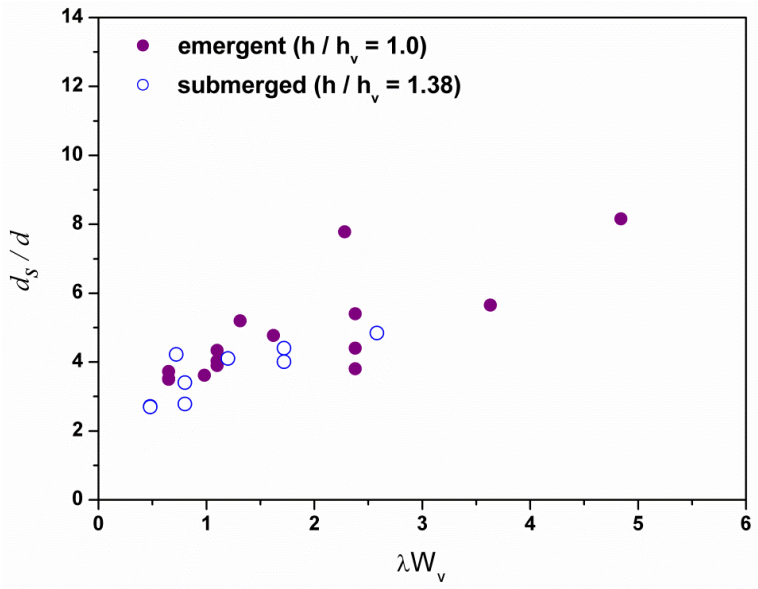


Fig. 2.13 Scour depth Scour depth according to the flow blockage under the flow above the threshold of sediment motion, where the solid symbols denote data of the emergent patches and the empty symbols denote data of the submerged patches.

2.3.3.4 Deposition in response to the patch

In the experimental data with the flow which exceeds critical value of sediment threshold, sediment deposition is observed in the Regions (d) and (e). Fig. 2.14 shows the ratio of depositional volume to input sediment volume according to the ratio of the flow rate through the Region (d), Q_v to the total flow rate, Q. The amount of deposition is only considered within and behind the patch, whereas the sediment deposited along the lateral edge and downstream of the Region (d) is excluded.

The ratio of deposition increases almost linearly with the increase in the ratio of the flow rate through the Region (d) regardless of emergent or submerged conditions within present hydraulic conditions. It is shown that for the same flow condition, the higher patch densities experience much smaller sediment accumulation than those of the low patch densities in the Regions (d) and (e). As the flow rate through the Region (d) increases (i.e. the flow velocity increases behind the patch as shown in Fig. 2.4), the diversion of flow from the Region (d) decreases. Therefore, as the patch density becomes denser, sediment is not transported into the Region (d) of downstream and the greater sediment volumes are carried away from the Region (d) since the more flow rate is diverted away from the

Region (d). It is found that a similar trend appears in that of the submerged condition and thus, the ratio of the flow rate through the patch versus the total flow rate can be a good predictor for sediment deposition volume in the Regions (d) and (e) as the flow condition exceeds the threshold of sediment motion.

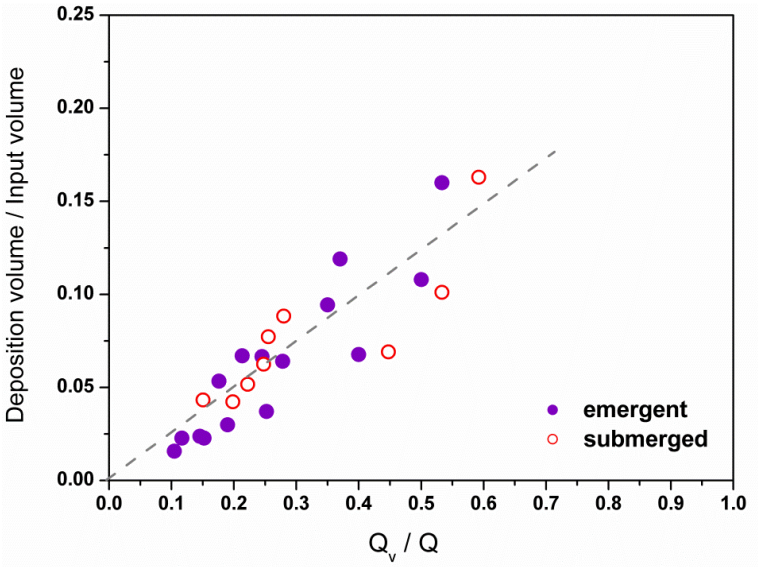


Fig. 2.14 Ratio of depositional volume to input sediment according to the flow rate through the patch where the solid symbols denote data of the emergent patches and the empty symbols denote data of the submerged patches.

Fig. 2.15 shows the ratio of deposition volume to input sediment volume according to the flow blockage. In this figure, the observed data of emergent ones are presented together with those of submerged ones. The experimental data are regressed for each obstruction ratio using power law and these are drawn on the data to distinguish between them. It can be seen that the ratio of deposition in the Regions (d) and (e) is clearly a function of the flow blockage regardless of submergence ratio. The flow blockage is strongly associated with the diversion of flow, so that the diversion of flow becomes higher as the flow blockage increases, which is reflected in much more loss of sediment volume from the leading edge of the Region (d). Thus, the sediment possible to go into the Region (d), after which it is accumulated in the Region (d) or (e), is diminished. It is found that the obstruction ratio shows a much greater influence on the ratio of deposition volume than the length scale of the patch. The length scale of the patch shows negligible effects in both

emergent and submerged conditions as shown in Fig. 2.15.

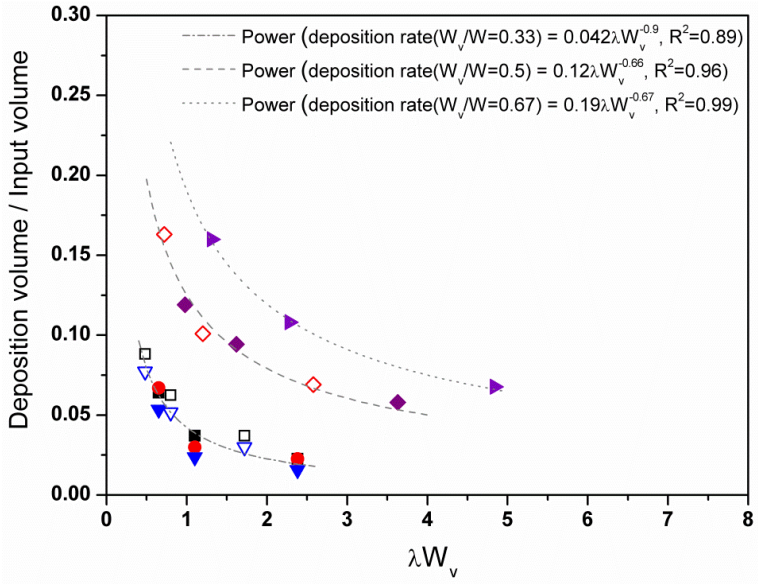


Fig. 2.15 Ratio of depositional volume to input sediment according to the flow rate through the patch where the solid symbols denote data of the emergent patches and the empty symbols denote data of the submerged patches. (when W_v = 0.2 m and L_v = 0.3 m, the data symbol is square; when W_v = 0.2 m and L_v = 0.5 m, the data symbol is circle; when W_v = 0.2 m and L_v = 1.0m, the data symbol is nabla; when W_v = 0.3 m and L_v = 0.5 m, the data symbol is diamond; when W_v = 0.4 m and L_v = 0.5 m, the data symbol is right-triangle.)

As the flow condition is above the critical value of sediment motion, the sediment transport arises actively, so the bedforms of rivers are considerably changed to those such as braiding bars and alternating bars. Vegetation is one of the important factors in channel evolutions since it can significantly affect morphological change (Tsujimoto, 1999; Jang and Shimizu, 2007; Crosato and Saleh, 2010), and its succession is related to the flow stage. We found that for low flow blockage, the sediment is deposited behind the patch. As the flow rate is reduced, the depositional mound behind the patch can therefore emerge from the water. Emerged mound creates new environments which provide more chances to sprout plant shoots and to grow. Plants established on the emerged mound accelerate the stability of the bed. It indicates that as the flow stages are repeated, the development of the

patch may be elongated in the streamwise direction. Also, as shown in our experiments, the length of the mound covered by plants becomes much longer as the flow blockage decreases. On the other hand, the succession of plants is inhibited in the lateral direction due to high bed shear stress as a result of diversion of flow. Tsujimoto (1999) conducted laboratory experiments on the process of degradation and expansion of the patch with repeated dry and flood seasons. They showed that the sandy island covered with vegetation is elongated with repeated floods in the streamwise direction due to the suspended sediment load. Edward et al. (1999) described that the scours are observed at the apex and the lateral edge along the length of the island in the Tagliamento River in Italy that inhibit growth of the island in the lateral direction. On the other hand, it is pointed out that the island with vegetation encourages deposited sediment at the downstream end of the island and thus, that is elongated with growing plants in downstream direction.

2.4 SUMMARY

For the planting management and river restoration, isolated patches of vegetation were practical for improving stream habitat and ecology. The effect of a finite patch of vegetation on flow and bed morphology in the open channel was investigated using laboratory experiments. The patch of emergent and submerged vegetation was modeled by circular cylinders and it was located along a side wall of the channel. Various configurations of the patch and submergence ratio were taken into account. Two flow conditions, which were below and above the threshold of sediment motion, were considered. For flows below the threshold of sediment motion, the erosion took place primarily opposite the patch and near the leading edge. The degree of scouring depth observed at both regions increased with the non-dimensional flow blockage (the product of the patch density and the patch width), and as the submergence ratio increased, the scour depth decreased. In contrast, for flows above the threshold of sediment motion, sediment deposition was observed near the patch due to reduction of bed shear stress, which was strongly influenced by the flow blockage and the obstruction ratio (the patch width to channel width). As the flow blockage increased or the obstruction ratio decreased, the deposition rate within and behind the patch decreased. Also, the deposition rate increased with an increase in the ratio of flow rate through the patch.

CHAPTER 3 EFFECT OF A PATCH OF VEGETATION IN OPEN CHANNEL FLOWS WITH ERODIBLE BANK

3.1 INTRODUCTION

In last decades, global warming has brought the regional torrential rain events, which has increased destructive floods. From the late 19th century, many channels have been denudated and straightened for improving discharge capacity when heavy rain occurs, but they have caused unexpected results such as the destruction of ecosystem and water pollution (Rominger et al., 2010). Recently, attempts to restore ecology and landscape of rivers have increased. Vegetation has been advocated as a complement for river restoration to improve water quality and in-stream habitat. The presence of vegetation in the watercourse dramatically alters flow directions, flow velocities, turbulence intensities and Reynolds stresses, laterally and vertically (Shimizu and Tsujimoto 1994, Bennett et al. 2002) and therefore, they induce significant sediment transport and morphological changes (Tsujimoto 1999, Coulthard 2005, Jang and Shimizu 2007, Tal and Paola, 2007, Bennett et al. 2008). Furthermore, vegetation reduces the local velocity, which causes a reduction in erosion and promotes deposition in the stream and floodplain. On the other hand, vegetation in the streams is sometimes considered undesirable due to fact that it significantly increases water levels in the flood stage. In fact, removing vegetation is one of the methods to reduce flood risk but it may exacerbate the ecology as mentioned above. Therefore, this is one of the issues how to balance between the ecology and the flood control (Leu et al. 2008).

A lot of experiments have been conducted on flow velocities and structures influenced by additional drag force from patches of vegetation, whereas few studies are performed to investigate the bed morphological changes with the patch of vegetation. White and Nepf (2007) carried out laboratory experiments on the flow structure and momentum exchange at interface between vegetation zone and non-vegetation zone in a partly vegetated open channel. They observed that coherent vortices were generated at the interface between them. To transform a straight channel into meandering channel, Bennett et al. (2002) conducted laboratory experiments on flow structures with emergent patches, which is alternatively

placed in a flume with fixed side walls, and measured surface velocities using PIV (particle image velocimetry). They showed that the flow velocity was decelerated in vegetation zone whereas it was accelerated and deflected toward the opposite bank. Based on above experiments of Bennett et al. (2002), Bennett et al. (2008) carried out experiments on morphological response to emergent patches of vegetation in a compound channel with mobile bed. They showed that alternating patches could alter a straight channel to meandering channel with riffle and pool development. Bouma et al. (2007) monitored the bed morphological changes near circular patches in a tidal area. The spatial distributions of sediment were strongly influenced by patch densities in which the local scour was observed near the leading edge of the patch in the high patch density whereas, the low patch density had a negligible effect on localized scour. Jang and Shimizu (2007) carried out laboratory experiments to investigate effects of vegetation on bed morphology with various vegetation densities. They observed that the flow direction is affected by vegetation, and vegetation stabilized banks. Rominger et al. (2010) conducted outdoor, field-scale experiments to examine influences of vegetation on sand bars in meandering channel and they found that added vegetation on sand bars caused erosion near the edges of vegetation zone and formed the new sand bar area due to the spatial acceleration. Based on experiments of Zong and Nepf (2012), Follett and Nepf (2012) performed laboratory experiments on the bed deformations around circular patches of emergent vegetation and described that local scour within the patch was associated with the patch density and was correlated to turbulent kinetic energy.

A number of numerical models have been proposed to simulate flow behaviour and fluvial processes in response to vegetation. To model open channel flows with vegetation, Darby (1999) developed the hydraulic model to predict stage-discharge curves in nonuniform channel cross sections with flexible or rigid vegetation. Tominaga et al. (1999) simulated mean flow structures and momentum transport processes in curved open channels with vegetation using a two dimensional numerical model including the dispersion term of the secondary current. Later, to deal with bed morphology with vegetation, Tusjimoto (1999) performed the numerical analysis of morphological changes around vegetated island using a two-dimensional depth averaged model with k-ε turbulence closure and the island was extended with increases in flood repetition, longitudinally and laterally. Wu et al. (2005)

presented a sophisticated depth averaged numerical model by introducing vegetation density into governing equations, which can account for the submergence ratio of vegetation, and the model was tested. The results were compared to existing experimental data and field data. The model reasonably predicted the flow and sediment transport with emergent vegetation. Jang and Shimizu (2005) developed a two-dimensional model with moving boundary-fitted coordinate and investigated the response of alternate bars in a compound channel with different vegetation densities on floodplains. The bar migration and lateral expansion of a channel were significantly influenced by vegetation density. Liu and Shen (2008) proposed a three dimensional model to simulate flow and sediment transport with vegetation, and the model was applied to open channel flows with a vegetated island by Tsujimoto (1998). They described that the numerical model could reproduce topography changes near the island. It was shown that the three-dimensional simulation was in better agreement with experimental data than a two-dimensional simulation.

Most of the laboratory experiments on morphological response with finite patches of vegetation have been conducted in flat sand bed with fixed side wall except experiments reported by Bennett et al. (2008) but they did not measure the bed elevation inside the patches, so that the detailed erosion and deposition patterns in the patches were not captured. While several numerical models tested and applied to open channel flows with vegetation, relatively few models were applied to fluvial processes with vegetation. In particular, it is apparent from above literature review that morphological changes within and near the patch have not been extensively studied, so that there is still a lack of understanding of morphological behaviour in and near the patch.

To be successful in river managements and restoration of ecology, it is important how the place, density and size of patches of vegetation give rise to impact on flows as well as erosion and deposition. The objective of this study is to demonstrate predictive capacities of a numerical model and to investigate the morphological behaviour in response to a finite patch of vegetation in an open channel with erodible bank using both experiments and computations. Laboratory experiments are conducted to examine bed morphological changes near the rigid-emergent patch of vegetation, especially within the patch, which is modelled as circular cylinders. Four experimental cases are tested with three patch densities and without a patch. A 2D depth-averaged model that is capable of simulating flow and

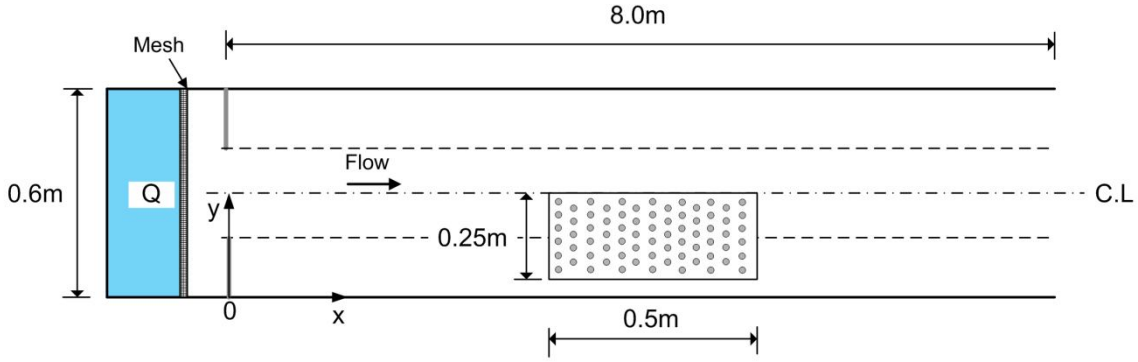
morphological change with a patch of vegetation in an open channel flow considering erodible bank is proposed. The model is applied to partly-vegetated open channel flows, and the simulated results are compared to measured data available in the literature for a validation of the model. The numerical simulations are performed for all experimental cases and the simulated results are compared with experimental data. The sensitivity to parameters directly related to sediment transport and morphological changes is investigated and the change in bed topography and the channel expansion in response to the patch are described. In addition, the distributions of flow rate with the patch density and time, the channel widening and sediment deposition in response to extent of the patch are presented.

3.2 EXPERIMENTAL SET UP

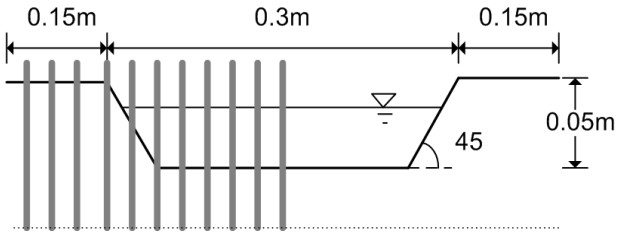
Experiments were conducted in a flume of 8.0 m long and 0.6 m wide with wooden sidewall (Fig. 3.1a). The flume was filled with well-sorted sand with 0.9 mm mean diameter and the initial channel was set to a compound channel with a main-channel width w_b of 0.2 m, a floodplain height h_0 of 0.05 m and 45° bank slope (Fig. 3.1b). The shape of a patch was rectangular 0.5 m long and 0.25 m wide. The model patch of vegetation which was idealized as emergent and staggered array of circular cylinders of diameter 5 mm was placed at the centre of the channel, beginning at 3.75 m from the upstream end (Figs. 3.1a and b). Three patch densities (φ= 3.12, 5.44 and 12.0 m^{-1}, where φ is the patch density) were considered. The patch density was defined to a frontal area per unit volume of the patch. Fig. 3.1 shows a definition of the patch where S_x and S_y were spacing of cylinders. For representing different densities, the spacing of 2.0 cm, 3.0 cm and 4.0 cm were used corresponding to φ= 12.0, 5.44 and 3.12 m^{-1}, respectively. The experimental parameters for the patch of vegetation are summarized in Table 3.1.

Four experimental cases in which three different discharges and a different channel slope used were performed with three patch densities and without the patch under subcritical flow conditions (Fr = 0.75 ~ 0.85). Initially, the discharge and the channel slope were set, and small discharge was run into the channel to saturate the bed. During experiments, sediment was supplied at upstream end of the channel to keep the bed shape without local disturbance such as scour. In all experiments, the traction force was above the threshold of sediment

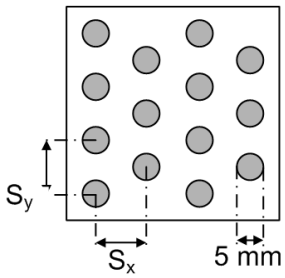
motion and the duration of each experiment was maintained to be 2 hours. To check the channel widening rate, the widths were measured at some locations every 30 min, using



(a) Top view.



(b) Initial channel with a patch of vegetation in a cross section.



(c) Cylinder arrangement

Fig. 3.1 Schematic diagram of the experimental flume.

point gages. The experiments were finished by stopping the flow and the water was drained slowly to ensure bed topography without deformations. After carefully removing the patch, the topography measurements were carried out using a laser bed profiler, which was mounted over the channel. The bed surface was surveyed every 10 cm in the longitudinal direction from 1.0 to 7.0 m, and every 0.4 cm in the transverse direction, except the area near

the patch where the topography measurements were done every 2 cm in the longitudinal direction (from 3.25 m to 4.75 m). After each experiment, an initial channel shape was reformed. The experimental conditions are summarized in Table 3.2.

Table 3.1 Experimental parameters for a patch of vegetation.

	Low density (LD)	Medium density (MD)	High Density (HD)
Spacing (S_x=S_y, m)	0.04	0.03	0.02
Number of cylinders	78	136	300
Density (m^{-1})	3.12	5.44	12

Table 3.2 Experimental conditions.

	Cases 1	Case 2	Case 3	Case 4
Discharge (L/s)	1.33	1.79	2.16	1.33
Initial Slope	1/250	1/250	1/250	1/180
Mean diameter (mm)	0.9	0.9	0.9	0.9

3.3 NUMERICAL MODEL

3.3.1 Governing equations of flow

A depth-averaged, two-dimensional numerical model was proposed to simulate flow, sediment transport and process of bed morphology in an open channel with vegetation. Governing equation of this model is based on depth-averaged continuity equation and momentum equations that take vegetation density into account. These are described as,

Continuity equation:

$$\frac{\partial\left[(1-c)h\right]}{\partial t}+\frac{\partial\left[(1-c)M\right]}{\partial x}+\frac{\partial\left[(1-c))N\right]}{\partial y}=0 \tag{3.1}$$

Momentum equation in *x*- and *y*-directions:

$$\frac{\partial\left[(1-c)M\right]}{\partial t}+\frac{\partial\left[(1-c)uM\right]}{\partial x}+\frac{\partial\left[(1-c)vM\right]}{\partial y}$$
$$=-gh(1-c)\frac{\partial H}{\partial x}-(1-c)\frac{\tau_{bx}}{\rho}+\frac{\partial\left[(1-c)(-\overline{u'^2}h)\right]}{\partial x}+\frac{\partial\left[(1-c)(-\overline{u'v'}h)\right]}{\partial y} \tag{3.2}$$
$$+\nu\left[\frac{\partial}{\partial x}\left(h\frac{\partial\left[(1-c)u\right]}{\partial x}\right)+\frac{\partial}{\partial y}\left(h\frac{\partial\left[(1-c)u\right]}{\partial y}\right)\right]-F_x$$

$$\frac{\partial\left[(1-c)N\right]}{\partial t}+\frac{\partial\left[(1-c)uN\right]}{\partial x}+\frac{\partial\left[(1-c)vN\right]}{\partial y}$$
$$=-gh(1-c)\frac{\partial H}{\partial y}-(1-c)\frac{\tau_{by}}{\rho}+\frac{\partial\left[(1-c)(-\overline{u'v'}h)\right]}{\partial x}+\frac{\partial\left[(1-c)(-\overline{v'^2}h)\right]}{\partial y} \tag{3.3}$$
$$+\nu\left[\frac{\partial}{\partial x}\left(h\frac{\partial\left[(1-c)v\right]}{\partial x}\right)+\frac{\partial}{\partial y}\left(h\frac{\partial\left[(1-c)v\right]}{\partial y}\right)\right]-F_y$$

where h = water depth; u, v = depth-averaged velocities; M, N = discharge fluxes($M = uh$, $N = vh$); c = concentration of vegetation; g = gravitational acceleration; ρ = density of water; τ_{bx}, τ_{by} = bottom shear stresses; H = water surface elevation($h + z_b$); $-\overline{u'^2}, -\overline{v'^2}, -\overline{u'v'}$ = depth-averaged Reynolds stresses; ν = molecular kinetic viscosity; F_x, F_y = drag forces exerted by vegetation.

Components of the bottom shear-stress vector are evaluated by

$$\tau_{bx} = f\rho u\sqrt{u^2+v^2} \qquad \tau_{by} = f\rho v\sqrt{u^2+v^2} \tag{3.4}$$

where f = friction coefficient, which is calculated using Manning's roughness coefficient as $gn^2 / R_s^{1/3}$. R_s is a spacing hydraulic radius in vegetated region which defined as $R_s = b_v h/(2h+b_v)$; b_v is the spacing of stems (Barfield et al., 1979). When vegetation density become very low or there is no vegetation, $R_s = h$.

Components of the drag force due to vegetation expressed by

$$F_x = \frac{1}{2}C_D\rho\varphi h u_v\sqrt{u_v^2+v_v^2} \;=\; C_D\rho\frac{2c}{\pi D}hu_v\sqrt{u_v^2+v_v^2} \tag{3.5}$$

$$F_y = \frac{1}{2}C_D\rho\varphi h v_v\sqrt{u_v^2+v_v^2} \;=\; C_D\rho\frac{2c}{\pi D}hv_v\sqrt{u_v^2+v_v^2} \tag{3.6}$$

with

$$\varphi = \frac{N_v D \min(h, h_v)}{L_v W_v h} \quad , \qquad c = N_v \frac{\pi D^2}{4} \frac{\min(h, h_v)}{L_v W_v h}$$

where C_D = drag coefficient; φ = vegetation density; N_v = the number of stems; D = diameter of a stem; L_v = length of vegetated area; W_v = width of vegetated area; h_v = vegetation height. In equations (3.5) and (3.6), u_v and v_v are the flow velocities acting on vegetation which should be equal to depth-averaged velocities, u and v, respectively for emergent conditions (Wu et al., 2005).

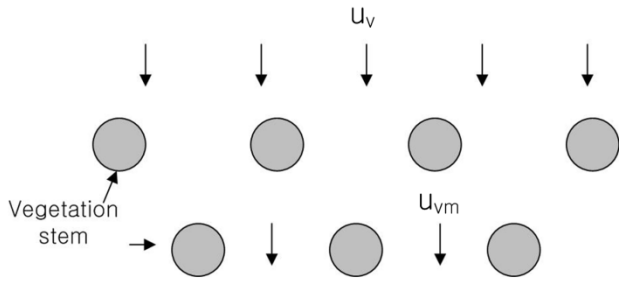


Fig. 3.2 Definitions of U_v and U_{vm} in vegetation region (Stone and Shen, 2002).

In an isolated cylinder, drag coefficient, C_D is based on upstream velocity of a cylinder, u_v shown in Fig. 3.2, so that in a cylinder array, the drag coefficient is significantly affected by population density of cylinders, influencing upstream velocity of cylinders. For instance, Tanino and Nepf (2008) presented that C_D increases with vegetation density and decreases with cylinder Reynolds number. Stone and Shen (2002) proposed the flow velocity, u_{vm} between cylinders and it had very little variation for a wide range of density and cylinder Reynolds number in comparison with u_v. They presented an averaged value, C_{DM} of 1.05 based on u_{vm}, which is a reasonable estimation for C_D. From assumption that spacing between vegetation stems are equal in staggered arrangement, the relation between C_{DM} and C_D can be derived in unit volume as

$$C_D = C_{DM} / \left(1 - \sqrt{\frac{4ch}{\pi \min(h, h_v)}}\right)^2 \tag{3.7}$$

Constitutive Equation of Reynolds Stress

For Reynolds stress tensor components in momentum equations, the following linear constitutive equation used

$$-\overline{u_i' u_j'} = \nu_{th}\left(\frac{\partial U_i}{\partial x_j}+\frac{\partial U_j}{\partial x_i}\right)-\frac{2}{3}k\delta_{ij} \qquad i = 1 \text{ or } 2, \quad j = 1 \text{ or } 2 \tag{3.8}$$

where ν_{th} is eddy viscosity coefficient. To obtain the eddy viscosity coefficient, both zero-equation model and k-ε model were applied and the simulated results were compared in terms of the depth averaged velocity and Reynolds stress.

1. Zero -equation model: In equation (3.8), the eddy viscosity is determined by

$$\nu_{th} = \alpha h u_* \tag{3.9}$$

where α = constant value between 0.1 and 1.0 (Kimura and Hosoda, 2004). In this study, 0.2 was used. Nezu and Nakagawa (1993) proposed an empirical formula for vertical distribution of k as

$$\frac{k}{u_*^2} = 4.78\exp\left(-2\frac{z}{h}\right) \tag{3.10}$$

where k = turbulent kinematic energy; z = distance from the bottom; u_* = local friction velocity. The turbulent kinetic energy integrated in vertical direction become the following formula

$$k = \gamma_k u_*^2 \qquad \gamma_k = 2.07 \tag{3.11}$$

2. k-ε model: In equation (3.8), the eddy viscosity is evaluated by

$$\nu_{th} = c_\mu \frac{k^2}{\varepsilon} \tag{3.12}$$

where c_μ is an empirical constant (= 0.09) and ε is the turbulence dissipation rate. The distributions of the turbulence kinetic energy and dissipation rate are determined form the following transport equations.

$$\frac{\partial hk}{\partial t}+u\frac{\partial hk}{\partial x}+v\frac{\partial hk}{\partial y} = \frac{\partial}{\partial x}\left(\frac{\nu_{th}}{\sigma_k}h\frac{\partial k}{\partial x}\right)+\frac{\partial}{\partial y}\left(\frac{\nu_{th}}{\sigma_k}h\frac{\partial k}{\partial y}\right)+\left(P_h+P_{kb}+P_v+\varepsilon\right)h \tag{3.13}$$

$$\begin{aligned}&\frac{\partial h\varepsilon}{\partial t}+u\frac{\partial h\varepsilon}{\partial x}+v\frac{\partial h\varepsilon}{\partial y} = \\ &\frac{\partial}{\partial x}\left(\frac{\nu_{th}}{\sigma_\varepsilon}h\frac{\partial \varepsilon}{\partial x}\right)+\frac{\partial}{\partial y}\left(\frac{\nu_{th}}{\sigma_\varepsilon}h\frac{\partial \varepsilon}{\partial y}\right)+h\left[c_{\varepsilon 1}\frac{\varepsilon}{k}\left(P_h+c_{\varepsilon 3}P_v\right)+P_{\varepsilon b}-c_{\varepsilon 2}\frac{\varepsilon^2}{k}\right]\end{aligned} \tag{3.14}$$

with

$$P_h = \nu_{th}\left[\left(2\left(\frac{\partial u}{\partial x}\right)^2 + \left(\frac{\partial u}{\partial y}+\frac{\partial v}{\partial x}\right)^2 + 2\left(\frac{\partial v}{\partial y}\right)^2\right)\right]$$

$$P_{kb} = c_f^{-1/2} u_*^3 / h$$

$$P_{\varepsilon b} = c_{\varepsilon\beta} c_\varepsilon c_\mu^{1/2} c_f^{-3/4} u_*^4 / h^2$$

$$P_v = c_{vk}\left(f_{dx} u_v + f_{dy} v_v\right)/\left(1-\phi\right)$$

where c_{vk}, $c_{\varepsilon 1}$, $c_{\varepsilon 2}$, $c_{\varepsilon 3}$,$c_{\varepsilon\beta}$, σ_k and σ_ε are empirical constants. In the present computation, we use the following standard values by Launder and Spalding (1974): σ_ε = 1.3, σ_k = 1.0, $c_{\varepsilon 1}$ = 1.44, $c_{\varepsilon 2}$ = 1.92 and Lopez and Garcia (1997): $c_{\varepsilon 3}$ = 1.33, c_{vk} = 1.0. Also, $c_{\varepsilon\beta}$ uses 3.6 (Rodi, 1993, Tsujimoto, 1998).

3.3.2 Sediment transport models

Two-dimensional sediment continuity equation is

$$\frac{\partial\left[\left(1-c\right)z_b\right]}{\partial t} + \frac{1}{1-\lambda}\left(\frac{\partial\left[\left(1-c\right)q_b^x\right]}{\partial x} + \frac{\partial\left[\left(1-c\right)q_b^y\right]}{\partial y}\right) = 0 \tag{3.15}$$

where z_b = bed elevation; λ = porosity of the bed material; q_b^x, q_b^y = bedload transport rates per unit width in *x*- and *y* - directions, respectively which are given by defining streamline direction, *s* and transverse direction, *n*:

$$q_b^x = q_b^s \cos\theta - q_b^n \sin\theta \tag{3.16}$$

$$q_b^y = q_b^s \sin\theta + q_b^n \cos\theta \tag{3.17}$$

where q_b^s, q_b^n = bedload transport rates in s and n directions, respectively.

The sediment transport rate along the streamline direction is calculated using the formula proposed by Kovacs and Parker (1994), included the effect of bank slope and gravity on side bank based on formula of the Ashida and Michiue (1972). Modified by Yamaguchi and Izumi (2005) as

$$q_b^s = \frac{a^{1/2}}{\mu_c}\left[\tau_* - \tau_{*c}\left(1+\frac{1}{\mu_c}\frac{\partial z_b}{\partial s}\right)\right]\left[\tau_*^{1/2} - \tau_{*c}^{1/2}\left(1+\frac{1}{2\mu_c}\frac{\partial z_b}{\partial s}\right)\right]\left(1-\frac{1}{\mu_c}\frac{\partial z_b}{\partial s}\right)\sqrt{Sgd^3} \tag{3.18}$$

with

$$a = \frac{u_*}{V}$$

where τ_* = non-dimensional shear stress, τ_{*c} = non-dimensional critical shear stress, μ_c = the dynamic Coulomb friction factor (= tanϕ, where ϕ = angle of repose), d = grain size, S = specific weight of sediment in fluid and $V = \sqrt{u^2 + v^2}$.

The sediment transport rate in the n - direction, q_b^n is calculated by using Hasegawa equation (2000) as

$$q_b^n = q_b^s\left[\frac{u_{bn}}{u_{bs}} - \sqrt{\frac{\tau_{*c}}{\mu_s\mu_k\tau_*}}\frac{\partial z_b}{\partial n}\right] \tag{3.19}$$

where u_{bs} and u_{bn} = near-bed velocities in the s- and n-directions; μ_s = static friction factor equal to 0.7 and μ_k = kinetic friction factor equal to 0.5.

The near-bed velocities in the s- and n- directions are evaluated by

$$u_{bs} = \beta V \tag{3.20}$$

where $\beta = 3(1-\sigma)(3-\sigma)$

$$u_{bn} = N_*\frac{h}{r_s}u_{bs} \tag{3.21}$$

where β was assumed to be parabolic distribution of flow in the vertical direction (Engelund, 1974).σ = 3/($\chi\kappa$+1); χ = velocity factor (= V / u_*); κ = von Karman constant(= 0.4); r_s = radius of curvature of the streamline; N_* = coefficient for secondary flow, which varies from 7.9 to 11.4 (Kikkawa et al. 1976). In present study, it is assumed to be 11.0.

In order to calculate channel widening due to bank erosion, the bank erosion model proposed by Hasegawa (1984) is employed. It is calculated under assumption that as the gradient of the bank becomes greater than the angle of repose, ϕ, bank corruption takes place until the new slope is identical to the angle of repose (Fig. 3.3). These processes are implemented through corrections of bed elevation and the angle of repose is calculated as follows

$$\tan\phi = \frac{(z1-\Delta z1)-(z2+\Delta z2)}{\Delta l} \tag{3.22}$$

where z1 and z2 are the bed elevation at p1 and p2, respectively. Δl is the distance adjacent to cell centres. $\Delta z1$ and $\Delta z2$ are the bed variation due to bank erosion, which indicate an increase and decrease in bed change, respectively. These processes are repeated in all computational cells, iteratively until the bed slope at whole domain becomes smaller than angle of repose. The failed sediment is included in the computation and the total sediment mass in the computational domain is conserved. In the present study, we test the sensitivity to angle of repose. The angle of repose is assumed to be 30 degrees as it will be discussed later.

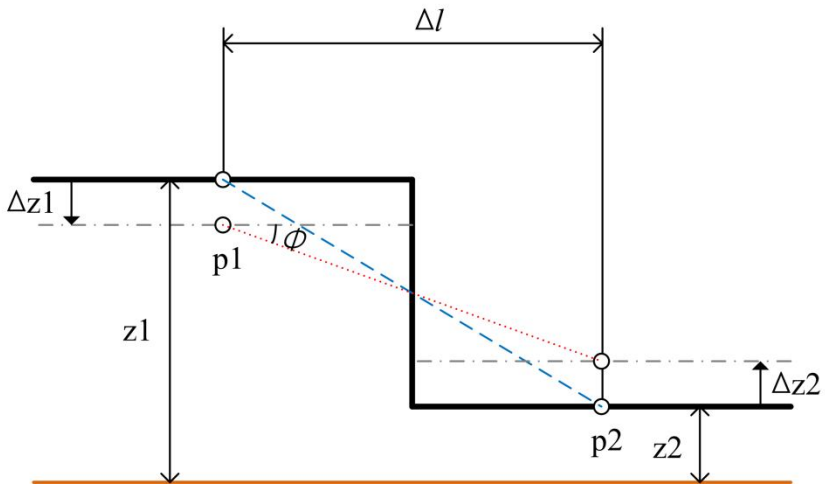


Fig. 3.3 Definition of bank erosion process. Dash line is a slope before bank collapse and dot line is a slope after bank collapse.

3.3.3 Numerical scheme and model set up

The governing equations, i.e. continuity and momentum equations for flow are solved with the finite-volume method (FVM) on a full staggered grid. The QUICK scheme, which has second order accuracy in space, is employed for the convection terms and central differencing is applied to the diffusion terms in momentum equations. The first order upwind scheme is used for continuity equation of sediment transport. The second order Adams-Bashforth scheme is used for time integration in all equations.

Computational domain is set to 8.0 m long and 0.6 m wide, which is identical to the

experimental flume. The number of computational cells is used with 400 in the stream-wise direction and 60 in the transverse direction. The time step is set to 0.001s and each simulation was lasted for 2hours. A specified discharge at upstream end and Neumann boundary condition at downstream end are given. A friction along solid boundaries and emerged banks is evaluated by the log-law. For the boundary of bedload flux, the Neumann boundary condition is imposed. Conditions such as discharge, channel slope, channel width and vegetation density used in the computations are given same as the present experimental conditions.

3.4 RESULTS AND DISSCUSSION

3.4.1 Validation

Validation of the developed model is conducted through comparisons with experimental data available in the literature reported by Tsujimoto and Kitamura (1995). They carried out laboratory experiments to investigate the hydraulic characteristics between vegetated and non-vegetated channel flows, and the depth averaged velocities and the Reynolds stresses were measured. The flume used in the experiments was 12 m long and 0.4 m wide where the vegetation zone was 0.12 m wide located at the side wall, consisting bamboos with diameter of 0.0015 m. The water depths were 0.0457 m for run 1 and 0.0428 m for run 2 with a slope of 0.0017. In the experiments of run 1 and 2, the spacing of bamboos was 0.028 m and 0.02 m, respectively. The number of computational cells is set to 240 and 40 in the x - and y - directions, respectively. Two turbulence models are tested with the zero-equation model and the standard k-ε model.

Figs. 3.4a and b show comparisons of experimental data and computed profiles for the depth-averaged velocity distribution. It can be seen that the velocity profiles in vegetation zone are nearly uniform in the lateral direction and the velocity rapidly increases from the interface between the vegetated channel and the non-vegetated channel, $y = 0$, and then it decreases near the side wall. The velocity distributions with the k-ε model agree well with experiment data, but the velocity profiles with the zero-equation model show discrepancies close to the interface between them. In particular, the high velocity gradient occurs due to fact that a strong shear layer is formed between the vegetated zone and the non-vegetated zone, and the mass and momentum exchange take place between them. The generation of

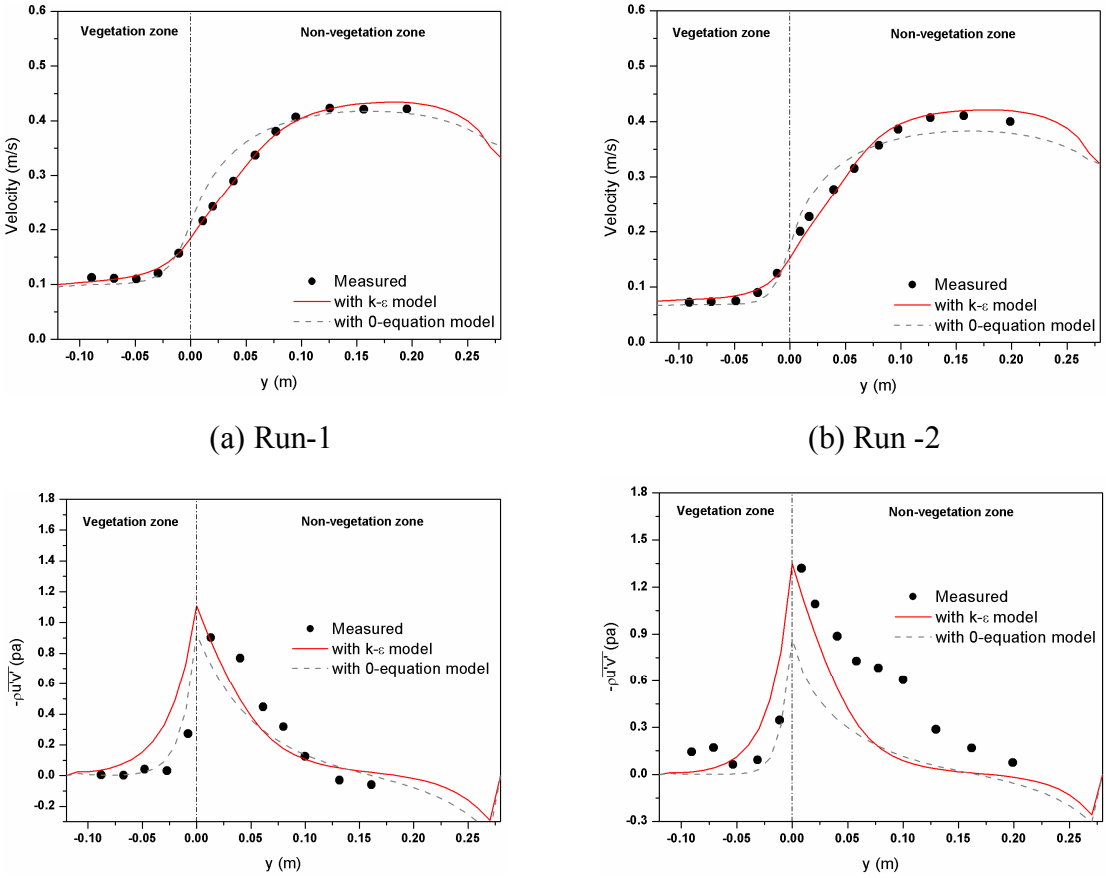


Fig. 3.4 Comparison of experimental and computed profiles of the depth-averaged velocity and Reynolds stress.

turbulence and the eddy viscosity seems to be not reproduced accurately using the zero-equation model, so that the depth averaged velocity profiles with the zero-equation model are over-estimated close to the interface in the open channel. Figs. 3.4c and d present comparisons of the experimental data and computed profiles of the Reynolds stress distribution. The maximum values of the Reynolds stress are found at the interface in both results. Overall, computed profiles with the *k-ε* model are in better agreement than computed ones with the zero-equation model, compared to the experimental data, even though the profiles of the Reynolds stress are under-estimated in the non-vegetated channel. The Reynolds stress is proportional to the velocity gradient in the lateral direction, so that the high Reynolds stresses reflect the high mass and momentum exchange. It is found, as a

whole, the distributions of the depth averaged velocity and the Reynolds stresses are predicted well by the present computational model with the k-ε model. Therefore, only the k-ε turbulence model is employed for computations here after in present study.

3.4.2 Sensitivity to parameters

In the computations, the channel expansion process due to bank erosion is associated with the angle of repose. In the simplified bank erosion model used in this study, the bank erosion is calculated as a local bed slope, which is calculated using the bed elevation of neighboring grids, is steeper than designated angle of repose. In addition, the bank is collapsed regardless of whether bank is submerged or not. In order to check the sensitivity to angle of repose for the bank erosion model, three different values of the angle of repose, i.e. ϕ = 25, 30 and 35 degrees, are tested, which is chosen from pervious literatures (Jang and Shimizu 2005, Jang and Shimizu 2007). Fig. 3.5 depicts a comparison of cross sectional bed elevations at the mid-channel of Case 2.

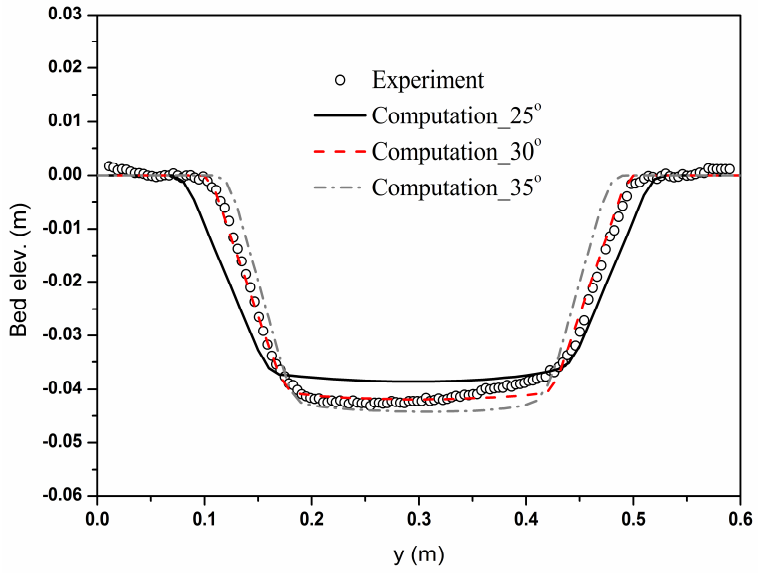


Fig. 3.5 Comparison of cross-sectional bed elevation without the patch.

Overall, the agreement between experimental and computational data appears to be good and particularly, the bank slopes are satisfactory, which demonstrates that the value of 30 degrees of angle of repose is appropriate. It is observed that the rate of bank erosion decreases with the greater angle of repose in Fig. 3.5. As the angle of repose becomes

smaller, the bed elevation increases since the sediment loading through the bank erosion increases, and then it is deposited on the low-water channel. On the other hand, the bank slope becomes steeper as the angle of repose is larger. Processes of bank erosion as well as the bed elevation in low-water channel are significantly affected by the angle of repose. It is found that as a whole, angle of repose of 30 degrees, which is chosen by trial and error, is in reasonable agreement through a comparison with experimental data, and it is applied in present study, here after.

To simulate reasonably morphological changes within the patch, the appropriate evaluation of bed shear stress is essential. Sensitivity of parameters used in the model, which directly influence bed shear stress, should be investigated. Thus, we consider the volume rate of vegetation, c in the equations, the drag coefficient, C_D and the hydraulic radius, R_s in bottom shear stress terms. In Fig. 3.6, the longitudinal bed profile for the LD patch of Case 4 at $y = 0.22$ m is shown. The bed profile (solid line) using R_s and Eq. (3.7) for evaluating C_D as well as considering c is compared with experimental data and the our result matches the experimental data well, even though the deposition is slightly under-predicted due to small-scale scour adjacent to cylinders. The bed profile without considering the volume rate of vegetation in Fig. 3.6 (red dashed line), i.e. $c = 0$, is mostly identical to the bed profile of full consideration (solid line), so that there is no effect of the volume rate of vegetation, c in the LD patch. In the present study, the values of volume rate are used from 0.013 to 0.046 for the patches and thus, in particular, the volume rate of the LD patch is negligible. However, in marsh area, the volume rate of vegetation can be as high as 0.15. In this case, the volume rate should be considered in the equations (Nepf, 2004).

To simulate flow through vegetation, the source terms have been added in momentum and turbulence transport equations to account for vegetation drag. In the source terms, the additional empirical constant is required for drag coefficient, C_D, which has been used within the range of 0.8 to 1.5. However, C_D is altered by vegetation density or Reynolds number (Stone and Shen, 2002; Tanino and Nepf, 2008), so that a formula proposed by Stone and Shen (2002), in which C_D is given as a function of vegetation density, is calibrated in this study. The bed profile (solid line) used by the formula is compared with that used with constant values assumed to be $C_D = 1.2$ and 1.5 in Fig. 3.6. It can be seen that the bed profile with $C_D = 1.2$ appears to be better than the result of full consideration (solid line). However,

it may lead to under-predictions of velocity opposite the patch, i.e. local scour and bank erosion opposite the patch, because the resistance is under-estimated. The sediment deposition that is simulated with $C_D = 1.5$ is under-predicted due to over-estimation of the vegetation drag. It indicates that the morphological behaviour in and near the patch is significantly influenced by drag coefficient, C_D and thus, the formula proposed by Stone and Shen (2002) calibrated in this study is fairly reliable.

In shallow water equations, we usually use water depth, h in bottom shear terms, but shear stress not only is generated from the bed but also occurs from cylinders in an array of cylinders. In Fig.3.6, the bed profile (solid line) calculated using the hydraulic radius, R_s (= $b_v h$ / ($2h+b_v$)) is compared to the bed profile using $R_s = h$. It can be seen that sediment deposition calculated with $R_s = h$ for evaluating bed shear stress in the patch of vegetation is significantly under-estimated within the patch because of under-predicting bed shear stress. It implies that the use of $R_s = h$ is incorrect to evaluate shear stress within the patch, so that the hydraulic radius, R_s is more suitable for evaluating shear stress instead of $R_s = h$.

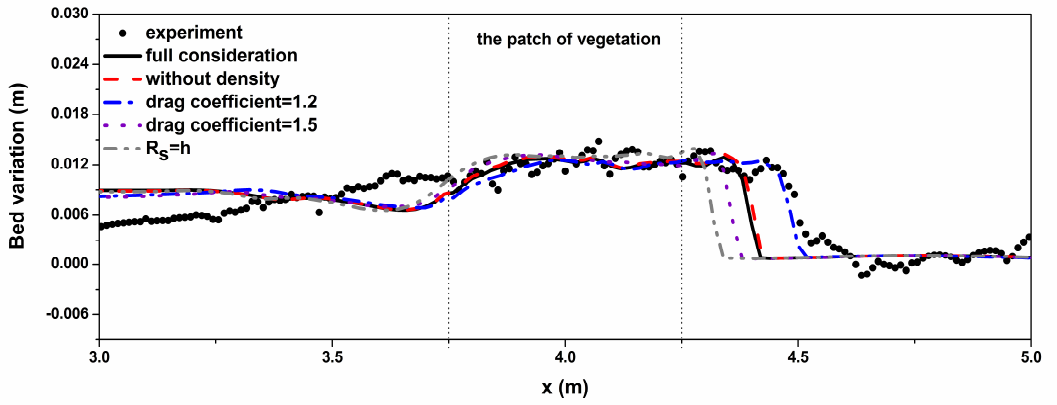
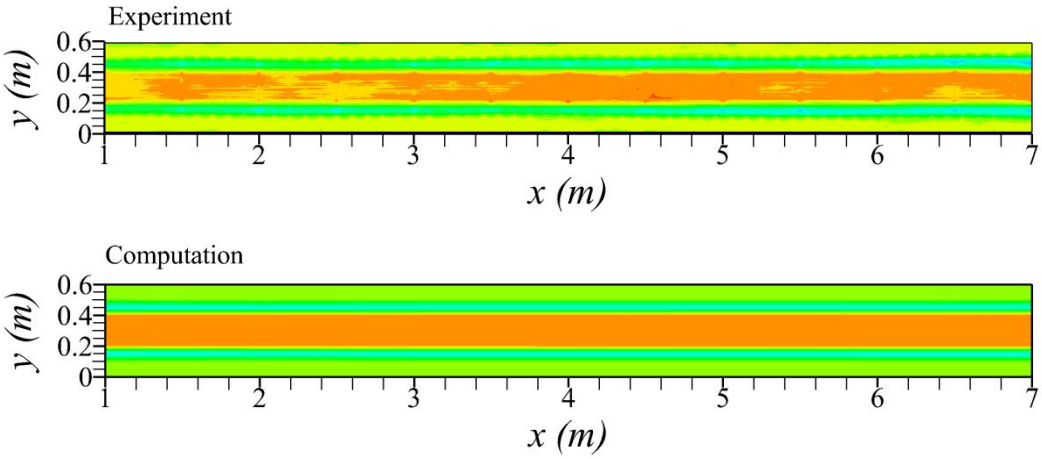


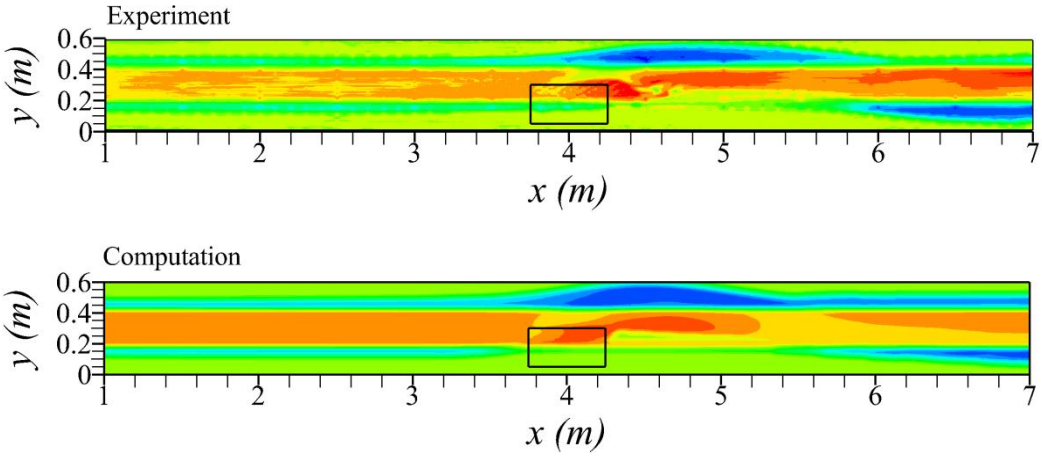
Fig. 3.6 Longitudinal bed profiles at $y = 0.22$m for the LD patch of Case 4.

3.4.3 Variation of bed topography

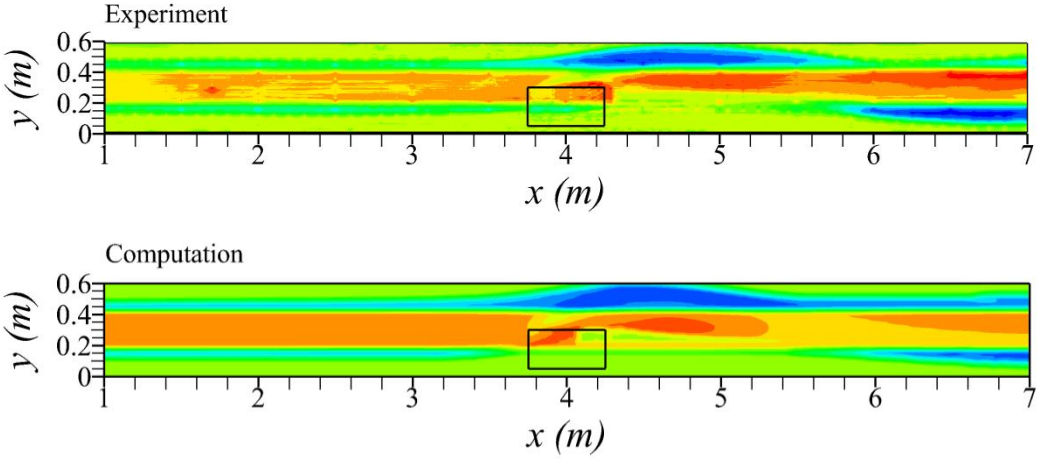
Vegetation introduced in open channels affects significantly water depth, velocity, flow directions and bed morphology in comparison with non-vegetated channels. Fig. 3.7 shows comparisons of variation of bed topography with varying patch densities between



(a) Non-vegetated Channel



(b) Low density (LD)



(c) Medium density (MD)

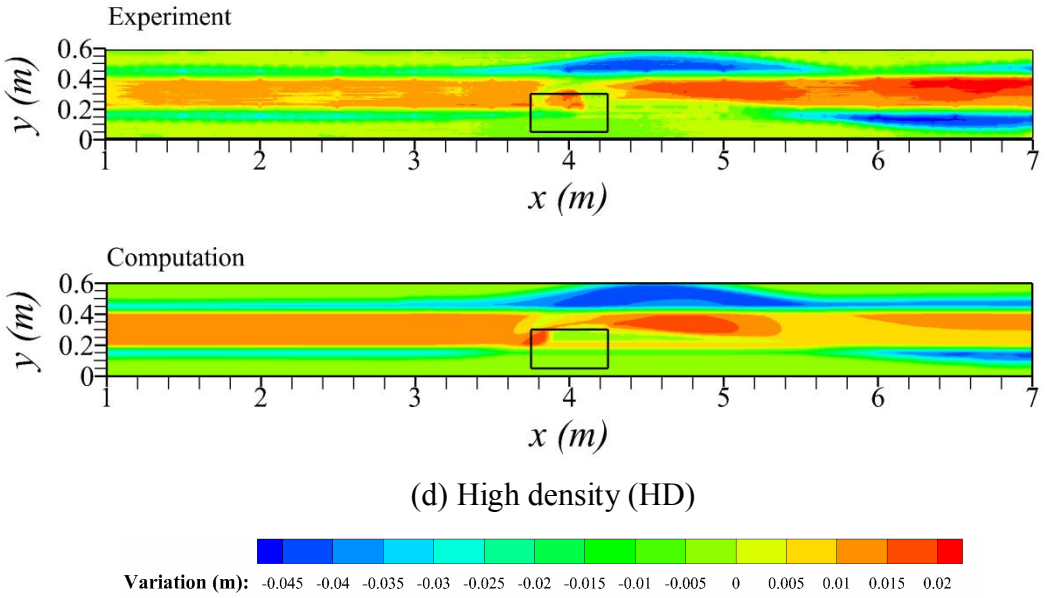


Fig. 3.7 Comparison of variation of bed elevation between experiment and computation for case 3: (a) Non-vegetated channel; (b) Low density (LD); (c) Medium density (MD); (d) High density (HD). Flow is from left to right. Solid line in the domain is a patch of vegetation.

experimental and computational results for Case 3. Without the patch of vegetation in Fig. 3.7a, the channel is expanded due to lateral bank erosion, which is almost symmetric along the centre line in the longitudinal direction. When the patch of vegetation is added in the mid-channel, considerable morphological changes are observed near and downstream of the patch. The flow directions are altered due to the erosion and deposition. The flows cause again lateral bank erosion further downstream of the patch and the opposite region eroded near the patch (Figs. 3.7b, c and d). Sediment deposition is observed in the mid-channel and downstream of the patch. Sediment is also deposited within and near the patch due to reduced bed shear stress caused by additional drag which is exerted by the patch of vegetation. In all cases, the flow conditions are above the threshold of sediment motions, so that the sediment is transported from upstream of the patch in which the sediment loading from bank erosion is contained. It is found that sediment deposited within the patch decreases as the patch density becomes higher. As flow approaches the patch, the flow is diverted away from the patch because of vegetation drag. Sediment load reaching the

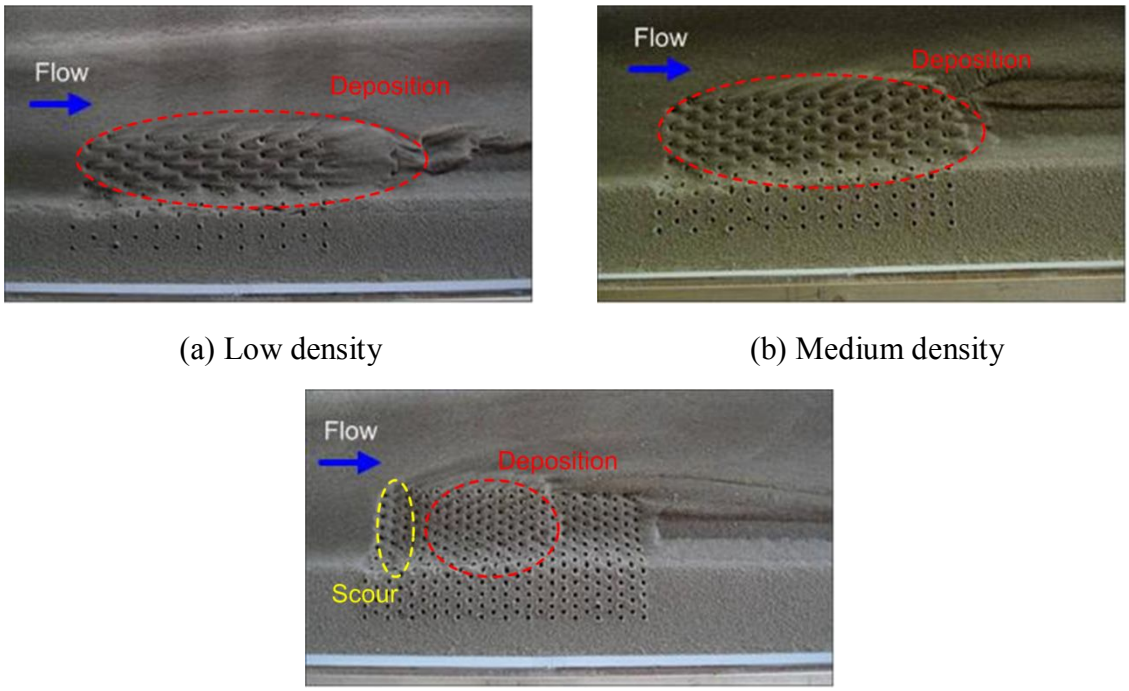
leading edge of patch can be either to be diverted away from the patch or to transport into the patch, after which it is deposited within or behind the patch due to a reduction in bed shear stress. Higher diversion of flow caused by higher patch density carries away sediment from the patch and thus the amount of sediment deposited in and behind the patch decreases with an increase in patch density. The added patch in open channel flows leads to significant bank erosion directly opposite and further downstream of the patch. These processes make channel topography altered from straight channel to meandering channel in Fig. 3.7. In fact, the present experiments are conducted for 2 hours before flow reaches the side walls and before it reaches the equilibrium states. However, if the duration becomes longer and the floodplain is wide enough, we expect that the amplitude of meandering channel may be increased and the channel shape would be more pronounced. Thus, an added patch in open channels is able to influence the channel geometries significantly. That is consistent with the results of Bennett et al. (2008) who investigated fluvial response to alternating patches of vegetation, which consisted of wooden dowels and located along the wall. They reported that the alternating patches were able to create a meandering channel and the amplitude of the thalweg could be adjusted by patch densities. Even though we conducted several experiments with a single patch, the results show similar trends which indicate that the patch of vegetation can influence bed morphological behaviour. The results of Case 3 are presented herein for illustration, but processes of erosion and deposition are almost similar for the other cases.

Numerical model reproduces reasonably variations of bed topography due to erosion and deposition near the emergent patch of vegetation. Numerical results show that the channel widening due to bank erosion opposite and downstream of the patch as well as deposition downstream from the patch is predicted satisfactorily for all patch densities. The spatial patterns of deposition within and behind the patch are somewhat different from experimental results. Those discrepancies between experimental and numerical results are probably due to the three-dimensional effects caused by flow around individual cylinders. Inside the patch, particularly, the turbulence levels are elevated around each individual cylinder and sediment is driven further downstream in the patches. It indicates that high bottom shear stresses occur in the vicinity of cylinders due to wake turbulences, whereas the model in the present study predicts a reduction in bottom shear stresses within the patch, which leads the deposition

throughout the patch. To simulate such erosion and deposition processes in and near the patch, a three-dimensional model should be used considering every cylinder, which is an inappropriate way in terms of river management. Overall, it can be seen that the present numerical model predicts well important spatial patterns due to erosion and deposition near and downstream of the patch, even though the small-scale erosion around individual cylinders is not simulated accurately.

3.4.4 Spatial variation of bed morphology

Fig. 3.8 displays spatial patterns of morphological changes near the patch of vegetation for Case 2. These are taken at the end of each experiment, after draining water and removing the patch.



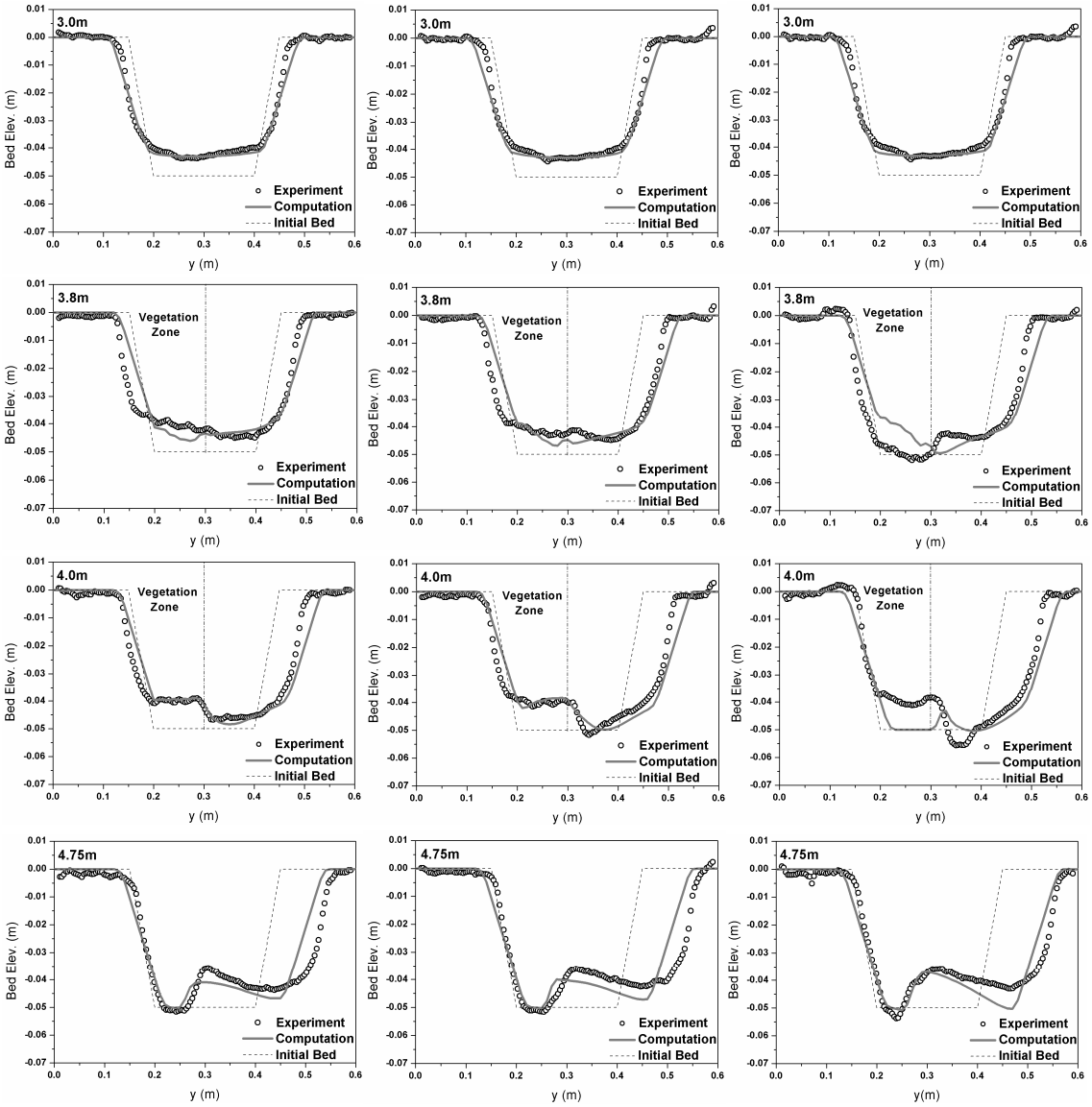
(a) Low density (b) Medium density

(c) High density

Fig. 3.8 Local spatial patterns around the patch for case 2: (a) Low density (LD); (b) Medium density (MD); (c) High density (HD). Flow is from left to right.

It is observed in the low density (LD) and medium density (MD) cases that small-scale scours occur in the immediate vicinity of cylinders (Figs. 8a and b). For the high density (HD), however, significant localized scour takes place at the leading edge of the patch, and

sediment deposition is observed just behind the scoured region (Fig. 3.8c). According to change in the patch density, different morphological behaviour is shown within and near the patch.



(a) Low density (b) Medium density (c) High density

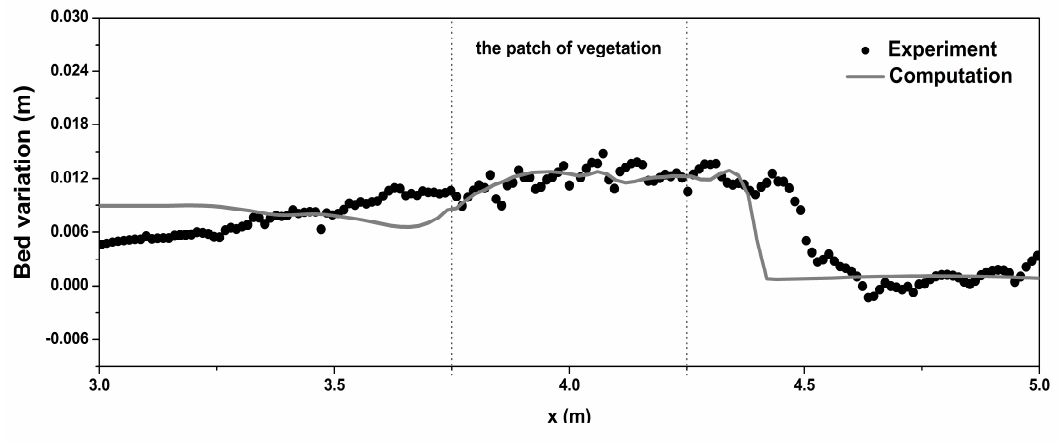
Fig. 3.9 Comparison of bed elevation between experiment and computation for case 2: (a) Low density; (b) Medium density; (c) High density.

Fig. 3.9 depicts comparisons of cross-sectional bed elevations between experimental and numerical results at 3.0 m, 3.8 m, 4.0 m and 4.75 m for Case 2. It indicates that the sections

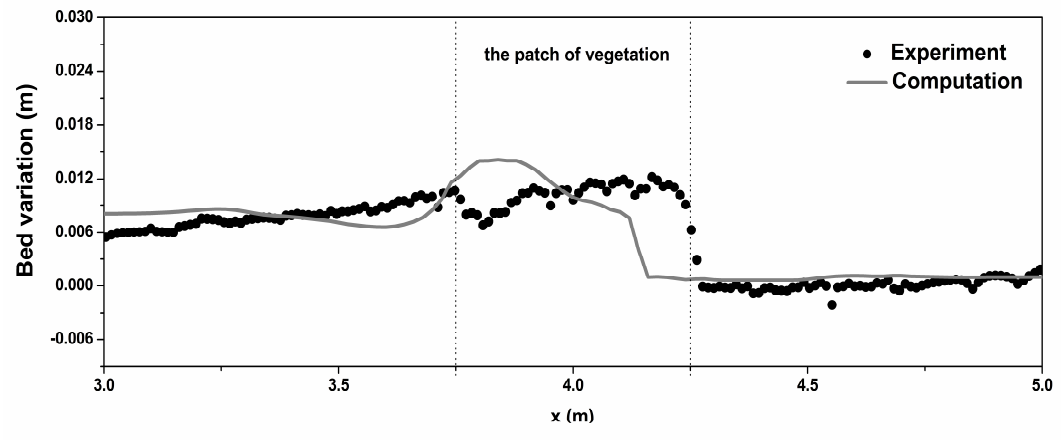
of 3.0 m and 4.75m are located upstream and downstream of the patch, respectively, and the other two sections, i.e. 3.8 and 4.0 m are within the patch. It can be seen that the channel expansion due to lateral bank erosion occurs and sediment is deposited in low water channels which have symmetric cross-sections at 3.0 m in Fig. 3.9. The bed elevations increase about 6 mm at low water channel and the simulated bed profiles agree well with experimental data. For the LD and MD patches at 3.8 m, sediment deposition is observed both within and opposite the patch due to a reduction of bed shear stress whereas the bed elevation of the HD shows that localized scour is observed at 3.8 m which is near the leading edge of the patch. The scoured bed elevation is similar to an initial bed elevation. Because of the patch of vegetation, the lateral bank erosion takes place directly opposite the patch and it becomes higher than that observed upstream of the patch. The simulated results of bank erosion and deposition show reasonable agreement with the experimental data except the HD, in which the local scour near the leading edge cannot be captured. At 4.0 m, the local scouring is observed near the lateral edge of patch and it increases with an increase in the patch density. This result is consistent with previous observations by Bouma et al. (2007) and Rominger et al. (2010). This is attributed to diversion of flow and vortex motions caused by the added patch of vegetation in open channel flows. The diversion of flow leads to erosion opposite and near the patch because of enhanced velocity and elevated turbulence. The magnitude of them increases as patch density increases. Choi and Kang (2006) simulated partly-vegetated open channel flows with various patch densities, using 3D numerical model with a Reynolds stress model. They reported that the secondary current was developed in the non-vegetated channel, and the magnitude of that increased with an increase in the patch density. Even though all results are not herein presented, the degree of local scouring increases with decreases in flow rate and channel slope because greater sediment is delivered from upstream of the patch as those increase. For the LD and MD patches, agreement between experimental and numerical results is reasonably good whereas the simulated local scour of the HD is slightly under-predicted because vortex motions produced by the patch of vegetation could not accurately be reproduced. It can be seen that in the HD patch sediment is deposited within the patch in experimental data, whereas the simulated bed elevation remains constant. The reason of this difference will be discussed later. It is observed at 4.75 m, which is located behind the vegetation patch, no erosion and

deposition occur near the right bank because of the reduced flow velocity and bed shear stress. It has been reported that bank vegetation increases the strength of banks and those are stabilized by vegetation root (Hicken, 1984; Millar and Qucik 1993). They observed that dense vegetation on banks caused lower channel widening with bank erosion than poor vegetation on banks. In the present results, relatively high bank erosion is observed opposite and downstream of the patch with increasing patch density, and the simulated results are in good qualitative agreement with the experimental data. The patch of vegetation in open channel flows leads to significant bank erosion and the morphological behaviour is influenced by it within and around the patch. Overall, the present 2D depth-averaged model predicted reasonably morphological patterns due to erosion and deposition near the patch of vegetation, even though some detailed phenomena such as local scour could not be reproduced.

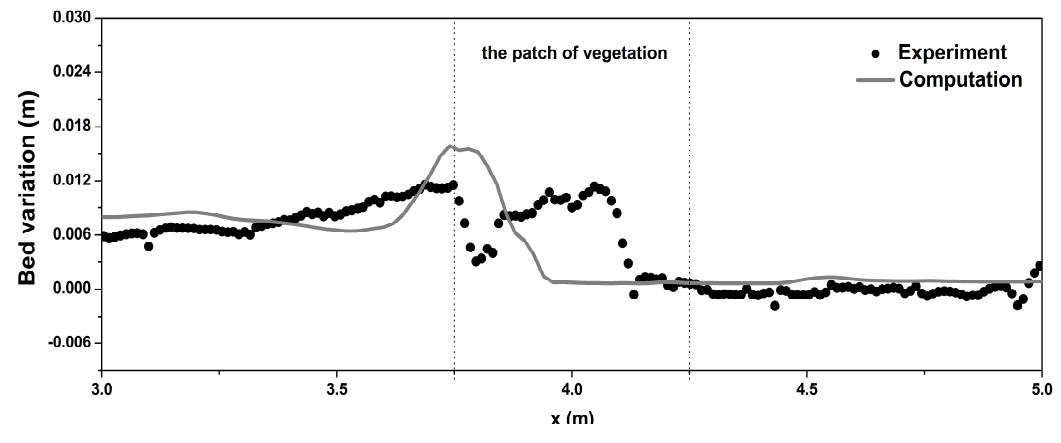
Fig. 3.10 shows longitudinal bed profiles (x = 3 m – 5 m) at y = 0.22 m for Case 4 to investigate detailed behaviour within and near the patch of vegetation. For the LD, sediment starts to deposit from upstream of the patch and the sediment which enters through the leading edge is deposited within and behind the patch due to reduction in bed shear stress. Within the patch, the sediment in the immediate vicinity of individual cylinders is transported further downstream because of elevated turbulence energy and deposited behind the patch. The flow passing through emergent vegetated region induces stem wakes which are able to contribute generation of additional turbulent energy (Nepf and Vivoni, 1999). The turbulence energy adjacent to cylinders is responsible for sediment entrainment. Sediment deposition is continued up to approximately x = 4.5 m beyond the patch in experimental data and the simulated bed profile for the LD matches the experimental data quite well. Figs 3.10b and c show that for the MD and HD, the deposition pattern shows a similar trend with the LD but the local scour is observed near the leading of the patch, which is more pronounced as the patch density increases. The scoured regions indicate a high bed shear stress. Sediment scoured near the leading edge of the patch is transported downstream of the region or is diverted away from the patch. As the sediment moves into the patch, it is deposited just beyond the scoured region. Overall agreement between experimental and numerical results is reasonable, but there are discrepancies of erosion and deposition patterns within the patch. In other words, the simulated depositional distances through the



(a) Low density



(b) Medium density



(c) High density

Fig. 3.10 Longitudinal bed profiles at $y = 0.22$m for case 4: (a) low density (LD); (b) Medium density (MD); (c) High density (HD).

patch are shorter than the experimental data whereas the deposited heights are higher, which implies that the present numerical model predicts reductions in bed shear stress from the leading edge of the patch. This is attributed to fact that the numerical model does not account for the local high bed shear stress caused by elevated turbulence from flow interference due to individual cylinders. Zong and Nepf (2011) observed high turbulent kinetic energy near the leading edge and found that it is increased with an increase in the patch density. As the cylinder spacing is reduced, flow begins to be interfered by upstream and lateral cylinders. The fact that the interference of flow caused by cylinders increases turbulence levels supports the local scour near the leading edge of the patch because local high turbulence is responsible for local erosion. Also, reduced spacing between cylinders leads to the increased size of horseshoe vortices and reinforcement effects of downstream cylinders (Raudkivi 1990, Ashtiani and Beheshti 2006), and thus those induce local high bed shear stress resulting in local high erosion. The present numerical model does not predict the local scouring near the leading edge because the model averaged over time and space is not able to consider local high bed shear stress. Bouma et al. (2007) found similar trends in field observations and they applied a three dimensional model to simulate spatial change in bed topography. They described that the model was not able to reproduce correctly the leading edge effects because their model could not account for elevated turbulence kinetic energy caused by flow interactions from cylinders. To reproduce local scour near the leading edge, each cylinder should be explicitly resolved by numerical grids, which is beyond the ability of the present computational resource. Zong and Nepf (2011) described that the deceleration in the longitudinal velocity began upstream of the patch and it continued decreasing until diversion of flow was ended. Thus, the fact that the distance of divergence flow decreases with increasing patch density supports the decrease in the depositional distance against the increase in patch density in both experimental and simulated results. On the other hand, the amount of sediment deposition within and behind the patch in both the experimental and numerical results seems to be similar, even though the distances of deposition are slightly under-predicted.

Fig. 3.11 shows a comparison of sediment deposition within and around the patch. The amount of sediment deposition increases if the patch density decreases or if the channel slope and the flow rate become larger. The simulated amount of sediment accumulated near

the patch agrees well with experimental data, which implies that the under-predicted depositional distance (i.e. erosion and deposition patterns) through the patch is due to local high bed shear stress induced by the elevated turbulence kinetic energy. It is found that the model can reliably predict both the morphological changes and the amount of sediment deposition for the LD, whereas, for the MD and HD patch, it cannot reproduce the bed

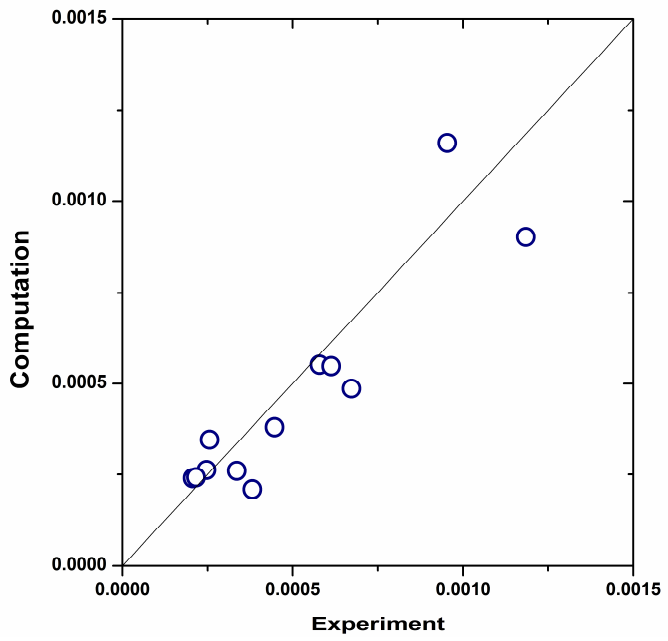


Fig. 3.11 Comparison of sediment deposition within and near the patch.

variation within the patch due to local scour. In other words, it indicates that the present numerical model not only offers reasonable perditions of morphological patterns and the amount of sediment deposition within and around the patch but also reproduces important features of erosion and deposition, yet it needs for refining further to deal accurately with the effect of leading edge of the patch.

3.4.5 Channel widening and deposition near the patch

Fig. 3.12 depicts comparisons of the experimental and numerical results for widening rate in which the channel width, w is normalized by the initial bottom width, w_b. It can be seen that the widening rate increases with increases in flow rate or channel slope. The widening rate of Case 2 and Case 3 increases approximately 16 % and 27 %, respectively, regardless of the patch density in comparison with that of Case 1. The widening rate of Case 4 is 14 %

larger than Case 1.

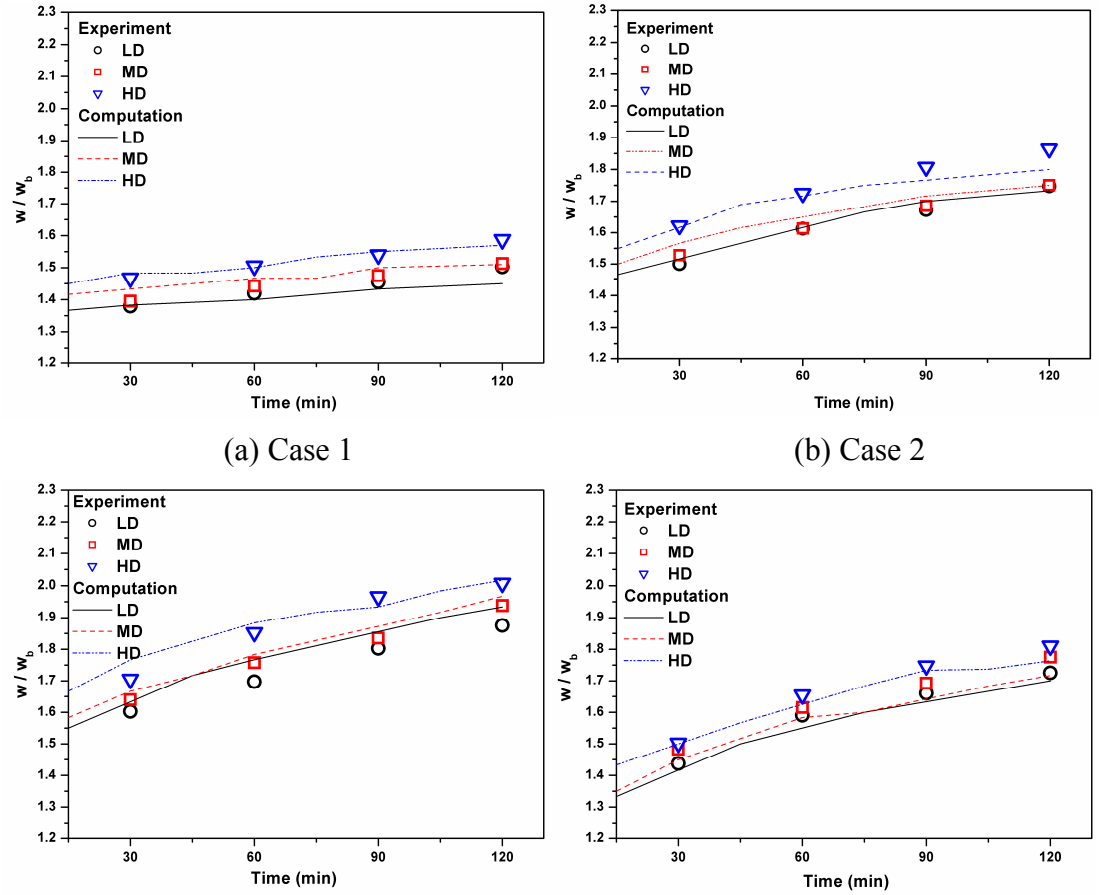


Fig. 3.12 Comparison of the widening rate with time: (a) Case 1; (b) Case 2; (c) Case 3; (d) Case 4.

As the patch density becomes higher, the widening rate increases with time for all cases. The simulated widening rate is in good agreement with the experimental data. Comparison between experimental and simulated results shows that the numerical model predicts well the temporal evolution of channel morphology in the presence of vegetation.

Through reasonable agreement with experimental results, the widening rate of the channel in response to the patch, and the deposition volume in and behind the patch are investigated numerically. To examine the influence of the patch width, length and density on the widening rate, additional numerical simulations with, i.e. $w_v = 0.2$ (reduced width) and 0.3

m (extended width), and L_v = 0.25 m (reduced length) and 0.75 m (extended length) are conducted with extra two patch densities, i.e. λ = 1.96 and 4.28 m^{-1} under the flow condition of Case 2.

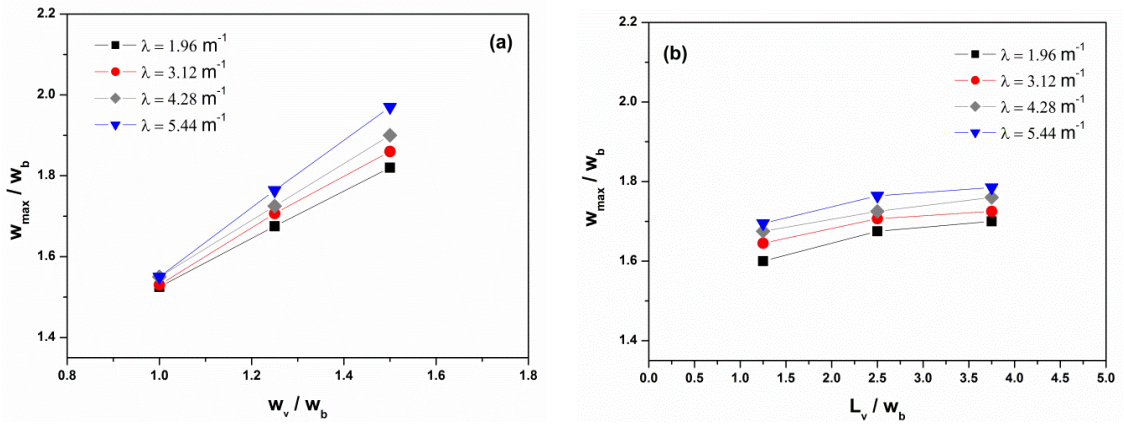


Fig. 3.13 Maximum widening rate according to (a) the ratio of the patch width and (b) the ratio of the patch length.

Fig. 3.13a shows the maximum widening rate of the channel, w_{max}, which is mainly observed directly opposite the patch, according to the ratio of patch width, w_v /w_b. The widening rates are quite similar to each other when the ratio of the patch width is 1.0, which indicates that the lateral bank erosion in response to the patch is significantly low. It can be seen that, as the ratio of patch width increases, the widening rates increase sharply regardless the patch density. It demonstrates that the channel widening due to the lateral bank erosion is considerably influenced by the ratio of the patch width. Also, as the ratio of patch width increases, the widening rate in response to the patch density becomes larger. Fig. 3.13b shows the maximum widening rate of the channel according to the ratio of patch length, L_v / w_b in which the patch widths are constant to 0.25 m. It can be seen that unlike the widening rate with respect to the ratio of patch width, the ratio of the patch length has less influence on the channel widening rate. The channel widening increases as the patch density becomes higher with almost equal rates.

Fig. 3.14a presents the deposition volume in and behind the patch according to the ratio of patch width, w_v / w_b. Sediment is transported from upstream of the patch due to bedload and sediment loading from bank erosion. It can be seen that sediment deposition is negligible

within and around the patch as the ratio of the patch width becomes 1.0, which implies that most sediment is transported through the opposite part of the patch. However, as the ratio of the patch width increases, the deposited sediment increases, which indicates that the ratio of patch width responds strongly to the sediment deposition in and behind the patch as the ratio is larger than 1.0. In particular, it is more pronounced when the patch density becomes lower. Fig. 3.14b shows the deposition volume in and behind the patch with respect to the ratio of patch length, L_v / w_b. It can be seen that the deposition is almost constant in response to the ratio of the patch length, which indicates that it has the negligible effects on sediment deposition in and behind the patch.

Thus, it can be found that the maximum widening rate of the channel and the sediment deposition in and behind the patch are significantly influenced by the ratio of the patch width, whereas the ratio of the patch length shows much less impact on them.

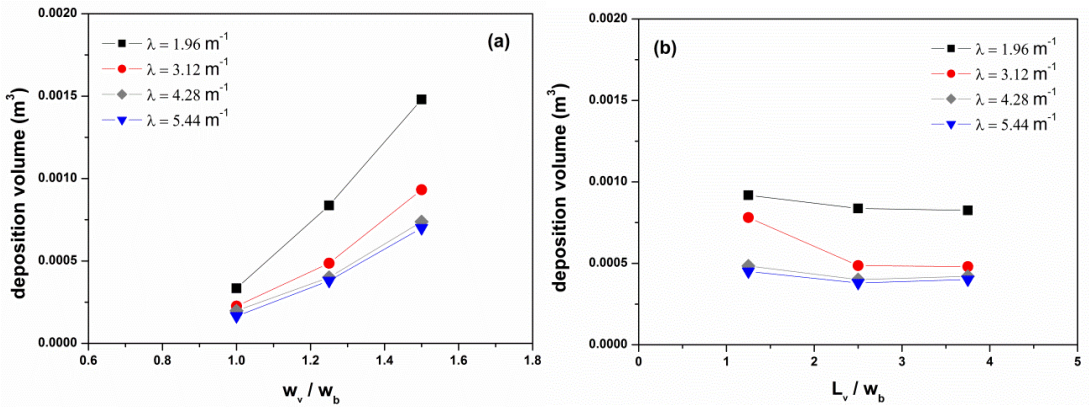
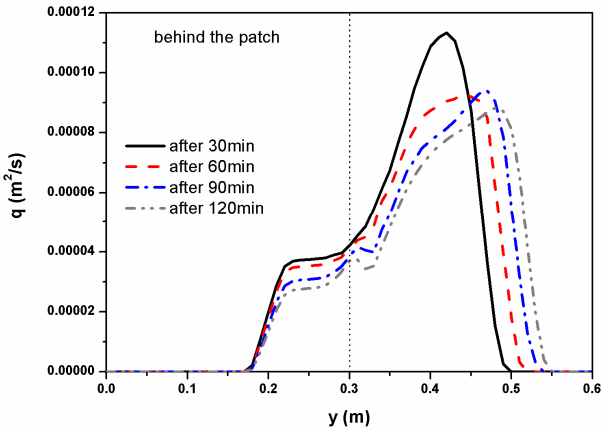


Fig. 3.14 Sediment deposition volume within and around the patch according to (a) the ratio of the patch width and (b) the ratio of the patch length.

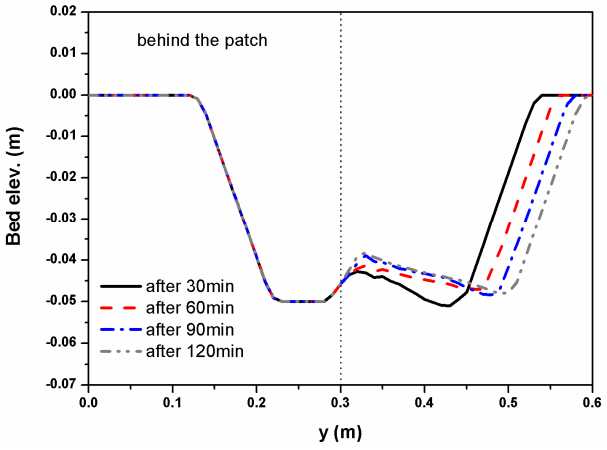
3.4.6 Change in flow and bank erosion

Fig. 3.15 depicts lateral profile of unit discharges and bed profiles with different times at x = 4.3 m for Case 2 of the MD patch. Distribution of unit discharge is varied with time in both behind the patch and opposite the patch.

It is found that maximum unit discharge occurs at the central channel opposite the patch in the beginning (i.e. after 30min), whereas unit discharge is considerably reduced behind the



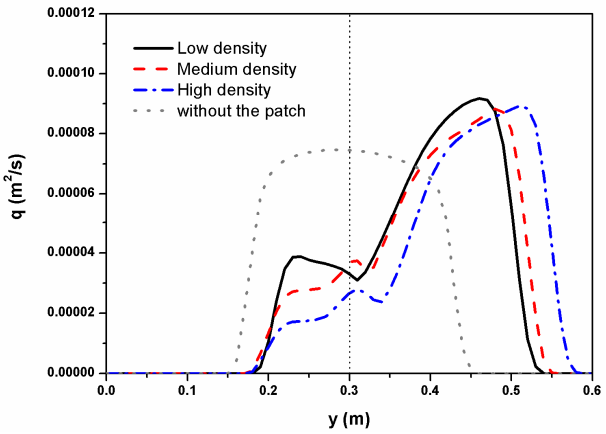
(a) Lateral unit discharges at different times for Case 2 of Medium density (MD)



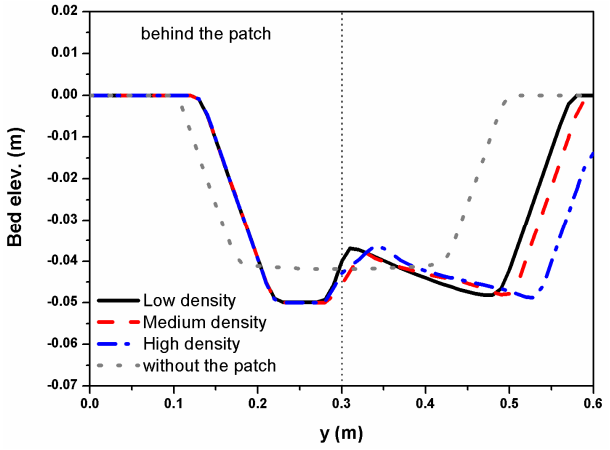
(b) Lateral bed profiles at different time for Case 2 of Medium density (MD)

Fig. 3.15 Lateral profile of unit discharges and bed profiles with different times at y = 4.3m for case 2 of the MD patch.

patch. Unit discharge decreases with time in both opposite and behind the patch, as lateral bank erosion increases opposite the patch as shown in Fig. 15b. It reveals that 77% and 83% of the total discharge are conveyed opposite the patch after 30min and 120min, respectively, so that the discharge passing through the patch decreases with increases in the lateral channel widening opposite the patch. Fig. 3.16 shows lateral profile of unit discharges and bed profiles with different patch densities at x = 4.3 m for Case 2. It can be seen that shapes of the unit discharge and the cross-sectional bed profile without the patch are symmetric whereas the shapes of them are considerably changed with the patch. Maximum unit discharge with



(a) Lateral unit discharges with different patch densities for Case 2 of Medium density.



(b) Lateral unit discharges with different patch densities for Case 2 of Medium density.

Fig. 3.16 Lateral profile of unit discharges and bed profiles with different times at $y = 4.3$ m for case 2 of the MD patch.

the patch is greater than that without the patch. It is found that the maximum unit discharge opposite the patch is quite similar regardless of the patch density, and that it moves gradually toward the opposite bank of the patch as the channel widening increases with an increase in the patch density. Also, unit discharge passing through the opposite part of the patch increases with increasing patch density from 79 % to 88 %, transferring greater discharge from the patch to the opposite region. On the other hand, behind the patch, unit discharge decreases with an increase in the patch density, where in turn, the flow velocity is

significantly reduced, so that the bank erosion is reduced compared to that without the patch. The patch is able to make diverse flow in stream habitats and increase bank strength and stability within and behind it. In particular, a refuge area is formed behind the patch due to low velocities and turbulences, so that fishes are sheltered in the area, reasoning that slower flow requires less energy for them. Thus, the finite patch of vegetation may provide a wide range of aquatic habitats and create better ecosystem.

3.5 SUMMARY

This study describes bed morphological changes near a finite patch in open channel flows with erodible banks employing both laboratory experiments and numerical simulations. The vegetation patch is modelled as emergent circular cylinders with a staggered array and it is located at the middle of the channel. A 2D (Two-dimensional) depth-averaged model is presented to simulate flow and sediment transport with vegetation. For non-vegetation cases, channel expansion occurs slightly with bank erosion, whereas the added patch in open channels causes significant bank erosion directly opposite and downstream of the patch, and eroded sediment is deposited near and downstream of the patch. For the LD (Low density) and MD (Medium density) patches, small-scale scour occurs in the immediate vicinity of cylinders within the patch, whereas for the HD (High density) patch, localized scour takes place near the leading edge of the patch due to elevated turbulence energy. Numerical simulations are performed and the sensitivity to parameters related to bank erosion and bed shear stress is analyzed. Numerical results are compared with experimentally obtained ones and the numerical model satisfactorily predicts bed variations, bank erosion and sediment deposition with the patch. The influence of the patch extent on the widening rate and deposition are investigated.

CHAPTER 4 SCOUR AND DEPOSITION PATTERNS DUE TO MUTUAL INTERACTIONS OF FINITE PATCHES OF VEGETATION

4.1 INTRODUCTION

In the past, vegetation in the natural stream has been considered as a component which has a negative impact of flood control and management due to an increase in flow resistance. Thus, aquatic and riparian vegetation have been cut and removed to increase flow conveyance. While the flooding risk has been reduced, the unintended consequences have appeared in the stream such as destroyed ecosystem, reduced ecological habitat and deteriorated water quality (Rominger et al., 2010).

The governments of many countries have invested a portion of national budget in river and stream restorations. Several restoration projects are launched to create scour pool habitats for endangered species (Hunter, 1991; Thompson, 2002). Flow deflectors similar to spur dikes and groins have been used to create local scour pools because those can recreate deeper water area, and thus aquatic habitats can arise from such instream structures. In addition, Shields et al. (1995) documented the scour pools caused by instream structures increase the number of fish, biomass and species. However, recently, to make close-to-nature stream, aquatic plant patches are preferred, because aquatic plants can not only create diverse habitats but also remove pollutants.

Vegetation significantly impacts on hydraulic and morphological features. The additional drag exerted by vegetation in natural rivers or streams reduces flow velocity within the vegetated region, and turbulence intensities and Reynolds stresses are influenced by vegetation, relative to un-vegetated region where in turn, the wake turbulences with stem scales are mainly generated within that region (Nepf and Vivoni, 1999). Thus, the bed shear stress decreases within vegetated region, which leads to encouragement to traps for sediment and contaminant. In addition, vegetation can alter geomorphology, for example, from braiding to single channel (Tal and Paola, 2007).

Because vegetation has abilities to improve ecology, it has been often used for an ingredient of river restorations. In addition, the finite patches of vegetation have great potentials and applications rather than infinite patch. Tsujimoto (1999) showed a patch of vegetation is extended, laterally and longitudinally, since the fine suspended sediment is deposited downstream of the patch. Bennett et al. (2008) conducted laboratory experiments in a flume, consisting of fine sands with a compound channel. The finite patches of vegetation were placed alternatively along the channel and then those could change flow and bed morphology. They described that the channel response is significantly influenced by patch densities and thus those could adjust the meandering wavelengths in a straight channel. Zong and Nepf (2010, 2011) carried out laboratory experiments to investigate spatial patterns of deposition within a finite patch which was located at the side wall. The deposition in the diverging region increased along streamwise direction and its pattern was uniform in the fully developed region, which was consistent with the velocity pattern. On the other hand, they observed high turbulence at the leading edge of the patch, so that the reduction in deposition occurred near that region. Bouma et al. (2007) conducted field monitoring on spatial patterns of deposition near circular patches in an intertidal area during two years. The patches consisted of bamboo canes and two patch densities (sparse and high density patches) were used. For the high density patch, the deposition was observed within and downstream of the patch, and local erosion occurred near the leading edge of the patch while the negligible bed morphological changes were observed in the sparse density patch. Follett and Nepf (2012) conducted experiments on morphological patterns near a circular patch of emergent vegetation on fine sandy bed. The two patch densities were tested under the flow above the threshold of sediment motion. The bed was scoured near the leading edge of the patch and then the sediment scoured from that region was deposited downstream of the patch. The scouring near the leading edge increased with increases in patch densities, which was associated with turbulence kinetic energy at that region. Similarly, Euler et al. (2012) showed that the reduction in patch density weakens local scouring near the leading edge of the patch and the frontal scouring leads to leeside deposition. Rominger et al. (2010) performed field-scale experiments in a meandering stream where vegetation was added to a point bar near convex bank. The sediment was deposited within the patch, while the local erosion was observed near the lateral edge of

the patch due to enhanced flow velocity, which led to the removal of vegetation. Consequently, the deposited region near the inner bend was lost.

A wide range of numerical models have been proposed to simulate the flow and morphological change with vegetation, ranging from simple one-dimensional model to three-dimensional model (Liu and Shen, 2008; Tsujimoto, 1999; Wu et al., 2005; Wu and He, 2009). For long-term and large-scale simulations of morphological processes with vegetation, a two-dimensional model is appropriate in computational efficiency (Wu et al., 2005). Tsujimoto (1999) developed a two-dimensional model in which the source terms were added in momentum and transport equations to model the effect of vegetation. Expanding process of a patch of vegetation was simulated and the results showed that the length and width of the patch increase with increasing the number of floods. Wu et al. (2005) developed a depth-averaged two-dimensional model considering the effect of vegetation density and the model was applied to various laboratory and field data to verify the model capacities. The model predicted fairly the flow and bed morphological changes with vegetation. Li and Millar (2010) carried out long-term simulations using a two-dimensional model to investigate effects of vegetated bank and floodplain. They described that vegetation stabilizes sediment on bank and floodplain, so that lateral expansion of a channel was constricted.

As above mentioned, vegetation previously encourages sediment deposition near the vegetated region, while local erosion near the finite patches have been observed in recent few studies, which lead to instability of vegetation and changes in morphological patterns. Possible local scours near the patches result in considerable damage to the stream such as the vegetation can be uprooted or the roots can be exposed above ground (Euler et al., 2012; Nepf, 2012; Rominger et al., 2010). Thus, the strategies based on scientific understandings are essential to avoid such failures, instead of reliance on empirical approaches (Khosronejad et al., 2013). Most of the studies associated with finite patches have considered an isolated patch of vegetation in an open channel, while as the finite patches are placed at nearby locations, the flow and morphological changes are significantly influenced by mutual interactions of flow as shown in Fig. 4.1. As the flow interferes due to patches, the local scour between the patches is driven by an increase in bed shear stress due to enhanced flow. The development of scour pool provides diverse aquatic habitats and

refuge area for fishes, and thus it enhances ecological functions in a stream (Kuhnle et al., 2002; Rodrigue-Gervais et al., 2011; Thompson, 2002). In such cases, the location and density of patches are crucial parameters related to stability of replanting vegetation in the streams since those affect the local flow and turbulence near the patches, which impact on the degree of local scour. Thus, to be successful in stream restorations, it is required how the location and density of finite patches of vegetation in a stream influence the local flow and scour.

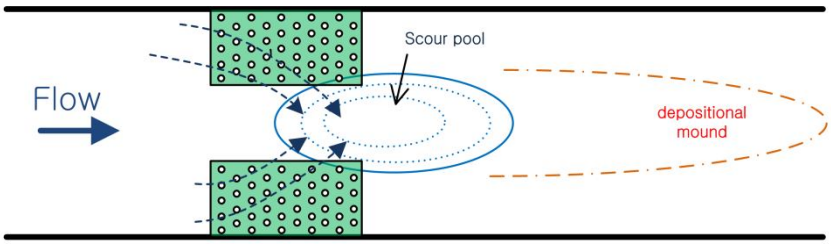


Fig. 4.1 Schematic view of the flow and bed morphology near the finite patches.

In this study, the influence of spacing between finite patches with the patch density on the flow and bed morphology is investigated by means of laboratory experiments and numerical computations. The simple finite rectangular patches that consist of circular cylinders with staggered array are used in a straight open channel and those are placed at both side walls as shown in Fig. 4.2. Laboratory experiments are conducted with various patch densities, and several patch widths are considered to investigate effects of the spacing between patches under the flow condition below the threshold of sediment motion. The changes in bed topography in and around finite patches are presented and the morphological patterns near the patches are described. To validate a two-dimensional computational model, the distributions of depth-averaged velocity, Reynolds stress and turbulence intensity are compared with laboratory data available in the literature and then the model is applied to all cases experimentally studied. The hydraulic characteristics in terms of flow rate and velocity distributions are analyzed on fixed bed. To investigate predictive capabilities of the computational model and emphasize its potential for computing local scour pools around the patches, extensive comparisons with experimental

data are carried out. The impact of the spacing between patches, patch densities and submergence ratio on the depth and volume of the local scour pool is analyzed.

4.2 EXPERIMENTAL SET UP

Laboratory experiments were conducted in a flume of 8 m long, L, 0.2 m wide, W, and 0.3 m deep with wooden side walls as shown in Fig. 4.2. The flume was filled with a 10 cm layer of sediment of median diameter of 0.76 mm and the initial channel was set to flat bed. Flow rate was controlled to be 0.0016 m^3/s by a manual valve at upstream tank. Initially, a small flow rate was drawn to saturate the sand bed as well as avoid initial scouring. A plastic mesh screen was installed to minimize water-surface oscillation at the entrance of the upstream channel. The flow condition was below the threshold of sediment motion, so that there was no sediment transport upstream of the patches ($\tau_* / \tau_{*c} = 0.97$). In other words, sediment transport was only induced by patches of vegetation. The channel slope was set to 1 / 800 and the duration of experiments was kept until the bed scouring reached the quasi-equilibrium state (i.e. after 9 hours).

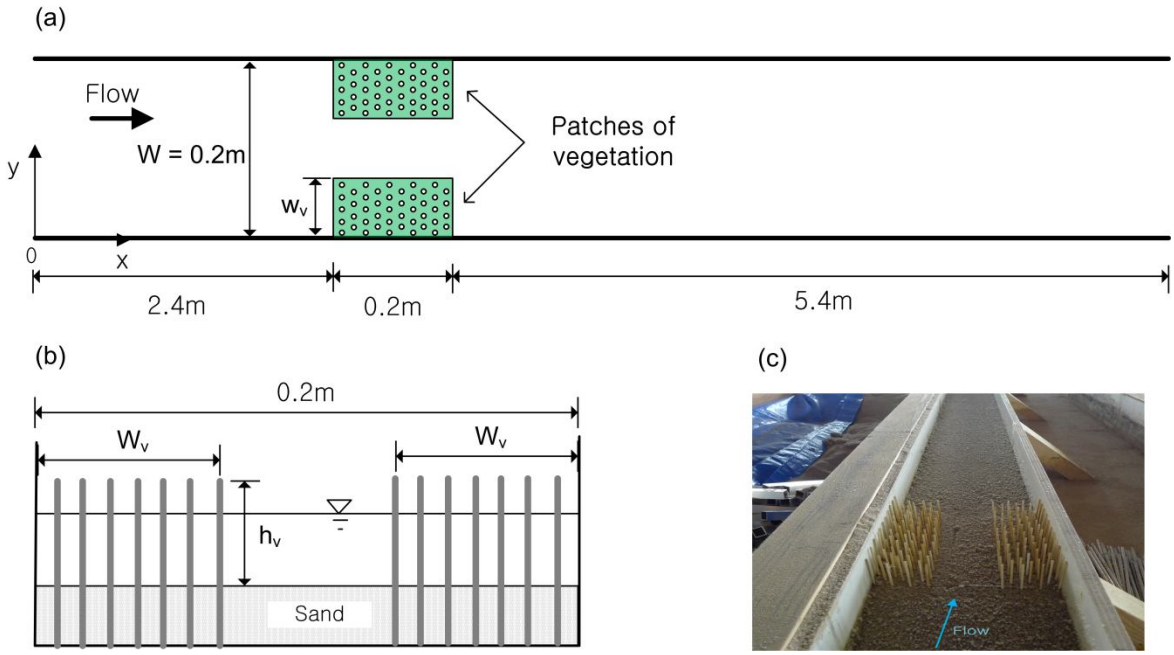


Fig. 4.2 Experimental channel; a) Top view, b) Initial channel with patches in a cross section, c) Picture of the channel near the patches.

Table 4.1 Experimental parameters of the patch

Exp #	L_v (m)	W_v (m)	D (m)	λ (m^{-1})	c	h_v/h	$2\lambda W_v$
1	0.2	0.02	-	-	1	1.0	-
2	0.2	0.02	0.005	25	.098	1.0	1.0
3	0.2	0.04	-	-	1	1.0	-
4	0.2	0.04	0.005	25	0.098	1.0	2.0
5	0.2	0.04	0.0025	12.5	0.025	1.0	1.0
6	0.2	0.04	0.005	6.25	0.025	1.0	0.5
7	0.2	0.06	0.005	25	0.098	1.0	3
8	0.2	0.06	0.0025	22.2	0.044	1.0	2.66
9	0.2	0.06	0.0025	12.5	0.025	1.0	1.5
10	0.2	0.06	0.005	11.1	0.044	1.0	1.33
11	0.2	0.06	0.0025	5.6	0.01	1.0	0.672
12	0.2	0.08	0.005	25	0.098	1.0	4.0
13	0.2	0.08	0.0025	12.5	0.025	1.0	2.0
14	0.2	0.08	0.005	6.25	0.025	1.0	1.0
15	0.2	0.04	0.005	15.63	0.061	0.625	1.25
16	0.2	0.06	0.005	15.63	0.061	0.625	1.875
17	0.2	0.06	0.0025	7.81	0.016	0.625	0.94
18	0.2	0.06	0.005	6.94	0.028	0.625	0.83
19	0.2	0.06	0.0025	3.5	0.006	0.625	0.42
20	0.2	0.08	0.005	15.63	0.061	0.625	2.5
21	0.2	0.08	0.0025	7.81	0.016	0.625	1.25

Rectangular patches were constructed with circular aluminum cylinders of 5 mm diameter, D, and bamboo sticks of 2.5 mm diameter, D, with a staggered array. In natural streams, vegetation could be emergent or submerged, so that both conditions were considered (emergent: $h_v/h = 1.0$, submerged: $h_v/h = 0.625$ where h and h_v are water depth and height of vegetation, respectively.). The leading edge of the patches was located at 2.4 m from the upstream of the channel entrance as shown in Fig. 4.2. To investigate the effects of the spacing between patches, the four patch widths (= 0.02, 0.04, 0.06 and 0.08 m) were considered, which were corresponding to 0.2, 0.4, 0.6 and 0.8 of the ratio of the

patch width, $2W_v$, to channel width, W. The patch density was described by the following two parameters: the patch density, λ (m^{-1}) that is a frontal area per unit volume of the patch (= $2Dh_v$ / S_xS_yh where S_x and S_y are the distance between stems, respectively) and the solid volume fraction, c (= πD^2h_v / $2S_xS_yh$). In this study, various patch densities were tested from 3.5 to 25.0 m^{-1}. The experimental parameters of the patch are summarized in Table 4.1.

The bed elevation was collected using the laser bed profiler, which is mounted on the flume. After each experiment, the flow was stopped and then the water was allowed to drain slowly to avoid changes in bed topography. The bed elevation was measured every 5.0 cm and 0.3 cm in longitudinal and lateral directions, respectively, except the region of the patch and close to the patch where the measurement was done every 2.5 cm (2.3 m to 2.8 m from upstream) in longitudinal direction. The change in bed topography was found from differences between before and after bed elevations.

4.3 COMPUTATIONAL MODEL

4.3.1 Governing equations

A depth-averaged, two-dimensional numerical model was employed to simulate the flow field with vegetation in a Cartesian coordinate system. The governing equations are based on continuity equation and momentum equations considered the occupation rate by vegetation. The governing equations are described as,

Continuity equation

$$\frac{\partial\left[(1-c)h\right]}{\partial t}+\frac{\partial\left[(1-c)M\right]}{\partial x}+\frac{\partial\left[(1-c)N\right]}{\partial y}=0 \tag{4.1}$$

Momentum equations in x- and y-directions

$$\begin{aligned}&\frac{\partial\left[(1-c)M\right]}{\partial t}+\frac{\partial\left[(1-c)uM\right]}{\partial x}+\frac{\partial\left[(1-c)vM\right]}{\partial y}\\&=-gh(1-c)\frac{\partial H}{\partial x}-(1-c)\frac{\tau_{bx}}{\rho}+\frac{\partial\left[(1-c)(-\overline{u'^2}h)\right]}{\partial x}+\frac{\partial\left[(1-c)(-\overline{u'v'}h)\right]}{\partial y}\\&+\nu\left[\frac{\partial}{\partial x}\left(h\frac{\partial\left[(1-c)u\right]}{\partial x}\right)+\frac{\partial}{\partial y}\left(h\frac{\partial\left[(1-c)u\right]}{\partial y}\right)\right]-F_x\end{aligned} \tag{4.2a}$$

$$\frac{\partial\left[(1-c)N\right]}{\partial t}+\frac{\partial\left[(1-c)uN\right]}{\partial x}+\frac{\partial\left[(1-c)vN\right]}{\partial y}$$
$$=-gh(1-c)\frac{\partial H}{\partial y}-(1-c)\frac{\tau_{by}}{\rho}+\frac{\partial\left[(1-c)(-\overline{u'v'}h)\right]}{\partial x}+\frac{\partial\left[(1-c)(-\overline{v'^2}h)\right]}{\partial y} \tag{4.2b}$$
$$+\nu\left[\frac{\partial}{\partial x}\left(h\frac{\partial\left[(1-c)v\right]}{\partial x}\right)+\frac{\partial}{\partial y}\left(h\frac{\partial\left[(1-c)v\right]}{\partial y}\right)\right]-F_y$$

where h = depth, u, v = depth-averaged velocities, M, N = discharge fluxs ($M = hu$, $N = hv$), g = gravitational acceleration, c = solid volume fraction, ρ = density of water, τ_{bx}, τ_{by} = bottom shear stresses, H = water surface elevation, $-\overline{u'^2}, -\overline{v'^2}, -\overline{u'v'}$ = depth-averaged Reynolds stresses, ν = molecular kinematic viscosity, F_x, F_y = drag force exerted by vegetation.

Components of the bottom shear stress are evaluated by

$$\tau_{bx}=f\rho u\sqrt{u^2+v^2} \qquad \tau_{by}=f\rho v\sqrt{u^2+v^2} \tag{4.3}$$

where f = friction coefficient, which is calculated using Manning's roughness coefficient, n, as $gn^2 / R_s^{1/3}$, where R_s is the spacing hydraulic radius in the patch of vegetation which is defined as $R_s = hb_v / (2h+b_v)$. If there is no vegetation or vegetation density is too coarse, R_s is equal to water depth, h. The flow through or over submerged vegetation is very complex, and the mean velocity profile no longer follows the logarithmic law. The velocity inflection is formed and the strong shear layer is created at the top of vegetation, which causes an additional shear stress. It is difficult to determine the shear stress both on the bed and at the top of vegetation using a two-dimensional, depth-averaged model. Instead of directly determining the shear stress, it is calculated as weighted average of the hydraulic radii in the above and within vegetated layers (Wu et al., 2005). The hydraulic radii is evaluated by

$$R_s=\frac{h_v}{h}\frac{h_v b_v}{2h_v+b_v}+\frac{h-h_v}{h}(h-h_v) \tag{4.4}$$

where b_v is the spacing of vegetation and h_v is the vegetation height. They explained that although equations (4.3) and (4.4) are physically not corrected on dense vegetation, these induce small errors, which have negligible effects due to fact that the bed shear stress is much smaller than the drag force exerted by vegetation.

Components of the drag force on vegetation are expressed by

$$F = \frac{1}{2} C_D \rho \lambda h \left| \bar{U}_v \right| U_v = C_D \rho \frac{2c}{\pi d} h \left| \bar{U}_v \right| U_v \tag{4.5}$$

where C_D = drag coefficient, λ = vegetation density. $\bar{U}_v$ (the resultant velocity acting on vegetation) is same as averaged velocity, $\bar{u}$ for emergent conditions (Wu et al., 2005), whereas $\bar{U}_v$ passing through submerged vegetation is determined by the analytical relation proposed by Stone and Shen (2002).

$$\bar{U}_v = \eta_v \bar{u} \left(\frac{h_v}{h} \right)^{0.5} \tag{4.6}$$

where the coefficient of η_v is 1.0.

In the literatures, various values for drag coefficients have been used, ranging from 0.8 to 1.5. On the other hand, the drag coefficient is significantly influenced by cylinder Reynolds number and vegetation density (Stoesser et al., 2010; Tanino and Nepf, 2008). Thus, few analytical and empirical formulas have been proposed (Dunn, 1996; Huthoff et al., 2007; Stone and Shen, 2002). Among them, the analytical formula proposed by Stone and Shen (2002) is adopted. They suggested that drag coefficient, C_{DM}, based on velocity between cylinders is more suitable than C_D based on commonly used apparent velocity. If the cylinder spacing is same in longitudinal and lateral directions with a staggered array, the relation between C_{DM} and C_D is described (Stone and Shen, 2002; Wu et al., 2005) as

$$C_D = C_{DM} \Big/ \left(1 - \sqrt{\frac{4\phi h}{\pi \min(h, h_v)}} \right)^2 \tag{4.7}$$

where the averaged C_{DM} is 1.05 (Stone and Shen, 2002).

4.3.2 Turbulence closure

For Reynolds stress tensors, the standard k-ε model uses the following eddy viscosity concept.

$$-\overline{u_i' u_j'} = \nu_{th} \left(\frac{\partial u_i}{\partial x_j} + \frac{\partial u_j}{\partial x_i} \right) - \frac{2}{3} k \delta_{ij} \qquad i = 1 \text{ or } 2, j = 1 \text{ or } 2 \tag{4.8}$$

where ν_{th} is the eddy viscosity, k is depth-averaged turbulent kinetic energy and δ is the Kronecker delta. In equation (4.8), the eddy viscosity is determined by

$$\nu_{th} = c_\mu \frac{k^2}{\varepsilon} \tag{4.9}$$

where c_μ is a empirical constant (= 0.09) and ε is the turbulence dissipation rate. The distributions of the turbulence kinetic energy and dissipation rate are determined form the following transport equations.

$$\frac{\partial hk}{\partial t} + u\frac{\partial hk}{\partial x} + v\frac{\partial hk}{\partial y} = \frac{\partial}{\partial x}\left(\frac{\nu_{th}}{\sigma_k} h\frac{\partial k}{\partial x}\right) + \frac{\partial}{\partial y}\left(\frac{\nu_{th}}{\sigma_k} h\frac{\partial k}{\partial y}\right) + \left(P_h + P_{kb} + P_v + \varepsilon\right) h \tag{4.10}$$

$$\begin{aligned} &\frac{\partial h\varepsilon}{\partial t} + u\frac{\partial h\varepsilon}{\partial x} + v\frac{\partial h\varepsilon}{\partial y} = \\ &\frac{\partial}{\partial x}\left(\frac{\nu_{th}}{\sigma_\varepsilon} h\frac{\partial \varepsilon}{\partial x}\right) + \frac{\partial}{\partial y}\left(\frac{\nu_{th}}{\sigma_\varepsilon} h\frac{\partial \varepsilon}{\partial y}\right) + h\left[c_{\varepsilon 1}\frac{\varepsilon}{k}\left(P_h + c_{\varepsilon 3}P_v\right) + P_{\varepsilon b} - c_{\varepsilon 2}\frac{\varepsilon^2}{k}\right] \end{aligned} \tag{4.11}$$

with

$$P_h = \nu_{th}\left[\left(2\left(\frac{\partial u}{\partial x}\right)^2 + \left(\frac{\partial u}{\partial y} + \frac{\partial v}{\partial x}\right)^2 + 2\left(\frac{\partial v}{\partial y}\right)^2\right)\right] \tag{4.12}$$

$$P_{kb} = c_f^{-1/2} u_*^3 / h \tag{4.13}$$

$$P_{\varepsilon b} = c_{\varepsilon\beta} c_\varepsilon c_\mu^{1/2} c_f^{-3/4} u_*^4 / h^2 \tag{4.14}$$

$$P_v = c_{vk}\left(f_{dx} u_v + f_{dy} v_v\right) / \left(1 - c\right) \tag{4.15}$$

where, c_{vk}, $c_{\varepsilon 1}$, $c_{\varepsilon 2}$, $c_{\varepsilon 3}$,$c_{\varepsilon\beta}$, σ_k and σ_ε are empirical constants. In the present computation, we use the following standard values by Launder and Spalding (1974): σ_ε = 1.3, σ_k = 1.0, $c_{\varepsilon 1}$ = 1.44, $c_{\varepsilon 2}$ = 1.92 and Lopez and Garcia (1997): $c_{\varepsilon 3}$ = 1.33, c_{vk} = 1.0. Also, $c_{\varepsilon\beta}$ uses 3.6 (Rodi, 1993). u_* is friction velocity.

4.3.3 Sediment transport model

The bed elevation is calculated by continuity equation of sediment considering occupation rate of vegetation.

$$\frac{\partial\left[\left(1-c\right) z_b\right]}{\partial t} + \frac{1}{1-\omega}\left(\frac{\partial\left[\left(1-c\right) q_b^x\right]}{\partial x} + \frac{\partial\left[\left(1-c\right) q_b^y\right]}{\partial y}\right) = 0 \tag{4.16}$$

where z_b= bed elevation; ω = porosity of bed (= 0.4); q_b^x, q_b^y = bedload transport rate per unit width in *x*- and *y*-directions, respectively, which are given by defining *s* in the direction of streamline and *n* in the normal to streamline.

$$q_b^x = q_b^s \cos\theta - q_b^n \sin\theta \tag{4.17}$$

$$q_b^y = q_b^s \sin\theta + q_b^n \cos\theta \tag{4.18}$$

To evaluate bedload flux in the streamline, the following formula is used, including the effect of bed slope in streamwise direction proposed by Kovacs and Parker (1994) and modified by Yamaguchi and Izumi (2005).

$$q_b^s = \frac{a^{1/2}}{\mu_c}\left[\tau_* - \tau_{*c}\left(1+\frac{1}{\mu_c}\frac{\partial z_b}{\partial s}\right)\right]\left[\tau_*^{1/2} - \tau_{*c}^{1/2}\left(1+\frac{1}{2\mu_c}\frac{\partial z_b}{\partial s}\right)\right]\left(1-\frac{1}{\mu_c}\frac{\partial z_b}{\partial s}\right)\sqrt{Sgd^3} \tag{4.19}$$

with

$$a = \frac{u_*}{V} \tag{4.20}$$

where, τ_*= non-dimensional shear stress; τ_{*c}= non-dimensional critical shear stress; μ_c= the dynamic Coulomb frictions factor (= tanϕ, where ϕ = angle of repose); d = grain size; S = specific weight in fluid; $V = \sqrt{u^2 + v^2}$.

The bedload flux in the normal to streamline is calculated by using the formula of Hasegawa (1984) as

$$q_b^n = q_b^s\left[\frac{u_{bn}}{u_{bs}} - \sqrt{\frac{\tau_{*c}}{\mu_s\mu_k\tau_*}}\frac{\partial z_b}{\partial n}\right] \tag{4.21}$$

where, μ_s and μ_k = static and kinetic frictions factors(= 0.7, 0.5); u_{bs} and u_{bn} = near-bed velocities in *s*- and *n*-directions and , which are determined by the relationship proposed by Engelund (1974)

$$u_{bs} = \beta V \tag{4.22}$$

$$u_{bn} = N_* \frac{h}{r_s} u_{bs} \tag{4.23}$$

where, β = 3(1-σ)(3-σ); σ = 3/($\chi\kappa$ +1); χ = velocity factor (= V/u_*); and κ = *von Kármán*

constant (= 0.4); r_s= radius of curvature of the streamline; and N_* = coefficient of the strength of secondary flow, which changes from 7.9 to 11.4 (Kikkawa et al., 1976). In the present computations, it is assumed to be a constant value (= 11.0).

4.3.4 Bed correction model

To deal with the bed slope that exceeds the sediment angle of repose, the bed correction model is adopted. As seen in Fig. 4.3, if the local bed slope, which is calculated by the gradient of the bed elevation at neighboring cell centers, exceeds the submerged angle of repose, sediment particles slide down the excess slope. After that, the new bed slope identical to the critical angle of repose is created. These processes are implemented through corrections of bed elevation, and the critical angle of repose is calculated as follows

$$\tan\phi_c = \frac{(z1 - \Delta z1) - (z2 + \Delta z2)}{\Delta l} \tag{4.24}$$

where z1 and z2 are the bed elevation at each cell, respectively. Δl is the distance adjacent to cell centers. Δz1 and Δz2 are the bed variation due to bed correction, which indicate an increase and decrease in bed change, respectively. These processes are repeated in all computational cells, iteratively until the bed slope at whole domain becomes smaller than the critical angle of repose. The failed sediment is included in the computation and the total sediment mass in the computational domain is conserved. In the present study, we test the sensitivity to critical angle of repose. The angle of repose is assumed to be 35° as it will be discussed later.

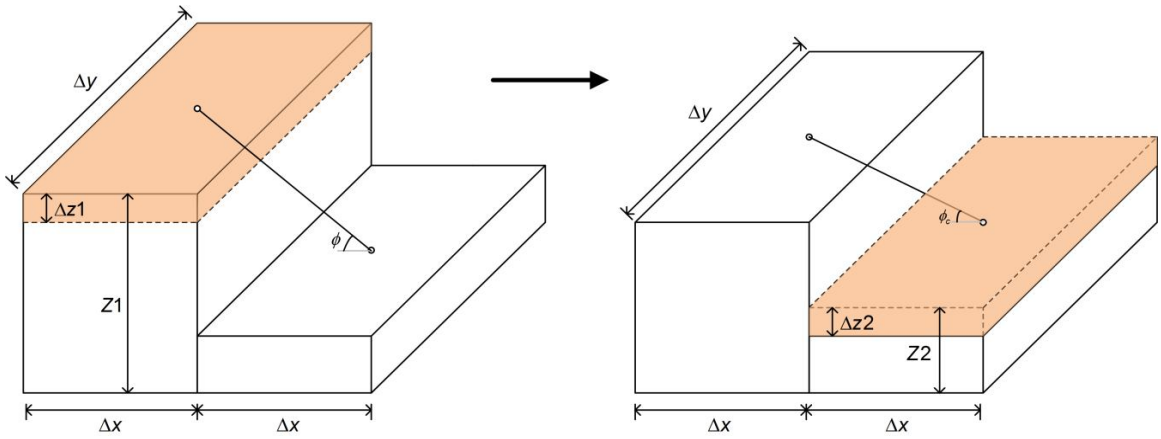


Fig. 4.3 Concept of the bed correction model.

4.3.5 Computational scheme and model set up

For 2D computational model, the finite-volume method (FVM) is used to discretize the governing equations for flow with full-staggered grid. A third order QUICK scheme is applied for the convection terms and a central differencing scheme is applied for the diffusion terms. The first order upwind scheme is used for the continuity equation of sediment transport. The Adams-Bashforth scheme with second order accuracy is employed for time integration for all equations.

For the 2D computational simulations, the computational domain is 8 m long and 0.6 m wide. The computational grids are used with 400 and 40 cells in the streamwise and transverse directions, respectively. At the upstream boundary, a specified discharge is given, and the velocities of $u = u_0$ and v=0 are imposed. At the downstream boundary, Neumann boundary condition is imposed as $\partial M/\partial x = \partial N/\partial x = 0$. A log-law function is applied for evaluating the friction of the side walls. For the outlet of the boundary of bedload flux, Neumann boundary condition is used as $\partial q_b^x/\partial x = \partial q_b^y/\partial x = 0 = 0$. Hydraulic conditions and parameters of the patch in the present computations are identical with the present experiments.

4.4 RESULTS AND DISCUSSION

4.4.1 Validation of the flow model

To understand ability to simulate flow characteristics in an open channel with a finite patch, the computational model is validated through comparison with experimental data carried out by Zong and Nepf (2010). Zong and Nepf (2010) experimentally investigated flow fields in an open channel with a finite patch as shown in Fig. 4.4 and the detailed measurements were made by ADV (Acoustic Doppler Velocimetry) . The experiments were conducted in a flume 16 m long and 1.2 m wide with horizontal slope. The patch model was constructed using circular cylinder of 6 mm with a staggered array. The patch was 8 m long by 0.4 m wide and it was started from 2 m from the upstream test section as shown in Fig. 4.4. The water depth was 0.14 m and the patch density was considered with 4 m^{-1}.

Fig. 4.5a shows comparison of observed and simulated lateral velocity profiles at x = 6.7m where the flow is fully developed. The dotted line denotes the edge of the patch. The

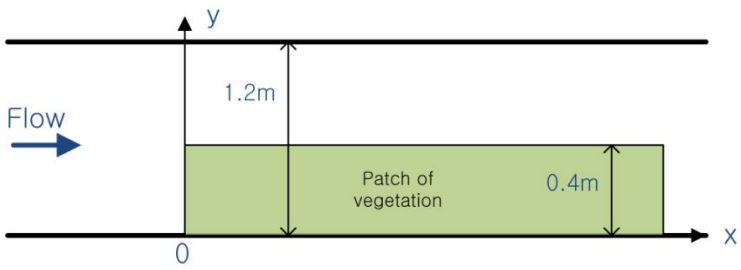


Fig. 4.4 Schematic diagram of the model validation (Zong and Nepf, 2010).

velocity is laterally uniform over the patch width and it shows high gradient in the interface between vegetation and free flow. Fig. 4.5b presents comparison of observed and simulated Reynolds stress profiles at x = 6.7 m. The highest Reynolds stress is found at the interface between vegetation and free flow, which indicates that the shear layer is generated. The increase in Reynolds stress indicates the development of shear layer, which contains coherent vortices (Zong and Nepf, 2010). The present computational model

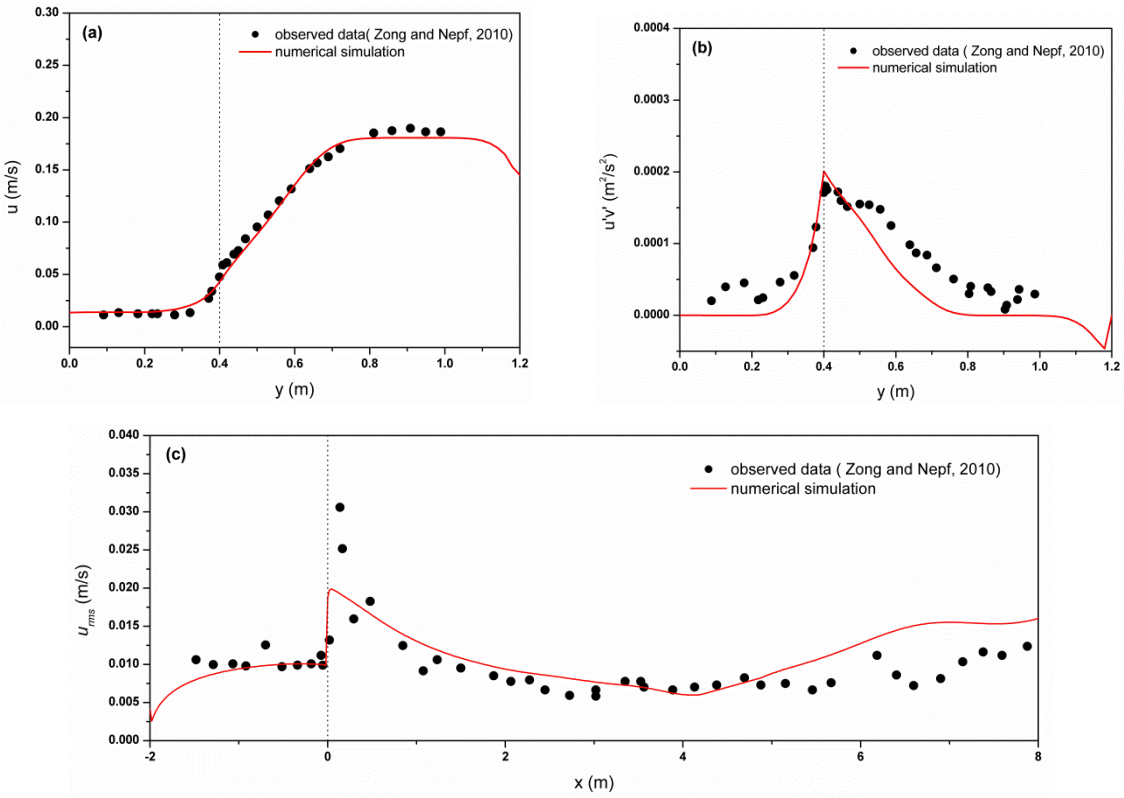
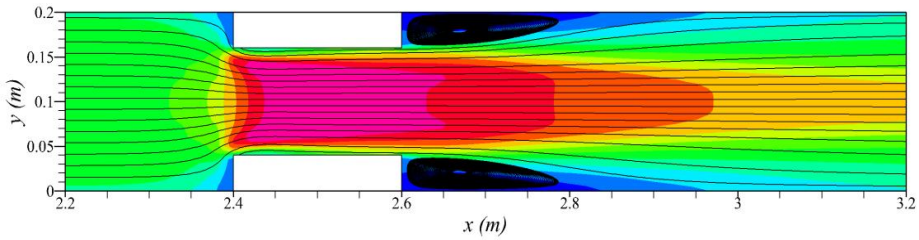


Fig. 4.5 Comparison of observed and simulated results; a) depth-averaged velocity (x = 6.7 m), b) Reynolds stress (x = 6.7 m), c) turbulence intensity (y = 0.2 m).

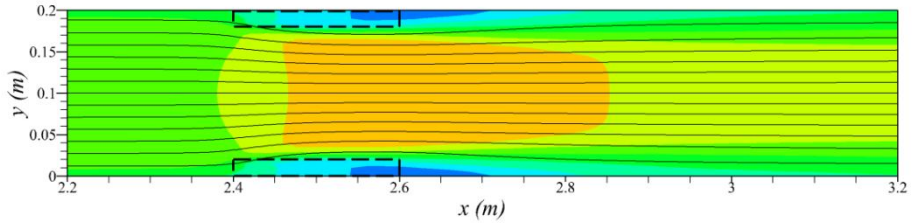
accurately represents the lateral velocity and Reynolds stress profiles, especially at the interface between vegetation and free flow regions. In Fig. 4.5c, the simulated profile of turbulence intensity of u_{rms} is compared with observed data, which was measured along centerline of the patch, y = 0.2 m. It can be seen that the turbulence intensity rapidly increases at the leading edge of the patch and it decreases gradually along the streamwise direction. The local increase in turbulence intensity is attributed to additional production of turbulence induced by wakes of vegetation stems. In addition, the turbulence intensity begin to increase beyond x = 6.0 m. This is associated with developed coherent vortices near the interface region. The simulated profile is in overall agreement with observed data, and notably, numerical model reproduces elevated turbulence intensity at the leading edge of the patch.

4.4.2 Flow field

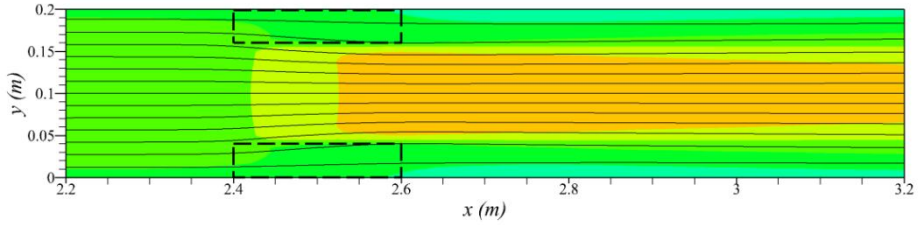
The obstructions in open channel flows can affect flow patterns and hydraulic features. Fig. 4.6 shows the contour of flow velocity with different flow blockages, $2\lambda W_v$ (non-dimensional parameter associated with the patch density and width), together with streamlines in which the velocity is normalized by the inlet velocity. In addition, the contour of flow velocity with solid objects (W_v = 0.04 m) is presented to compare difference of flow characteristics with porous patches. In this figure, the patches and solid objects are emergent. It can be seen in Fig. 4.6a that the flow velocity is concentrated and there is a high acceleration of flow between solid objects. There are distinct recirculation zones behind the solid objects. On the other hand, the flow patterns with porous patches differ very markedly from those of solid objects, especially around the patches because the flow can go through the patches. For $2\lambda W_v$ = 1.0 (W_v = 0.02 cm and λ = 25 m^{-1}), the flow velocity slightly increases between patches, which indicates that the flow interaction is negligible. The streamline is shifted near the leading edge of the patch and the flow velocity is significantly reduced within and behind the patches. For $2\lambda W_v$ = 0.5 (W_v = 0.04 cm and λ = 6.25 m^{-1}), the streamlines are almost straight, which means that there is less diverging flow from the patches. It also leads to less acceleration of flow between patches. For higher patch density where the flow blockage is 2.0 (W_v = 0.04 cm and λ = 25 m^{-1}), the increase in flow velocity between patches accompanies the reduction in flow velocity within and behind the patches. Unlike lower patch density (Fig. 4.6c), the mutual



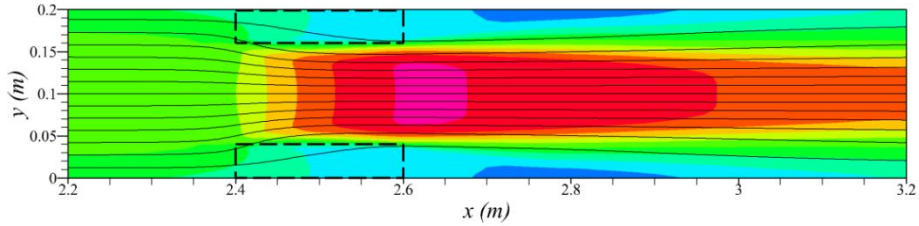
a) solid object and W_v = 0.04 m



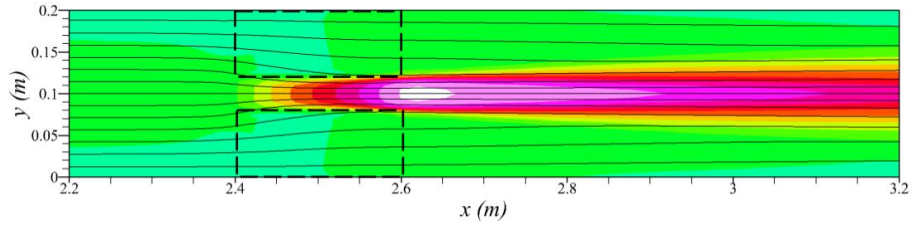
b) $2\lambda W_v$ = 1.0 and W_v = 0.02 m.



c) $2\lambda W_v$ = 0.5 and W_v = 0.02 m.



d) $2\lambda W_v$ = 2.0 and W_v = 0.02 m.



e) $2\lambda W_v$ = 4.0 and W_v = 0.02 m.

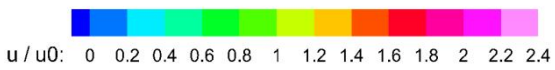


Fig. 4.6 Contour of flow velocity with streamlines. Flow is left to right and the dash lines denote patches of vegetation.

interference of flow would occur between and downstream of the patches. For $2\lambda W_v$ = 4.0 (W_v = 0.08 cm and λ = 25 m^{-1}), especially, the jet-like flow appears between patches due to high patch density and a contracted region between patches. The streamlines through the patches increase as the ratio of the patch width to the channel width increases at the same patch density. It indicates that greater flow rate passes through the patch with an increase in the ratio of patch width. It is found that for $2\lambda W_v$ = 1.0 (W_v = 0.02 cm) and $2\lambda W_v$ = 1.0 (W_v = 0.04 cm), the sheltered regions with low velocity are formed behind the patches, while the relatively high velocity takes place when the flow blockage, $2\lambda W_v$, becomes 4.0. The effects of patch density affect flow velocity and streamline patterns. It can be seen in Figs. 4.6c and d that the flow velocity behind the patches decreases, when the patch density increases. On the other hand, in Fig. 4.6e, the increase in the ratio of patch width reflects increases in flow velocity both behind and between patches. From comparison in Fig. 4.6, this is demonstrated that the streamline curvatures near the leading edge of the patches decrease with a reduction in the patch density, which implies that the diverging flow from the patches is reduced with a decrease in the patch density. It can be also seen that the flow velocity between patches increases with increasing the flow blockage, $2\lambda W_v$.

As seen in Fig. 4.6, the highest velocity is found near downstream of the patches, which can lead to high erosion. The flow velocity normalized by the inlet velocity is presented according to the flow blockage, $2\lambda W_v$, in Fig. 4.7. The velocity increases almost linearly with an increase in the flow blockage. In other words, the patch density and width impact on flow velocity between and downstream of the patches. Fig. 4.8 shows the flow rate through the patches with respect to the patch density where q is the unit flow rate over the channel width and q_v is the unit flow rate through the patches. In this figure, the linear lines are plotted to each ratio of the patch width to emphasize difference among various patch widths. It can be seen that the flow rate through the patches decreases with an increase in the patch density, transferring flow rate from the patches to free flow (i.e. between patches). The decreasing ratio of the flow rate is mostly identical regardless of the ratio of the patch widths and thus the flow rate through the patches is a clearly function of the patch density. A greater impact on flow rate is the ratio of the channel width to patch width. The flow rate increases as the ratio of the patch width increases.

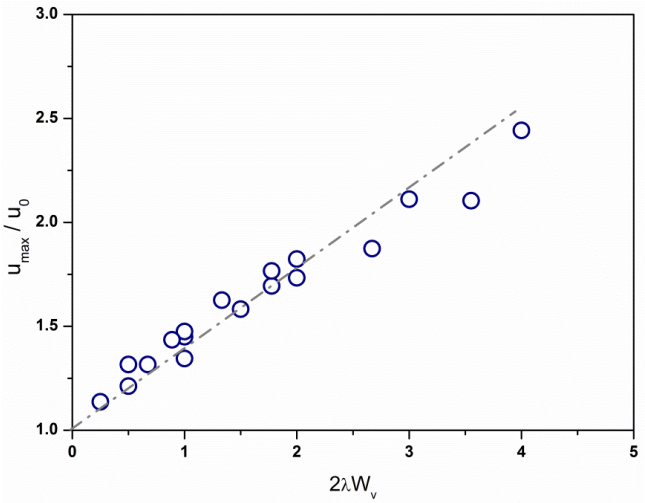


Fig. 4.7 Flow velocity according to the flow blockage, $2\lambda W_v$.

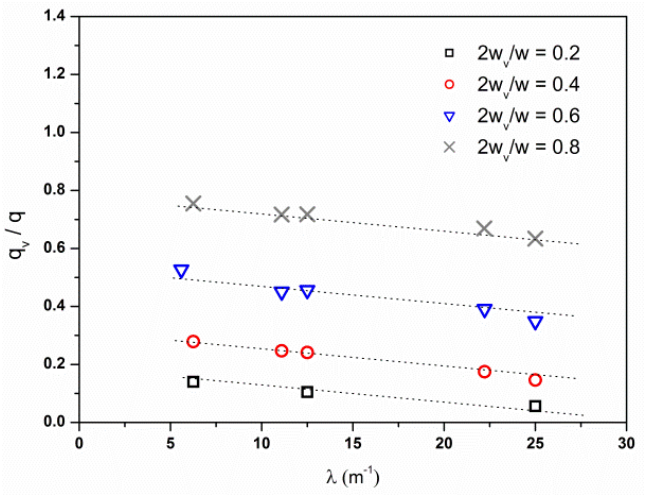


Fig. 4.8 Flow rate through the patches with respect to patch density.

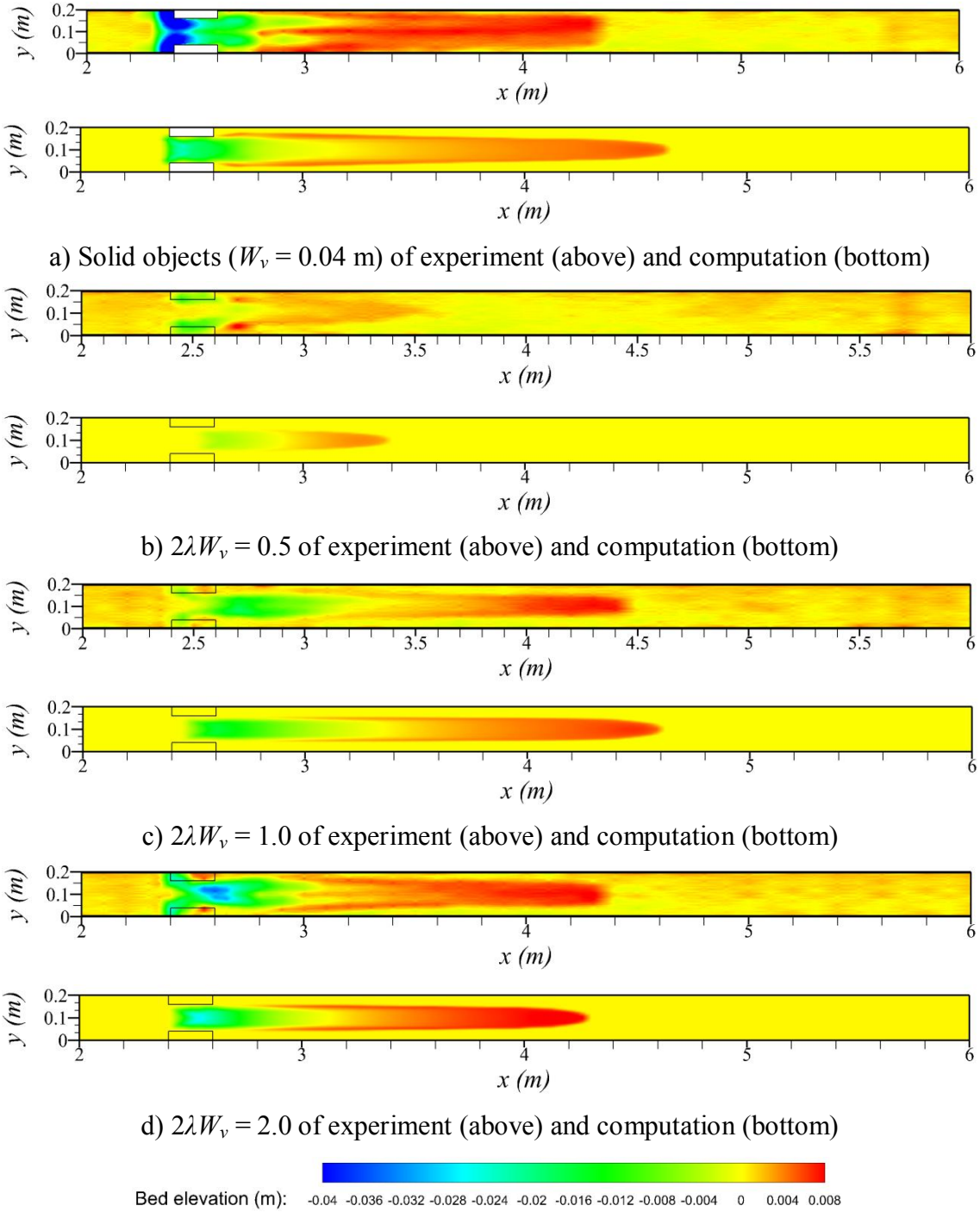
4.4.3 Morphological change

4.4.3.1 Changes in bed topography

The morphological response to added patches of vegetation in an open channel is associated with the patch density and the ratio of the patch width to the channel width. On the other hand, the solid objects, which have same extent to porous patches, would show different morphological behaviors, compared to those of the porous patches. To investigate difference of morphological changes between solid objects and porous patches, we first describe morphological behavior near the solid objects. Fig. 4.9a presents the changes in

bed topography near the solid objects where the width is 0.04 m and the length is 0.2 m with an emergent condition. Flow is left to right and the white rectangles denote solid objects. It can be seen in the experiment that significant local scours are observed at the front of the solid ones and those are extended to upstream and lateral side of the solid ones. The relatively low erosion takes place between solid ones and the sediment scoured from solid objects is deposited downstream region. In the computational result, the local erosion between patches is captured, but the high local scour near the front of the patches is not reproduced due to an inherent defect of the computational model. Such local scour is mainly caused by well-known flow structures such as energetic horseshoe vortices, which is a full three-dimensional flow phenomenon.

The change in bed topography observed with three patch densities in experiments is shown in Fig. 4.9 together with those of computations. As seen in experimental results, the scour and deposition patterns differ substantially from those observed with solid objects. Unlike scours near the front of the solid ones, the local scours near the leading edge of the patches are significantly weakened or not observed. In case that the local scours are observed near the leading edge, the scours occur with distances inside the patches because the flow can be penetrated through patches. In addition, unlike high scours around the solid ones, local high erosions are observed between or downstream of the patches, which create a scour pool in an open channel. This implies that the diversion of flow from the patches is interfered at the contracted region and thus flow velocity is accelerated as shown in Fig. 4.9. For $2\lambda W_v = 0.5$ ($\lambda = 6.25$ m^{-1}) of the experiment, the local scour pool is not developed between patches, whereas the low scour is observed near the each patch, which indicates that the flow interference is negligible as shown in Fig. 4.6. For $2\lambda W_v = 1.0$ ($\lambda = 12.5$ m^{-1}), the local scour pool appears between and downstream of the patches. For higher flowblockage ($2\lambda W_v = 2.0$), the local scour pool not only is observed, but also merges with local scour at the leading edge of the patches induced by the diversion of flow and elevated turbulence. As the scour pool begins to be developed, its depth increases with an increase in the flow blockage. From the analysis of experimental results, the development of scour pool is found to appear as the flow blockage, $2\lambda W_v$, is approximately larger than 1.0 due to flow interference, while the local pool does not occur when the ratio of patch width to the channel width, $2W_v/W$, is smaller than 0.4 because the flow induced by the patches is



a) Solid objects (W_v = 0.04 m) of experiment (above) and computation (bottom)

b) $2\lambda W_v$ = 0.5 of experiment (above) and computation (bottom)

c) $2\lambda W_v$ = 1.0 of experiment (above) and computation (bottom)

d) $2\lambda W_v$ = 2.0 of experiment (above) and computation (bottom)

Fig. 4.9 Change in bed topography.

independent. It is found that the scoured region induced by acceleration of flow moves further downstream as the flow blockage decreases. While the computational model cannot accurately reproduce the local scour around solid objects, the model captures reasonably overall scour and deposition patterns near the patches. In particular, the scoured location and the depth of scour pool are in reasonable agreement with experimental data, which implies that the local scour pool is developed due to a mostly two-dimensional flow with the diverging flow from the patches and acceleration of flow between and downstream of the patches. In addition, the computational model reproduces adequately the length of depositional mound downstream of the patches.

4.4.3.2 Lateral bed variation near the finite patches

Recent few studies showed that local scour appears at the leading edge of the patches due to diversion of flow (Bouma et al., 2007; Rominger et al., 2010; Follett and Nepf, 2012). In the section 4.3.1, the similar local scour is observed at the leading edge of the patches at high flow blockage and the local scour pool is developed between or downstream of the patches, which would be associated with stability of the patches. Thus, to understand influence of the flow blockage on local erosion and stability of the patch, we discuss the local erosion near the patches.

Fig. 4.10 presents comparison of lateral bed profiles with emergent and submerged patches of vegetation between experimental and computational data at x = 2.55 m where the section is located near the middle of the patches. For $2\lambda W_v$ = 1.0 (λ = 25 m^{-1}, emergent), the erosion is observed near the lateral edges of the patches and the bed elevation remains unchanged near the center of the channel, which implies that there is no flow interaction and thus the local scouring occurs independently. As seen in Figs. 4.10a – d, it is observed that the local scour pool distinctly takes place between patches and its depth increases with an increase in the flow blockage. It demonstrates that as mentioned above, the scour pool is developed between patches as the ratio of the patch width is larger than 0.2 and the flow blockage is about more than 1.0. It can be seen in Fig. 4.10 that the localized scour is accompanied with an expansion of lateral erosion due to an excess of submerged angle of repose. In other words, the local scour between patches leads to steep bed slope, so that the sediment particles slide down until the local bed slope becomes stable. The extent of lateral erosion increases with an increase in the flow blockage and especially in $2\lambda W_v$ = 4.0 (λ =

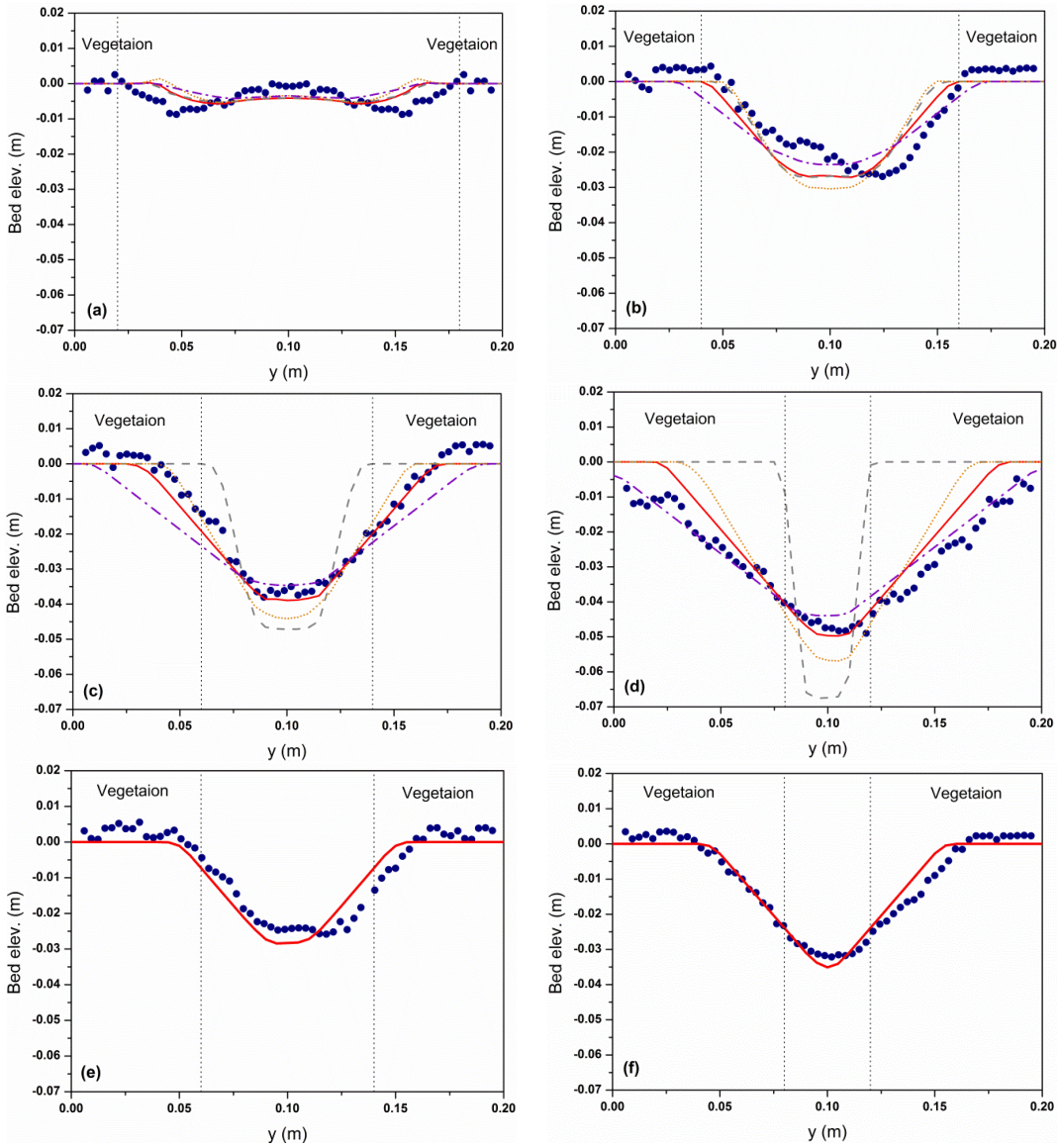


Fig. 4.10 Comparison of lateral bed profiles with emergent and submerged patches between experimental and computational data at x = 2.55 m; a) $2\lambda W_v$ = 1.0 (W_v = 0.02 m, λ = 25 m^{-1}, emergent), b) $2\lambda W_v$ = 2.0 (W_v = 0.04 m, λ = 25 m^{-1}, emergent), c) $2\lambda W_v$ = 3.0 (W_v = 0.06 m, λ = 25 m^{-1}, emergent), d) $2\lambda W_v$ = 4.0 (W_v = 0.08 m, λ = 25 m^{-1}, emergent), e) $2\lambda W_v$ = 1.875 (W_v = 0.06 m, λ = 15.63 m^{-1}, submerged), f) $2\lambda W_v$ = 2.5 (W_v = 0.08 m, λ = 15.63 m^{-1}, submerged). Solid symbols (experimental data), dash dot lines (computational data with angle of repose, 25°), solid lines (computational data with angle of repose, 35°), short dash lines (computational data with angle of repose, 45°) and dash lines (without angle of repose).

25 m^{-1}, emergent), considerable lateral erosion is observed within the patches. Such extensive erosion within the patches is able to make it easy to expose vegetation roots, so that it significantly causes instability of the patches and thus has high possibility to uproot vegetation. Similar patterns of local scour between patches are observed with submerged patches and the degree of scour is dominated by the flow blockage, which indicates that the local scour pool is developed due to similar flow response (i.e. increase in bed shear stress because of acceleration of flow between patches). For $2\lambda W_v$ = 2.5 (λ = 15.63 m^{-1}, submerged), even though the patches of vegetation are submerged, the lateral erosion is observed and it expands into the patches. Thus, the lateral erosion associated with stability of the patches is highly influenced by the ratio of the patch width.

In Fig. 4.10, the computed lateral bed profiles with patches of vegetation are compared to experimental data and extensive sensitivity analysis of the bed correction model is carried out. To investigate the sensitivity of the critical angle of repose in bed correction model, which is an indicator of sand-sliding, the bed profiles with various angles of repose and without the bed correction model are compared with experimental data. For $2\lambda W_v$ = 1.0 (λ = 25 m^{-1}, emergent), the computed bed profile is slightly different from experimental data. The computed bed profile shows that the bed elevation is slightly low, whereas the bed is not only scoured near the lateral edge of the patches, but also constant near the center of the channel. This is due to fact that the computational model is not able to capture the erosion caused by cylinders near the lateral edges. As the flow blockage is greater than 1.0 and the ratio of the patch width is larger than 0.2 (i.e. the local scour pool is developed between and downstream of the patches), the computed bed profiles, in which the bed correction model is employed with the critical angle of repose of 35°, are in good agreement with experimental data and the sand-sliding from the patches is captured by adopting the bed correction model. This implies that the local scour pool between patches is mostly dominated by enhanced flow. The sensitivity of the angle of repose increases as the flow blockage and the ratio of the patch width. It can be seen that the depth of scour pool increases and the sand-sliding from the patches decreases as the angle of repose increases. In contrast, the depth of local scour pool between patches is under-predicted and the lateral erosion near the patches is over-predicted as the angle of repose decreases. Thus, the critical angle of repose in the bed correction model should be appropriately adjusted

and the bed profiles with the critical angle of repose of 35° show overall agreement with experimental data. Kim et al. (2013) and Jang and Shimizu (2005) carried out numerical simulations to investigate pure bank erosion in a compound channel and they found that the critical angle of repose of 30° shows reasonable agreement with experimental data. It indicates that the bed slope near the patches of vegetation is steeper than the pure sediment angle of repose which is consistent with previous studies in the field. Vegetation on the bank increases the bank strength due to a reduction in shear stress and the influence of roots on bank erodibility (Hickin, 1984; Millar and Quick, 1993). It is shown in the computations that the local bed slope can be controlled by the tuning of the critical angle of repose in bed correction model and the angle of repose of 35° is valid near the patch of vegetation. As seen in Fig. 4.10, if the bed correction model is not adopted for simulating local scour pool, the computation causes erroneous results of bed profiles, especially with higher flow blockage where the local scour pool becomes much deeper and narrower. Thus, it is apparent that significant improvement is accomplished by employing the bed correction model. It can be seen in Figs. 4.10e and f (submerged patches) that the lateral bed profiles with the angle of repose of 35° match quite well experimental data, which indicates that the critical angle of repose near the patch is not affected by the submergence ratio.

Fig. 4.11 shows longitudinal bed profiles along the center of the channel with emergent and submerged patches, and the computational bed profiles are compared with experimental data. There is no change in bed elevation upstream of the patch because the flow is below the threshold of sediment motion. It can be seen that local scour pool is observed past the patches (i.e. about x = 2.4 m from upstream entrance). The maximum scour regions occur around the middle of the patches in longitudinal direction. As shown in Fig. 4.10, the depth of scour pool increases as the flow blockage increases. The local bed slope upstream of the maximum scour region becomes steeper as the flow blockage increases. The computed bed profiles with emergent patches, in which the critical angle of repose of 35° is used, show reasonable agreement with experimental data. On the other hand, for the computed bed profile with submerged patches, the erosion past the maximum region is slightly over-predicted.

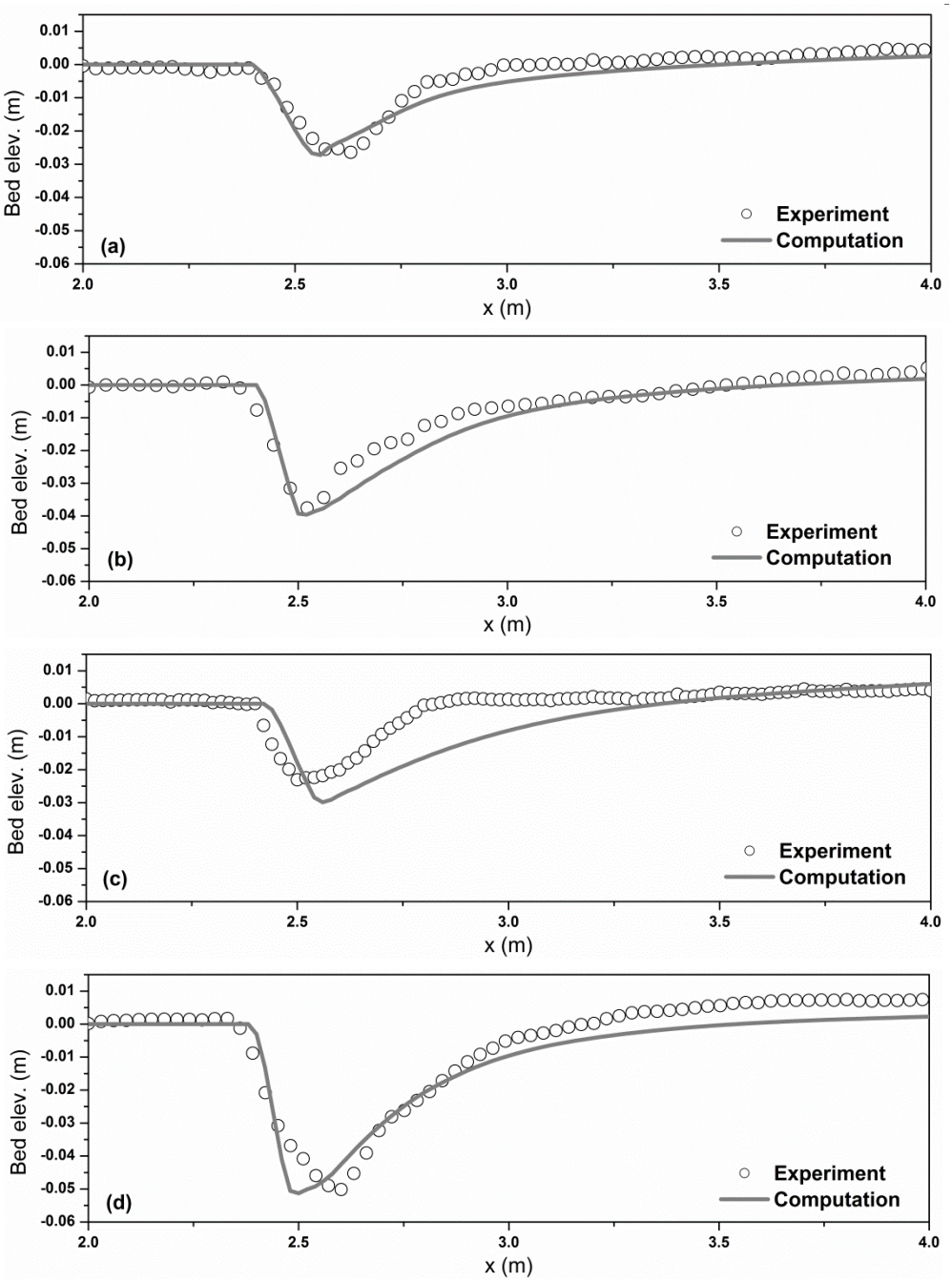


Fig. 4.11 Longitudinal profiles of experiment and computation along the center of the channel with emergent and submerged patches; a) $2\lambda W_v = 2.0$ ($W_v = 0.04$ cm, $\lambda = 25$ m^{-1}, emergent), b) $2\lambda W_v = 3.0$ ($W_v = 0.06$ cm, $\lambda = 25$ m^{-1}, emergent), c) $2\lambda W_v = 1.875$ ($W_v = 0.06$ cm, $\lambda = 15.63$ m^{-1}, submerged), d) $2\lambda W_v = 4.0$ ($W_v = 0.08$ cm, $\lambda = 25$ m^{-1}, emergent).

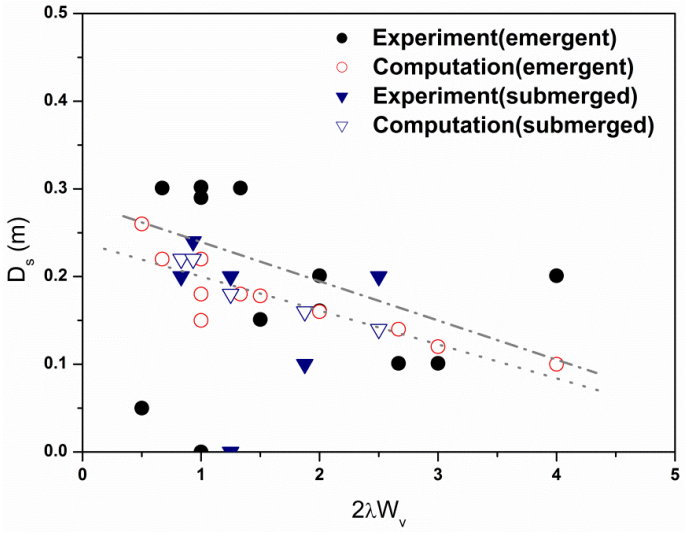
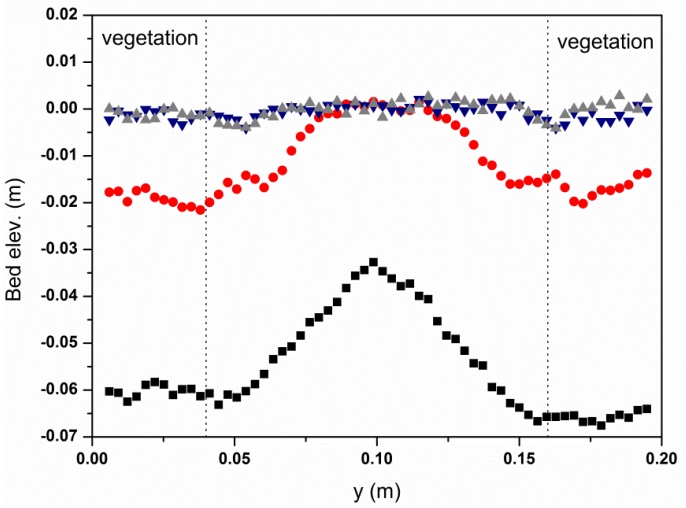


Fig. 4.12 Location of the maximum scour region with respect to the flow blockage, $2\lambda W_v$.

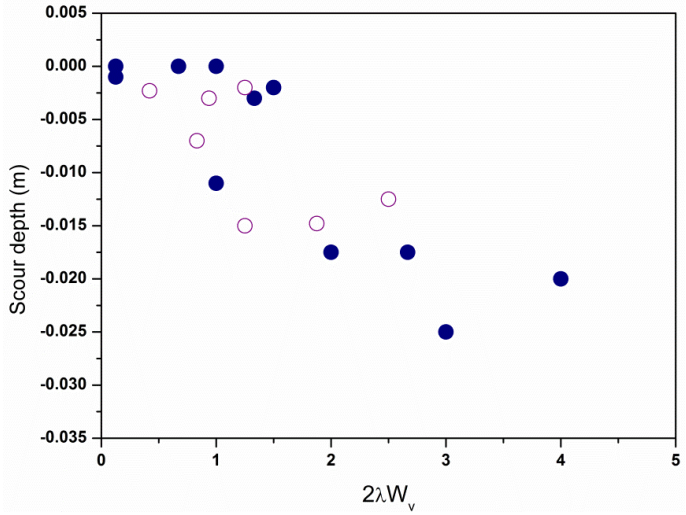
Fig. 4.12 presents location of the maximum scour region with respect to the flow blockage where the location is from the leading edge of the patch. In this figure, the dash dot (experiment) and dot (computation) linear lines are fit to experimental and computational data to distinguish between them. It can be seen that the location of the maximum scour region exhibits decreasing trends in both the experiment and computation.

This is attributed to the diversion of flow from the patch, which is associated with the patch density. The flow approaching the high density patches, such as solid obstructions, begin to be diverted away upstream of the solid ones. As the patch density increases, the diverging region through the patches drops off gradually. Thus, the enhanced flow induced by the diversion of flow between patches occurs further downstream with a reduction in the patch density. As seen in Fig. 4.12, some of the locations are observed near the leading edge of the patches ($D_s = 0$) because the maximum scour near the leading edge is higher than that observed between and downstream of the patches.

Fig. 4.13a shows comparison of lateral bed profiles with different flow blockages at the leading edge, $x = 2.4$ m in which the ratio of the patch width is 0.4. In addition, the bed profile of solid objects is presented in this figure. It can be seen that the considerable local erosion is observed with solid objects at the leading edges and the scoured depth is about 0.06 m at the front of solid ones. The scoured regions at the front of solid ones are mostly



a) Comparison of lateral bed profiles with different flow blockages, $2\lambda W_v$ at $x = 2.4$ m. Square symbol (solid objects), Circular symbol ($2\lambda W_v = 2.0$, $D = 0.005$ m), Inverted triangle symbol ($2\lambda W_v = 1.0$, $D = 0.0025$ m), Triangle symbol ($2\lambda W_v = 0.5$, $D = 0.005$ m).



b) Local scour depth at the leading edge of the patch, $x = 2.4$ m.

Fig. 4.13 Flow rate through the patches with respect to patch density.

flat. The local erosion occurs between solid ones since the local bed slope exceeds the submerged angle of repose. In other words, the local scour causes the steep bed slope, which leads to instability of sediment due to gravity. When the patches of vegetation are added in an open channel, the degree of local scour is significantly weakened. For $2\lambda W_v = 2.0$ ($\lambda = 25$ m^{-1}, $D = 0.005$ m), the local scours are observed at the leading edge of the

patches and the scoured depth is about 0.02 m, which is 33 % of scour observed at solid ones. Unlike local erosion with the solid ones, the bed elevation remains unchanged near the center of the channel, and low erosion is observed near the lateral edge of the patches. For $2\lambda W_v = 1.0$ ($\lambda = 12.5$ m^{-1}, $D = 0.0025$ m) and $2\lambda W_v = 0.5$ ($\lambda = 6.25$ m^{-1}, $D = 0.005$ m), the local scour does not take place at the leading edge of the patches. Fig. 4.13b presents the local scour depth observed at the leading edge of the emergent and submerged patches according to the flow blockage. It can be seen that the local scour is observed with the flow blockage lager than 1.0 and it increases with increasing the flow blockage regardless of the submergence ratio. However, the local scour is reduced beyond the flow blockage of 3.0 because the high flow blockage provokes an increase in flow resistance with patch drag, so that the approaching velocity is highly decelerated. In contrast, the scour is negligible with $2\lambda W_v < 1.0$. The local scour near the leading edge of the patches, which is significantly associated with stability of vegetation, is influenced by the flow blockage.

Planting of vegetation is advocated as ecosystem engineer in streams whereas local erosion has been observed in this study. We consider local erosion near the leading edge of the patches. Similar patterns of local scouring near the leading edge of the patches were observed in the field as well as laboratory experiments (Bouma et al., 2007; Follett and Nepf, 2012; Rominger et al., 2010). In Bouma's field observation, the local scour was observed near the leading edge of a dense patch and laboratory experiments of Follett and Nepf (2012) found that the local scour occurred near the leading edge and the degree of scour increased with patch density. This is consistent with our results and this phenomenon is similar to group piles of scour (Ataie-Ashtiani and Beheshti, 2006). Local scour near the leading edge can cause instability of vegetation because roots of vegetation are exposed above ground, which makes it easy to uproot during high flow. In addition, the region that has potential erosion hampers growth of vegetation.

The buffer regions behind the patches and scour pools provide diverse benefits to fish. Those places serve ecological needs of the species such as offering spawning and resting areas, and refuges for fish (Lutz, 2007). Our results show that the finite patches can create a scour pool and low velocity region behind the patches, while the lateral erosion is observed for the high flow blockage. Unlike real vegetation in natural streams, the bamboos and circular cylinders used in this study result in rather high erosion since the

influence of root system of vegetation is not accounted for. Hickin (1984) and Millar and Qucik (1993) showed that the erosion was reduced at the vegetated banks because the sediment was bound by root masses. Nevertheless, the lateral erosions observed in the experiments and computations indicate potential instability of the patches of vegetation.

4.4.3.3 Scour and deposition

In the experimental and computational data, the scour pool is observed between the patches with flow interference and the degree of scour increases with the flow blockage (Figs. 4.10 and 11). Fig. 4.14a shows the maximum scour depth of experimental data according to the flow blockage. In this figure, an increase in scour depth indicates negative value.

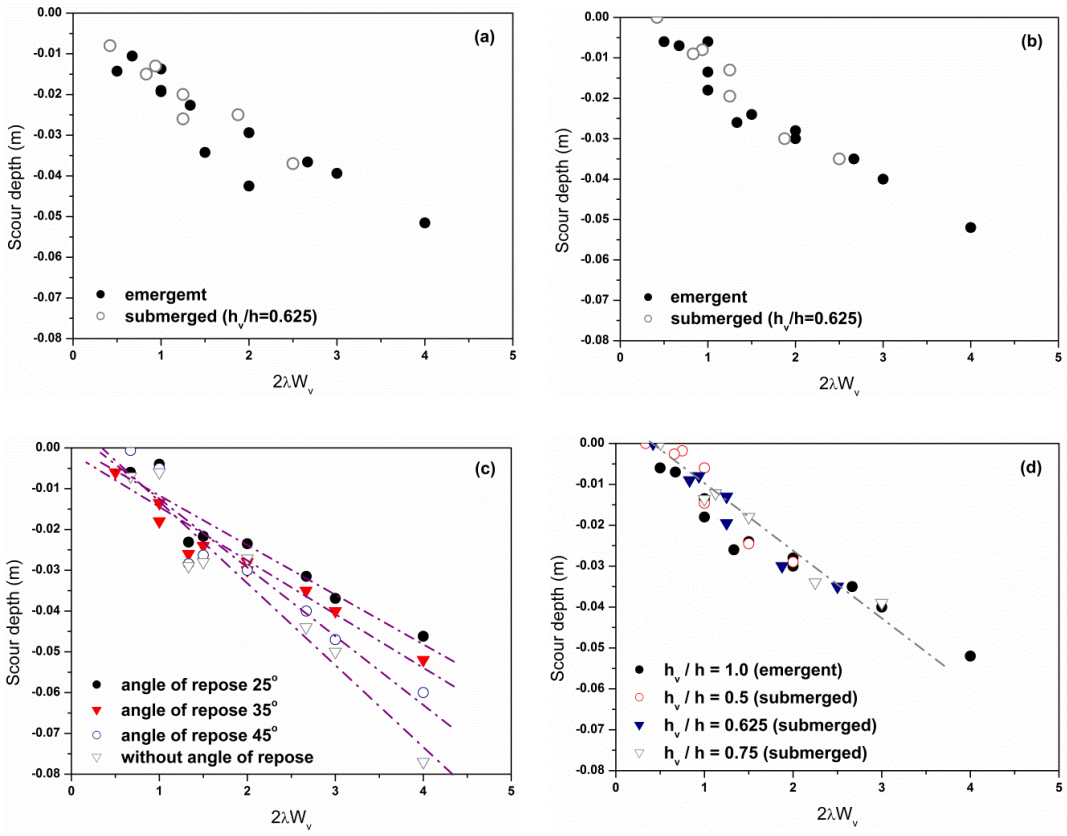


Fig. 4.14 Maximum scour depth according to the flow blockage; a) experimental data of emergent and submerged patches, b) computational data of emergent and submerged patches, c) computation with different angle of repose, d) computation with different submergence ratio.

It can be seen that the scour depth increases with increasing flow blockage regardless of the submergence ratio. For $2\lambda W_v$ < 1.0, the scour pool is not developed between or downstream of the patches, while the local erosion takes place near and at the leading edge of each patch in experiments. It is found that as the scour pool begins to be developed between and downstream of the patches, the depth of scour pool increases almost linearly with the flow blockage. This is corresponding to a linear increase in maximum flow velocity between the patches as shown in Fig. 4.7. Fig. 4.14b presents the maximum scour depth of computational data versus the flow blockage. As seen in experimental data, the maximum scour depth not only increases with an increase in the flow blockage, but also is in reasonable agreement with experimental data. For $2\lambda W_v$ < 1.0, however, the computed scour depth is under-predicted because the local scour is observed near the patches at the leading edges in the experiment. As shown in the previous section, the depth of local scour pool in computations is affected by the critical angle of repose. In Fig. 4.14c, the computed maximum scour depth with different angles of repose and without the bed correction model is shown.

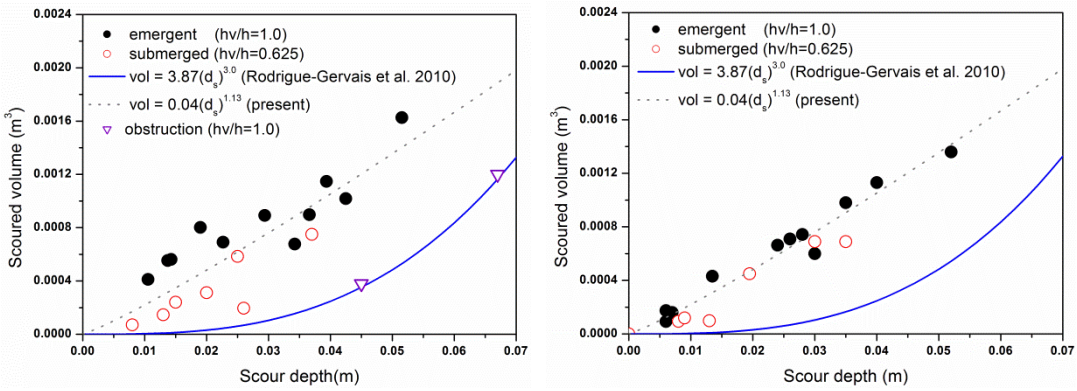


Fig. 4.15 Scoured volume around the patches according to the scour depth; a) experiment b) computation.

In this figure, dash dot linear lines are fit to each case to emphasize the difference between them. It can be seen that the angle of repose has a negligible impact on maximum scour depth when the flow blockage is less than 2.0. For $2\lambda W_v$ > 2.0, however, there is significant influence on local scour depth. Especially, if the bed correction model is not adopted, the depth of scour pool is considerably over-predicted. Based on agreement of the

submerged cases with experimental data, additional computations are carried out to investigate the effect of the submergence ratio in Fig. 4.14d. It is demonstrated that the depth of scour pool increases almost linearly with an increase in the flow blockage regardless of the submergence ratio.

The local scour pool has an advantage to stream ecosystem, so that the scoured region caused by the patches of vegetation is very beneficial. The scour region produced by the patches has many environmental benefits because it provides not only diverse aquatic habitats but also shelter for fish in the event of flooding. The estimation of volume of scoured region around the patches is very important. Fig. 4.15 shows scoured volume around the patches according to the scour depth. In the experimental result in Fig. 4. 15a, regression analysis is used to determine whether there is predictive relationship between scour depth and volume. Through power function, the scoured volume around the patches increases with an increase in scour depth to the power of 1.13. For the solid obstructions, however, the relation between scoured volume and depth shows a quite different trend, and thus scoured volume increases with an increase in scour depth to the power of 3.0 (Rodrigue-Gervais et al., 2010). The present experimental data of solid obstructions are good agreement with their trend and thus, this suggests that the properties of in-stream structures (i.e. solid and porous structures) alter the relationship between scour pool depth and volume. In Fig. 4. 15b, computational results are presented with the regression line of power function based on experimental data. The computational results align very closely to the regression line and thus, the numerical model predicts well the depth and volume of scour pool around the porous patches in open channels.

4.5 SUMMARY

This study describes the local scour pool caused by finite patches of vegetation by means of laboratory experiments and numerical computations. To investigate impacts of spacing between patches with various patch densities on morphological changes, diverse ratio of the patch width is considered. The finite patches of vegetation are modeled as circular cylinders and bamboo sticks. Local scour driven by acceleration of flow past patches is observed between or downstream of the patches. Local scour pool begins to be developed as the flow blockage (the product of patch density to patch widths) is larger than 1.0 and the ratio of the patch width (the ratio of patch width to channel width) is greater

than 0.2. The depth of local scour pool increases almost linearly with an increase in the flow blockage regardless of the submergence ratio. The volume of scoured region increases with increasing flow blockage. A two-dimensional computational model adopting the bed correction model is applied and computational results are in a good agreement with experimental data in terms of the bed profiles and maximum scour depth. Especially, the lateral erosion due to sand-sliding near the patches is reasonably captured. Through the sensitivity of the critical angle of repose in bed correction model, it is found that the angle of repose of 35° is in the best agreement with experimental data. Also, the impacts of critical angle of repose in the bed correction model on the bed profiles and maximum sour depth increase with increasing flow blockage. If the bed correction model is not adopted in computations, the depth of local scour pool is significantly over-predicted and the lateral erosion caused by sand-sliding is not reproduced.

CHAPTER 5 NUMERICAL INVESTIGATION OF LOCAL SCOUR AROUND CYLINDERS IN A TURBULENT FLOW

5.1 INTRODUCTION

Three dimensional flows around vertical obstructions in natural rivers or streams are significantly complex because of generation of flow separation and turbulence structures in a wide range of scales (Ataie-Ashtiani and Beheshti, 2006; Kirkil et al., 2009). Such complex flows interact with sediment on the bed and drive local scour process around the obstructions. This process causes instability of streambed and weakens the structural safety (Khosronejad et al., 2012). The local scour is one of the main reasons for the failure of bridge piers and abutments. Moreover, there are similar phenomena at the individual tree and shrub, which are considerably associated with stability of vegetation (Euler et al., 2012; Kim et al., 2013). A prediction of local scour depth around vertical obstructions such as spur dikes, bridge piers and rigid vegetation is necessary for safe designs and river training works. Several experimental studies have been conducted to estimate scour depth, mainly around piers and then semi-empirical equations for maximum scour depth were proposed (Richardon and Davis, 2001; Melville, 2000; Sheppard and Renna, 2005). However, most of these equations yielded overestimation of scour depth due to fact that the similitude of large scale turbulence structures formed by cylinders was not accounted explicitly in the equations (Ettema et al., 2006; Lee and Sturm, 2008; Kirkil et al., 2009).

On the other hand, several three-dimensional numerical studies around a single vertical circular cylinder have been conducted to study the scour process and estimate the scour depth. Olsen and Melaaen (1993) and Olsen and Kjellesvig (1998) conducted three-dimensional simulations of flow and scour around a circular pier in order to predict local scour considering non-cohesive sediment bed. They used a three-dimensional steady RANS model with k-ε turbulence closure in corporation with a sediment transport model. The results were compared with experimentally observed bed elevation data and a reasonable agreement was obtained. Roulund et al. (2005) carried out three-dimensional numerical simulations of flow and scour around a circular pile with the flows above the

threshold of sediment motion, using unsteady Reynolds averaged Navier-Stokes (URANS) models incorporated with k-ω turbulence closure. They showed that the simulated process of scour agrees fairly with experimental results, while the prediction of scour depth by the model is underestimated with 15 % due to inability of URANS models, which does not account for the fluctuating components of horseshoe vortices at the junction of the pile. Zhao et al. (2010) developed a three-dimensional finite element model for simulating flow and scour around submerged vertical cylinders. URANS equations were solved with k-ω turbulence closure and an empirical formula was employed for calculating bed load transport. They described that the computed scour depth was underpredicted by 10% to 20%. Khosronejad et al. (2012) investigated the predictive capabilities of a URANS model for various bridge pier geometries (cylindrical, square and diamond shape geometries). The governing equations with k-ω turbulence closure were numerically solved in combination with a curvilinear immersed boundary method to deal with the deformations of sand bed. They presented that for a diamond pier, the numerical model shows reasonable agreement of scour depth and process, but for the square and cylindrical piers, there were differences of scour pattern and depth between measured and simulated results. They described that this is due to the deficiency of the URANS model or the morphodynamic model. In order to reproduce accurately vortical structures in a turbulent flow and to consider directly the effect of the instantaneous flow field on sediment transport, Escauriaza and Sotiropoulos (2011) developed a detached-eddy simulation (DES) model coupled with a bed load transport model in which the sediment is solved as spherical particles in a Lagrangian framework. They simulated erosion and bed morphodynamic around a cylindrical pier and their results showed that the ripple dynamics, which evolve from the interactions between turbulent horseshoe vortices and mobile-bed, are captured by the numerical model. The purpose of their simulations was to describe the detailed bed form phenomena around a cylindrical pier, such as the initial stage of bed forms within and around the scour hole. This means that the growth of scour and the equilibrium scour depth were not investigated.

For construction of bridge piers in rivers, pier groups are increasingly preferred as an economic aspect because the construction cost is lower than that of spread footing pier. A number of studies around pile groups (Hannah, 1978; Ataie-Ashtiani and Beheshti, 2006; Amini et al., 2012) were experimentally conducted. Most of studies were focused on

prediction of equilibrium scour depth and carried out to investigate the effect of cylindrical obstruction spacing on scouring depth longitudinally and transversely. The mechanisms of scour with multiple obstructions are much more complex than those of a single obstruction due to interference of the flow and sediment transport around obstructions.

In addition, the popularity of stream and river restoration works have been recently grown and vegetation is often advocated as a component for a restoration technique for improving ecological functions because it can remove nutrients and provide ideal areas for aquatic habitats. Few experimental and field studies have been carried out to investigate response to patches of vegetation in open channel flows. Rominger et al. (2010) observed the removal of planted vegetation on sand bars in a meandering channel. From the field monitoring in a tidal flat, Bouma et al. (2007) observed the local erosion at the leading edge of circular patches with high vegetation density, whereas for sparse patches of vegetation, there was no local scour at that region. Kim et al. (2013) conducted laboratory experiments to investigate influence of patch density on local scour around the patch, consisting of rigid and circular cylinders and they showed that the local scour depth at the leading edge of the patch increased with increasing patch densities. Thus, the patch density is an important factor to local scour around the patch, which is strongly associated with vegetation stem spacing, so that this phenomenon is similar to the local scouring and patterns (Rominger et al., 2010; Kim et al., 2013).

Aforementioned, numerical studies have been confined to a single cylinder. In spite of fundamental interests, however, there is none of the numerical investigations around multiple circular cylinders in terms of scour depth, scouring phenomena and process. Therefore, to understand scour mechanism and transport processes around cylindrical objects, study on flow and local scour by means of numerical model capable of simulating detailed hydrodynamic and morphodynamic with complex geometries is still a challenging task.

The objective of present paper is two-fold: (1) to extend recent developed morphodynamic model (Nabi et al., 2013) to flows and bed mophodynamics past cylinders in a sand bed; (2) numerically investigate the effect of cylinder spacing, longitudinally and transversely, on scour evolution, phenomenon and maximum scour depth. This is achieved computationally using the large eddy simulations (LES) for flow coupled with a sediment

transport model in a Lagrangian framework and a morphodynamic model. At the present study, simple arrangements, i.e., side-by-side and tandem arrangements, are chosen to simulate the growth of scour holes and scouring phenomena around cylindrical objects. For turbulent channel flows past cylinders, LES is carried out with a ghost-cell immersed boundary method to treat the cylinders and the bed surface. A model for sediment motion is employed in which the sediment is considered as spherical particles and the sediment motion stage such as pick up, transport and deposition are solved in a Lagrangian framework. To validate the LES incorporated with sediment transport and morphodynamic models, time-averaged velocity and turbulence intensity are compared with available data of Liu et al. (2008). The bed evolution of scour and bed topography at the equilibrium state around a single cylinder are compared with laboratory data of Khosronejad et al. (2012). To investigate the effects of cylinder spacing, side-by-side and tandem arrangements are considered with diverse distances between two cylinders. The numerical simulations are performed with various cylinder spacing, and the scour and deposition patterns and bed evolution of local scour are investigated. In addition, the computed maximum scour depth is compared with experimental data reported by Hannah (1978) and Ataie and Beheshti (2006).

5.2 HYDRODYNAMIC MODEL

5.2.1 Governing equations of flow

We employ LES to simulate instantaneous unsteady three-dimensional turbulent flow around complex geometries (Nabi et al., 2012b). The governing equations of flow are the unsteady, incompressible filtered Navier-Stokes equations as

$$\frac{\partial \overline{u}_j}{\partial x_j} = 0 \tag{5.1}$$

$$\frac{\partial \overline{u}_i}{\partial t} + \frac{\partial \overline{u}_i \overline{u}_j}{\partial x_j} = -\frac{1}{\rho}\frac{\partial \overline{P}}{\partial x_i} + \frac{\partial}{\partial x_j}\left[2\nu \overline{S}_{ij} - \tau_{ij}^{SG}\right] \tag{5.2}$$

where x_i's are the coordinates, t is the time, $\overline{P}$ is the modified pressure, ρ is the density of fluid, $\overline{u}_i$ and $\overline{u}_j$ (i or j = 1,2 or 3) are the resolved velocity vectors, v is the molecular

viscosity. S_{ij} is the filtered strain-rate tensor, defined as

$$\overline{S}_{ij} = \frac{1}{2}\left(\frac{\partial \overline{u}_i}{\partial x_j} + \frac{\partial \overline{u}_j}{\partial x_i} \right) \tag{5.3}$$

The sub-grid-scale (SGS) stresses $\tau_{ij}^{SG} = \overline{u_i u_j} - \overline{u}_i \overline{u}_j$ appear, resulting from the unresolved eddies by the computational grid. These stresses are modeled using the Smagorinsky sub-grid model (Smagorinsky, 1963).

$$\tau_{ij}^{SG} = -2\nu_t S_{ij} + \frac{1}{3}\tau_{kk}\delta_{ij} \tag{5.4}$$

$$\nu_t = \left(C_s \overline{\Delta} \right)^2 \left| \overline{S} \right| \tag{5.5}$$

where C_s is the Smagorinsky constant, which is approximately 0.16, $\left|\overline{S}\right| = \sqrt{2\overline{S}_{ij}\overline{S}_{ij}}$ and Δ is the filter size given as follows,

$$\Delta = \left(\Delta x . \Delta y . \Delta z \right)^{1/3} \tag{5.6}$$

5.2.2 Numerical methods

The detailed numerical methods for the flow field have been documented by Nabi et al. (2012b), therefore, we briefly explain the primary methods in this section.

Equations (5.1) and (5.2) are solved with two-step fractional step. The advection and diffusion terms in momentum equations are discretized in space on a staggered grid with a second-order finite-volume method. A second order Adamsh-Bashforth scheme is used for the time integration of the advection term, while Cranck-Nichelson method is applied for the diffusion term.

A ghost-cell immersed boundary method based on Cartesian grids is used for treating the bed surface and the solid objects. This method forces the flow at the boundaries, directly, which is a function of time and space. The location of this force is not necessary to consistent with a grid point, so interpolation or extrapolation to these points is required. The ghost-cell is located on the normal vector passing through the bed (or solid) and it forms an imaginary point, which is extended into the fluid for a trilinear interpolation.

In the Cartesian grid system, uniform grids have low efficiency (computationally demanding) for simulating flow and morphological processes because a huge number of

grids are demanded to reproduce small-scale turbulence eddies. To resolve such problems, we employ an adaptive multi-level structure-Cartesian grid with local refinement. In the regions with high gradients (i.e. near the bed surface and the solid objects), finer grid cells are placed. For more details, we refer to Nabi et al. (2012b).

5.3 SEDIMENT TRANSPORT MODEL

In this section, we briefly describe the sediment transport model that can account for the effect of instantaneous velocity fluctuations on the sediment particle. The sediment particles are assumed to be spherical particles. The sediment transport model consists of pickup, transport in suspension, deposition and sliding, and it is modeled in a Lagrangian framework. This concept not only increases the realistic phenomena of the sediment motion but also provides more physical understanding of the sediment transport processes. The sediment particles are initiated when the bed shear stress is above a certain value. For calculating the pickup rate, the following formula (Nabi et al., 2013) is incorporated in the model, which is similar to the pickup formula proposed by De Ruiter (1983).

$$E = \varepsilon \rho_s \sqrt{\frac{\rho_s - \rho}{\rho_s} g d \left(\tau_* - \tau_{*_c} \right)} \tag{5.7}$$

where E is the pickup rate, ε is a constant for uniform spherical particles equal to 3.67×10^{-4} (Nabi et al., 2013), τ_* is the dimensionless local bed shear stress, τ_{*_c} is the dimensionless critical bed shear stress, ρ_s is the density of particle, g is the gravitational acceleration and d is the grain size. The instantaneous volume of pickup rate over an area of a cell on the bed, S, during time step, Δt, is determined by

$$V_E = E \frac{S}{\rho_s} \Delta t \tag{5.8}$$

The number of particles picked up from each cells is estimated as follows

$$n_{pickup} = \frac{V_E}{V_P} \tag{5.9}$$

where V_p is the volume of single particle.

The sediment particles picked up from the bed are transported by the forces exerted by the flow. The momentum equation for velocity of each sediment particle considering drag,

lift, gravity, the effect of pressure force and the added mass is described as follows (Maxey and Riley, 1983)

$$\rho_s V_p \frac{d\vec{v}_p}{dt} = (\rho_s - \rho) V_p \vec{g} + \rho V_p \frac{D\vec{u}_f}{Dt} + \frac{1}{2}\rho V_p \left(\frac{D\vec{u}_f}{Dt} - \frac{d\vec{v}_p}{dt} \right)$$

$$+ \frac{3}{4}\frac{C_D}{d}\rho V_p \left| \vec{u}_f - \vec{v}_p \right| \left(\vec{u}_f - \vec{v}_p \right) + \frac{3}{4}\frac{C_L}{d}\rho V_p \left(\left| \vec{u}_f - \vec{v}_p \right|^2_{top} - \left| \vec{u}_f - \vec{v}_p \right|^2_{bottom} \right) \vec{n} \tag{5.10}$$

where $\vec{v}_p$ is the velocity of the sediment particle, u_f is the fluid velocity at the particle location, C_D is the drag coefficient which can be evaluated by formulas proposed by Morsi and Alexander (1972), $\vec{g}$ is the gravity vector. D/Dt is the material derivatives (= $\partial / \partial t + \vec{u} \cdot \nabla$). Because it is very difficult to determine the lift coefficient, C_L, and to interpolate the flow velocity in the top of bottom of the particle, the theoretical and experimental relations proposed by McLaughlin (1991) and Mei (1992) are employed to evaluate the lift force term. $\vec{n}$ is normal unit vector. In the model, the particle interactions are neglected.

Each particle location is calculated by the trajectory equation as

$$\frac{d\vec{x}_p}{dt} = \vec{v}_p \tag{5.11}$$

where, $\vec{x}_p$ is the position vector of the particle. Eqs. (5.10) and (5.11) are calculated until the particles are deposited on the bed. As the particles interact with the bed, they may show two mechanisms, namely elastically rebound or viscously damping. Schmeeckle et al. (2001) described an appropriate physical scaling for these mechanisms by Stokes number. As the particles are dominated by the viscous pressure, these are deposited on the bed. In contrast, as the partially elastic collision occurs, the new velocities take place. The velocities are calculated as follows

$$v_{n,new} = -\alpha_n v_{n,old} \tag{5.12}$$

$$v_{t,new} = \alpha_t v_{t,old} \tag{5.13}$$

where, v_n and v_t are the normal and tangential velocities, respectively. The elastic coefficients of normal and tangential directions, α_n and α_n are set to be 0.65 and 1.0, which

are determined by experiments (Schmeeckle and Nelson, 2003).

5.4 MORPHODYNAMIC MODEL

In order to describe the instantaneous bed elevation, we employ the new morpodynamic model developed by Nabi et al. (2013). The number of particles that is picked up or is deposited is calculated by aforementioned equations and thus the addition or subtraction of sediment is determined from the cell. In the morphodynamic model, the volume of sediment due to the sliding effect is also taken into account. The change in bed elevation can be determined as

$$\Delta z = \frac{A_2}{A_3}\frac{V_p\left(n_{depos} - n_{pickup}\right)}{S.C_{frac}} + \frac{\delta P_s}{\Delta x \Delta y} \tag{5.14}$$

where A_2 and A_3 are shape coefficients for spherical grains of $\pi / 4$ and $\pi / 6$, respectively, which are two- and three-dimensional geometrical properties. S is the area of a cell on the bed and C_{frac} is a clustering factor (= 1.0). The n_{depos} and n_{pickup} are the number of picked up and deposited particles, respectively. The second term in the right hand side indicates the change in the bed elevation associated with particle sliding, which is calculated by the sliding sediment volume, $\delta P_s = P_{s,in} - P_{s,out}$, where $P_{s,in}$ denotes the sediment volume coming from the neighboring cells to the present cell and $P_{s,out}$ denotes the sediment volume going out from the present cell to adjacent cells (Nabi, 2012a). The bed elevation is defined in the center of cells and is interpolated to other points using bilinear interpolation with second order accuracy.

5.5 VALIDATION

5.5.1 Flow field

For the validation of the present model for flow through multiple cylinders, time-averaged velocities and turbulence intensities are compared with the literature data reported by Liu et al. (2008). Liu et al. (2008) conducted laboratory experiments to investigate the detailed flow structure past cylinders with a staggered array in a flume using laser doppler velocimeter (LDV). The velocity measurements were made at several locations in the vertical direction as shown in Fig 5.1. The Flume was 4.3 m long, 0.3 m wide with a constant discharge of 0.0044 m^3/s which is corresponding to a water depth of

0.065 m. The slope was kept constant as 0.003. In the flume, cylinders of 6.35 mm in diameter D, were placed with a distance of 10D between cylinders.

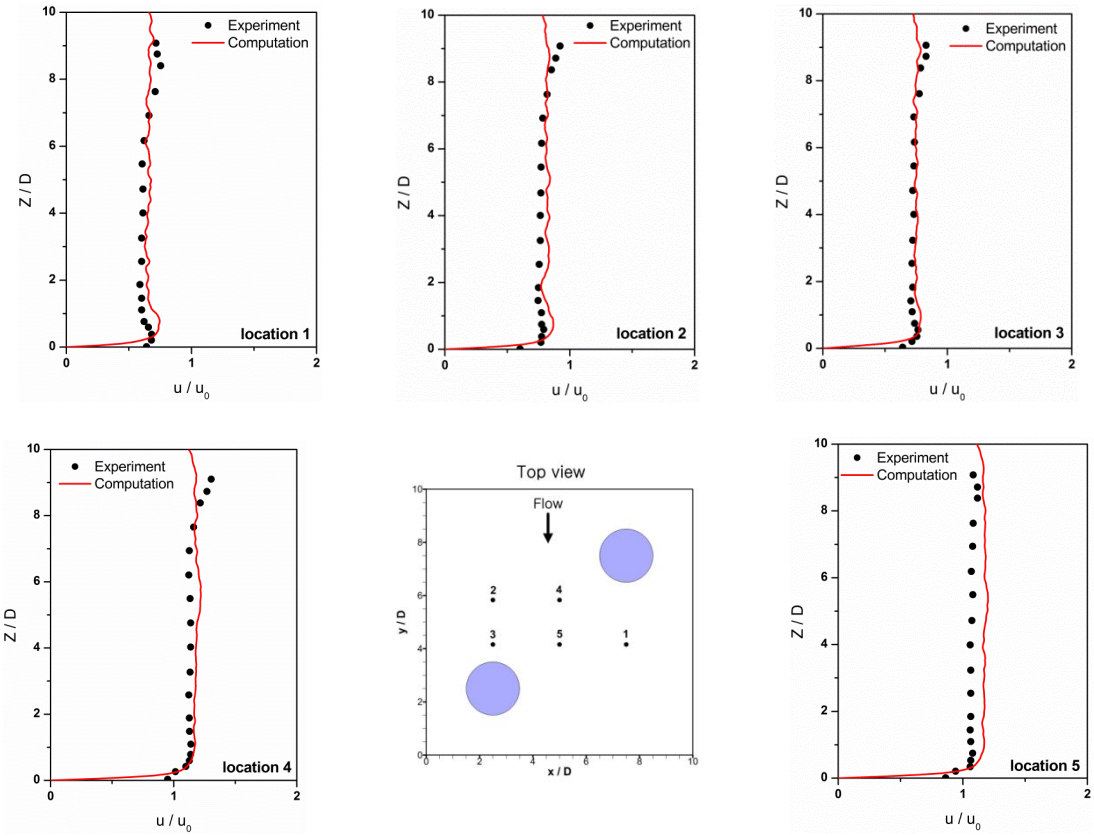


Fig. 5.1 Time-averaged streamwise velocity profiles at five locations.

Fig. 5.1 shows the time-averaged streamwise velocities, which is normalized with the bulk velocity at five locations. In this figure, the simulated profiles are compared with the observed data. It can be seen that the overall agreement between simulated and observed velocity distributions is found to be good. Especially, the velocity profiles in front of the cylinder and behind the cylinder, i.e. the locations 1, 2 and 3 show a closer agreement with experiment rather than those between cylinders. In locations 4 and 5, the simulated streamwise velocities are slightly overpredicted. At the location 1, the velocity spike is observed near the bed due to fact that the high momentum flux caused by vortices transferred into the wake region near the bottom (Liu et al., 2008), which is predicted well by the present model. Fig. 5.2 presents the turbulence intensities, u' normalized by the bulk velocity at five locations. The simulated streamwise turbulence intensity profiles are

compared with observed data. In the figure, the comparison of simulated results with observed data is in satisfactory agreement. The relatively high turbulence intensity is observed behind the cylinder because of vortex shedding. It can be seen that the present model captures the spikes of turbulence intensities, which appear near the bed at the locations 4 and 5. The turbulence intensity profiles are straight in vertical directions, which are significantly different from the open channel without cylinders (Stoesser et al., 2010). Overall good agreement is found between observed and simulated results, which indicate that the computational model is reliable for simulating flow past multiple cylinders.

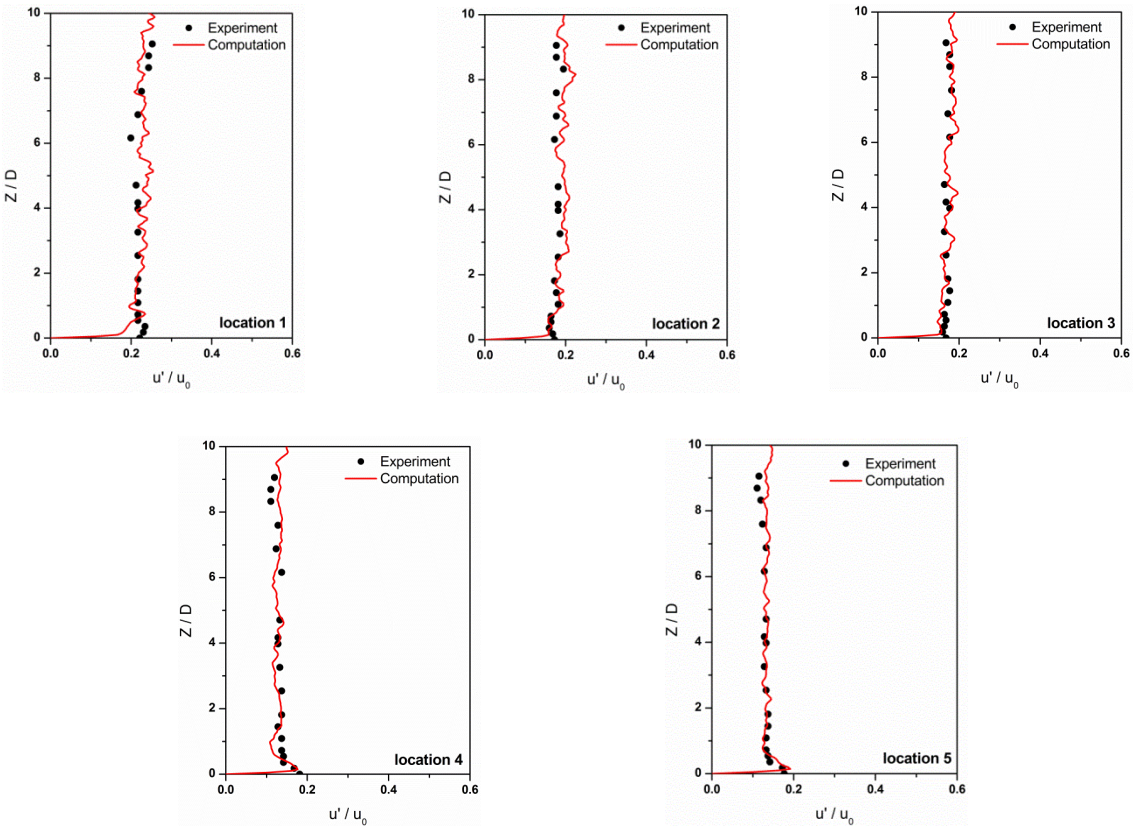
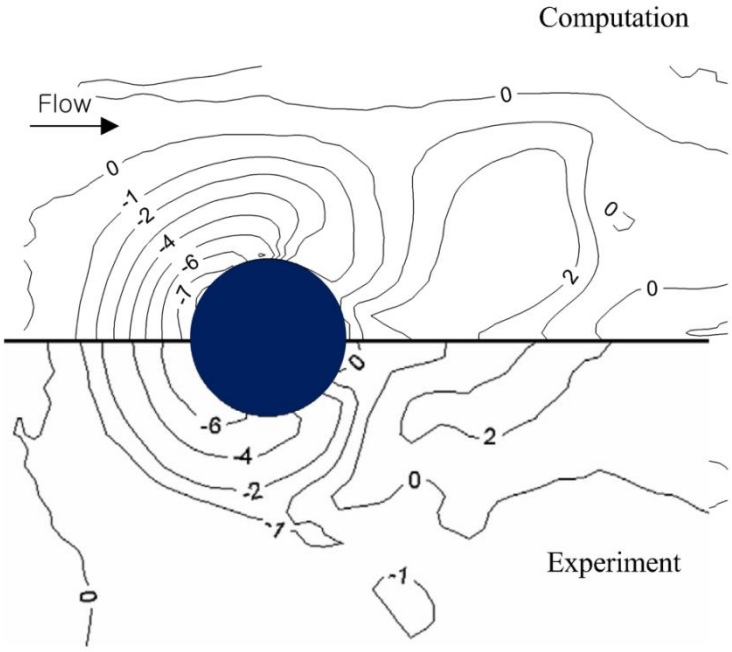


Fig. 5.2 Streamwise turbulence intensity profiles at five locations.

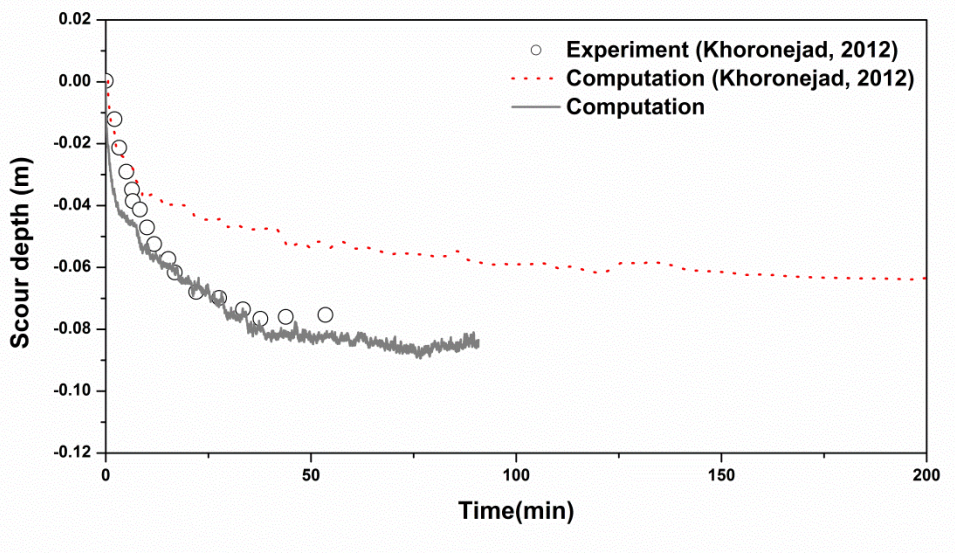
5.5.2 Bed morphodynamics

For scouring depth and process with a cylindrical object, there are several experimental data. Among them, the recent experimental data reported by Khosronejad et al. (2012) is chosen as a validation of the sediment transport and morpholodaynamic models. The

experiment was carried out in a channel of 10 m long, 1.21 m wide and 0.45 m deep. The non-cohesive sediment was used with a mean diameter of 0.85 mm and a circular cylinder diameter of 16.51 cm, D, was placed in the channel. A bulk velocity of 0.25 m/s was used which was corresponding to a water depth of 0.186 m. In the experiment, Reynolds number was 46,000 and Froude number was 0.18. The simulated results are compared with experimental data in terms of bed topography at equilibrium state and time evolution of maximum scour depth. Fig. 5.3a presents simulated bed topography (top) together with experimental data (bottom). In the experiment, the scouring is initiated at an angle of 45° from the plane of symmetry. At the equilibrium state, the area of measured maximum scour is observed near the side of a cylinder with an angle of $\pm 40^{\circ}$ from the plane of symmetry and sediment is deposited downstream of the cylinder (Fig. 5.3a). The scoured pattern near the circular cylinder embedded on the bed is captured well by our computations as shown in Fig. 5.3a. Especially, the maximum scour region and the gradient of scour hole upstream of a cylinder are in a good agreement with experimental data. On the other hand, the measured deposition region is located slightly more downstream from a cylinder than that of numerical simulation. In Fig. 5.3b, the simulated time evolutions of maximum scour depth are compared together with the measured and simulated results by Khosronejad et al. (2012). They used the URANS equations with k-ω turbulence closure and non-equilibrium sediment model. In the experiment in Fig. 5.3b, the scouring depth increases rapidly with time during initial stages and it reaches the equilibrium state after 60 min in which the equilibrium scour depth is about 0.077 m. It can be seen that simulated scour depth also evolve quickly and the scoured bed becomes the equilibrium state at approximately 50 min. As shown in Fig. 5.3b, the simulated bed scouring is slightly faster than measured data until approximately 15 min, after which the bed evolution of scour is in a good agreement with measured data. This is attributed to different initial conditions. In other words, while the simulation of morphodynamics starts after turbulent flow with corresponding Reynolds number are fully-developed over the fixed flat bed, in the experiment, additional time is required to establish fully-developed turbulent flow. Thus, the simulated bed evolution of scour becomes slightly faster at the start. In the simulation, the equilibrium scour depth of 0.084 m is within a range of about 9 % of the measured value. In the URANS simulation conducted by Khosronejad et al. (2012) in Fig. 5.3b, the scour evolution agrees well with



(a) Bed topography (cm) at the equilibrium state; computation (top) and experiment (bottom).



(b) Time evolution of maximum scour depth.

Fig. 5.3 Comparison of bed topography and time evolution of maximum scour depth; (a) Bed topography (cm) at the equilibrium state; computation (top) and experiment (bottom), (b) Time evolution of maximum scour depth.

measured data during the early stages (i.e. until 5 min), after that the growth rate of bed scouring becomes increasingly slower with time. The local scour reaches the equilibrium state beyond about 150 min, which is three times longer than the experiment. The equilibrium scour depth is 0.063 m, which indicates that it is apparently under-predicted about 18% of the measured value. As reported by Khosronejad et al. (2012), this is due to fact that URANS model cannot resolve unsteady horseshoe vortices around upstream of the base of a cylinder and the morphodynamic model does not consider sediment entrainment due to locally increased turbulence. Overall, the present LES results incorporated with sediment transport in a Largrangian framework and morphodynamic models are in a better agreement with experimental data than the URANS results in terms of time evolution of maximum scour depth and maximum value of equilibrium scour. In addition, even though the bed topography of URANS is not presented in this study, the maximum scoured region is observed at the side of a cylinder unlike the experiment and the LES, which implies that the present model is able to reproduce local high bed shear stress at the upstream edge of a cylinder induced by turbulent horseshoe vortex dynamics whereas those are not resolved by the URANS model. From comparisons, it is demonstrated that the present model can not only capture the spatial patterns of local scour and deposition but also predict accurately equilibrium scour depth and the time series of scour development.

5.6 COMPUTATIONAL EXPERIMENTS

For simulating two cylinders with side-by-side and tandem arrangements, the channel length is set to be 10 m (= 62.5*D*) and the channel width is set to be 2.42 m (= 15*D*), which are similar to those of Khosronejad et al. (2012). On the other hand, the channel width is doubled, comparing to that of Khosronejad et al. (2012) because the side wall effects need to be minimized for simulating two cylinders (Fig. 5.4). We use the water discharge of 0.1 m^3/s corresponding to a water depth of 0.15 m. It leads to a Reynolds number of 41,500 and Froude number of 0.23. The diameter of circular cylinder, *D*, is 0.16 m and the non-cohesive sediment is used with a mean diameter of 0.85 mm. For simulation of the side-by-side arrangement, two circular cylinders are located at a distance of 4 m (= 25*D*) from the inlet boundary and five cases are considered with s / D = 1.25, 1.875, 2.5, 3.75 and 5.0 for which the distances between cylinders are 0.2, 0.3, 0.4, 0.6 and 0.8m,

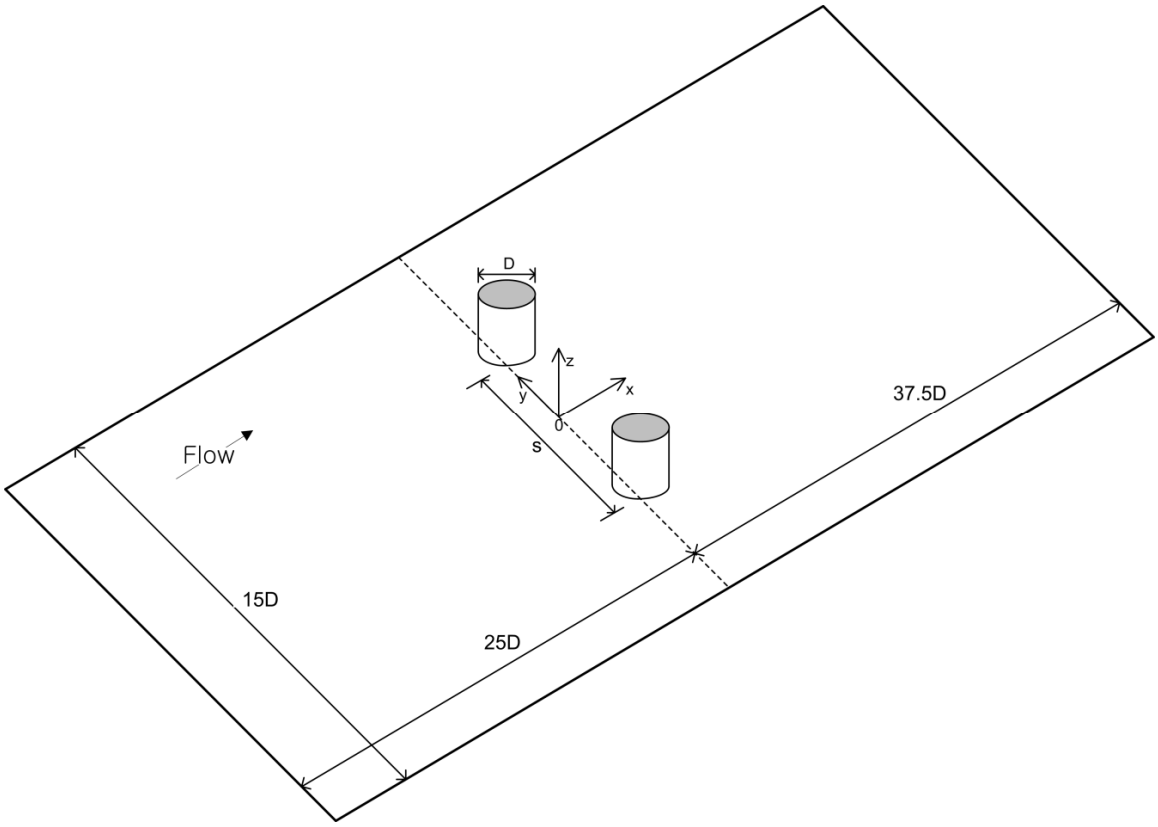


Fig. 5.4 Computational domain for the side-by-side arrangement of cylinders.

respectively as shown Fig. 5.4 where s is spacing between centers of two cylinders. For simulations of cylinders in tandem arrangements, two cylinders are placed along the center plane intersection with s / D = 1.25, 2.5, 3.75 and 5.0 corresponding to 0.2, 0.4, 0.6 and 0.8 m of distances between cylinders, respectively. In addition, to compare the scour depth and pattern of a single cylinder, the scour around a single cylinder, which is placed at a distance of 4 m (= 25D) from the inlet boundary, is simulated. The base grids of 256 × 64 × 16 are used with three levels of local refinement and the finest grids are located near the bed, side walls and cylinders. For instance, local grid refinement near the cylinders is shown in Fig. 5.5. A no-slip condition is imposed at solid walls and the free surface is set as a plane of symmetry which means that there is no friction in horizontal directions. The computations use an adjustable time step in which the maximum CFL number is set to 0.35. The flow field past cylinders is only simulated over fixed flatbed for approximately 250 sec to establish fully-developed turbulent flows and then the sediment transport and morphodynamic models are turned on. This process is continued until the maximum scour depths reach equilibrium states.

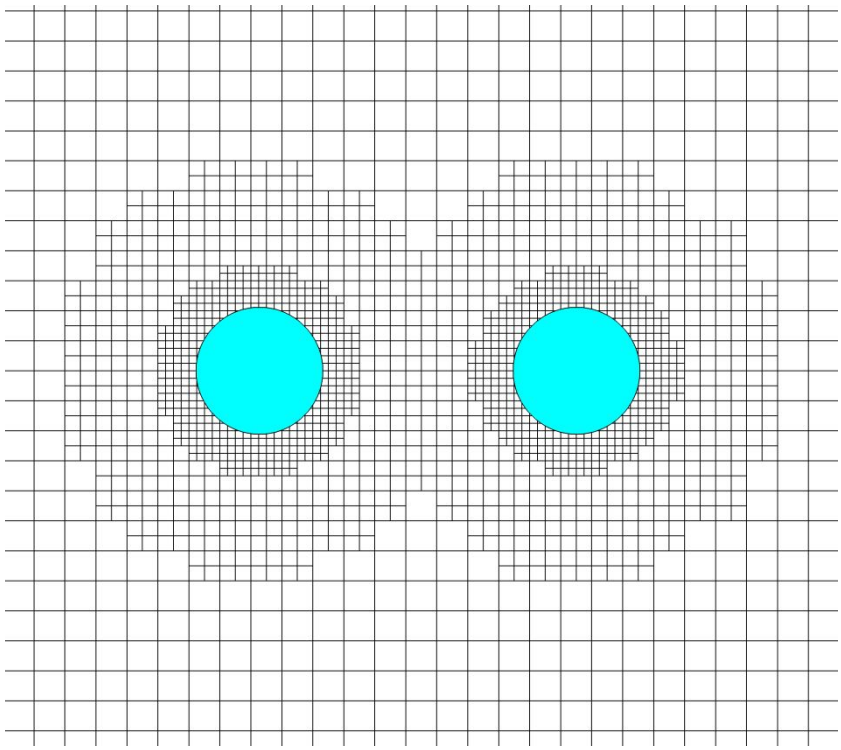


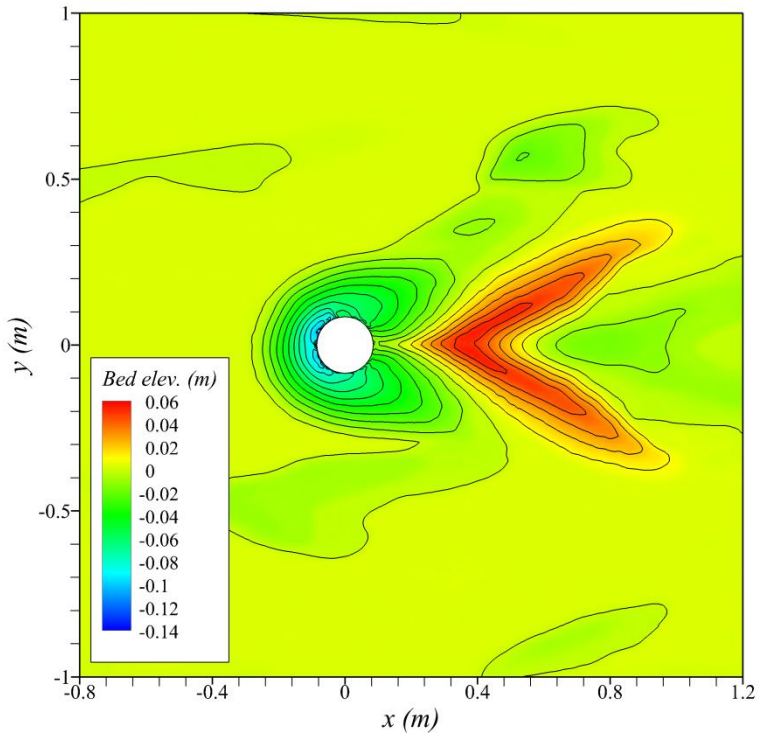
Fig. 5.5 Computational grid near the cylinders in a horizontal plane.

5.7 RESULTS

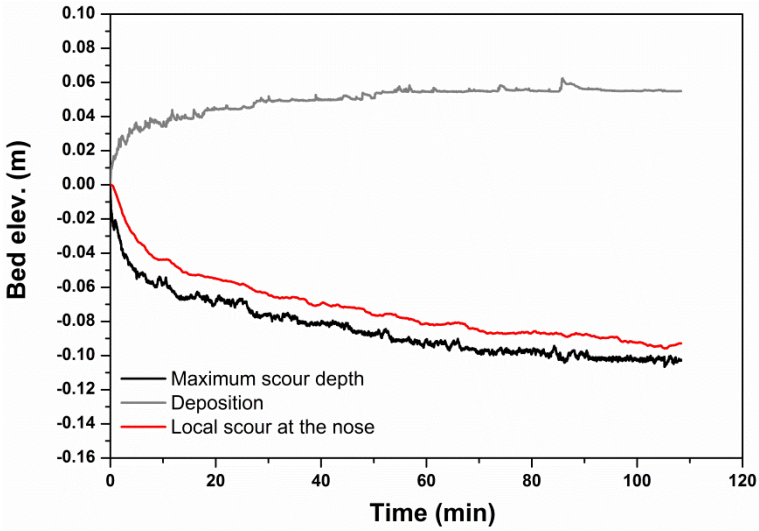
5.7.1 Local scour around a single cylinder

Comparison of local scour and deposition between a single cylinder and two cylinders with side-by-side and tandem arrangements is essential because if the cylinders are placed at nearby locations, it results in different morphological changes around cylinders. Thus, the local scouring process around a single cylinder is simulated.

Fig. 5.6a shows the bed topography around the cylinder at the equilibrium state. In the simulation, the maximum scour depth takes place at an angle of approximately 40° from the plane of symmetry as observed in the experimental result of Khosronejad et al. (2012). The scoured area is expanded into surrounding and upstream of the cylinder. The scoured sediment is accumulated behind the cylinder. Fig. 5.6b presents the time evolutions of scour depth and deposition. The maximum scour depth grows rapidly at an initial stage,



(a) Bed topography at the equilibrium state



(b) Time evolution of scour depth and deposition

Fig. 5.6 Bed topography and time evolution of scour depth and deposition for a single cylinder; (a) Bed topography at the equilibrium state, (b) Time evolution of scour depth and deposition.

after which it slows down and reaches an equilibrium state beyond about 95 min in which

the value of maximum scour depth is estimated to be 0.1 m. The local scour at the nose of the cylinder shows a similar trend of maximum scour depth and the scour depth immediately in front of a cylinder is predicted to be 0.094 m, which is 94 % of maximum value. This is consistent with experimental trend reported by Khosronejad et al. (2012), which confirms that the LES incorporated with physics-based morphodynamic model predicts accurately the maximum scour depth and the local scouring at the nose of a cylinder which is the region of high instantaneous bed shear stress due to unsteady horseshoe vortices.

5.7.2 Side-by-side arrangement of cylinders

In this section, we show the simulated results of local scouring around side-by-side circular cylinders with various distances between cylinders, which are varied from s / D = 1.25 to 5.0. Fig. 5.7 presents the three-dimensional process of scour development around the side-by-side arrangement of cylinders of s / D = 1.25 (t = 1, 5, 30, 60 and 108 min), which provide easy understanding of scouring process with time. It can be seen in Fig. 5.7a that the local scour is observed at the sides of cylinders because of acceleration of flow during the first 1min, which is similar trend of the single cylinder. After 5min, the scouring at the sides of cylinders persists and the local scouring in front of cylinders emerges due to turbulent horseshoe vortices which are responsible for local scour. At 30 min, the scoured region is extended around the cylinders and the sediment deposition is observed downstream of cylinders. It can be seen at 60 min (Fig. 5.7d) that the scour holes around two cylinders are clearly overlapped and thus the scour depth increases smoothly due to elevated turbulence dynamics and compressed horseshoe vortices (Ataie-Ashtiani and Beheshti, 2006; Raudkivi, 1990). The deposition downstream and between cylinders appears due to the jet-like flow. In fact, as the s / D is significantly small or 1.0, the effect of acceleration of flow between two cylinders is negligible. For s / D = 1.25, however, the jet-like flow becomes effective, which implies that the flow and turbulence are highly influenced by lateral cylinders. At 108min (i.e. the equilibrium state), the scour hole can be seen clearly surrounding cylinders and the shape of scour hole becomes semi-circular where the scoured region is similar to that of single scour with about twice the diameter of the cylinder. The deposition height downstream of cylinders increases and it moves toward further downstream. It is found that the distinct deposition induced by the jet-like flow

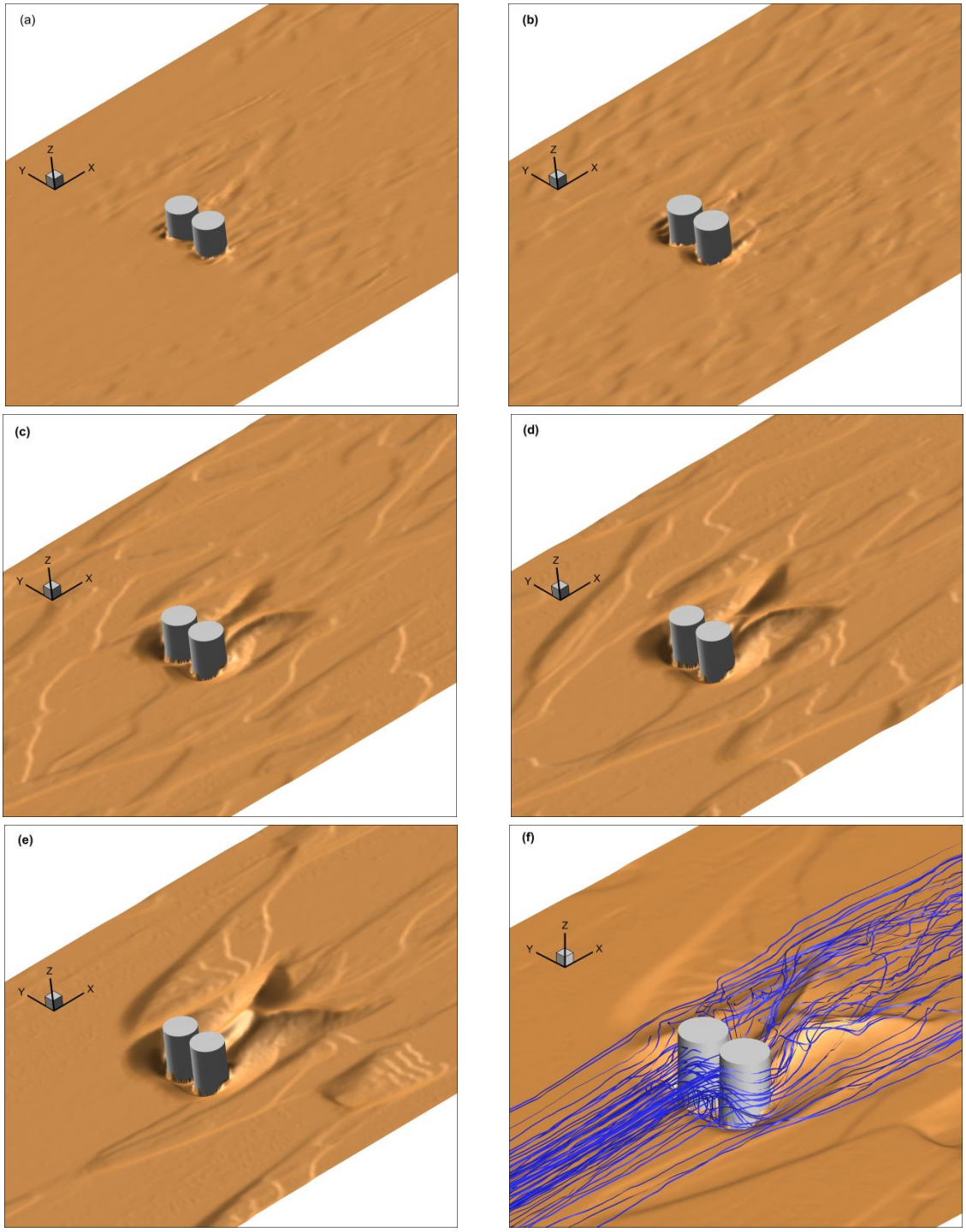


Fig. 5.7 Three-dimensional process of scour development around the side-by-side arrangement of cylinders of s / D = 1.25; (a) 1 min, (b) 5min, (c) 30 min, (d) 60 min, (e) 108 min, (f) streamlines around two cylinders at the equilibrium state.

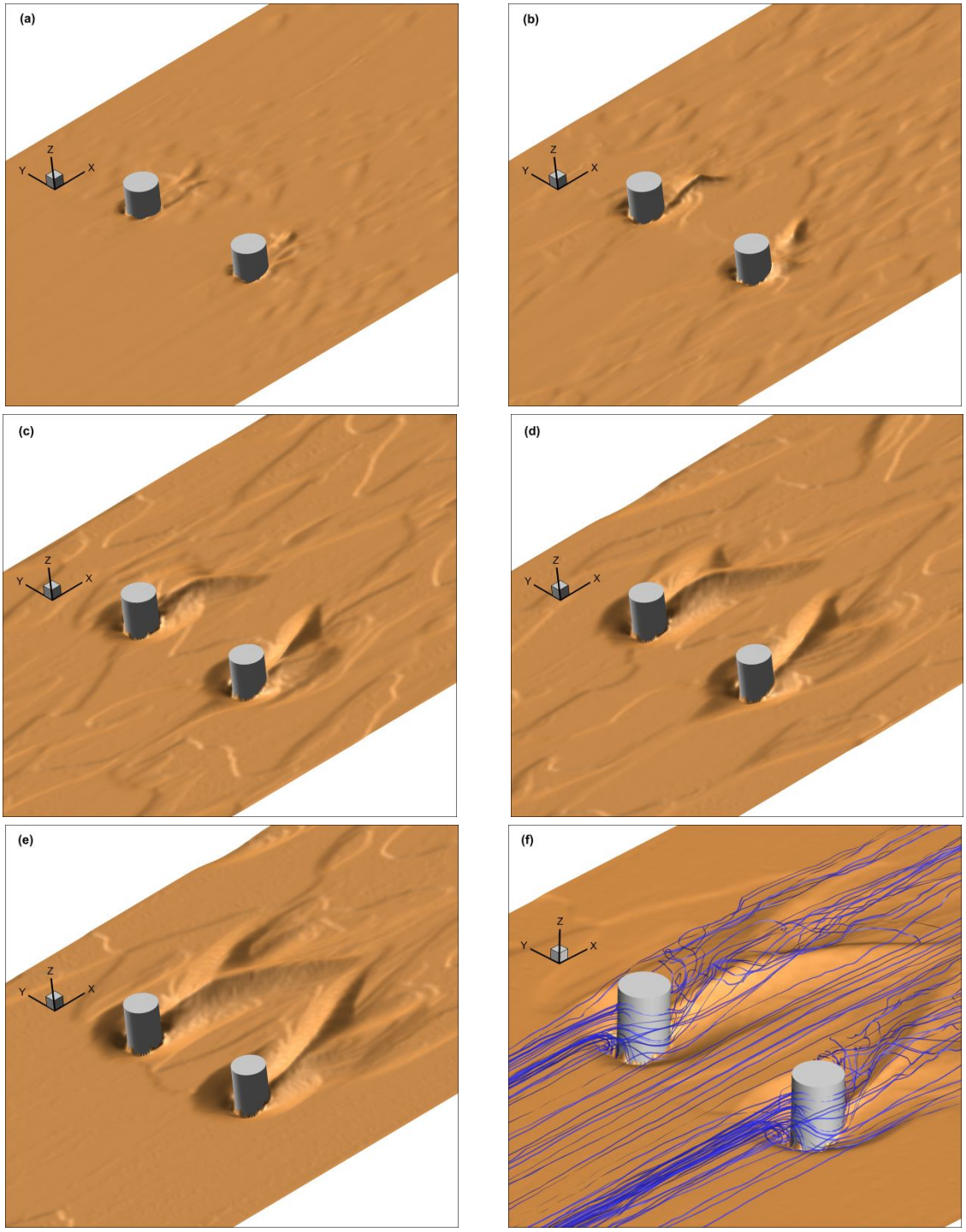


Fig. 5.8 Three-dimensional process of scour development around the side-by-side arrangement of cylinders of s / D = 5.0; (a) 1 min, (b) 5min, (c) 30 min, (d) 60 min, (e) 108 min, (f) streamlines around two cylinders at the equilibrium state.

appears since the acceleration of flow between two cylinders pushes sediment into downstream region and local erosion is reflected by the high turbulence due to flow interference from lateral cylinders. It indicates that at initial stages, the small deposition caused by the jet-like flow appears whereas a considerable increase in sediment load is obviously observed at later stages (after 60 min). This is attributed to significant increase of turbulence stress between cylinders with development of scour hole which is related to high interaction of turbulent horseshoe vortex dynamics. Fig. 5.7f shows streamlines around two cylinders at the equilibrium state. It can be seen that there is downflow in front of cylinders and thus horseshoe vortices are formed in the scour hole which cause suspension of sediment from the scour hole. The suspended sediment is deposited downstream of cylinders or it is washed away further downstream. The significantly irregular flows occur behind the cylinders due to the interference of large-scale coherent structures in the wake region.

Fig. 5.8 shows the three-dimensional process of scour development around the side-by-side arrangement of $s / D = 5.0$ (t = 1, 5, 30, 60 and 108 min). Similarly, the local scouring starts at the sides of both cylinders which occur at an angle of about 40° from the plane of symmetry at 1 min. After 5 and 30 min, local scoring is developed not only at sides of cylinders but also at upstream of cylinders due to well-known horseshoe-vortices system. This process is attributed to fact that the locally enhanced flow at the sides merges with turbulent horseshoe vortices in front of cylinders with bed evolution of local scouring. At later stages (i.e. 60 and 108 min), the local scour around two cylinders evolves steadily with time because of intense contribution of the high turbulent horseshoe vortex system in the sour hole, continuously. The sediment deposition downstream of cylinders is developed and moves further downstream with vortex shedding. The scour development of $s / D = 5.0$ is similar to that of local scour of a single cylinder which implies that the flow interference from cylinders is significantly weakened with an increase in a distance of cylinders in comparison with that of $s / D = 1.25$. Thus, unlike local erosion and deposition induced by the jet-like flow between two cylinders for $s / D = 1.25$ as shown in Fig. 5.7, there are no local scouring and deposition between them for $s / D = 5.0$. Fig 5.8f shows the streamlines around two cylinders at the equilibrium state. It can be seen that the downflow in front of cylinders and the horseshoe vortices upstream of them take place with undisturbed flow

and the wake vortices are independent. As shown in Fig. 5.8f, the streamlines between cylinders are almost straight, which confirms that the jet-like flow has negligible effects for local mophodynamics when s / D becomes 5.0. This is consistent with results of Elliott and Baker (1985) who suggested that as s / D is larger than 7.0, the flow interference triggered by lateral cylinders is negligible.

Fig. 5.9 shows the contour of bed elevations at the equilibrium state for the side-by-side arrangement with various distances between cylinders. It can be seen that the simulated bed elevation patterns are significantly influenced by cylinder spacing, s / D. For s / D = 1.25 in Fig. 5.9a, the scour hole is similar to that of single cylinder but the radius of it seems to be double. The deepening scour region is overlapped between cylinders and a deposition mound is observed downstream of two cylinders. For s / D = 1.875 (Fig. 5.9b), the scour development of two cylinders merges and the shape of scour hole still remain similar to that of single scour hole. For s / D = 2.5, even though the scour holes become overlapped, the scour holes of two cylinders begin to be separated as it can be seen via the contours in the upstream of cylinders in Fig. 5.9c. As the distance of two cylinders increases, the scour depth observed between cylinders decreases because the jet-like flow between cylinders, which leads to acceleration of flow and elevated turbulence, is weakened (Fig. 5.9d). From comparisons between s / D = 1.25, 1.875 and 2.5, which have morphodynamic interactions, on the other hand, different deposited mound patterns are found. As described above, the single depositional mound is captured downstream of cylinders whereas the fraction of sediment accumulated through two cylinders moves further downstream as the cylinder spacing increases. The bed elevation patterns of cases for which scour holes are overlapped are mostly symmetric along the section of symmetry (i.e. y = 0). The local scour depth between cylinders increases with decreases in distances of two cylinders, so that the bed scouring becomes deeper and approximately 0.043, 0.067 and 0.1 m for s / D = 2.5, 1.875 and 1.25, respectively. For s / D = 1.25, in particular, high interactions of turbulent horseshoe vortices and acceleration of flow occur near the junction between cylinders. It is found that as the cylinder spacing, s / D, is larger than 2.5, the local scour holes are separately developed at each cylinder and the depositional mounds are also observed behind individual cylinders. For s / D = 3.75, even though the scour holes and depositions seem to be completely separated, the scouring and deposition

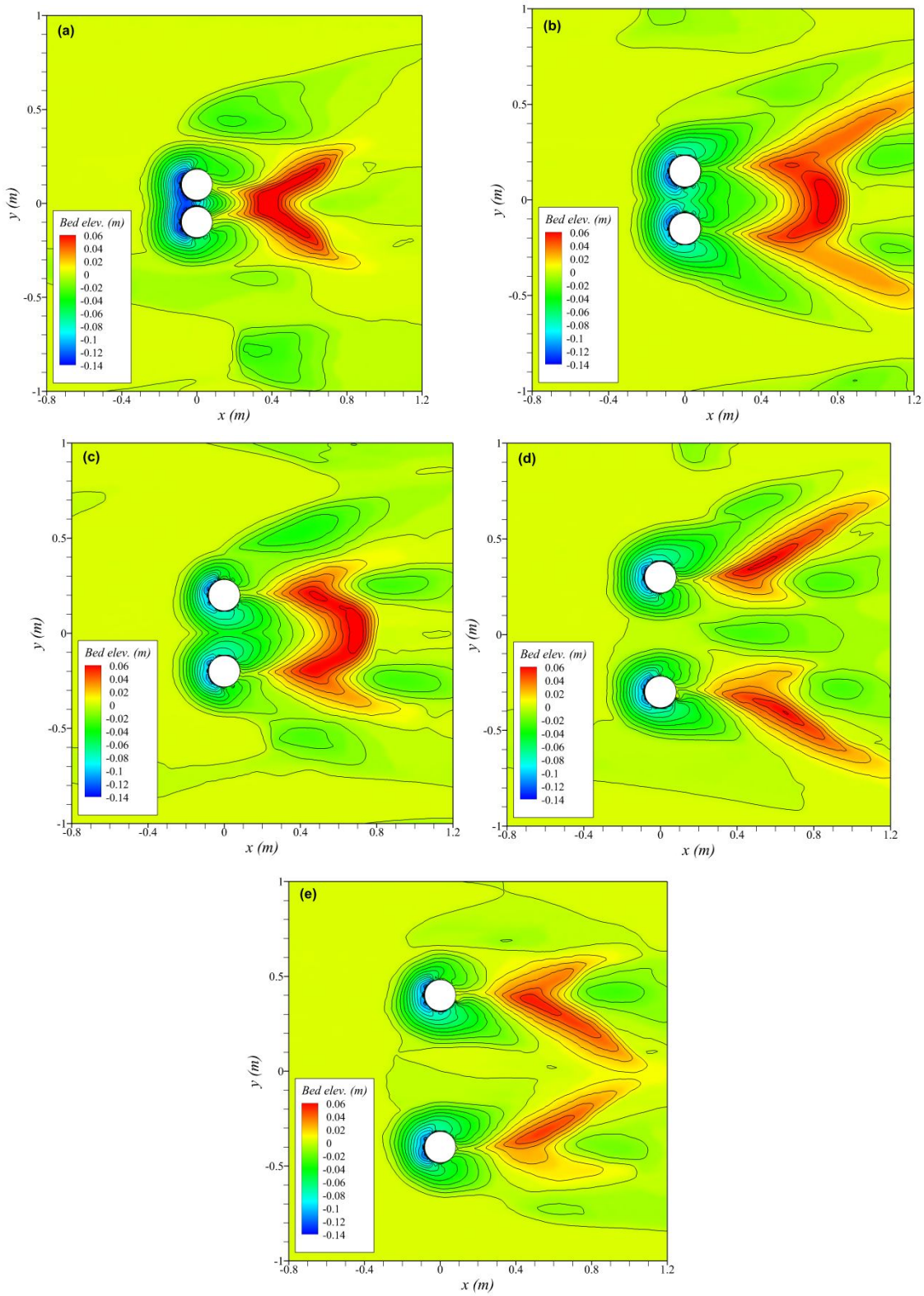


Fig. 5.9 Contour of bed elevations at the equilibrium state for the side-by-side arrangement; (a) s / D = 1.25, (b) s / D =1.875, (c) s / D = 2.5, (d) s / D = 3.75, (e) s / D = 5.0.

remain influenced by interactions of two cylinders. It can be seen that sediment accumulated near the inner parts between and downstream cylinders decreases which implies that there are still effects of enhanced flow and turbulence, and thus the sediment in that region is washed away. For s / D = 5.0, the local scour and deposition are mostly identical to those of a single cylinder.

Fig. 5.10 exhibits time evolutions of bed elevation for maximum scour depth over the domain together with local scouring at two locations, P1 and P2 (upstream of cylinder with distance of 0.09 m from the each center of cylinders) where the horseshoe vortices are highly generated in front of cylinders. For s / D = 1.25, the bed scouring increases sharply at the initial stages (until about 13 min) after which the bed evolution of scour becomes slower with time. The maximum scouring is highly oscillated during later stages and the maximum scour is estimated to be 0.136 m. The time evolutions of local scouring at two locations of P1 and P2 are mostly akin and the both local scours are predicted to be 0.117 m which is 86 % of maximum scour. For the other cases (i.e. s / D = 1.875, 2.5, 3.75 and 5.0), the similar trends of time evolutions for the maximum scouring and the local scour at two locations are shown in Fig. 5.10. In simulated results, the growth rate of local scouring of both locations is almost identical regardless of cylinder spacing, which is coincident with those of symmetric morphological patterns along the section of y = 0 as shown in Fig. 5.9. The scour depths at the nose of cylinders are estimated to be 0.105, 0.097, 0.098 and 0.102 m for s / D = 1.875, 2.5, 3.75 and 5.0, respectively, which is corresponding to 87, 85, 89 and 89 % of the maximum scour depth, respectively. It is found that the bed scouring at either side of cylinders is relatively deeper than that at the nose of cylinders, as compared to the result of a single cylinder. In other words, the computed scour in front of the cylinder is averagely 88 % of maximum scour depth unlike the local scour at the nose of the single cylinder in which it is 94 % of maximum scour depth, as mentioned in section 7.1. This is probably due to fact that flow interference between cylinders makes local acceleration of flow and this acceleration as well as horseshoe vortices at the sides of cylinders on the deformed bed is stronger. It can be seen that the evolutions of deposition height are developed at much earlier time (i.e. within about 5min) than local scouring, after which these are slow down as seen in Fig. 5.10. The similar trend is shown in all computed results.

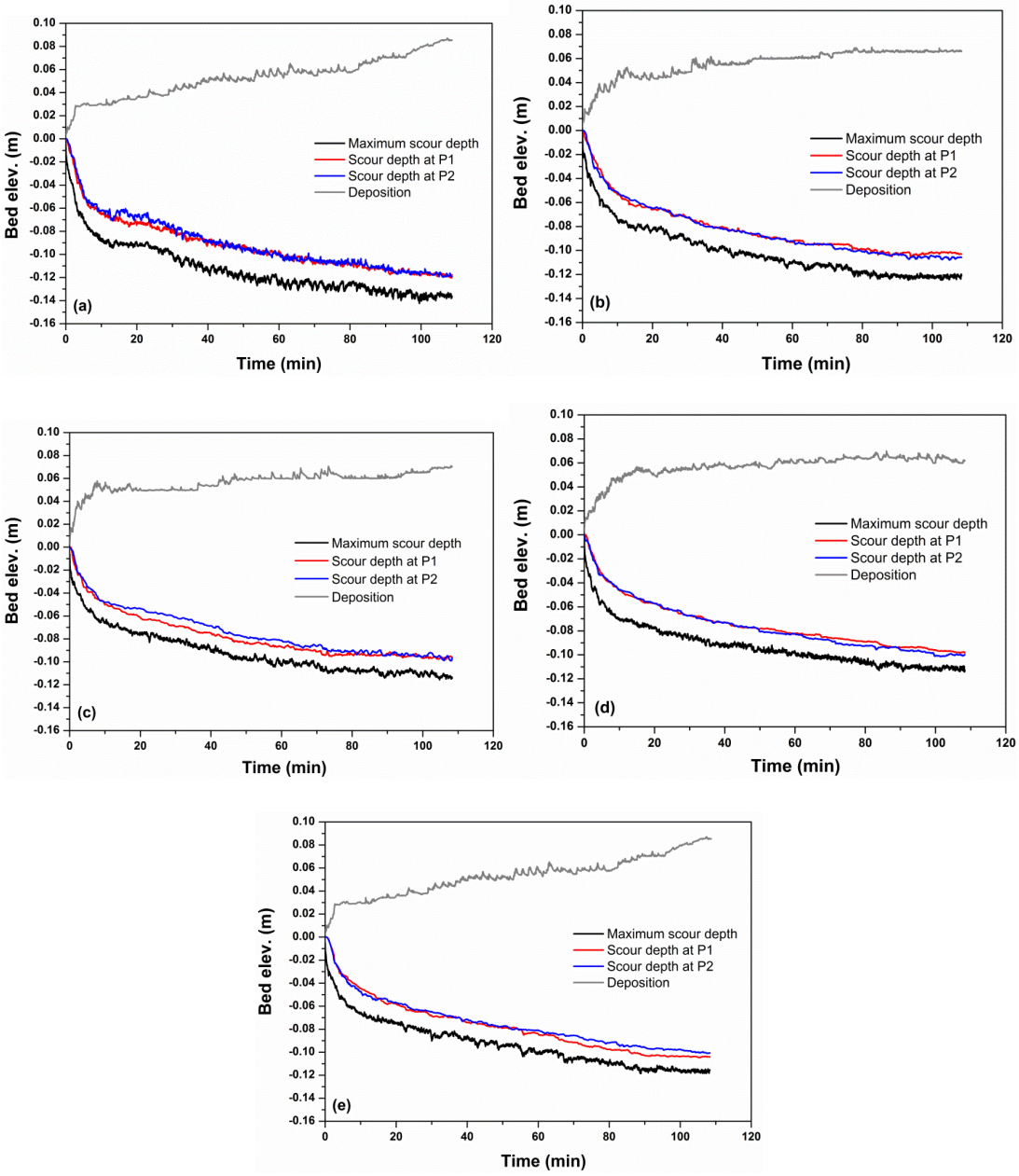


Fig. 5.10 Time evolutions of scour depth and deposition; (a) s / D = 1.25, (b) s / D =1.875, (c) s / D = 2.5, (d) s / D = 3.75, (e) s / D = 5.0

5.7.3 Tandem arrangement of cylinders

If the circular cylinders are arranged in tandem, the flow and turbulence behind the front cylinder impinge on downstream cylinder. The flow interference significantly alters the flow structure and turbulence (Carmo and Meneghini, 2006; Wu et al., 1994), so that it influences morphodynamics around cylinders. In this section, the local scouring and

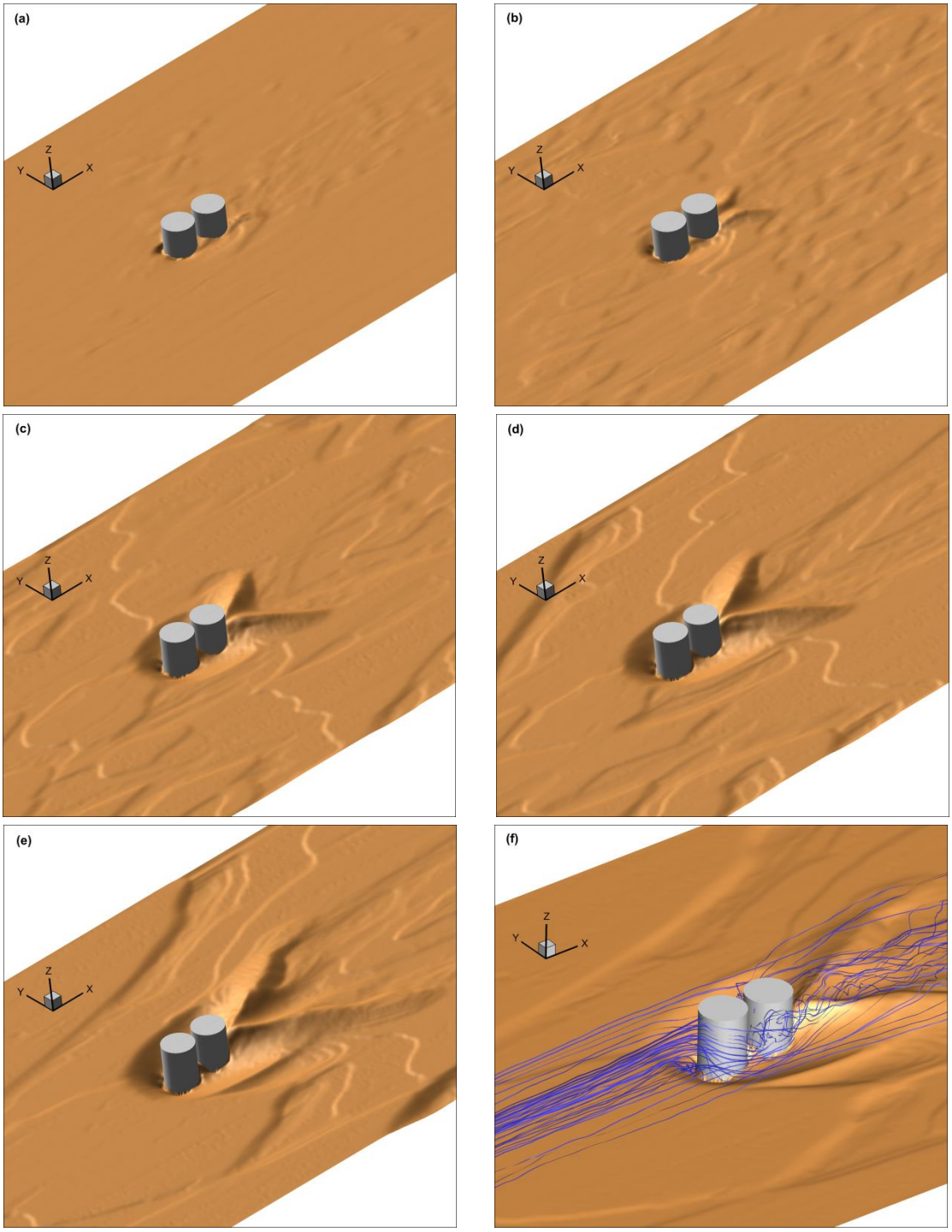


Fig. 5.11 Three-dimensional process of scour development around the tandem arrangement of cylinders of $s / D = 1.25$; (a) 1 min, (b) 5min, (c) 30 min, (d) 60 min, (e) 108 min, (f) streamlines around two cylinders at the equilibrium state.

deposition phenomena are investigated in tandem arrangement of two cylinders with various center-to-center spacing of cylinders, s / D = 1.25, 2.5, 3.75 and 5.0. Fig. 5.11 shows the three-dimensional process of scour development around tandem arrangement of two cylinders for s / D = 1.25 (t = 1, 5, 30, 60 and 108 min). At the first minute in Fig. 5.11a, the local scouring at sides of a front cylinder takes place as observed for the side-by-side arrangement whereas the relatively low scouring occurs near a rear cylinder. After 5 min, the erosion at both sides of the front cylinder merges not only with local scouring at the nose of the cylinder but also into local erosion between two cylinders. The sediment deposition begins behind a rear cylinder. It can be seen at 30 min in Fig. 5.11c that the scour is clearly developed near the front cylinder and the erosion is observed at sides of the rear cylinder. The deposition is only located downstream of the rear cylinder which implies that the vortices shed from the front cylinder impinge on that region between cylinders. At later stages (after 60 and 108 min), the growth of local scouring increases with time due to reinforcement of the rear cylinder and the scour holes overlap which causes deeper scour depth than that of a single cylinder. Finally, the bed scouring reaches the equilibrium state and a single scour hole can be observed. The deposition downstream of the rear cylinder not only increase with time but also is elongated further downstream. It is notable that the local scouring at the nose of the rear cylinder is significantly reduced as compared to the scour of the front cylinder since the presence of the front cylinder leads to a decrease in approach velocity of the rear cylinder which indicates that the intensity of turbulent horseshoe vortices are lower than that of the front cylinder. Unlike deposition of the side-by-side arrangement in Figs. 5.7 and 9, it is found that considerable accumulation of sediment is observed just downstream of the rear cylinder, which speculates that the fluid momentum from two sides of scour hole near the bed at the rear cylinder is undermined due to upstream cylinder. Also, it is inferred that few sediments between two cylinders are picked up originated by wake vortices which are responsible for sediment entrainment although the bed remains almost flat. Fig. 5.11f presents streamlines around tandem arrangement of two cylinders for s / D = 1.25 at the equilibrium state. It can be seen that the downflow driven by the pressure gradient and the vortex systems are observed in front of the front cylinder as seen in the side-by-side arrangement in Figs. 5.7 and 8 whereas the downflow is almost omitted which also reflects

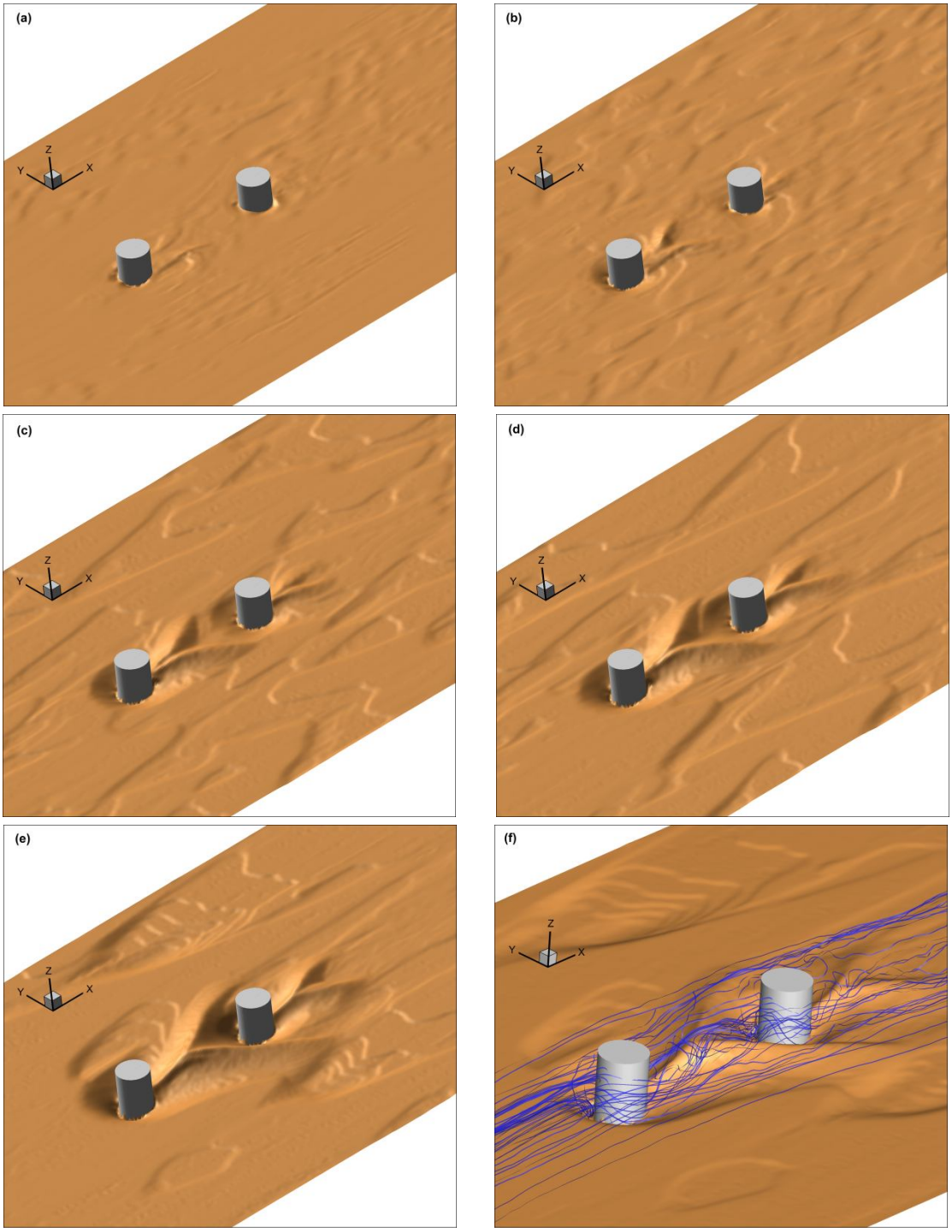


Fig. 5.12 Three-dimensional process of scour development around the tandem arrangement of cylinders of $s / D = 5.0$; (a) 1 min, (b) 5min, (c) 30 min, (d) 60 min, (e) 108 min, (f) streamlines around two cylinders at the equilibrium state.

the deficit of horseshoe vortices at the rear cylinder. The flow passing through the front cylinder convects with interference to the rear cylinder and the shear layers originated from the front cylinder impinge on the rear cylinder, which lead to complex flows between cylinders as shown in Fig. 5.11f.

Fig. 5.12 shows the three-dimensional process of scour development around tandem arrangement of two cylinders for $s / D = 5.0$. At initial stages (1 and 5 min) in Figs. 5.12a and b, the initial development of local scouring around two cylinders is similar to that of a single cylinder. Unlike the development of scour hole for the side-by-side arrangement of $s / D = 5.0$, however, the local scour at the rear cylinder is lower than that of the front cylinder. At 30 min, while the development of scour hole and deposition downstream of a cylinder are pronounced at the front cylinder, both of them are relatively low at the rear one. At later stages (after 60 and 108 min), the scour hole is fully-developed at the front cylinder and the accumulation of sediment increases with time at downstream of the front cylinder. As observed at the initial stages, all morphodynamic changes are reduced at the rear cylinder, where in turn, the growth of local scouring and the deposition decrease significantly in comparison with those of the front cylinder. On the other hand, the development of local scour increases and the accumulation of sediment becomes lower at the rear cylinder as compared to those of $s / D = 1.25$ case which indicates that flow structures and horseshoe vortex system are altered with variation of cylinder spacing. The influence of the front cylinder is reduced with increases in cylinder spacing, so that the local scour hole at the nose of the rear cylinder is formed which implies that the turbulent horseshoe vortices are generated. The streamlines around tandem arrangement of $s / D = 5.0$ are shown in Fig. 5.12f. The flow near the front cylinder is mostly identical to that of the single cylinder or the side-by-side arrangement for $s / D = 5.0$. However, the flow passing through the front cylinder impinges on the downstream of the cylinder. Especially, it is found that the streamlines along the bed at the sides of front cylinder move toward the free surface due to upwelling phenomena and then these flows enter the scour hole at the rear cylinder. This is one of evidences that the local scour depth becomes lower since the sediment particles scoured from the front cylinder are suspended and those are deposited near the rear cylinder.

Fig. 5.13 presents the contour of bed elevations at the equilibrium state for tandem

arrangement with various distances between cylinders (s / D = 1.25, 2.5, 3.75 and 5.0). The simulated bed elevation patterns are not only entirely different from those of the side-by-side arrangement but also are influenced by cylinder spacing, s / D. For s / D = 1.25, the single scour hole is developed around two cylinders in tandem, whereas the scoured region is extended to sides of cylinders and elongated toward downstream along cylinders as compared to that of single cylinder. It can be seen that the local scouring at the front cylinder shows similar features to typical local scour around a circular cylinder, whereas the bed scouring is substantially weakened near the rear cylinder, specially, at the nose of the rear one where the local scour is slightly observed. The sediment is accumulated at downstream of the rear cylinder and the formation of sediment deposition deviates from the plane of symmetry. For s / D = 2.5, the scoured region is more extended to downstream and the accumulation of sediment becomes greater than that of s / D = 1.25. It is found that while local scour at the front cylinder is mostly identical to that of a single cylinder as seen for s / D = 1.25, the sediment deposition is observed in front of the rear cylinder where the horseshoe vortices occur in the vicinity of cylinder. Based on the results of simulated bed contour for s / D = 1.25 and 2.5, this demonstrates that the turbulent horseshoe-vortices system is seriously weakened due to presence of a upstream cylinder, so that the local scouring is sheltered in front of the rear cylinder. For s / D = 1.25, on the other hand, the horseshoe vortices driven by downflow are difficult to be developed at the nose of the rear cylinder (i.e. between cylinder) and thus the erosion in that region is attributed to wake vortices from deformed bed behind the front cylinder which causes high vertical momentum to flow and amplifies turbulent kinetic energy. It is notable that for s / D = 2.5, the deposition occurs upstream of the rear cylinder, even though the cylinder spacing increases. We speculate that the region is coincident with that of sediment deposition induced by the front cylinder, so that weakened horseshoe vortex system due to a decrease in velocity which is responsible for local scouring cannot contribute local erosion at the nose of the rear cylinder. As seen in Fig. 5.13, as the cylinder spacing, s / D is larger than 2.5, the bed scouring and deposition are considerably altered as compared to those of smaller spacing of cylinders. Unlike cases that cylinder spacing, s / D, is 1.25 and 2.5, in particular, the bed scouring and deposition are observed at the rear cylinder, separated from those of the front cylinder. For s / D = 3.75, the bed scouring begins to

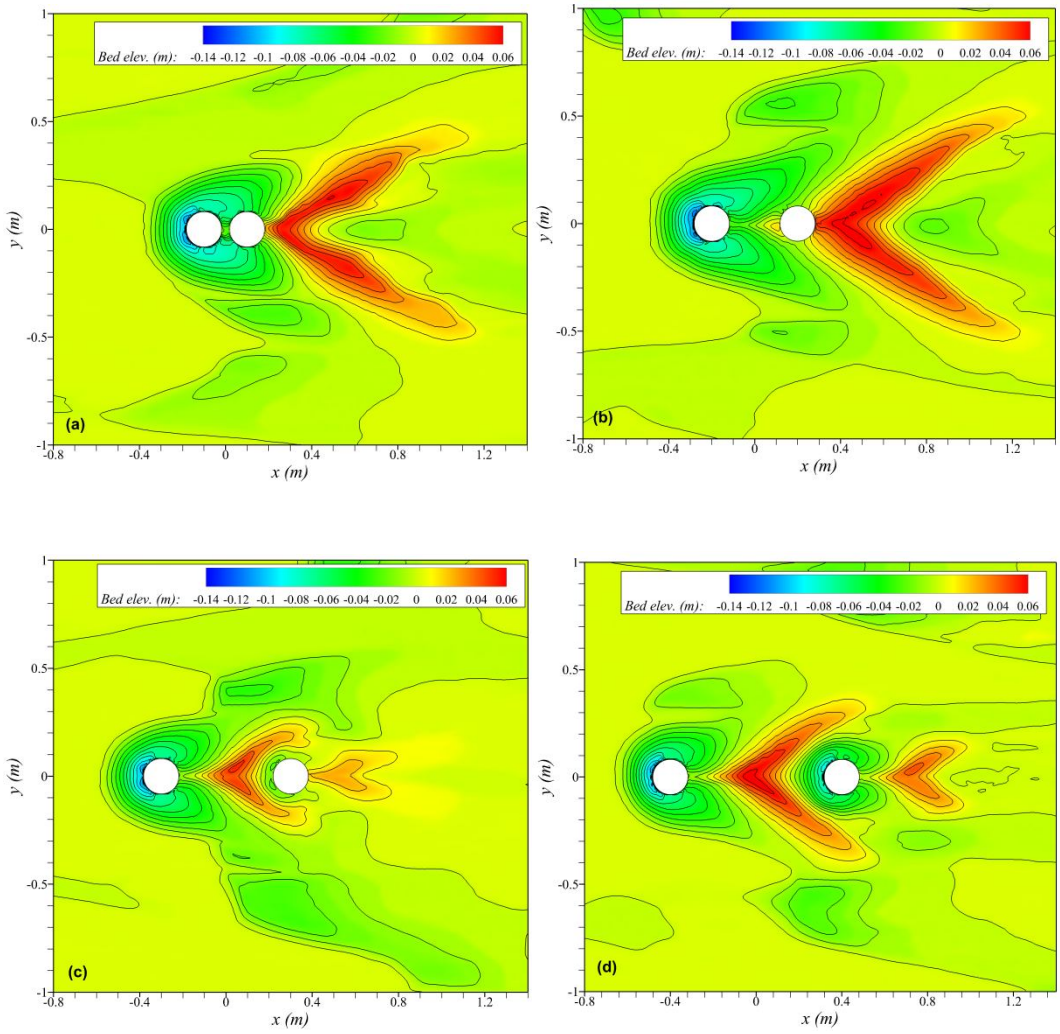


Fig. 5.13 Contour of bed elevations at the equilibrium state for the side-by-side arrangement; (a) $s / D = 1.25$, (b) $s / D = 2.5$, (c) $s / D = 3.75$, (d) $s / D = 5.0$

occur at the nose of the rear cylinder and two depositional mounds are observed behind each cylinder. The case of $s / D = 5.0$ shows similar features of erosion and deposition to case of $s / D = 3.75$. From comparison between $s / D = 3.75$ and 5.0, it is found that the accumulation of sediment behind both cylinders increases with increases in cylinder spacing, s / D and the local scour development at the rear cylinder increases as the cylinder spacing increases. The fact that the local scour takes place and it increases with cylinder spacing supports that the influence on disturbance of flow induced by upstream cylinder

decreases and thus the sheltering effect becomes lower (Raudkivi, 1990). This demonstrates a progressive increase in instantaneous bed shear stress near the rear cylinder caused by the dynamics of horseshoe vortices with increasing cylinder spacing, s / D. On the other hand, the deposited mound behind the front cylinder migrates downstream, so that it influences the growth of scour hole at the rear cylinder.

Fig. 5.14 depicts time series of bed elevation for maximum scour depth over the domain along with local scouring at two locations, P1 (front cylinder) and P2 (rear cylinder) where those are in front of cylinders with distance of about 0.09 m from the center of cylinders. The bed evolutions of maximum scouring increase rapidly during initial stages (i.e. until about 10 min) for all cases. Subsequently, the speeds of local scouring decrease with time and these reach the equilibrium state after about 100 min, which is mostly similar with those of the side-by-side arrangement of cylinders. However, the bed scouring observed at the nose of cylinders shows quite different trends as compared to those of the side-by-side arrangement of cylinders in which the results present almost same values and tendencies of local scour at the two locations as shown in Fig. 5.10. For all cases of the tandem arrangement (s / D = 1.25, 2.5, 3.75 and 5.0), the local scouring at the nose of the front cylinder is estimated to be 0.102, 0.1199, 0.108 and 0.107 m, which is corresponding to 94, 88, 87 and 85 % of maximum scour, respectively. Unlike the local scour due to high erosion induced by turbulent horseshoe vortices at the front cylinder, P1, the erosion is significantly reduced or the deposition is observed in front of the rear cylinder, P2, as seen in Figs. 5.11 and 13. Consequently, relatively little scouring occurs at the nose of the rear one. For s / D = 1.25, the bed evolution remains mostly stationary until approximately 39 min, after which it slowly decreases until the end of simulation. The final value of local scour is estimated to be 0.023 m. For s / D = 2.5, the bed elevation becomes constant until about 5 min and then it slightly increases with time which means that the sediment is deposited in front of the rear cylinder as seen in Fig. 5.13b. For s / D = 3.75, the rate of scouring grows slowly until about 60 min, corresponding to scour depth of 0.026 m. After 60 min, the scour depth slightly decreases with time and the final value is estimated to be 0.02 m. For s / D = 5.0, the bed scouring evolves continuously since the start of calculation of morphodynamic. The scour depth is estimated to be 0.076 m which is corresponding to 71 % and 84 % of the maximum scour depth and the local scour at the P1, respectively.

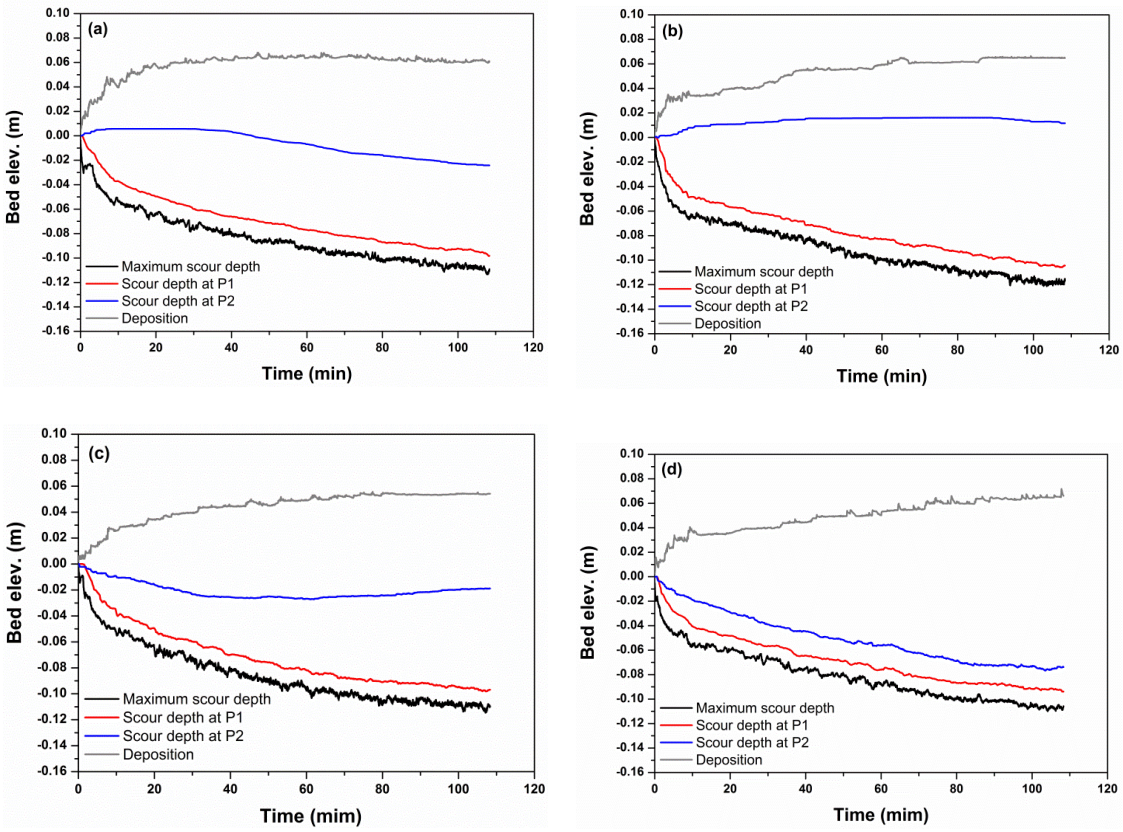
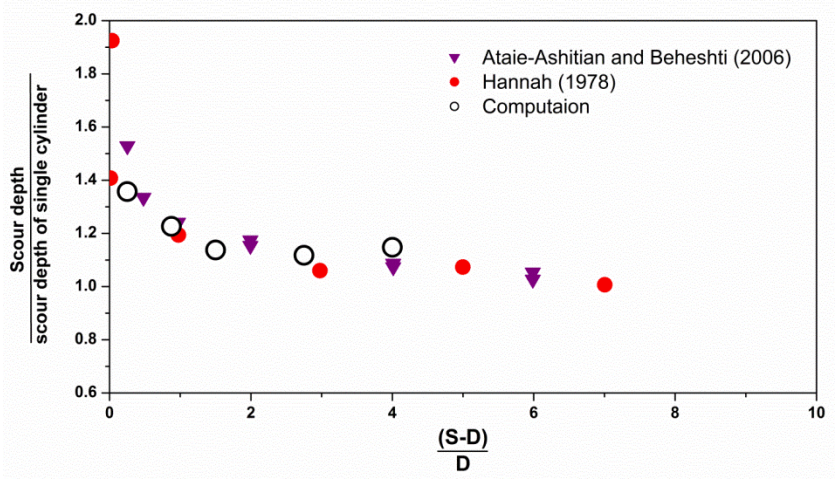


Fig. 5.14 Time evolutions of scour depth and deposition; (a) $s / D = 1.25$, (b) $s / D = 2.5$, (c) $s / D = 3.75$, (d) $s / D = 5.0$

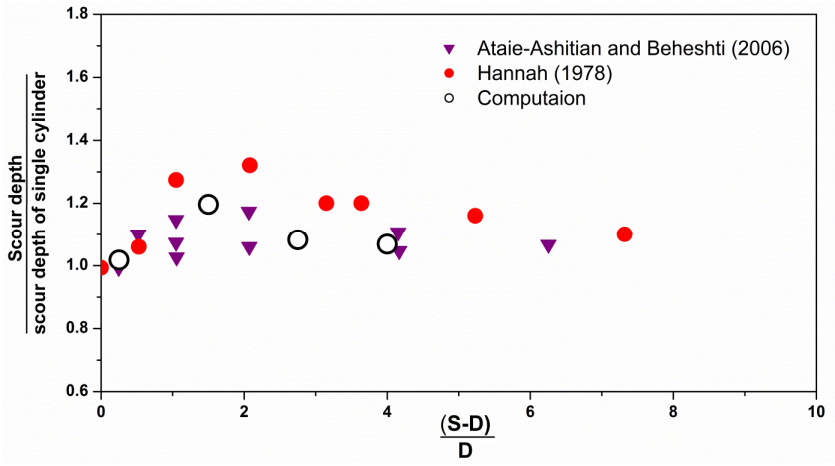
It is found that when $s / D \leq 2.5$, the local erosion caused by turbulent horseshoe vortices at the nose of the rear cylinder is considerably weakened and have negligible effects. On the other hand, as $s / D > 2.5$, the bed scouring at the nose of the rear one increases with an increase in cylinder spacing which implies that the influence of a upstream cylinder on approach velocity disappears and thus the effect of horseshoe vortex begins to dominate. It can be seen that the maximum heights of sediment deposition for s / D =1.25, 2.5 and 5.0 show similar trends and values, whereas for $s / D = 3.75$, the growth rate of deposition becomes slower and lower. It is worthy of notice that the sediment accumulated behind the front cylinder migrates toward downstream due to periodic vortex shedding, so that the sediment is deposited on the deformed bed in front of the rear cylinder, which induces a decrease in the deposition behind the front cylinder and influences the bed scouring at the nose of the rear one.

5.7.4 Comparison of maximum scour depth

As seen in the previous sections, the bed scouring is significantly influenced by cylinder spacing longitudinally and transversely. In this section, we exhibit computed maximum scour depth as a function of the distance of cylinders, $G = (s - D) / D$, together with measured values of Hannah (1978) and Ataie and Beheshti (2006).



(a) Side-by-side arrangement case.



(b) Tandem arrangement case.

Fig. 5.15 Maximum scour depth as a function of the distance of cylinders, G; (a) side-by-side arrangement, (b) tandem arrangement

The maximum scour depth normalized by the scour depth of a single cylinder is shown for cases of the side-by-side arrangement of cylinders in Fig. 5.15a. The scour depth

decreases with the distance of cylinders, G, and is identical to that of single cylinder at G = 7. In the measured data, when the two cylinders are touched, the scour depth becomes approximately 1.93 times of a single cylinder. It can be seen that when $G < 1.0$, the scour depth increases rapidly with reduction of the distance of cylinder, G, whereas as $G \geq 1.0$, the scour depth decreases gradually with G. The computed scour depth shows a good agreement with measured values. Fig. 5.15b shows the maximum scour depth versus the distance of cylinders, G for the tandem arrangement of cylinders. Unlike the side-by-side arrangement, when the two cylinders are touched, the scour depth is identical to that of single cylinder. The scour depth increases with the distance of cylinder, G, and it has maximum value at $G \approx 2.0$, after which it decreases with an increase in G. This is due to reinforcement effect of downstream of cylinders (Ataie and Beheshti, 2006; Raudkivi, 1990). In other words, the scour holes are overlapped due to downstream cylinder, which is possible to pick up much more from the scour hole, and consequently, the scour becomes deeper. The computed results match the measured trends quite well and especially, the computed scour depths are in a reasonable agreement with measured value of Ataie and Beheshti (2006).

In section 5.2, URANS model showed under-prediction of local scour depth and time evolution of scour since the fluctuating component of horseshoe vortex system and instantaneous high stress are not accounted for (Khosronejad et al., 2012; Roulund et al., 2005; Zhao et al., 2010). Also, a lot of the dimensionless equations and empirical equations are over-predicted for the maximum scour depth due to a deficiency of the turbulent flow structure (Ataie and Beheshti, 2006; Melville, 2000). The obvious agreement with measured data demonstrates that the LES incorporated with physically based sediment transport and morphodynamic models can estimate accurately local scour depth around cylinders, which implies that the model captures instantaneous turbulent stress and horseshoe vortex dynamics, which are main roles of erosion around cylinders.

5.8 SUMMARY

Numerical simulations are conducted to investigate local scour around cylinders with the side-by-side and tandem arrangements. For simulating flow, large eddy simulations (LES) are applied with Smagorinsky sub-grid model and the model is combined with a ghost-cell immersed boundary method to treat the solid boundaries. The grids are locally refined and

the equations are solved on multi-level grids. Detailed simulation of bed scouring is realized by incorporating sophisticated sediment and morphodynamic models in which the sediment is considered as spherical particles in the flow and solved in a Lagrangian framework. Thorough comparison for scour of a single cylinder with experimental data, the model shows reasonable agreement of scour patterns and evolution of local scouring. For the cylinders, scour patterns and depths are significantly influenced by cylinder spacing. For the side-by-side arrangement of cylinders, the bed scouring at the nose of both cylinders is mostly identical and the bed morphological changes are almost symmetric along the center plane intersection in a streamwise direction. For the tandem arrangement, the upstream cylinder affects the local scouring at the rear cylinder, so that the deposition and scour patterns around cylinders are considerably altered. While the bed evolution of scour at the nose of front cylinder is undisturbed, the scour at the rear cylinder is affected by the front one, which leads to significant reduction of scour near the rear one. Maximum scour depth for the side-by-side cases exhibits a growing trend with decreases in distances of cylinders whereas for tandem cases, it increases with distances of cylinders and it decreases gradually beyond the peak point. The computed maximum scour depths and trends show good agreement with measurement data of previously published literatures.

CHAPTER 6 THREE-DIMENSIONAL NUMERICAL COMPUTATIONS OF LOCAL AND GLOBAL SCOUR AROUND CYLINDER GROUPS

6.1 INTRODUCTION

The circular pile groups have been widely used in river and marine engineering which are more practical and economical than spread footing. Flows around circular pile groups are not only significantly different from those observed near a circular single pile but also are much complicated. Such complex flows around pile groups lead to interference of flow around individual piles, which amplifies turbulence levels. Also, turbulent flows are dominated by energetic coherent vortical structures (Khosronejad et al., 2012). The vortical structures as well as interference of flow around circular pile groups interact with sediment on the bed, and those induce local erosion around them. Extensive local scour can potentially put pile groups in danger and have a high possibility to their failure, which indicates that scour around pile groups is associated with stability of them.

The change in flow patterns induced by interference of flow around circular cylinders is well documented in many previous studies. Sumner et al. (2000) investigated flow patterns around two cylinders arranged in staggered configurations on rigid flat bed using flow visualization and particle image velocimetry (PIV). The processes of shear reattachment, vortex pairing and vortex impingement were observed and vortex shedding frequencies were highly related to individual shear layers. Akilli et al. (2004) conducted experiments on flow around two and three cylinders with a side-by-side arrangement in shallow water by means of the PIV. They reported that the flow structure becomes asymmetrical at the small spacing between cylinders due to jet-like flow, whereas a symmetric flow structure is observed at relatively large cylinder spacing. Takemura and Tanaka (2007) investigated flow characteristics around a circular emergent patch, consisting of several circular cylinders mounted on a rigid flat bed. When the cylinder spacing was small, a large scale vortex sheet with patch-scale was generated behind the patch, but vortex sheets with

cylinder-scale were observed behind individual cylinders as the cylinder spacing increases. In addition to interference of flow around circular cylinders, the horseshoe vortex with intense unsteadiness was one of the main mechanisms of local scour around cylinders. Dargahi (1989) carried out experiments on flow field around a circular cylinder in a turbulent flow using hydrogen bubble flow visualization and hot film measurements. He reported that complex horseshoe vortex system appears in front of the cylinder with a quasi-periodic manner and the vortex system consists of at least five vortices in turbulent flows. The vortex system was independent of wake vortices and the number of vortices increased with an increase in Reynolds number. Based on the energetic unsteady flow field of Dargahi (1989), Dargahi (1990) conducted laboratory experiments on the scour mechanism coupled with three-dimensional separation in front of the cylinder in a mobile bed. It was found that the main cause of local scour in front of the cylinder is a turbulent horseshoe vortex system and the process is characterized by a periodic transport. The formation of ripples was observed around the cylinder and was migrated downstream region. Unger and Hager (2007) conducted extensive experiments to investigate the flow around a bridge pier embedded on sediment bed using the PIV. The strong downflow and horseshoe vortices were the main agent of scour initiation and development in front of the cylinder. They also reported that the horseshoe vortex develops with time.

While the several experimental works on flows around circular cylinders were investigated, relatively few experimental studies on scour around circular cylinder groups have been made. Most of these studies have focused on the variation of scour depth at cylinder groups with respect to change in cylinder spacing and development of a formula for prediction of maximum scour depth. Firstly, Hannah (1978) examined scour around cylinders with side-by-side and tandem arrangements for different spacing between cylinders. For the side-by-side arrangement, equilibrium scour depth increased with decreasing cylinder spacing, while for the tandem arrangement, the scour depth increased with increasing cylinder spacing until G / D was about 2.0 where G is the gap between cylinders and D is a cylinder diameter, after which it decreased with cylinder spacing. Ataie-Ashtiani and Beheshti (2006) carried out laboratory experiments on local scour with a variety of conditions such as different cylinder arrangements, spacing, flow rate and sediment size under steady clear-water conditions. Similar trends of the maximum scour

depth around cylinder groups were observed in Hannah's results (1978). Sumer and Fredsøe (1998) carried out experimental investigation on scour around group of vertical cylinders with different configurations exposed to waves. They reported that the local scour depth was significantly influenced by cylinder arrangement and the number of cylinders. In addition, if the cylinder spacing was fixed, the scour depth was governed by the Keulegan-Carpenter number associated with the wave periodic and bed shear velocity. Amini et al. (2011) investigated local scour around cylinder groups in shallow water flow with various cylinder spacing and submergence ratio, and they found that scour depth is dependent on cylinder diameter, spacing and submergence ratio. The new method for prediction of the maximum scour depth was proposed and it showed reasonable scour depth predictions. Similar phenomena were observed around patches of vegetation in experiments and fields (Bouma et al. 2007; Follett and Nepf, 2012; Rominger et al., 2010). They described that the scour depth within and around the patch increases as the patch density increases.

In addition to the several experiments, many numerical investigations of local scour around cylinders have been reported in previous literatures. Olsen and Melaan (1993) simulated local scour around a circular cylinder in non-cohesive bed using three-dimensional steady Reynolds-averaged Navier-Stokes models. The simulated local scour patterns were compared with experimental data and showed a reasonable agreement. Roulund et al. (2005) conducted numerical simulations of local scour process around a vertical circular cylinder mounted on the bed covered with sediment. They used unsteady Reynolds-averaged Navier-Stokes (URANS) models with k-ω turbulence closure and reported that the main features of scour process and the formation of bars and ripples are captured, but local scour depth is underpredicted with approximately 15 %. Khosronejad et al. (2012) investigated the predictive capabilities for local scour around bridge piers with different shapes, using URANS models with k-ω turbulence closure. They showed that for the diamond shape pier, the simulated local scour matches well experimental data because the sediment transport is driven by shear layers at the sharp edges, whereas for the circular and square shape piers, the scour depth is significantly underpredicted at the front of the piers where flows are dominated by the energetic horseshoe vortices. Because of inherent limitations of URANS models and empirical bedload models, recent studies have

employed the detached-eddy simulation (DES) or the large-eddy simulation (LES) with sediment transport models in a physics-based way to reproduce accurately local scour induced by turbulent horseshoe vortices around vertical obstructions. Escauriaza and Sotiropoulos (2011) investigated dynamics of bedforms around a circular cylinder during the initial stage of scour using the DES coupled with new bedload transport models. They showed that the model can capture propagation and development of bedforms around a cylinder, and the celerity and dynamics of the ripples are consistent with features observed in experimental and field data. Kim et al. (2013) carried out numerical computations on local scour around two cylinders with side-by-side and tandem arrangements, employing the LES coupled with sediment transport in a Lagrangian framework and morphodynamic models. They found that the LES coupled with sediment transport and morphodynamic models improves dramatically local scour at the front of the cylinder where vortical structures occur with intense unsteadiness. The scour patterns and depths around cylinders were significantly influenced by different arrangements and cylinder spacing. From comparison with experimental data, it was shown that the model in physics-based way can reasonably predict local scour depth around cylinders.

As mentioned above, most of the experiments have been investigated around square cylinder groups according to variation of cylinder spacing and have main purpose to obtain the maximum scour depth (Amini et al., 2011;Ataie-Ashtiani and Beheshti, 2006; Hannah, 1978). On the other hand, global scour, which can be observed around cylinder groups, and transport process past cylinder groups are not investigated. In addition, there are several cylinder groups in marine structures, bridge piers and rigid vegetation, which have a variety of arrangements such as grid, staggered or random array. Such different arrangements can alter flow and turbulent structures, and thus local and global scour are significantly affected by them. Even though it is of considerable interest how different arrangements with variation of cylinder spacing impact scour patterns, depth and physical transport process around cylinder groups, these phenomena have yet to be demonstrated. Especially, numerical computation on local and global scour around cylinder groups is still challenge because as mentioned in above previous literatures of computational investigation on local scour, most of these studies have focused on local scour around a single cylinder except for the study of Kim et al. (2013).

The objective of present paper is two-fold: (1) to numerically investigate local and global scour around cylinder groups in terms of scour evolution, phenomenon and maximum scour depth; (2) demonstrate difference of local and global scour between grid and staggered arrangements of cylinders. To address these challenging tasks, the LES coupled with sediment transport in Lagrangian frame work and morphodynamic models which is able to provide physical transport phenomena. The sediment is considered as spherical particles and sediment transport process is solved in a Lagrangian framework. To deal with the cylinders and the bed surface, a ghost-cell immersed boundary method is implemented for the cells which intersect the immersed boundary. To compute local and global scour around cylinder groups, square cylinder groups (2×2) are selected with diverse cylinder spacing. The growth of local and global scour, and physical transport process past cylinder groups are described. In addition, influence of different cylinder arrangements (i.e. grid and staggered array) on the evolution of scour and patterns of scour and deposition is investigated. The computed maximum scour depth is compared with experimental data available in a literature of Ataie and Beheshti (2006).

6.2 NUMERICAL COMPUTATIONS

We employ the LES to resolve all turbulence scales induced by turbulence horseshoe vortices and interference effect around the cylinder groups. The novel sediment transport and morphodyanmic models (Nabi et al., 2013) are utilized to increase the physical realism of morphodynamics around cylinder groups. For all cases, the computational domain is set to be 10 m long (= 62.5D) and 2.42 m wide (= 15D) as shown in Fig. 6.1, which is same as that of Kim et al. (2013). The flow rate is 0.1 m^3/s, corresponding to a uniform flow depth of 0.15m with corresponding to Reynolds number of 41,500 and Froude number of 0.23. The diameter of a circular cylinder, D, is 0.16 m and the mean size of non-cohesive sediment used in this computation is 0.85 mm. The center of the cylinder groups are placed at a distance of 4.0 m (= 25D) from the inlet boundary. For the grid arrangement, five cases are considered with s / D = 1.25, 1.875, 2.5, 3.75 and 5.0, corresponding to 0.2, 0.3, 0.4, 0.5 and 0.6 m of cylinder spacing, respectively, where s is a center-to-center distance of cylinders. The base grid of 256 × 64 × 16 is used with three levels of local refinement where the finest grids are located close to the bed, side wall and cylinders as shown in Fig. 6.2. A no-slip condition is applied to solid walls and the free surface is set to be the

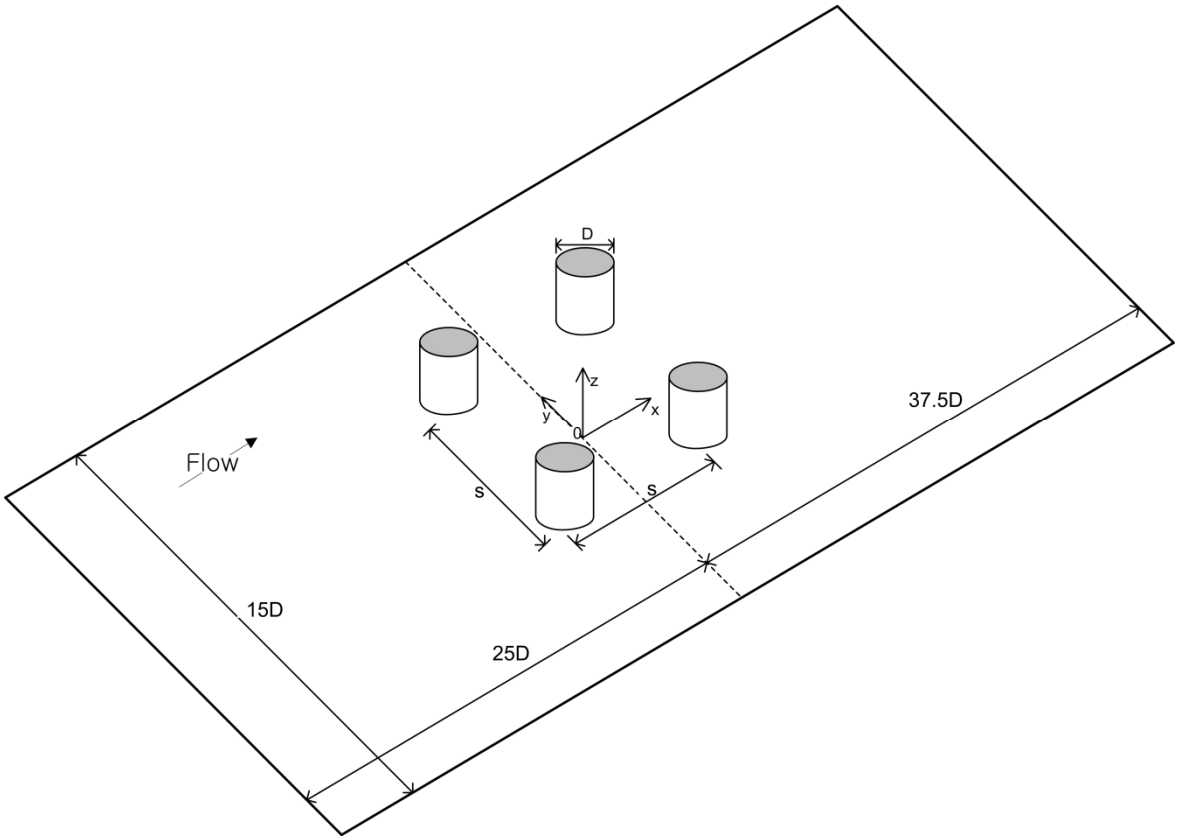


Fig. 6.1 Computational domain with the cylinder group.

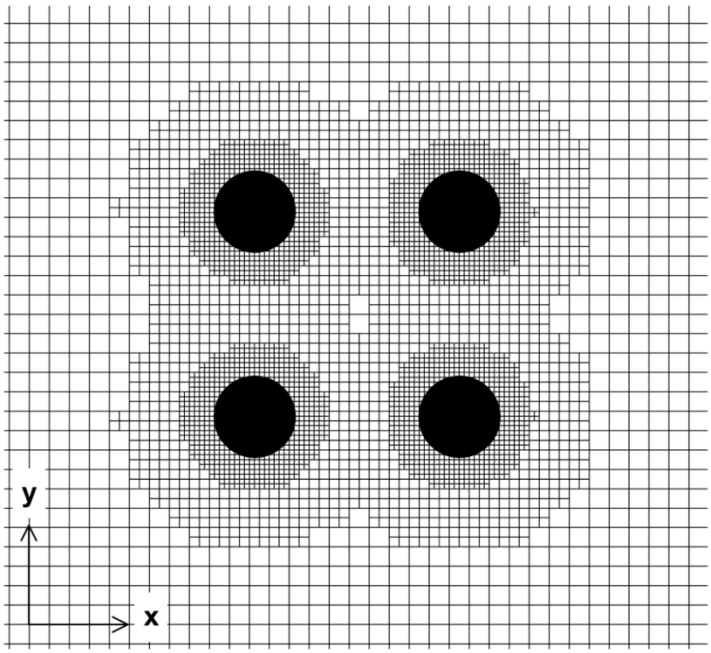


Fig. 6.2 Computational grid near the cylinder group in a horizontal plane.

symmetry plane, which is suitable for this flow of low Froude number. The computations are continued until an equilibrium state of the maximum scour depth is achieved.

6.3 RESULTS AND DISCUSSION

6.3.1 Grid arrangement

6.3.1.1 Morphological process

In this section, the computed results of morphological changes around cylinder groups of the grid arrangement with diverse distances between cylinders are shown. The cylinder spacing, s / D, is varied from 1.25 to 5.0. To understand physical transport and scour

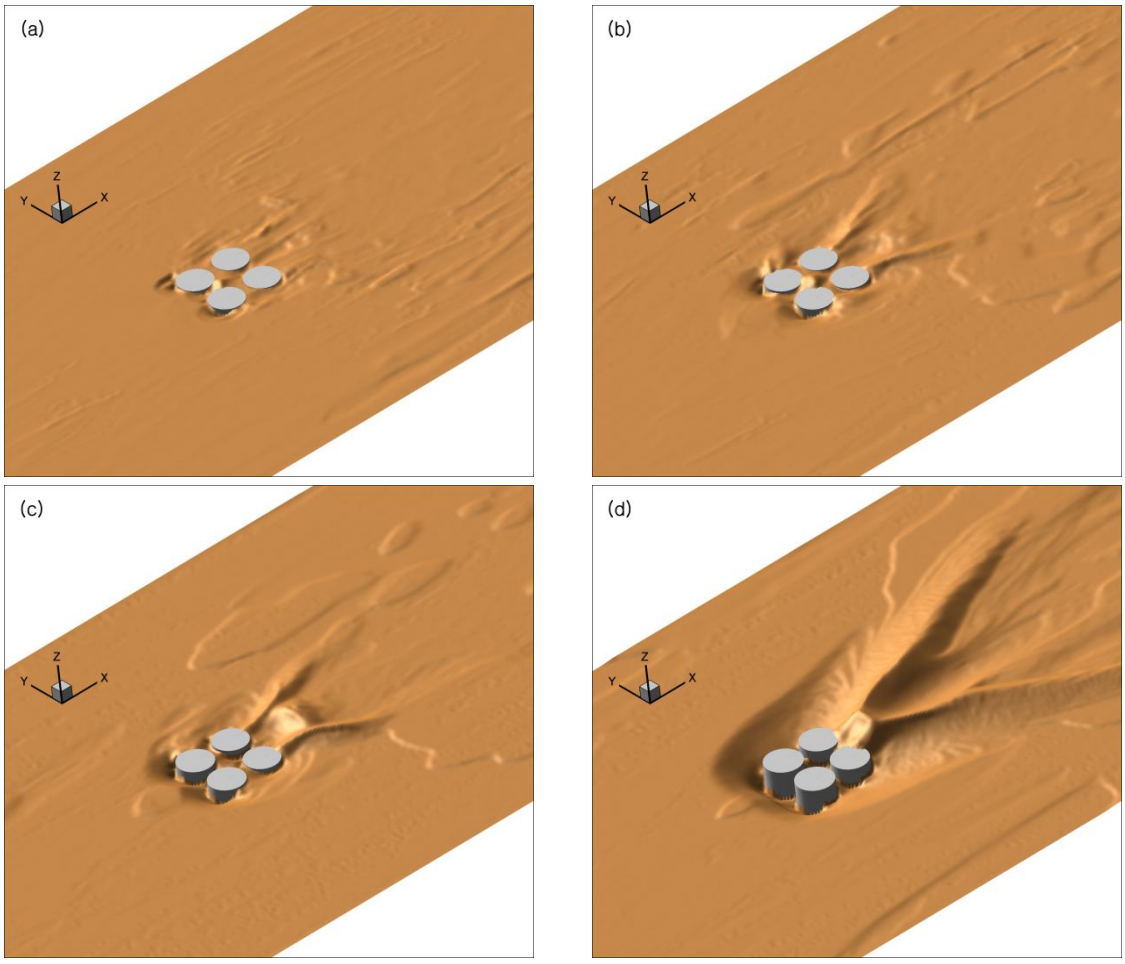


Fig. 6.3 Three-dimensional process of scour development around the cylinder group of s / D = 1.25; (a) 1 min, (b) 5 min, (c) 20 min, (d) equilibrium state.

processes around cylinder groups, the three-dimensional process of the instantaneous elevation of the bed for s / D = 1.25, 2.5 and 5.0 is presented in Figs. 6.3 – 5. In the figures, the gray-colored cylinders indicate the cylinder groups, where the top surfaces of the cylinders are identical to an initial bed elevation to distinctly exhibit morphological evolution of scour and deposition.

Firstly, Fig. 6.3 shows the instantaneous elevation of the bed around the cylinder group of s / D = 1.25 (t = 1, 5, 20 min and equilibrium state). The local erosion begins from the outside of the front cylinders at an angle of approximately 20° - 50° from the symmetry plane and it simultaneously starts between the front two cylinders during the first 1 min. After 5 min, the local erosion at the sides of the front cylinders persists due to acceleration of flow, whereas the bed elevation is constant behind the front cylinders (i.e. between two cylinders in a streamwise direction) because of a weak flow. The small deposition is observed inside the cylinder group, which is attributed to contraction flow between the two front cylinders. At 20 min, the erosion at the sides of the front cylinders merges with local scour at the nose of the cylinders induced by energetic turbulent horseshoe vortices. The local scour upstream of the front cylinders becomes more pronounced. It is observed that the sediment accumulated inside the cylinder group travels further downstream and the deposition increases downstream of the cylinder group due to continuous high fluid momentum on deformed bed caused by jet-like flow, which is responsible for an increase in local scour. At the equilibrium state, it can be seen that significant bed evolution of scour around and inside the cylinder group occurs and the sediment scoured around the cylinder group is accumulated behind the cylinder group. The sediment accumulated just behind the cylinder group is mainly driven by the contraction flow and dynamics of the near-bed turbulence due to interference of flow from the lateral cylinders. The deposition downstream of the cylinder group increases and elongates with time, whereas the transfer of sediment accumulated between and downstream of the rear cylinders is significantly reduced. This is attributed to weakened flow caused by a quite small gap between cylinders. The scoured region is extended around the cylinder group and thus, scour hole can be seen obviously surrounding the cylinder group because the turbulence structures travel around the flanks of the front cylinders together with acceleration of flow, which is a primary mechanism of local scour. In this case (s / D = 1.25), the scour and deposition patterns

around the cylinder group are analogous to those around a single cylinder, even though the erosion and deposition are observed due to jet-like flow and turbulence between cylinders.

Fig. 6.4 presents the instantaneous elevation of the bed around the cylinder group of s / D = 2.5 (t = 1, 5, 20 and equilibrium state). At t = 1 min, the erosion starts from the sides of the front cylinders from the symmetry plane, which is a somewhat different feature to

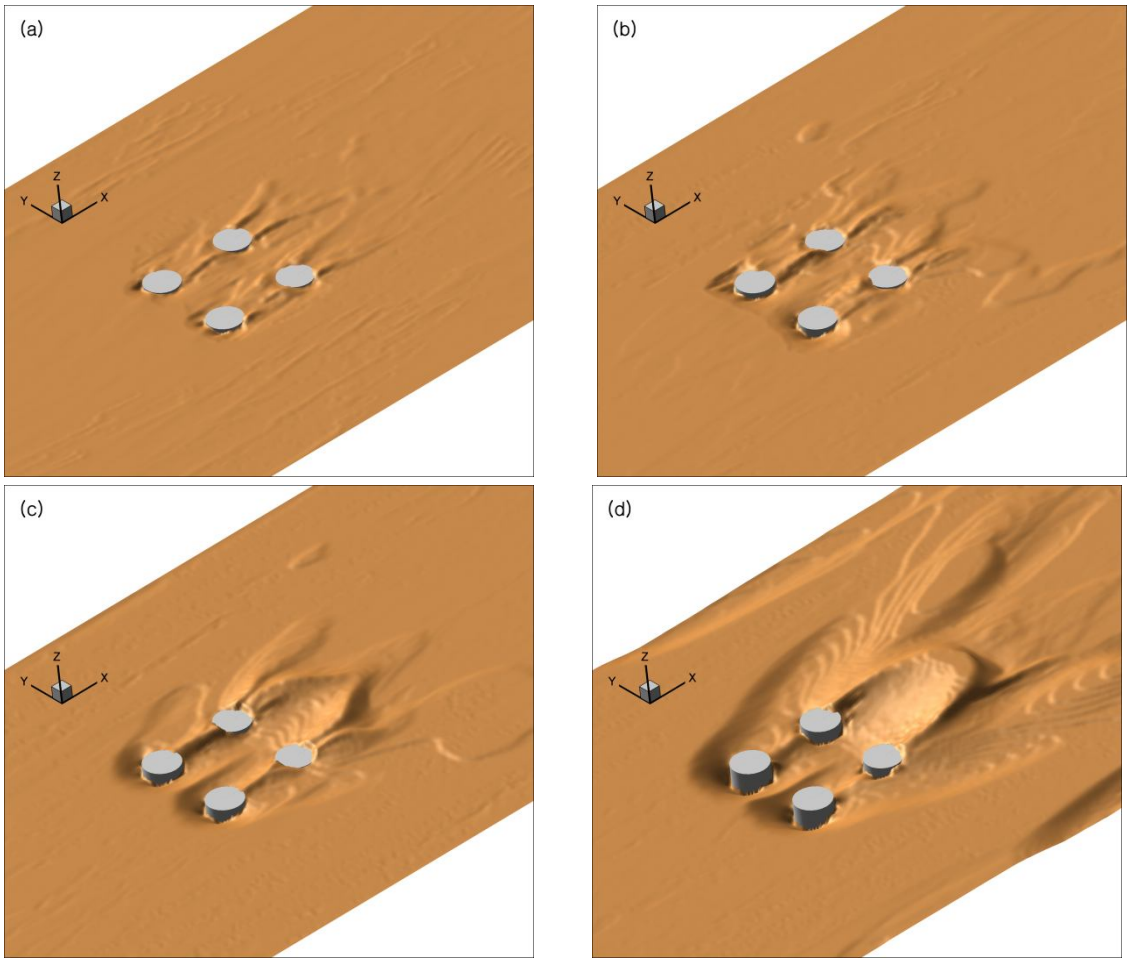


Fig. 6.4 Three-dimensional process of scour development around the cylinder group of s / D = 2.5; (a) 1 min, (b) 5 min, (c) 20 min, (d) equilibrium state.

the trend of s / D = 1.25. On the other hand, the bed elevation remains mostly constant around the rear cylinders, except for the accumulation of sediment behind the rear cylinders. It can be seen after 5 min shown in Fig. 6.4b that the erosion observed at the sides of the front cylinder merges into a single scour hole around the upstream of the

cylinders, whereas the deposition is observed behind the front cylinders, especially in front of the rear cylinders. At 20 min, the local scour persists around the front cylinders with increases in scoured region and depth. In addition, the accumulation of sediment increases continuously both upstream and downstream of the rear cylinders. It is worth mentioning that the local scour in front of the rear cylinders is significantly diminished since the presence of upstream cylinders interrupts approach velocity to the rear cylinders, which leads to a significant decrease of downflow together with acceleration of flow. It indicates that the turbulent horseshoe vortices, which are the main mechanism of the growth of scour hole, are weakened around the upstream base of the rear cylinders. The instantaneous bed elevation at the equilibrium state seen in Fig. 6.4d has more advanced status of erosion and deposition around the cylinder group. A great change in bed elevation at the later stage shown in Fig. 6.4d is not only dominated by energetic turbulent horseshoe vortices around cylinders but also induced by large-scale wake vortices behind cylinders. Unlike the overlapped scour around the front cylinders shown in Fig. 6.3, the local and global scours are distinguishable. It can be seen that the accumulation of sediment upstream of the rear cylinders is observed until 20 min, whereas the bed is eroded behind the front cylinders at the later stage because of a wake vortex shedding and interference of flow from lateral cylinders. The interference of flow can amplify vortex magnitude and turbulent kinetic energy, which are responsible for bed load transport and erosion process. In fact, Kim et al. (2013) showed that the computation of scour and transport process around two cylinders in tandem (s / D = 2.5) is carried out and sediment is slightly accumulated upstream base of the rear cylinder. Thus, this implies that an increase in bed scouring around the upstream of the rear cylinders is significantly influenced by the interference of flow from the lateral cylinders. The accumulation of sediment is observed downstream of the cylinder group and it is located further downstream, compared to that observed at s / D = 1.25. This implies that the contraction flow between lateral cylinders becomes more effective as the cylinder spacing increases.

Fig. 6.5 shows the three-dimensional global view of the instantaneous elevation of the bed around the cylinder group of s / D = 5.0. Similarly, the local scour starts from the sides of cylinders at 1 min, which takes place at an angle of ±40° from the symmetry plane, which is consistent with an initial event observed around a single cylinder (Khosronejad et

al. 2012; Kim et al. 2013). At t = 5 and 20 min, there is a steady morphodynamic evolution of the bed around cylinders and thus, the bed variation increases gradually due to a growth of horseshoe vortex system along with development of scour holes. On the other hand, it can be seen that the presence of the front cylinders still impinges on the growth of local scour around the rear cylinders, even though the cylinder spacing (s / D) becomes double, compared to that of s / D = 2.5. At the equilibrium state shown in Fig. 6.5d, the

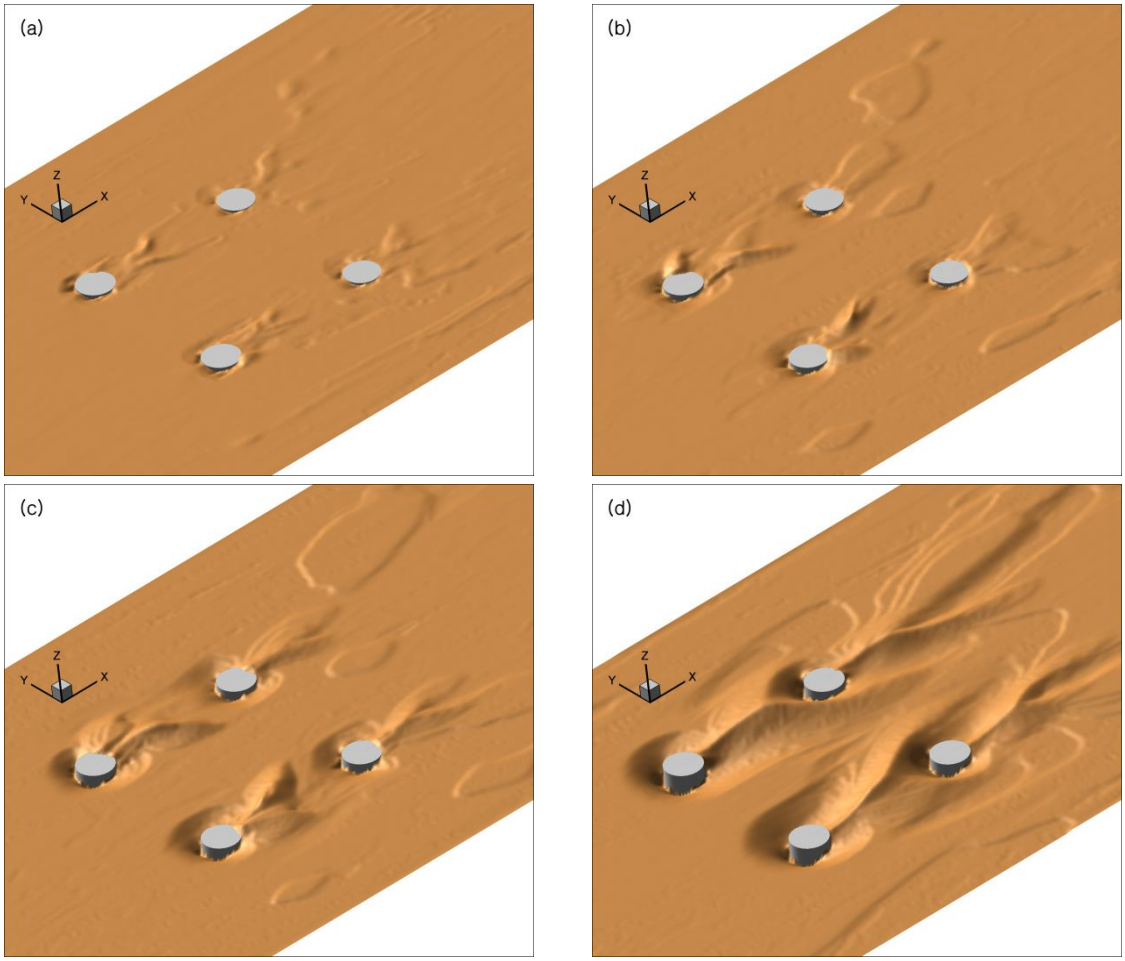


Fig. 6.5 Three-dimensional process of scour development around the cylinder group of s / D = 5.0; (a) 1 min, (b) 5 min, (c) 20 min, (d) equilibrium state.

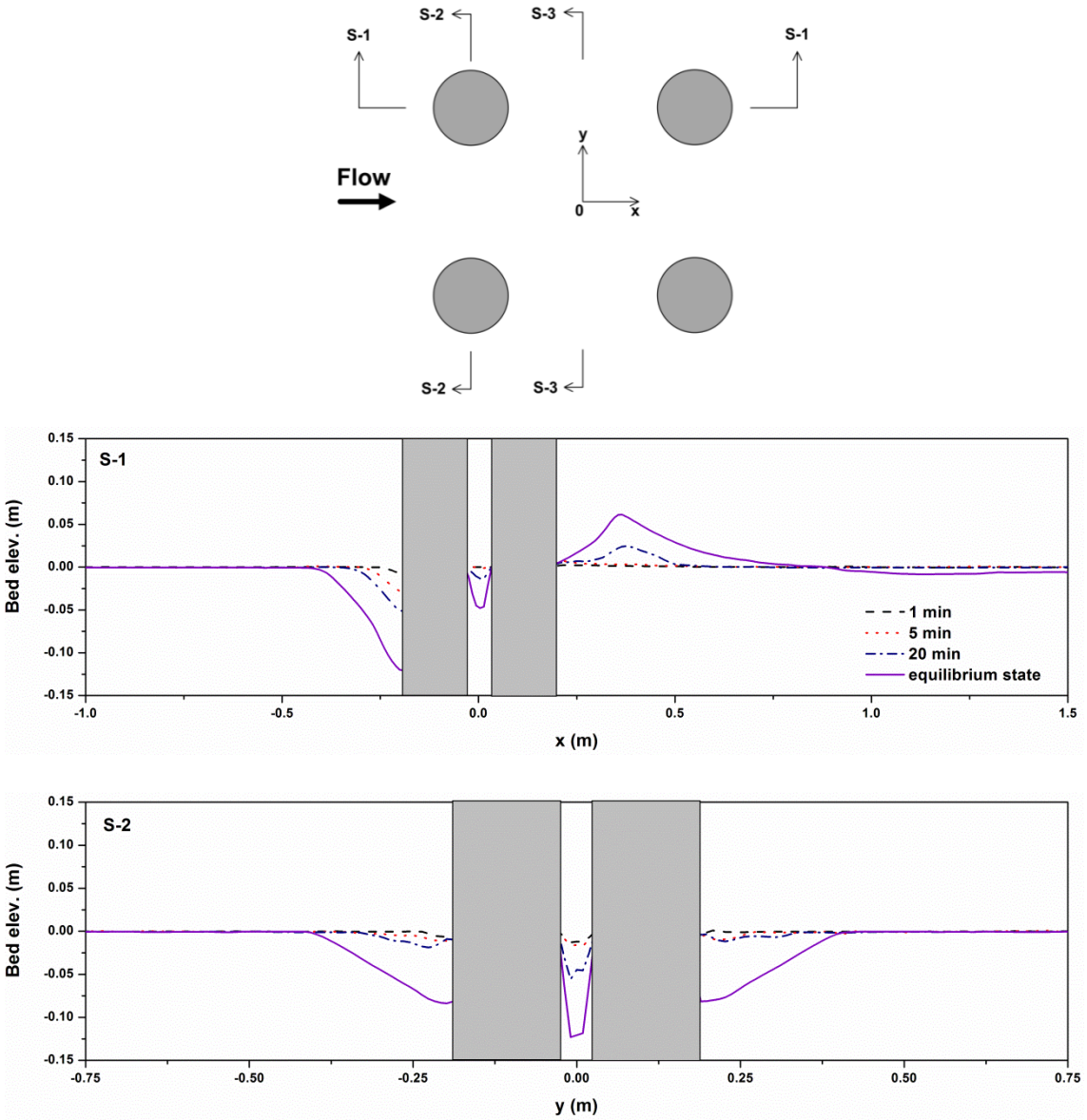
development of local scour and deposition is clearly observed around the front cylinders, which are mostly similar to those of a single cylinder reported by several observations (Dargahi, 1990; Khosronejad et al. 2012). Unlike the scour between cylinders observed in

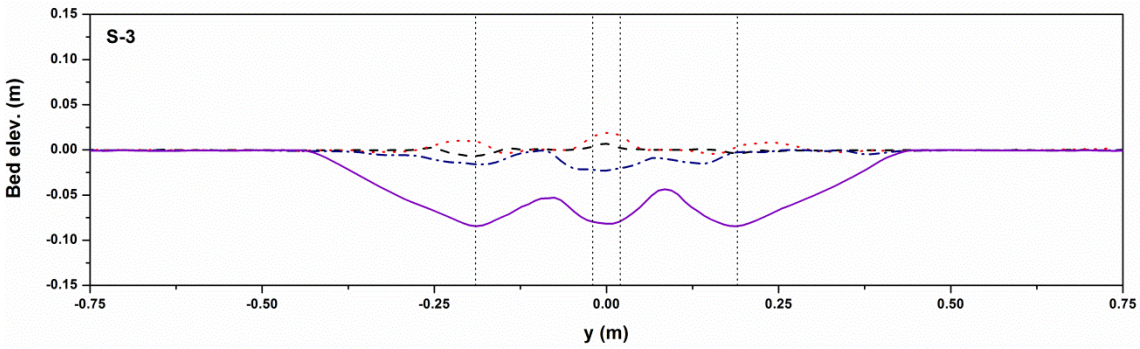
the cases of s / D = 1.25 and 2.5, there is no scour of the bed between cylinders at the equilibrium state, which indicates that the impact on bed erosion induced by a gap flow between cylinders is negligible. In other words, the local scour and deposition around each cylinder are laterally independent. The sediment accumulated behind the front cylinders increases and migrates downstream region due to vortex shedding in the wake zone of downstream of the front cylinders. On the other hand, the impact of the front cylinders on local scouring around upstream base of the rear cylinders drops off according to an increase of cylinder spacing. Nevertheless, the growth of scour around upstream of the rear cylinders is affected by the presence of the front cylinders as well as the migration of sediment accumulated downstream of the front cylinders.

6.3.1.2 Lateral and longitudinal bed profiles

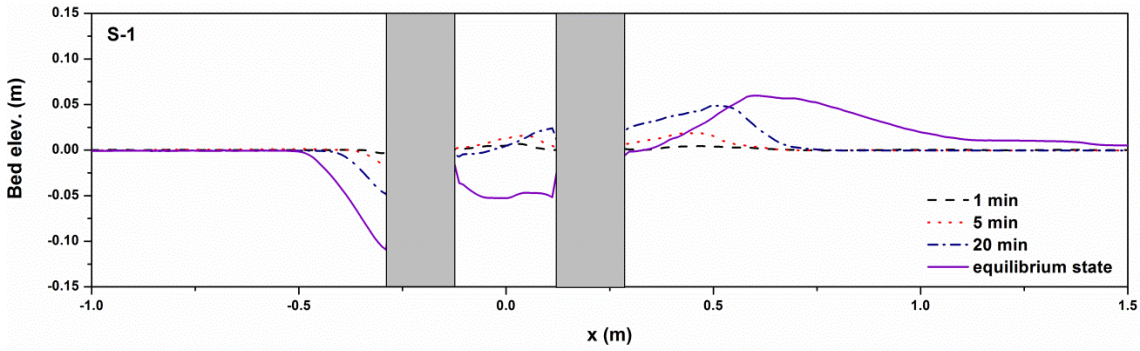
Fig. 6.6 presents the computed morphological process in one longitudinal and two lateral bed profiles around cylinder groups for s / D = 1.25, 2.5 and 5.0 corresponding to t = 1, 5, 20 min and equilibrium state where the zero bed elevation indicates an initial flat bed. As seen in S-1 which is longitudinal bed profiles through two cylinders, the scouring of the bed increases with time at the nose of the front cylinder regardless of the cylinder spacing where the rich dynamics of turbulent horseshoe vortices are dominated. For s / D = 1.25 and 2.5, the bed elevation remains mostly flat between cylinders until 20 min, after which the bed elevation descends at the later stage (t > 20 min). It is notable that turbulent stress amplified by interference of flow from the lateral cylinders highly increases with deformation of the bed around cylinder groups, even though the impact of turbulent horseshoe vortices disappears around the upstream base of the rear cylinder. Thus, the group of sediment particles between cylinders is washed away further downstream, which leads to a decrease in bed elevation behind the front cylinder. For s / D = 2.5, in particular, the bed elevation becomes low over the entire region between cylinders. For s / D = 5.0, on the other hand, the accumulation of sediment is observed behind the front cylinder, which increases with time and transfers to downstream direction. Unlike the cases of s / D = 1.25 and 2.5, the local scouring is captured in front of the rear cylinder and the scour depth deepens gradually. Not only the scoured region is less extended upstream of the rear cylinder but also the scour depth at the nose of the rear cylinder is relatively low, compared to that of the front cylinder, which are caused by the effect of the front cylinder and the

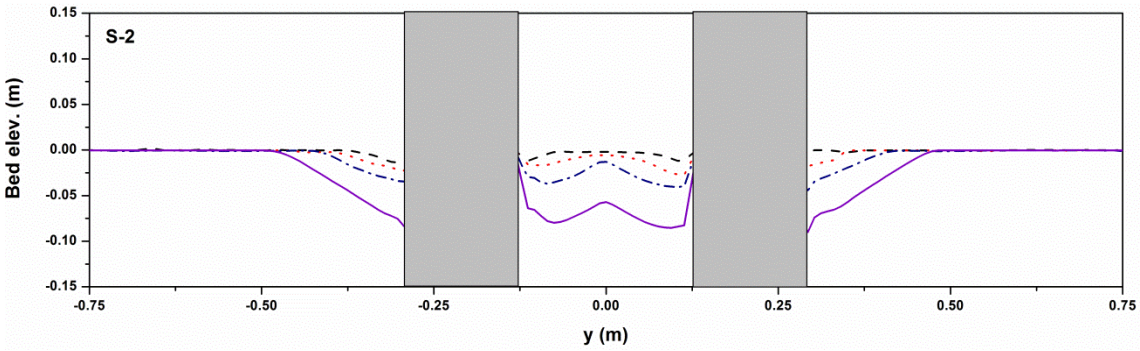
migration of deposition mound, as mentioned above. For s / D = 1.25, the height of the accumulation of sediment increases and elongates with time. For the other cases, the sediment accumulated behind the rear cylinder not only increases but also travels to downstream with time, even though the relatively low deposition is observed behind the rear cylinder for s / D = 5.0. The sediment accumulated downstream of the cylinder group is significantly influenced by cylinder spacing. It can be seen in S-2 which is the lateral bed profiles across the front cylinders that scour occurs at the sides of the cylinders, which increases with time and is extended around the cylinders according to a decrease in

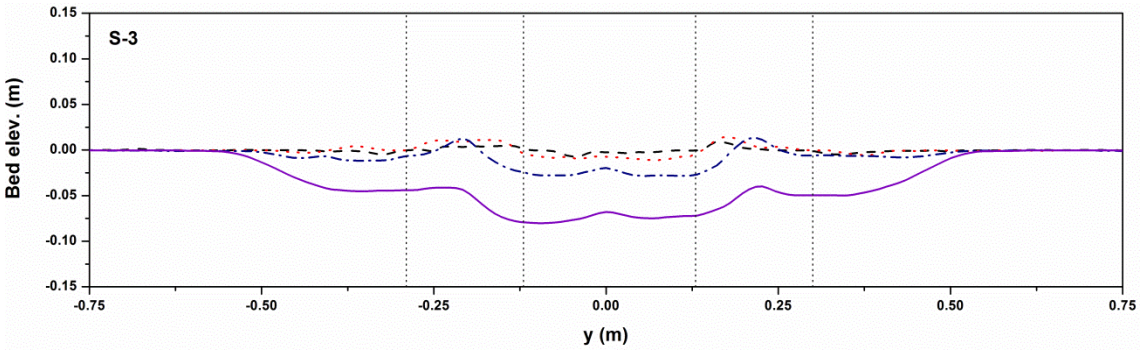




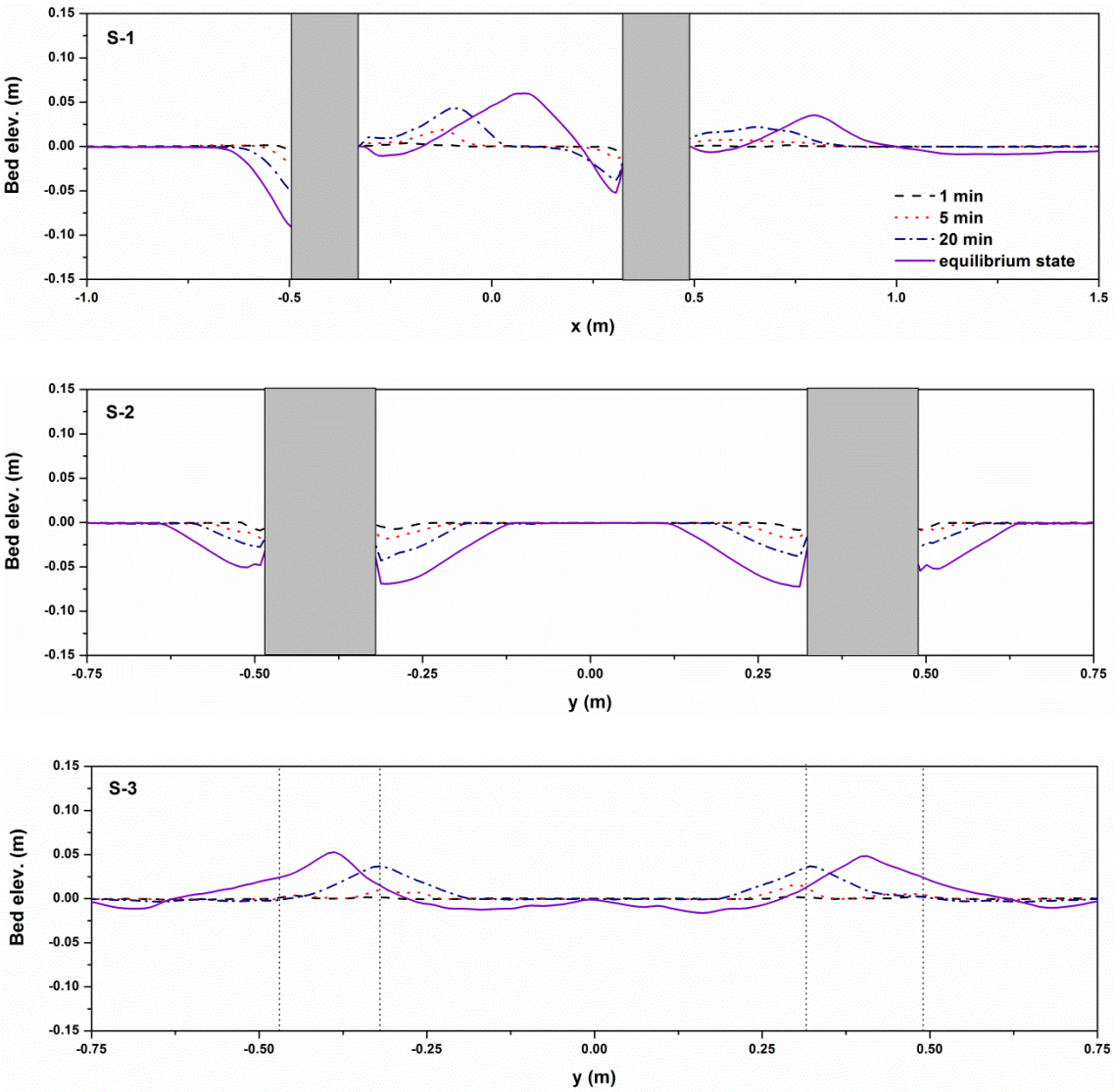
(a) s / D =1.25







(b) s / D = 2.5



(c) s / D = 5.0

Fig. 6.6 Lateral and longitudinal bed profiles around the cylinder group.

cylinder spacing. A particular feature of global scour, which occurs because of acceleration of flow velocity and an increase in turbulence intensity, is observed between the cylinders (Sumer et al., 2005). For s / D = 1.25, the scour depth increases with time and this is much deeper than that around the outside of the cylinders. It is found in s / D = 2.5 shown in Fig. 6.6b that the bed is eroded in time, which implies that the acceleration of flow and turbulence are still effective, and a particular characteristic of global scour, which can be distinguishable from local erosion at the sides of the cylinders, is captured. As seen

in s / D = 5.0, the bed elevation remains the initial flat bed due to fact that the influence of lateral cylinders on erosion driven by an increase in bed shear stress due to interference of flow is significantly weakened as shown in Fig. 6.5. The S-3 indicates lateral bed profiles at the coordinate origin, which is the center of the cylinder groups. After 5 min in s / D = 1.25, there are three convex regions between the cylinders and at the sides of the cylinders. At 20 min, the convex regions are changed to depression. At the equilibrium state, there are three depressions behind the front cylinders, which is coincides with the regions where the flow is enhanced and complex turbulent horseshoe vortices travel. It can be seen in s / D = 2.5 that the global lowing of bed elevation between and behind the front cylinders increases with time. It is evident that the turbulent stress near the bed produced by the interference of flow and turbulence structure increases inside cylinder groups since the erosion of the bed inside cylinder groups is much higher than that at the sides of the cylinders. It is shown in s / D = 5.0 that the morphological changes are significantly different from the other cases as seen above. This is attributed to the significant increase of cylinder spacing, so that typical deposition mound is observed behind the front cylinders. The sediment accumulated behind the cylinders increases with time and move away from the inside of the cylinder groups.

6.3.1.3 Bed topography

Fig. 6.7 shows the contour of bed elevations around the cylinder groups with variation of cylinder spacing (s / D = 1.25, 1.875, 2.5, 3.75 and 5.0) at the equilibrium state. In addition, the contour of bed elevation around a circular cylinder computed by Kim et al. (2013) is displayed for comparison as shown in Fig. 6.7a. In the morphological changes around a circular cylinder, the maximum scour occurs at an angle of about ±40° from the symmetry plane and the scoured region is extended around a circular cylinder. The accumulation of sediment is observed downstream of the cylinder. As shown in Fig. 6.7, the morphological patterns around the cylinder groups are considerably affected by variation of cylinder spacing, compared to those of a circular cylinder. It can be seen for s / D = 1.25 in Fig. 6.7b that the single scour hole is developed around the cylinder group due to overlapped scour region. It is found that the significant scour occurs between the front cylinders due to highly enhanced flow and generation of compressed horseshoe vortices, so that the maximum scour locations are changed, unlike that around a circular cylinder. The global

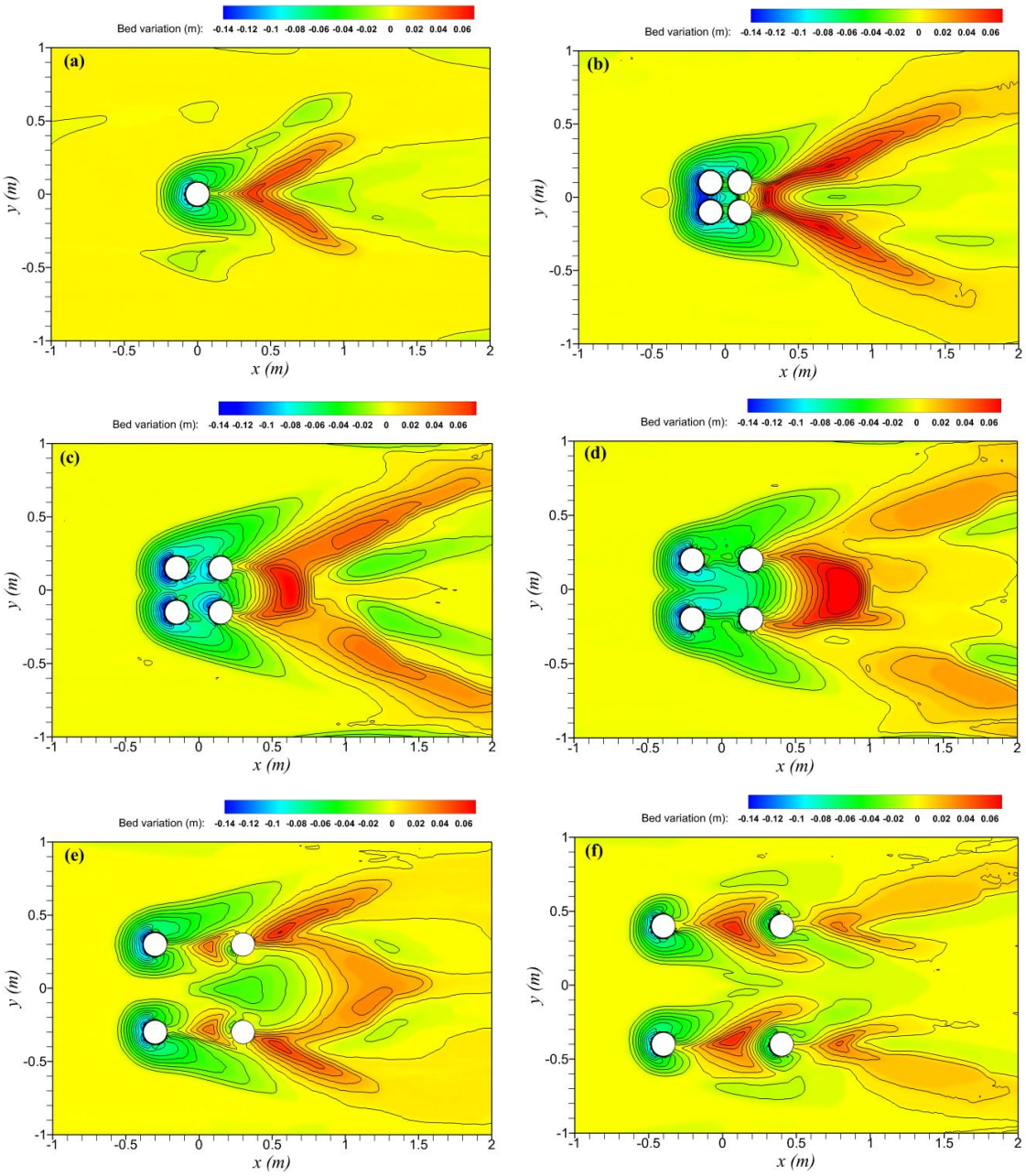


Fig. 6.7 Contour of bed elevations at the equilibrium state around the cylinder group; (a) single cylinder, (b) $s / D = 1.25$, (c) $s / D = 1.875$, (d) $s / D = 2.5$, (b) $s / D = 1.25$, (e) $s / D = 3.75$. (f) $s / D = 5.0$.

and local scour at cylinder groups are observed as the cylinder spacing, s / D, is smaller than 3.75. In this case, one deposition mound is formed downstream of the cylinder groups and its position migrates further downstream with an increase of cylinder spacing.

Moreover, the global scour observed between the front cylinders becomes low and overlapped scour hole between the front cylinders is separated as the cylinder spacing increases because of the influence of a weakened gap flow. A particular characteristic of morphological changes at the cylinder groups is global scour, which cannot be seen in the scour around a simple geometry. It can be seen in Fig. 6.7 that significant erosion is observed inside the cylinder groups as seen in Fig. 6.6, which occurs due to an increase in turbulence intensity produced by interference impact of the lee-wake vortices. Sumer et al. (2002) reported that the implication of an increase in turbulence inside the cylinder groups can substantially increase in bed load flux and sediment transport, so that it leads to global lowering of the bed elevation. It is important to note that the global scour produced by the increase of turbulent stress of the bed due to interference effect is reproduced by present computational model, and in addition, it is attributed to fact that LES model captures all the essential turbulences, which is correctly reflected in sediment transport and morphodynamic models. It is found that the scour holes are developed individually at each cylinder, that is, the global scour mostly disappears as the cylinder spacing, s / D, is larger than 2.5. As seen in Figs. 6.7e and f, the local scour around the front cylinders shows a similar feature to that at a single cylinder in Fig. 6.7a. On the other hand, the sediment accumulated behind the front cylinders increases with an increase in the cylinder spacing. Also, the scour depth increases, and the scoured region is extended around the rear cylinders as the cylinder spacing increases. These results demonstrate that the reduction in implication of upstream cylinders due to an increase in cylinder spacing is the primary cause that leads to an increment in scour around the upstream base of the rear cylinders. In other words, the sheltering effect becomes lower and the intensity of turbulent horseshoe vortex system, which is the main mechanism of local scour at the front of the cylinder under clear water scour, increases as the cylinder spacing increases. For $s / D = 3.75$, the scour around the rear cylinders is substantially affected by the migration of the deposition mound downstream of the front cylinders, that is, the groups of sediment particles comes into the scour hole around the rear cylinders, which are transported with much faster flow, and those are accumulated behind the rear cylinders. For $s / D = 5.0$, the impact of the migration of deposition decreases. In the cases that the global scour is not observed, the morphological patterns around the cylinder groups show similar characteristics to those of

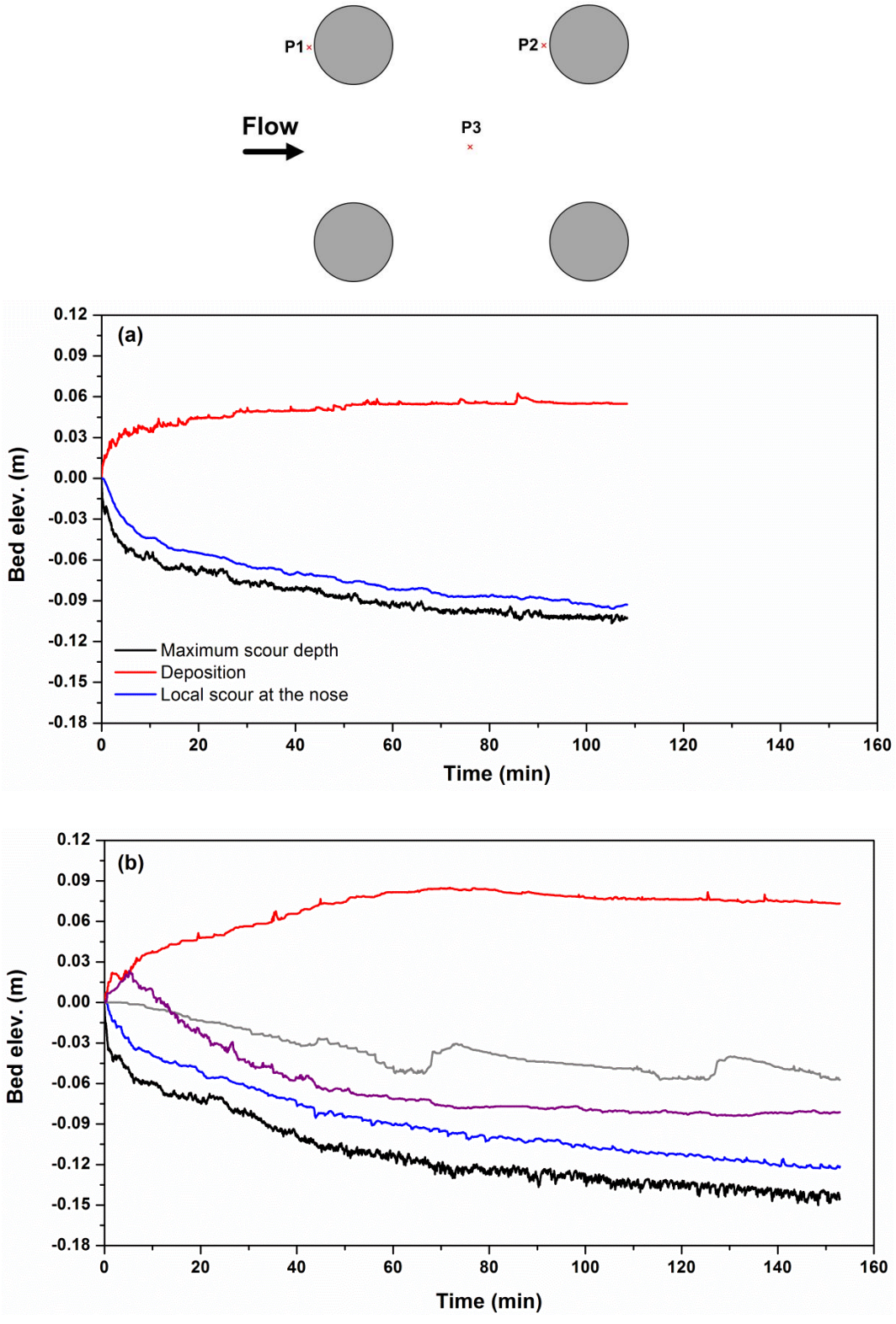
two cylinders in tandem reported by Kim et al. (2013).

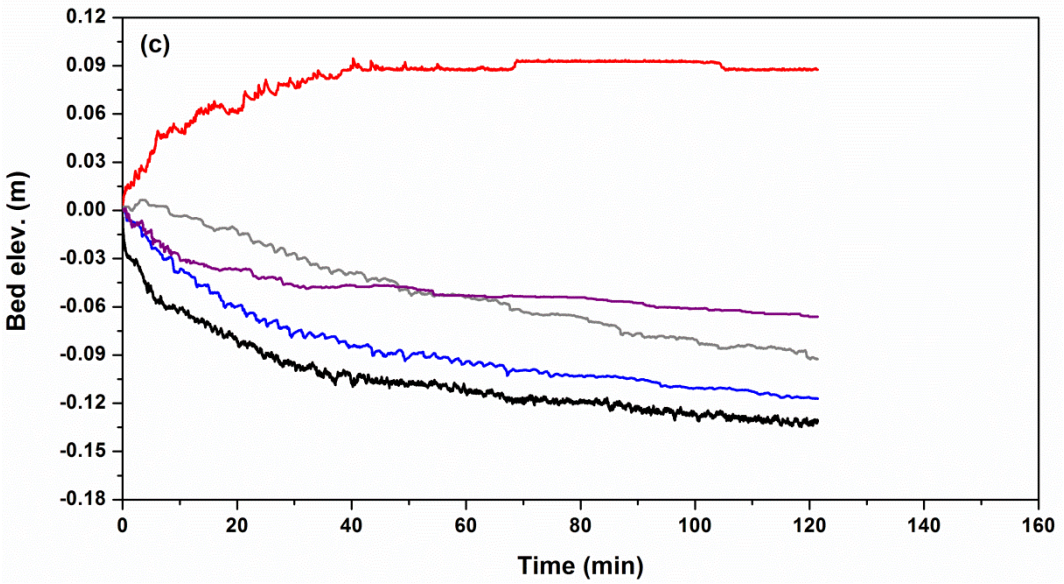
6.3.1.4 Time evolution of the bed

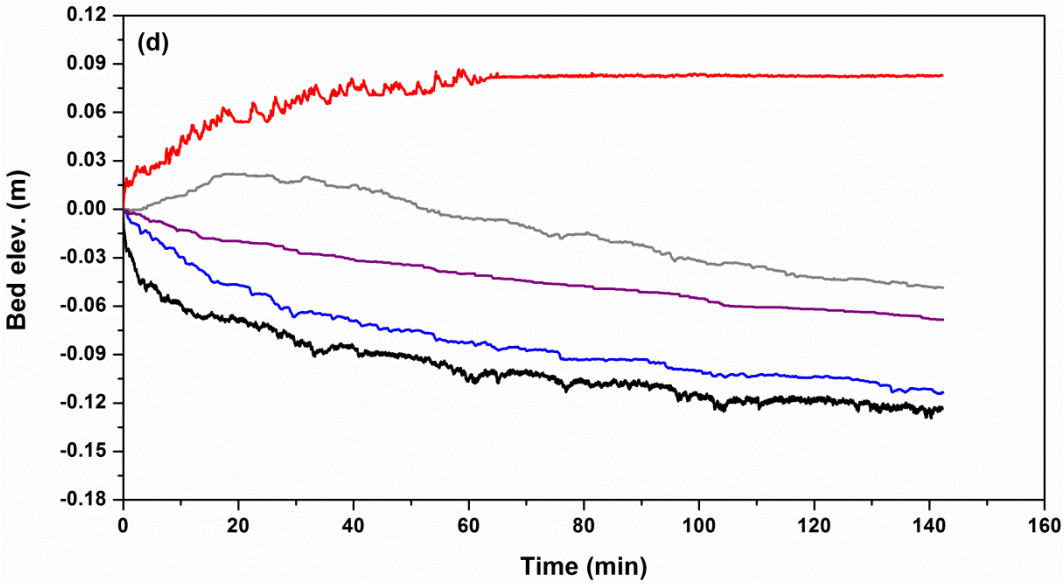
Fig. 6.8 shows the time evolution of the maximum scour depth over the entire domain together with three points where P1, P2 and P3 are located at the nose of the front and rear cylinders (upstream of cylinders with distance of 0.09 m from the center of cylinders), and the center of the cylinder groups (i.e. the coordinate origin), respectively. In this figure, the time evolution of the maximum deposition height is also displayed. To compare the trend of scour, the time evolution of the maximum and local scour at the nose around a single cylinder computed by Kim et al. (2013) is presented in Fig. 6.8a. As seen in Fig. 6.8a, the bed around a single cylinder evolves rapidly during 20 min, after which the growth rate of scour slows down and the bed reaches an equilibrium state at about 100 min. It can be seen that the local scour at the nose of the cylinder shows the similar trend of bed evolution and a final scour depth is predicted to 0.094 m, which is 94 % of the maximum scour depth (= 0.1 m). They reported that this coincides with the observation of Khosronejad et al. (2012). As shown in Fig. 6.8, the growth rate of the maximum scour depth around the cylinder groups, which is always observed around the sides of the front cylinder, increases sharply during approximately the first 20 min. The scour rate slows down and reaches a quasi-equilibrium state after approximately 120 min. The time series of the maximum scour depth show a similar trend for all the cylinder groups regardless of cylinder spacing. As seen in Fig. 6.8, the height of the maximum deposition evolves rapidly at the early stage, after which the growth rate of deposition slows down and reaches a statically dynamic equilibrium. This is a quite similar trend to that of the maximum scour process.

It can be seen that the evolution of scour observed at the nose of the front cylinder, P1, where the horseshoe vortices are located shows similar features to the tendency of the growth rate of the maximum scour depth. The scour depth at the symmetry plane is lower than that of maximum erosion in time where the local shear stress has the highest magnitude (Escauriaza and Sotiropoulos, 2011). The computed scour depth at the nose of the front cylinder is predicted to 0.124, 0.116, 0.109, 0.108 and 0.092 m, corresponding to s / D = 1.25, 1.875, 2.5, 3.75 and 5.0, respectively. The computed scour depth is corresponding to 86, 87, 87, 89, 88 and 90 % of the maximum scour depth for s / D = 1.25, 1.875, 2.5, 3.75 and 5.0, respectively. This implies that the relatively high erosion occurs at

the sides of the front cylinders due to the interference effect, as compared to that of a single cylinder.




(c)
Bed elev. (m)
Time (min)
0.12
0.09
0.06
0.03
0.00
-0.03
-0.06
-0.09
-0.12
-0.15
-0.18
0
20
40
60
80
100
120
140
160


(d)
Bed elev. (m)
Time (min)
0.12
0.09
0.06
0.03
0.00
-0.03
-0.06
-0.09
-0.12
-0.15
-0.18
0
20
40
60
80
100
120
140
160

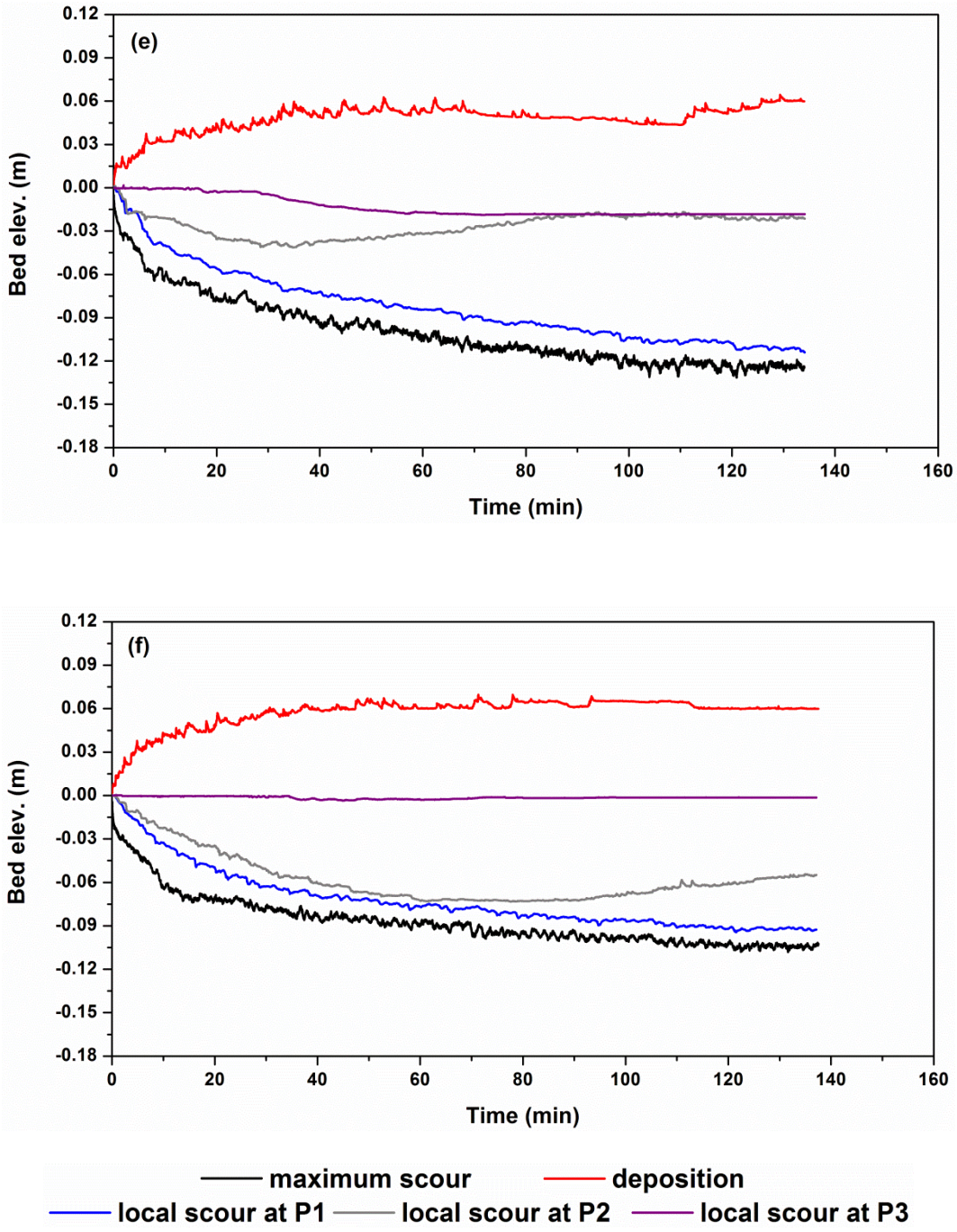


Fig. 6.8 Time evolution of scour and deposition; (a) single cylinder, (b) $s / D = 1.25$, (c) $s / D = 1.875$, (d) $s / D = 2.5$, (b) $s / D = 1.25$, (e) $s / D = 3.75$. (f) $s / D = 5.0$.

On the other hand, the computed evolution of scour at the nose of the rear cylinder, P2, is obviously differentiated from the growth trend of the maximum scour and the local scour at the nose of the front cylinder. As shown in Fig. 6.8b ($s / D = 1.25$), the evolution of the

erosion increases smoothly until approximately 70 min, after which it rapidly decreases, that is, the sediment is accumulated at the point. After that, the evolution of scour grows continuously, but the similar transition is shown beyond approximately 126 min. This location is attributed to high interaction of the wake vortices, which is associated with near-bed turbulent stress, so that the progression of dynamic flow features causes the instantaneous variation in the bed morphodynamics around the upstream base of the rear cylinder. For $s / D = 1.875$, the evolution of scour around the upstream of the rear cylinder is developed gradually, and the obtained value of the final scour depth is 0.088 m, which is lower than that of the front cylinder. For $s / D = 2.5$, it is found that the elevation of the bed increases until approximately 17 min as seen in Fig. 6.8d, after which the growth rate of scour evolves smoothly and continuously at the end of the computation due to an increases rich dynamics of turbulence produced by interference effect with deformation of the bed. In the cases that the global scour occurs, the local scour depth in front of the rear cylinder is mainly caused by the substantial increase in turbulence inside the cylinder group. When the cylinder spacing (s / D) is 1.875, the scour depth is the deepest, which reveals that the magnitude of turbulence generated by the interference effect from the cylinders is the strongest at $s / D = 1.875$. As shown in Fig. 6.8e ($s / D = 3.75$), the evolution of scour at the rear cylinder grows until approximately 30 min, corresponding to scour depth of about 0.038 m. After that, the bed elevation increases gradually until approximately 90 min, after which the temporal variation becomes constant and it continues until the end of the computation. This implies that the temporal variation of the bed at this location becomes the dynamic equilibrium much faster than other cases. The final scour depth at the nose of the rear cylinder is estimated to 0.02 m. It is notable that the local scour induced by turbulence horseshoe vortices is observed at the early stage as the cylinder spacing, s / D, is larger than that of $s / D = 2.5$, but the contribution of horseshoe vortices to erosion process is diminished around the upstream of the rear cylinder beyond the time. This indicates that not only the migration of deposited mound behind the front cylinder driven by the large-scale vortices in the wake region affects the scouring of the bed but also the flow undergoes significant changes due to the accumulation of sediment. For $s / D = 5.0$, the similar tendency of the rate of scour growth to that of $s / D = 3.75$ can be seen in Fig. 6.8f. The deepening of scour at the nose of the rear cylinder occurs smoothly and the scour

depth is mostly consistent with that at the upstream of the front cylinder until approximately 65 min. This result demonstrates that the impact of the presence of the upstream cylinders on turbulent horseshoe vortices in front of the rear cylinders is considerably weakened. At later stage (t > 65 min), however, the growth rate of scour shows a decrease trend according to time. Thus, the finding from the results is that the main culprit for disturbing scour growth at the nose of the rear cylinder is the migration of deposited mound. As shown in Fig. 6.8, the overall scour depth around the upstream of the rear cylinder is lower than that observed at nose of the front cylinder over the whole ranges of cylinder spacing, s / D (= 1.25 – 5.0).

It can be seen that the global scour at the center of the cylinder groups occurs when s / D < 3.75 as shown in Fig. 6.7 and the evolution of scour increases gradually at all time. The global scour at the center of the cylinder groups is estimated to 0.08, 0.067 and 0.067 m for s / D = 1.25, 1.875 and 2.5, respectively, which are corresponding to 55, 50, and 62 % of the maximum scour depth. The global scour has a negligible effect as the cylinder spacing, s / D, is larger than 2.5.

6.3.2 Staggered arrangement

The morphological evolution of the bed is computed around the cylinder group of the staggered arrangement. The change in the cylinder group configuration is strongly associated with the interference effect of the wake vortices and horseshoe vortex (Summer et al., 2002). Thus, apparently, the scour process and pattern can be substantially affected. In this section, the computed results of morphological changes around the cylinder group of a staggered arrangement are shown. To understand transport and scour processes around cylinder group, the three-dimensional global view of the instantaneous elevation of the bed for s / D = 5.0 is presented in Fig. 6.9. In the figures, the gray cylinders indicate the cylinder groups, whereas the top surfaces of the cylinders are identical to an initial bed elevation to distinctly exhibit morphological evolution of scour and deposition around cylinder groups.

During the first 1 min, the local scour starts from the sides of each cylinder driven by an increase in the bed shear stress due to the local flow acceleration. At later time (t > 1min), the morphodynamic evolution of the bed around cylinders occurs continuously and thus, the variation of the bed grows gradually due to fact that the energetic horseshoe vortices

dominate, so that the scour process at the upstream of the cylinders persists. It can be seen that the scour around the upstream of the rear cylinders is much pronounced because of the interference effect driven by the cylinder located at the center of the cylinder group. This will be discussed later. At the equilibrium state shown in Fig. 6.9d, the growth of local scour is obviously represented around individual cylinders of the cylinder group and the shape of scour hole is mostly identical with that observed at the cylinder group with the grid arrangement of $s / D = 5.0$ as shown in Fig. 6.5.

On the other hand, the cylinder group with the staggered arrangement of $s / D = 5.0$ has one more cylinder in the group, compared to that of the grid arrangement with identical

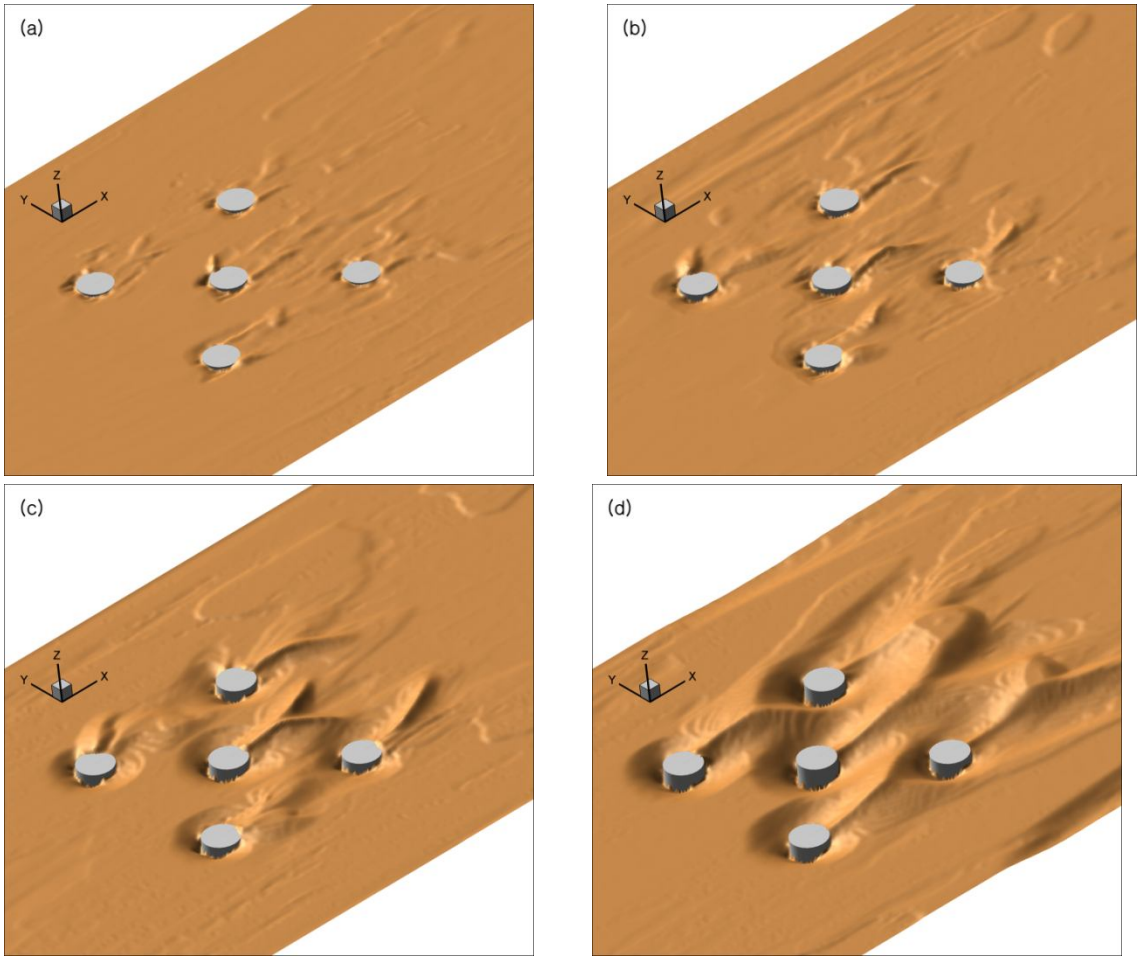


Fig. 6.9 Three-dimensional process of scour development around the cylinder group with the staggered arrangement of $s / D = 5.0$; (a) 1 min, (b) 5 min, (c) 20 min, (d) equilibrium state.

cylinder spacing. In other words, the solid volume fraction (SVF) of the cylinder group with the staggered arrangement is two times larger than that of the grid arrangement. In spite of an increase in the SVF for the cylinder group with the staggered arrangement, the evolution of scour at the cylinder group grows separately around individual cylinders, that is, the global scour can hardly be discovered around the cylinder group. For the grid arrangement, however, the increase of the SVF (s / D = 2.5), which is identical to that of the staggered arrangement, has a significant global scour around the cylinder group driven by the increase in turbulence intensity due to the interference effect. It is worth noting that the local and global scour processes depend strongly on the configuration of the cylinder group, which is attributed to significantly different flow features produced by the interference effect around the cylinder group. Recent several studies on morphological changes around the patch of rigid vegetation carried out and the erosion was observed within and around the patch (Bouma et al., 2007; Follett and Nepf, 2012; Kim et al., 2013). They reported that the degree of the erosion is depending on the SVF and the increase in turbulence kinetic energy is highly associated with local scouring near the leading edge of the patch. Nepf (2012) reported that there is spatial variation of bed shear stress within the patch due to individual stems, which is similar phenomenon at the cylinder groups. The present results provide evidence about significant changes in the bed shear stress and turbulence level, in part, by the variation of scour process according to the cylinder configuration. It reveals, therefore, that the variability in bed shear stress within the patch of vegetation is affected by the SVF as well as cylinder configuration.

Fig. 6.10 shows the time evolution of the maximum scour depth over the whole domain along with three points where P1, P2 and P3 are located at the nose of the front, rear and center cylinders, respectively. In this figure, the time evolution of maximum deposition height is also presented. The overall trend of the growth rate of scour is similar to that observed at the cylinder group of the grid arrangement (s / D = 5.0). On the other hand, the location of the maximum scour transfers from the nearby front cylinders to the sides of the center cylinder. This implies that the wake vortices from the front cylinders impinge on the approach velocity to the center cylinder, which is related to the magnitude of horseshoe vortices, and turbulence stress. It is notable that for the cylinder group with the grid arrangement, the maximum scour depth occurs at the sides of the front cylinders due to the

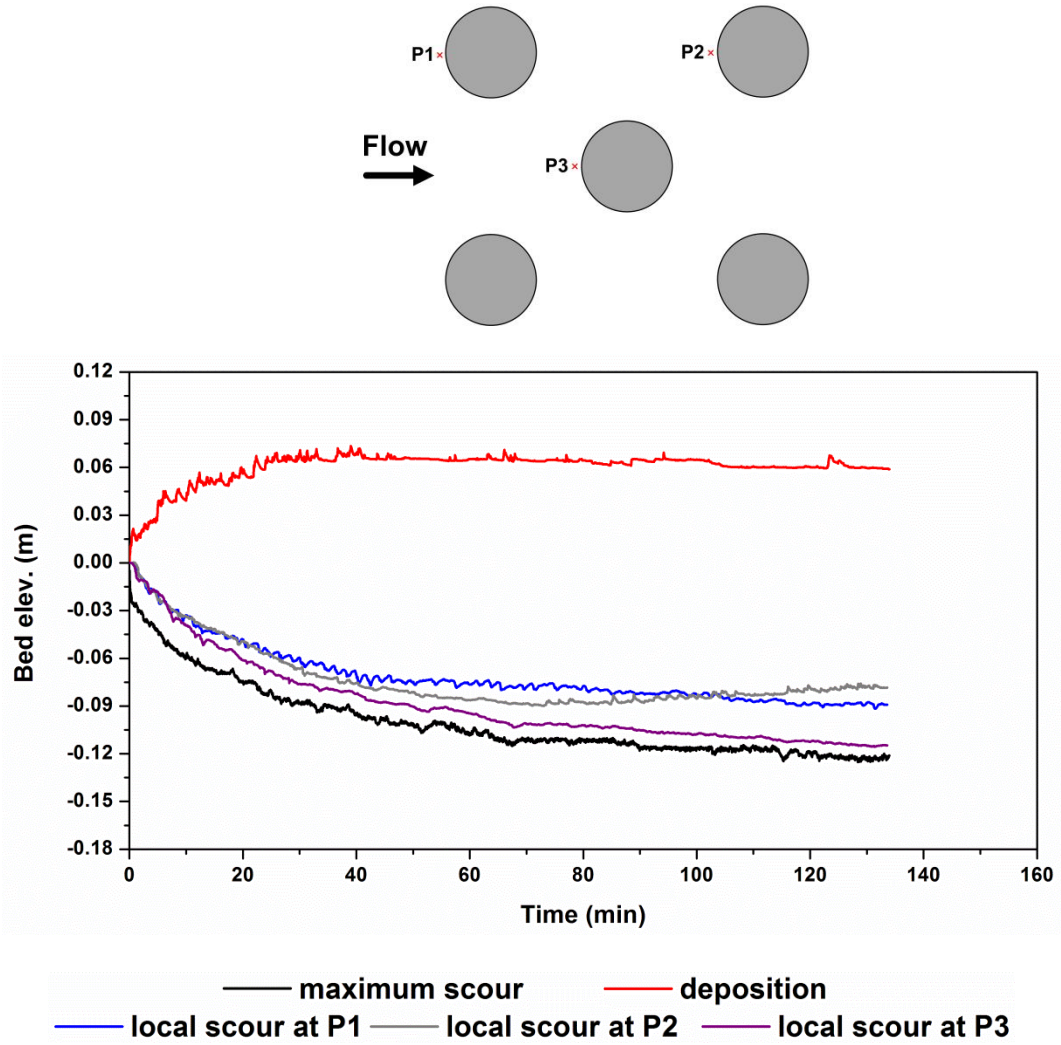


Fig. 6.10 Time evolution of scour and deposition around the cylinder group with the staggered arrangement of $s / D = 5.0$.

most exposed cylinders to flow, which is consistent with that observed by Sumer et al. (2002). The maximum scour depth is estimated to 0.124 m, which is approximately 20 % larger than that of the cylinder group of the grid arrangement ($s / D = 5.0$). However, the maximum scour depth is mostly identical to that of the cylinder group of the grid arrangement ($s / D = 2.5$). It can be seen that at an initial time, the evolution of the local scour at the nose of the cylinders is slower than that of the maximum scour. This is due to different mechanisms that at the initial time, the local scour occurs at the sides of the cylinders because of acceleration of flow and after few minutes, it takes place at the nose of the cylinders where turbulent horseshoe vortices dominate. The local scour depth at the

nose of the front cylinder, P1, is estimated to 0.09 m, which is same as that obtained at the cylinder group of the grid arrangement (s / D = 5.0) due to the undisturbed flow properties. The scour depth at the upstream of the rear cylinder shows a similar trend of that of the grid arrangement (s / D = 5.0), whereas the corresponding scour depth of 0.08 m is larger than that attained at the cylinder group of the grid arrangement (s / D = 5.0), which is 0.055 m. This is attributed to presence of the center cylinder, which certainly increases in the magnitude of horseshoe vortex system due to high interaction of flow. In the cylinder group with the staggered arrangement, a strong gap flow emerges with high velocities upstream and downstream of the center cylinder. The flows push shear layers shed from the one of the front cylinders to pass through the gap region, which give rise to acceleration of flow in the gap region and an increase of magnitude of vortex shedding (Borazjani and Sotiropoulos, 2009). Then, through the interactions with the center cylinder, the dynamics of the flow trigger a sequence of very complicated turbulence structure that enhance the bed load transport and scour process. In the same manner, a strong gap flow triggered from the center cylinder is advected further downstream, which impinges on horseshoe vortex system and flow velocity. Thus, the scouring of the bed is much stronger than that of the grid arrangement (s / D = 5.0) around the upstream of the rear cylinders. This result demonstrates that the variation of cylinder configuration not only impinges on the scour depth around individual cylinders, but also modifies the location of the maximum scour depth. This is identified that the LES coupled with sediment transport and morphodynamic models in physics-based manner reproduce complex flow structures and successfully implements physical transport phenomena around the cylinder group with the staggered arrangement.

6.3.3 Maximum local and global scour

As shown in above sections, the impact of the cylinder spacing, s / D, at the cylinder groups with the grid arrangement gives rise to the significant variation of the local and global scour. Fig. 6.11a shows the computed maximum scour depth versus the gap between cylinders, $G = (s - D) / D$, together with measurements of Ataie and Beheshti (2006). In this figure, the maximum scour depth is normalized by the scour depth at a single cylinder. It can be seen that the maximum scour depth increases with a decrease in the gap, G, and it is consistent with the scour of a single cylinder beyond G = 4.0. For G < 2.0, the maximum

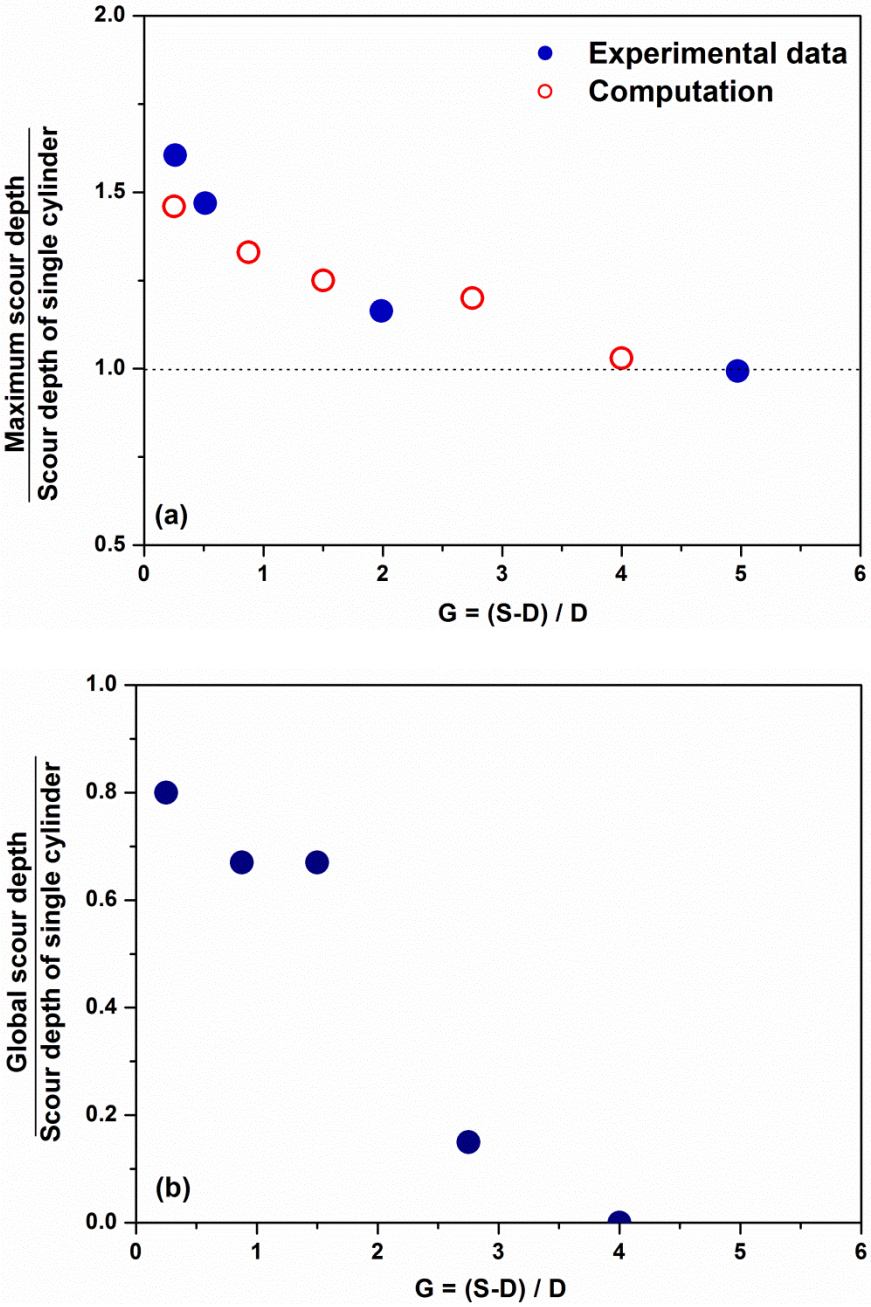


Fig. 6.11 Time evolution of scour and deposition around the cylinder group with the staggered arrangement of $s / D = 5.0$.

scour depth increases dramatically with decreasing the gap, G, whereas it decreases with an increases in the gap. This tendency has similar features to that of two cylinders with the side-by-side arrangement (Kim et al., 2013). The computed maximum scour depth is in

good agreement with measurement data.

Unlike the scour around a single cylinder, the global scour, which is a specific characteristic, occurs around the cylinder groups. Because the global scour depth varies with the locations around the cylinder groups, in this study, we suppose the mean global scour depth is practically equivalent to the scour depth at the center of the cylinder groups. Fig. 6.11b presents the computed global scour depth around the cylinder groups with the grid arrangement normalized by the scour depth of a single cylinder with respect to the gap between cylinders, G. The global scour depth increases with a reduction in the gap, G, and it becomes negligible beyond approximately $G = 3.0$. This implies, partly that the increase in turbulence due to the interference effect is much pronounced as the gap, G, of the cylinder groups decreases.

6.4 SUMMARY

Three-dimensional numerical computations were performed to examine local and global scour around cylinder groups. For computing the detailed hydrodynamic and morphodynamic, the LES coupled with sediment transport in a Lagrangian framework and morphodynamic models was used. The sediment was considered as spherical particles moving with the fluid.

The square cylinder groups (2×2) were selected and diverse cylinder spacing was considered to analyze the effect of cylinder spacing of the cylinder groups on scour and deposition processes. The morphological evolution of the bed and the degree of scour and deposition strongly depended on the cylinder spacing (s / D). When the cylinder spacing was smaller than 3.75, the scour holes around individual cylinders of the cylinder groups were overlapped, and thus global scour occurred. It was caused by an increase in turbulence due to interference effect from the lateral cylinders, which led to a considerable increase in scouring of the bed around the cylinder groups. Even though the magnitude of turbulent horseshoe vortices significantly decreased due to the presence of the upstream cylinders, the bed elevation descended around the upstream of the rear cylinders because of the increase in turbulence stress produced by the interference effect. On the other hand, as the cylinder spacing (s / D) was larger than 3.75, the local scour was observed around individual cylinders of the cylinder groups. While the scour process around the front cylinders was similar to that of a single cylinder, the local scour around the rear cylinders

was considerably influenced by the presence of the upstream and the migration of deposition behind the front cylinders.

The change in the configuration of the cylinder group affected the morphological process and the degree of scour. For the cylinder group with the staggered arrangement, the location of the maximum scour depth was changed from the adjacent front cylinders to the nearby center cylinder of the cylinder group and the maximum scour depth was deeper than that around the cylinder group of the grid arrangement. In addition, the presence of the center cylinder led to an increase of local scour around the rear cylinders.

The maximum scour depth increased as the cylinder spacing decreased, and the computed results were in good agreement with experimental data. Also, the computed global scour showed a decreasing trend with increasing cylinder spacing.

CHAPTER 7 CONCLUSIONS

7.1. CONCLUSIONS

This thesis provides a better understanding of flow and bed morphology around finite patches in open channels by means of laboratory experiments. A two-dimensional depth-averaged model capable of simulating flow and morphological changes with vegetation is developed, and validated by comparing the experimental data. Furthermore, a computational study is carried out to provide a physical insight into transport and scour process around cylinders by employing LES coupled with sediment transport and morphodynamic models.

In Chapter 2, the bed morphological changes in response to a finite patch, consisting of the emergent and submerged cylinders in an open channel were investigated using laboratory experiments. Two hydraulic conditions, which were below and above the threshold of sediment motion, were tested with various configurations of the patch as well as the submergence ratio. The finite patch in open channel flows altered flow patterns, which significantly reduced the mean velocities in and behind the patch and caused the diversion of flow from the patch, depending on the patch density. The bed morphological changes near the finite patch were highly influenced by altered flows.

When the bed shear stress was below the threshold of motion (Case 1), the erosion was primarily observed not only opposite the patch due to the acceleration of flow but also near the leading edge of the patch because of elevated turbulence levels and the diversion of a flow. We found that the scour depth observed both opposite the patch and near the leading edge was strongly dependent on the flow blockage, i.e., the product of obstruction ratio and the patch density. The submergence ratio affected the magnitude of erosion at both regions, which was reduced as the submergence ratio increased since the turbulence levels and diversion of flow were weakened. The degree of the scouring depth increased with the flow blockage.

For Case 2, in which the bed shear stress exceeded the critical values of sediment motion, unlike the Case 1, the sediment deposition as well as the erosion was observed near the finite patch in the open channel flows. While the trend of erosion was similar to that of

Case 1, the difference between the emergent and submerged patch was not evident. The sediment deposition began upstream of the patch, and local erosion occurred from the leading edge of the patch to downstream, after which deposition was observed just beyond the scoured region that was consistent with the interior adjustment region. It was found that sediment deposition near the finite patch was strongly influenced by the flow blockage, so that as the patch density increased, the deposition rate became lower since higher patch densities led to higher diversion of flow, and thus it carried away much more sediment loading from the patch. Also, greater influences on deposition near the patch were the obstruction ratio and the ratio of flow rate through the patch, whereas the length scale of the patch had a negligible effect on sediment deposition.

In Chapter 3, we examined morphological changes in open channel flows with a finite patch of vegetation by means of laboratory experiments and numerical simulations. Four cases were tested with three different types of patches and without the patch to elucidate the influence of the patch in open channel flows with erodible bank. A two-dimensional depth averaged model was proposed to simulate flow and sediment transport in open channels with vegetation, and the model was applied to open channel flows with a finite patch of vegetation experimentally conducted in this study.

For non-vegetated channel, channel widening due to bank erosion occurred symmetrically, whereas when the finite patch was added in an open channel, the bank was considerably eroded directly opposite the patch, and sediment was deposited within and downstream of the patch. Flow direction was affected by the patch, which is dependent on the patch density and it caused channel geometric changes. Local erosions were observed near the lateral edge of the patch due mainly to diversion of flow and those increased with an increase in the patch density. For the LD and MD patches, small-scale scours took place at the vicinity of cylinders, which has negligible effects, whereas localized scour was observed near the leading edge of the patch in the result of the HD because the increase in the patch density induced high turbulence kinetic energy and horseshoe vortices, which reflected high bed shear stress. The sediment deposition increased within and around the patch as the patch density decreased, and the widening rate due to bank erosion not only increased with increasing patch density but also it is significantly influenced by the flow rate and channel slope.

Numerical simulations were performed and the sensitivity of numerical model to parameters associated with sediment transport within the patch was examined. The results revealed that morphological behaviour near the patch was affected by drag coefficient and evaluation of bed shear stress in the patch. The present numerical model simulated reasonably morphological changes with a finite patch, and especially, the predicted processes of bank erosion and the amount of sediment deposition within and around the patch showed satisfactory agreement with the experimental data. On the other hand, it was shown that, as the patch density became high, the depositional distances through the patch were under-predicted because the local scour caused by high shear stress due to the elevated turbulence from flow interference could not be captured. From the examinations of sediment deposition near the patch, it was found that the under-prediction of depositional distance was due to effect of elevated turbulence from each cylinder which was negligible for the LD and MD. The flow rate through the opposite part of the patch increased with increasing time and with lateral bank erosion. The influence of ratio of the patch width and length was investigated and the results showed that the widening rate and sediment deposition were significantly influenced by the ratio of patch width, but the ratio of patch length had little impact on them. It can be concluded that the present computational model could capture the important features of morphological behaviour within and around the finite patch of vegetation with erodible bank.

In Chapter 4, the local scour pool around finite patches of vegetation was investigated by means of laboratory experiments and numerical computations. To investigate impacts of spacing between patches with various patch densities on morphological changes, diverse ratio of the patch width was considered. The finite patches of vegetation were modeled as circular cylinders and bamboo sticks.

The local scour patterns around the patches were quite different from those of solid objects. For local scour around the solid objects, it was largely observed in front of the solid ones. On the other hand, the local scour at the leading edge of the patches of vegetation was significantly weakened, and the scour pool was developed between or downstream of the patches. It was shown that the scour pool began to be developed with $2W_v/W > 0.2$ and $2\lambda W_v > 1.0$. The depth of scour pool produced by the patches increased almost linearly with an increase in the flow blockage regardless of the submergence ratio.

Also, the volume of the scoured region as the aquatic habitats and shelter increased with increasing flow blockage and it slightly decreased as the submergence ratio increased.

A two-dimensional computational model was applied to flow and morphological changes with finite patches of vegetation. Through comparison with experimental data, computational results were in good agreement as the scour pool was developed between or downstream of the patches, which indicated that the scour pool caused by patches was attributed to largely two-dimensional flow response. In particular, the lateral erosion induced by sand-sliding near the patch was reasonably captured by adopting the bed correction model. If the bed correction model was not employed in the computations, the depth of scour pool was over-predicted and the lateral erosion by sand-sliding was not reproduced. From the extensive angle of repose in the bed correction model, it was found that the critical angle of repose of 35° was in best agreement with experimental data in terms of the lateral bed profiles and maximum scour depth. Also, the impact of critical angle of repose in the bed correction model on the bed profiles and maximum sour depth increased with increasing flow blockage.

Therefore, a two-dimensional computational model can adequately resolve local scour pool between or downstream of the finite patch of vegetation because the scour is driven by the increase in bed shear stress due to enhanced flow. Our results showed that a present computational model adopting the bed correction model for computing local scour pool with finite patches of vegetation was useful and practical. The computational model can be used for designing patches of vegetation in streams for ecological restorations.

In Chapter 5, a computational study was performed to investigate local scouring around two cylinders with the side-by side and tandem arrangements, which can be seen in natural streams such as bridge piers or colonies of rigid vegetation. The LES coupled with sediment transport and morphodynamic models which were directly linked with effects of the instantaneous flow properties is applied.

For flow field through cylinders, the measured data of Liu et al. (2008) was used to verify the flow model by means of the streamwise velocities and turbulence intensities at several points. The reasonable agreement between computed and measured data was shown with satisfactory accuracy. For the scour patterns, scour depth and time evolution of scour around a single circular cylinder, the recent experimental data and computed results

of Khosronejad et al. (2012) is used to validate the model. The computed scour patterns at the equilibrium stage and the growth rate of scour were compared with experimental data and both of them were in a good agreement with experimental data. In addition, the computed results were compared with simulated results of Khosronejad et al. (2012) who used URANS model with k-ω turbulence closure and it was found that the LES results performed herein were consistently in a better agreement with experimental data than URANS results, which implied that the local erosion induced by horseshoe vortex system around a cylinder was captured accurately.

Numerical simulations with various distances of cylinders were carried out to study the effect of cylinder spacing on scour and deposition patterns, time evolution of scour and local scour depth. For the side-by-side arrangement, when the s / D is greater than 2.5, the local scour and deposition patterns are similar to those of a single cylinder, whereas the two scour holes were overlapped and significant depositions were observed at the downstream and between cylinders due to the effect of jet-like flow as the s / D is smaller than 3.75. The maximum scour depths were observed at the angle of approximately 40◦ and the local scouring at the nose of cylinders was approximately 88 % of the maximum scour depth, which was slightly lower than that of a single cylinder (94 %). The local scouring in front of both cylinders is mostly identical on each other in terms of the scour depth and time evolution of scour, and local scour and deposition patterns were almost symmetric along the section of center in streamwise direction. For the tandem arrangement, the upstream cylinder affected the local scouring at the rear cylinder, so that the local scouring at the nose of the rear cylinder was significantly weakened or the sediment was accumulated at this region, while the bed evolution of scour at the nose of front cylinder showed similar trends of scour of a single cylinder. When s / D was smaller than 3.75, the effect of horseshoe vortices at the nose of the rear cylinder was significantly reduced, whereas the local scour increased with cylinder spacing as s / $D \geq 3.75$, which implied that the influence of presence of upstream cylinder decreased with increases in cylinder spacing. Maximum scour depth for the side-by-side cases exhibited a growing trend with decreases in distances of cylinders, while for tandem cases, it increased with distances of cylinders and it decreased gradually beyond the peak point at $G \approx 2.0$. The computed maximum scour depths of values and trends were in a reasonable agreement with measured data

reported by Hannah (1978) and Ataie and Beheshti (2006) which indicated that our model was able to estimate accurately local scour depth around cylinders.

To our knowledge, this was first three-dimensional simulation to investigate local scour and deposition processes and estimate maximum scour depth around cylinders using LES. It was found that the LES coupled with sediment transport and morphodynamic models was able to capture all erosion and deposition phenomena through cylinders with high accuracy. Thus, it can be expanded to investigations of flow and morphodynamics through multi-cylinders with various arrangements such as patches of vegetation for river restorations.

In Chapter 6, a numerical study was performed to examine local and global scour around cylinder groups. For computing the detailed hydrodynamic and morphodynamic, the LES coupled with sediment transport in a Lagrangian framework and morphodynamic models was employed. The sediment was considered as spherical particles moving with the fluid.

The square cylinder groups (2×2) were selected and diverse cylinder spacing was considered to analyze the effect of cylinder spacing of the cylinder groups on scour and deposition processes. The morphological evolution of the bed and the degree of scour and deposition strongly depended on the cylinder spacing (s / D). When the cylinder spacing was smaller than 3.75, the scour holes around individual cylinders of the cylinder groups were overlapped, and thus global scour occurred. It was caused by an increase in turbulence due to interference effect from the lateral cylinders, which led to a considerable increase in scouring of the bed around the cylinder groups. Even though the magnitude of turbulent horseshoe vortices significantly decreased due to the presence of the upstream cylinders, the bed elevation descended around the upstream of the rear cylinders because of the increase in turbulence stress produced by the interference effect. On the other hand, as the cylinder spacing (s / D) was larger than 3.75, the local scour was observed around individual cylinders of the cylinder groups. While the scour process around the front cylinders was similar to that of a single cylinder, the local scour around the rear cylinders was considerably influenced by the presence of the upstream and the migration of deposition behind the front cylinders.

The change in the configuration of the cylinder group affected the morphological process and the degree of scour. For the cylinder group with the staggered arrangement, the

location of the maximum scour depth was changed from the adjacent front cylinders to the nearby center cylinder of the cylinder group and the maximum scour depth was deeper than that around the cylinder group of the grid arrangement. In addition, the presence of the center cylinder led to an increase of local scour around the rear cylinders.

The maximum scour depth increased as the cylinder spacing decreased, and the computed results were in a good agreement with experimental data. Also, the computed global scour showed a decreasing trend with increasing cylinder spacing.

REFERENCES

[1] Akilli, Hm Akar, A. and Karakus, C. (2004). Flow characteristics of circular cylinders arranged side-side in shallow water. *Flow Measurement and Instrument*. 15, 187-197.

[2] Amimi, A., Melville, B. W., Ali, T. M. and Ghazali, A. H. (2012) Clearwater local scour around pile groups in shallow-water flow. *Journal of Hydraulic Engineering*. 138(2),177-185.

[3] Ashida, K. and Michiue, M. (1972). Study on hydraulic resistance and bed-load transport rate in alluvial streams, *Proc. JSCE*. 201, 59-69.

[4] Ataie-Ashtiani B. and A. A Beheshti. (2006). Experimental investigation of clear-water local scour at pile groups. *Journal of Hydraulic Engineering*. 132(10), 1100-1104.

[5] Ballio, F., Radice, A. and Dey, S. (2010). Temporal scales for live-bed scour at abutments. *Journal of Hydraulic Engineering*. 136(7), 395-402.

[6] Barfield, B. J., E. W. Tollner, and J. C. Hayes. (1979). Filtration of sediment by simulated vegetation: I. Steady-state flow with homogeneous sediment. *Trans. Am. Soc. Civ Eng. Soil Water Div.*, 4451, 540-556.

[7] Bennett, S., Pirim, T. and Barkdoll, B. (2002). Using simulated emergent vegetation to alter stream flow direction within a straight experimental channel. *Geomorphology*. 44, 115-126.

[8] Bennett, S., Wu, W., Alonso, C. and Wang, SSY. (2008). Modeling fluvial response to in-stream woody vegetation: implications for stream corridor restoration. *Earth surface Processes and Landforms*. 33, 890-909.

[9] Borazjani, I. and Sotiropoulos, F. (2009). Vortex-induced vibration of two cylinders in tandem arrangement in the proximity-wake interference region. *Journal of Fluid Mechanics*. 621, 321-364.

[10] Bouma, T. J., Temmerman, S., Duren, L. A., Martini, E., Vandenbruwaene, W., Callaghan, D. P., Balke, T., Biermans, G., Klaassen, P. C., Steeg, P., Dekker, F., Koppel, J., Vries, M. B. and Herman, P. M. J. (2013). Organism traits determine the

strength of scale-dependent bio-geomorphic feedbacks: A flume study on three intertidal plant species. *Geomorphology*. 180-181, 57-65.

[11] Bouma, T, J., van Duren, L. A., Temmerman, S., Claverie, T., Blanco-Garcia, A., Ysebaert, T. and P. M. J. Herman. (2007). Spatial flow and sedimentation patterns within patches of epibenthic structures: combining field, flume and modeling experiments. *Continental Shelf Research.* 27, 1020-1045.

[12] Carmo, B.S. and Meneghini, J.R. (2006). Numerical investigation of the fow around two circular cylinders in tandem. *Journal of Fluids and Structures*, 22, 979-988.

[13] Chambers, P A. and Prepas, E. E. (1994). Nutrient dynamics in riverbeds - the impact of sewage effluent and aquatic macrophytes. *Water Research*. 28(2), 453-464.

[14] Chen, Z., Ortiz, A., Zong, L. and Nepf, H. M. (2012). The wake structure behind a porous obstruction and its implications for deposition near a finite patch of emergent vegetation. *Water Resources Research*. 48, W09517.

[15] Choi, S. –U and Kang, H. (2006). Numerical investigations of mean flow and turbulence structures of partly-vegetated open-channel flows using the Reynolds stress model. *Journal of Hydraulic Research.* 44(2), 203-217.

[16] Coulthard, T. (2005). Effects of vegetation on braided stream pattern and dynamics. *Water Resources Research.* 41, W04003.

[17] Crosato, A. and Saleh, M. S. (2010). Numerical study on the effects of floodplain vegetation on river planform style. *Earth surface Processes Landforms*. 36(6), 711-720.

[18] Darby, S. E. (1999). Effect of riparian vegetation on flow resistance and flood potential. *Journal of Hydraulic Engineering*. 125(5), 443-454.

[19] Dargahi, B. (1989). The turbulent flow field around a circular cylinder. *Experiments in Fluid*. 8, 1-12.

[20] Dargahi, B. (1990). Controlling mechanism of local scouring. *Journal of Hydraulic Engineering*. 116(10), 1197-1214.

[21] Dunn, C. J. (1996). Experimental determination of drag coefficient in open channel with simulated vegetation. M. S. Thesis, University of Illinois at Urbana Champaign, Urbana, IL.

[22] De Ruiter JCC. (1993). Incipient motion and pick-up of sediment as function of local variables. Technical Report R 657-XI, Delft Hydraulics Laboratory, Delft, Netherlands.

[23] Edwards, P. J., Kolmann, J., Gurnell, A. M., Petts, G. E., Tockner, K. and Ward, J. V. (1999). A conceptual model of vegetation dynamics on gravel bars of a large alpine river. Wetlands Ecology and Management. 7, 141-153.

[24] Elliott, K. R. and Baker, C. J. (1985). Effect of pier spacing on scour around bridge piers. *Journal of Hydraulic Engineering.*111, 1105-1109.

[25] Engelund, F. (1974). Flow bed topography in channel bend. *Journal of the Hydraulics Division.* 100(11), 1631-1648.

[26] Escauriaza, C. and Sotiropoulos, F. (2011). Initial stages of erosion and bed form development in a turbulent flow around a cylindrical pier. *Journal of Geophysical Research,* 116, F03007.

[27] Ettem, R., Kirkil, G. and Muste, M. (2006). Similitude of large-scale turbulence in experiments on local scour at cylinders. *Journal of Hydraulic Engineering*. 132(1), 33-39.

[28] Euler, T., Zemke, J., Rodrigues, S. and Herget, J. (2012). Influence of inclination and permeability of solitary woody riparian plants on local hydraulic and sedimentary processes. *Hydrological Processes.* hyp.9655.

[29] Follett, E. and Nepf, H. M. (2012). Sediment patterns near a model patch of reedy emergent vegetation, *Geomorphology*. 179, 141-151.

[30] Gambi, M., Nowell, A. and Jumars, P. (1990). Flume observations on flow dynamics in Zostera marina (eelgrass) beds. *Marine Ecology Progress Series.* 61, 159-169.

[31] Hasegawa, K. (1984). Hydraulic research on planimetic forms , bed topographies and flow in alluvial rivers. *PhD thesis*, Hokkaido University(in Japanese).

[32] Hasegawa, K. (2000). Hydraulic characteristics of mountain streams and their practical application, *Lecture Notes of the 33rd Summer Seminar on Hydraul. Eng.*, JSCE, A-9-1-20, (in Japanese)

[33] Hannah, C. R. (1978). Scour at pile groups. Research Report. No 28-3, Civil Engineering Dept. Univ. of Canterbury: Christchurch; New Zealand.

[34] Hicken, E. J. (1984).Vegetation and river channel dynamics. *Canadian Geographer*. XXX III(2), 111-126.

[35] Hunter, C. J. (1991). *Better trout habitat*. Island, Washington, D. C.

[36] Huthoff, F., D. C. M. Augustijn. and S. J. M. H. Hulscher. (2007). Analytical solution of the depth-averaged flow velocity in case of submerged rigid cylindrical vegetation. *Water Resources Research*. 43, W06413.

[37] Iwagaki, Y. (1956). Hydrodynamical study on critical tractive force. *Proceeding of Japan society civil engineering*, JSCE, 41, 1-21 (in Japanese).

[38] Jang, C. –L. and Shimizu, Y. (2005). Numerical simulations of behavior of alternate bars with different bank strengths. *Journal of Hydraulic Research*. 43(6), 595-611.

[39] Jang, C. –L, Shimizu, Y. (2007). Vegetation effects on the morphological behavior of alluvial channels. *Journal of Hydraulic Research.* 45(6), 763-772.

[40] Kemp, J L., Harper, D M. and Crosa, G A. (2000). The habitat-scale ecohydraulics of rivers. *Ecological Engineering*. 16(1), 17-29.

[41] Khosronejad, A., Kang, S. and Sotiropoulos, F. (2012). Experimental and computational investigation of local scour around bridge piers. *Advance in Water Resour*ces. 37, 73-85.

[42] Khosronejad, A., Hill, C., Kang, S. and Sotiropoulos, F. (2013). Computational and experimental investigation of scour past laboratory models of stream restoration rock structures. *Advance in Water Resour*ces. 54, 191-207.

[43] Kikkawa, H., Kitagawa, A. and Ikeda, S. (1976). Flow and bed topography in curved open channels. *Journal of the Hydraulics Division.* 102(9), 1327-1342.

[44] Kim, H. S., Kimura, I. and Shimizu, Y. (2013). Impact of a patch of vegetation in open channel flows with erodible banks. *Journal of Hydraulic Research*. Submitted

[45] Kim, H. S., Kimura, I. and Shimizu, Y. (2013). Characteristics of bed morphological changes around a finite patch of vegetation. *Geomorphology*. Submitted

[46] Kim, H. S., Nabi, M., Kimura, I. and Shimizu, Y. (2013). Numerical investigation of local scour around cylinders in a turbulent flow. *Advance in Water Resources*. Submitted.

[47] Kimura, I. and Hosoda, T. (2004). Computations of 2D shallow mixing layers in open channel flows using a modified depth-averaged model. *Proc., 4th Int. Symp. On*

Environmental Hydraulics and 14th Congress of Asia and pacific Division (IAHR), 15-18 December 2004, Hong Kong, Balkema, Rotterdam, 981-987.

[48] Kirkil, G., Constantinescu, G. and Ettema, R. (2009). Detached eddy simulation investigation of turbulence at a circular pier with scour hole. *Journal of Hydraulic Engineering*. 135(11), 888-901.

[49] Koken, M. and Constantinescu, G. (2008). An investigation of the flow and scour mechanisms around isolated spur dikes in a shallow open channel: 1. Conditions corresponding to the initiation of the erosion and deposition process. *Water Resources Research*. 44, W08406.

[50] Kovacs, A. and Parker, G. (1994). A new vectorial bedload formulation and its application to the time evolution of straight river channels. *Journal of Fluid Mechanics*. 267, 153-183.

[51] Kuhnle, R. A., Alonso, C. V. and Jr. Shields, F. D. (2002). Local scour associated with angled spur dikes. *Journal of Hydraulic Engineering*. 128(12), 1087-1093.

[52] Launder, B. E. and Spalding, D. B. (1974). The numerical computation of turbulent flow. *Computer Methods in Applied Mechanics and Engineering*. 3, 269-289.

[53] Lee, SO, Sturm, T. W. (2009). Effect of sediment size scaling on physical modeling of bridge pier scour. *Journal of Hydraulic Engineering*. 135(10), 793-802.

[54] Leu, J. M., Chan, H. C., Jia, Y., He, Z. and Wang, S S Y. (2008). Cutting management of riparian vegetation by using hydrodynamic model simulations. *Advance in Water Resources*. 31, 1299-1308.

[55] Liu, D., Diplas, P., Fairbanks, J. D. and Hodges, C. C. (2011). An experimental study of flow through ridge vegetation. *Journal Geophysical Research* , 113, F04015.

[56] Liu, S. and Shen, Y. M. (2008). Flow structure and sediment transport with impacts of aquatic vegetation. *Journal of Hydrodynamics*. 20(4), 461-468.

[57] Li, S. S. and Millar, R. G. (2010). A two-dimensional morphodynamic model of gravel-bed river with floodplain vegetation. *Earth surface Processes and Landforms*. 36(2), 190-202.

[58] Lopez, F. and Garcia, M. (1997). Open channel flow through simulated vegetation: turbulence modeling and sediment transport, Wetland Research Program Technical Report WRP-CP-10, Waterways Experiment Station, Vicksburg, MS.

[59] Lutz, K. J. (2007). *Habitat improvement for trout streams*. Pennsylvania Fish & Boat Commission, Harrisburg.

[60] Mayer-Peter, E. and Muller, R. (1948). Formulas for bed-load transport. *Proceeding of 2nd Congress*, IAHR, Stockholm.

[61] Maxey, M. R. and Riley, J. J. (1983). Equation of motion for a small ridge sphere in a nonuniform flow. *Physics of Fluids.* 26(4), 883-889.

[62] McLaughlin, J. B. (1991). Inertial migration of a small sphere in linear shear flows. *Journal of Fluid Mechanics*. 224, 261-274.

[63] Mei, R. (1992). An approximate expression for the shear lift force on a spherical particle at finite Reynolds number. *International Journal of Multphase Flow.* 18(1), 145-147.

[64] Melville, B. W. and Coleman, S. (2000) Bridge scour. Water Resources Publication:Colo.

[65] Millar, R. G. and Qucik, M. C. (1993). Effect of bank stability on geometry of gravel rivers, *Journal of Hydraulic Engineering*. 119(12), 1343-1363.

[66] Millar, R. G. (2000). Influence of bank vegetation on alluvial channel patterns. *Water Resources Research*. 36(4), 1109-1118.

[67] Morsi, S. A. and Alexander, A. J. (1972). An investigation of particle trajectories in two-phase flow systems. *Journal of Fluid Mechanics.* 55(2), 193-208.

[68] Nabi, M, Vriend, de H. J., Mosselman, E., Sloff, C. J. and Shimizu, Y. (2012). Detailed simulation of morphodynamics: 1. Hyrodynamic model. *Water Resources Research.* 48, W12523.

[69] Nabi, M, Vriend, de H. J., Mosselman, E., Sloff, C. J. and Shimizu, Y. (2013). Detailed simulation of morphodynamics: 2. Sediment pick-up, transport and deposition. *Water Resources Research*. 49, 4775-4791.

[70] Nepf, H. M. (2012). Hydrodynamics of vegetated channels. *Journal of Hydraulic Research*. 50(3), 262-279.

[71] Nepf, H. M. (2004). Vegetated flow dynamics, *Coastal and Estuarine studies*. 59, 137-163.

[72] Nepf, H. M. and Vivoni, E. R. (1999). Flow structure in depth-limited vegetated flow. *Journal of Geophysical Research*. 105(28), 547-557.

[73] Nezu, I. and Nakagawa, H. (1993). *Turbulence in open channel flows*. IAHR Monograph, Balkema, Rotterdam, The Netherlands.

[74] Nicolle, A. and Eames, I. (2011). Numerical study of flow through and around a circular array of cylinders. *Journal of Fluid Mechanics.* 679, 1-31.

[75] Olsen, N. and Kjellesvig, H. M. (1998). Three dimensional numerical flow modeling for estimation of maximum local scour depth. *Journal of Hydraulic Research.* 36(4), 579-590.

[76] Olsen, N. and Melaaen, C. (1993). Three dimensional calculation of scour around cylinders. *Journal of Hydraulic Engineering.* 119(9), 1048-1054.

[77] Raudkivi, A. J. (1990). *Loose boundary hydraulics*. 3rd edition, Pergamon Press.

[78] Richardson, E. V. and Davis, S. R. (2001). Evaluating scour at bridges. *Hydrulic Enineering Circular No. 18* (HEC-18). *Rep. No. FHWA NHI 01-001*, Federal Highway Administration; Washington, D.C.

[79] Rodi, W. (1993). *Turbulence modeling and their application in hydraulics*. Monograph, IAHR, Delft, The Netherlands.

[80] Rodrigue-Gervais, K., Biron, P. M. and Lapointe, M. F. (2011). Temporal development of scour holes around submerged stream deflectors. *Journal of Hydraulic Engineering*. 137(7), 781-785.

[81] Rominger, J. T., Lightbody, A. and Nepf, H. M. (2010). The Effects of Added Vegetation on Sand Bar Stability and Stream Hydrodynamics. *Journal of Hydraulic Engineering*. 136(12), 994-1002.

[82] Rominger, J. T. and Nepf, H. M. (2011). Flow adjustment and interior flow associated with a rectangular porous obstruction. *Journal of Fluid Mechanics.* 680, 636-659.

[83] Roulund, A., Sumer, B. M., Fredsoe, J. and Michelsen, J. (2005). Numerical and experimental investigation of flow and scour around a circular pile. *Journal of Fluid Mechanics.* 534, 351-401.

[84] Schmeeckle, M. W. and Nelson, J. M. (2003). Direct numerical solution of bedload transport using local, dynamic boundary condition. *Sedimentology*. 50, 279-301.

[85] Schmeeckle, M. W., Nelson, J. M., Pitlick, J. and Bennett, J. P. (2001). Interparticle collosion of natural sediment grains in water. *Water Resources Research*. 37(9), WR000531.

[86] Schulz, M., Kozerski, H. P., Pluntke, T. and Rinke, K. (2003). The influence of macrophytes on sedimentation and nutrient retention in the lower river spree (Germany). *Water Research*. 37(3), 569-578.

[87] Sheppard, D. M. and Renna, R. (2005). *Bridge scour manual*. Florida Department of Transportation, 605 Suwannee street, Tallahassee, Florida.

[88] Shields, F. D., Jr., Cooper, C. M. and Knight, S. S. (1995). Experiment in stream restoration. *Journal of Hydraulic Engineering*. 121(6), 494-502.

[89] Shimizu, Y. and Tsujimoto, T. (1994). Numerical analysis of turbulent open-channel flow over vegetation layer using a k-eps turbulence model, *Journal of Hydroscience and Hydraulic Engineering*. 11(2), 57-67.

[90] Smagorinsky, J. S. (1963). General circulation experiments with the primitive equations. Monthly weather review, 91, 99-164.

[91] Stoessor, T., Kim, S. J. and Diplas, P. (2010). Turbulent flow through idealized emergent vegetation. *Journal of Hydraulic Engineering*. 136(12), 1003-1017.

[92] Stoesser, T., Salvador, G. P., Rodi, W. and Diplas, P. (2009). Large eddy simulation of turbulent flow through submerged vegetation. *Transport and porous media*. 78(3), 347-365.

[93] Stone, B. M. and H. T. Shen. (2002). Hydraulic resistance of flow in channels with cylindrical roughness. *Journal of Hydraulic Engineering*. 128(5), 500-506.

[94] Sumner, D., Price, S. J. and Païdoussis, M. P. (2000). Flow-pattern identification for two staggered circular cylinders in cross-flow. *Journal of Fluid Mechanics*. 411, 263-303.

[95] Sumer, B. M. and Fredsøe, J. (1998). Wave scour around group of vertical piles. *Journal of Waterway, Port, Coastal and Ocean Engineering*. 124(5), 248-256.

[96] Sumer, B. M. and Fredsøe, J. (2002). *The mechanics of scour in the marine environment*. World Scientific.

[97] Sumer, B. M., Bundgaard, K. and Fredsøe, J. (2005). Global and local scour at pile groups. *International Journal of Offshore and Polar Engineering*. 15(3), 204-209.

[98] Takemura, T. and Tanaka, N. (2007). Flow structures and drag characteristics of a colony-type emergent roughness model mounted on a flat in uniform flow. *Fluid Dynamics Research*. 39, 694-710.

[99] Tal, M. and Paola, C. (2010). Effects of vegetation on channel morphodynamics: results and insight from laboratory experiments. *Earth Surface Processes and Landforms*. 35(9), 1014-1028.

[100] Tal, M. and Paola, C. (2007). Dynamic single-thread channels maintained by the interactions flow and vegetation. *Geology*. 35(4), 347-350.

[101] Tanino, Y. and Nepf, H. M. (2008). Laboratory investigation of mean drag in a random array of rigid, emergent cylinders, *Journal of Hydraulic Engineering*. 134(1), 34-41.

[102] Thompson, D. M. (2002). Channel-Bed scour with high versus low deflectors. *Journal of Hydraulic Engineering*. 128(6), 640-643.

[103] Tominaga, A., Nagao, M. and Nezu, I. (1999). Flow structure and momentum transport processes in curved open channels with vegetation. *Proceeding of 28th congress of International Association of hydraulic Research.* Technical University of Graz, 22-27 August, Austria (CD-ROM).

[104] Tsujimoto, T. (1998). Development sand island with vegetation in fluvial fan river under degradation. *Water Resources Engineering '98*. 1, 574-579.

[105] Tsujimoto, T. and Kitamura, T. (1995). Lateral bed load transport and sand-ridge formation near vegetation zone in an open channel. *Journal of Hydroscience and Hydraulic Engineering*. 13, 35-45.

[106] Tsujimoto T. (1999). Fluvial processes in streams with vegetation. *Journal of Hydraulic Research.* 37(6), 789-803.

[107] Unger, J. and Hager, W. H. (2007). Down-flow and horseshoe vortex characteristics of sediment embedded bridge piers. *Experiments in Fluid*. 42, 1-19.

[108] White, B. and Nepf, H. M. (2007). A vortex-based model of velocity and shear stress in a partially vegetated shallow channel. *Water Resources Research*. 44, W01412.

[109] Wu, J., Welch, L. W., Welsh, M. C., Sheridan, J. and Walker, G. J. (1994). Spanwise wake structures of a circular-cylinder and 2 circular cylinders in tandem. *Experimental Thermal and Fluid Science*. 9(3), 299-308.

[110] Wu, W. and He, Z. (2009). Effects of vegetation on flow conveyance and sediment transport capacity. *International Journal of Sediment Research*. 24, 247-259.

[111] Wu, W., Shields, F. D. Jr., Bennett, S. and Wang, S S Y. (2005). A depth-averaged two-dimensional model for flow, sediment transport, and bed topography in curved channels with riparian vegetation. *Water Resources Research.* 41, W03015.

[112] Yamaguchi, S. and Izumi, N. (2005). Weakly nonlinear analysis of dunes by the use of a sediment transport formula incorporating the pressure gradient. *Proceeding of the 4th IAHR Symposium on River, Coastal and Estuarine Morphodynamics, RCEM 2005*, Urbana, Illinois, USA, 813-820.

[113] Zhao, M., Cheng, L. and Zang, Z. (2010). Experimental and numerical investigation of local scour around a submerged vertical circular in steady currents. *Coastal Engineering*. 27, 709-721.

[114] Zong, L. and Nepf, H. M. (2010). Flow and deposition in and around a finite patch of vegetation. *Geomorphology*. 116, 363-372.

[115] Zong, L. and Nepf, H. M. (2011). Spatial distribution of deposition within a patch of vegetation. *Water Resources Research*. 47, W03516.

[116] Zong, L. and Nepf, H. M. (2012). Vortex development behind a finite porous obstruction in a channel. *Journal of Fluid Mechanics.* 691, 368-391.